COSMOLOGICAL ASPECTS OF MINIMAL AND EXTENDED HIGGS SECTORS

DISSERTATION

ZUR ERLANGUNG DES DOKTORGRADES AN DER FAKULTÄT FÜR
MATHEMATIK, INFORMATIK UND NATURWISSENSCHAFTEN

FACHBEREICH PHYSIK DER UNIVERSIÄT HAMBURG

VORGELEGT VON
JULIA ANABELL ZIEGLER

HAMBURG, 2026

GUTACHTER:INNEN DER DISSERTATION:

Prof. Dr. Gudrid Moortgat-Pick

Dr. Bibhushan Shakya

ZUSAMMENSETZUNG DER PRÜFUNGSKOMMISSION:

Dr. Thomas Konstandin

Prof. Dr. Jochen Liske

Prof. Dr. Gudrid Moortgat-Pick

Prof. Dr. Peter Schleper

Dr. Bibhushan Shakya

VORSITZENDER DER PRÜFUNGSKOMMISSION:

Prof. Dr. Jochen Liske

DATUM DER DISPUTATION:

17. April 2026

VORSITZENDER DES FACH-PROMOTIONSAUSSCHUSSES PHYSIK:

Prof. Dr. Johannes Haller

LEITER DES FACHBEREICHS PHYSIK:

Prof. Dr. Markus Drescher

DEKAN DER FAKULTÄT MIN:

Prof. Dr.-Ing. Norbert Ritter

Abstract

Despite the huge success of the Standard Model (SM) of particle physics, many open problems indicate the need for New Physics. One particular extension of the SM is the Two Higgs doublet model with an additional complex scalar singlet (2HDMS). This model provides an enlarged scalar sector resulting in seven physical Higgs particles, of which one is a suitable candidate to explain dark matter (DM). In this work the DM and collider phenomenology of the 2HDMS is investigated. Representative benchmark points with light, intermediate-range and heavy masses for the DM candidate are chosen. The benchmark points are consistent with all theoretical and experimental constraints and, in some cases, also accommodate the excess around 95 GeV, observed in the $b\bar{b}$ channel at the Large Electron-Positron Collider (LEP) and in the $\gamma\gamma$ channel at the Large Hadron Collider (LHC). In terms of DM phenomenology, the focus is on matching the required DM relic density, as well as direct and indirect detection bounds of DM. In terms of collider phenomenology, the focus is on relevant signatures at the LHC and at proposed future lepton colliders, such as electron-positron colliders and a proposed muon collider.

The 2HDMS model, as well as other beyond-the-Standard Model (BSM) theories, can provide a first-order electroweak phase transition (EWPT), which proceeds via the formation of bubbles. A second focus of this work is the investigation of the wall velocity of expanding bubbles from first-order phase transitions (FOPTs) with symmetry breaking and with symmetry restoration. In standard symmetry-breaking FOPTs, the frictional pressure on the expanding bubble walls can be dominated by transition radiation, the process of one particle from the surrounding plasma passing into the bubble and radiating off an additional particle. This process is enhanced in the soft-momentum limit of the radiated particle, and is known to produce significant frictional effects that are proportional to the Lorentz factor γ of the bubble wall. This dependence of the frictional pressure on the Lorentz factor prohibits runaway behaviour of the bubble walls. The focus of this work is on the analogous pressure for phase transitions with symmetry restoration. It is shown that, in such transitions the pressure due to transition radiation can be negative for small and intermediate Lorentz factors, leading to a further acceleration of the bubble wall. However, for very large Lorentz factors the pressure approaches the same positive scaling as the standard symmetry-breaking scenarios. Therefore, the terminal Lorentz factor of the bubble wall can be significantly larger (by more than an order of magnitude) than in the corresponding symmetry-breaking scenario. This can carry important implications for various phenomenological applications, from gravitational waves (GWs) up to BSM physics.

Zusammenfassung

Trotz des großen Erfolgs des Standard Modells (SM) der Teilchenphysik, gibt es noch viele offene Probleme, die auf die Notwendigkeit neuer Physik hindeuten. Eine mögliche Erweiterung des SM is die Erweiterung um ein zusätzliches komplexes skalares Doublett und ein komplexes skalares Singulett, das sogenannte 'Two Higgs doublet model with an additional complex scalar singlet' (2HDMS). Dieses Modell bietet einen erweiterten skalaren Sektor und führt zu insgesamt sieben physikalischen Higgs-Teilchen, von welchen eines ein geeigneter Kandidat ist, um dunkle Materie (DM) zu erklären. In dieser Arbeit wird die Phänomenologie des 2HDMS-Modells mit Blick auf DM und Beschleunigerexperimente untersucht. Dafür werden repräsentative Benchmark-Szenarios mit unterschiedlichen Massen für den DM-Kandidaten ausgewählt - im Bereich leichter, mittlerer und schwerer Masse. Die ausgewählten Benchmark-Szenarios stimmen mit allen herkömmlichen theoretischen und experimentellen Grenzen überein und können in einigen Fällen sogar einen experimentellen Überschuss, der bei etwa 95 GeV im $b\bar{b}$-Kanal am Large Electron-Positron Collider (LEP) und im $\gamma\gamma$-Kanal am Large Hadron Collider (LHC) beobachtet wurde, berücksichtigen. Mit Hinblick auf die Phänomenologie von DM liegt der Fokus darauf, die experimentell vorhergesagte Dichte von DM im heutigen Universum zu erreichen. Außerdem werden experimentelle Grenzen von direkten und indirekten Detektionsexperimenten berücksichtigt. Mit Hinblick auf die Phänomenologie von Beschleunigerexperimenten mit Teilchenkollisionen liegt der Fokus auf experimentellen Signaturen, die relevant sind für den LHC und vorgeschlagene Leptonen-Teilchenbeschleuniger, wie Elektronen-Positronen-Beschleuniger und Myonen-Beschleuniger.

Das 2HDMS-Modell, sowie andere Theorien, die über das SM hinaus gehen, kann einen Phasenübergang erster Ordnung untergehen. Ein solcher Phasenübergang erfolgt über das Formen von Blasen-artigen Regionen der neuen Phase. Ein weiterer Fokus dieser Arbeit beschäftigt sich mit der Geschwindigkeit der sich ausdehnenden Blasen in solchen Phasenübergängen erster Ordnung, wobei Phasenübergänge mit Symmetrie-Brechung und mit Symmetrie-Wiederherstellung betrachtet werden. Dabei können die Teilchen des umgebenden Plasmas einen Reibungsdruck auf die Wände der Blasen auswirken. In standardmäßigen Übergängen mit Symmetrie-Brechung kann dieser Druck von einem Vorgang namens 'Transition Radiation' dominiert werden. Bei diesem Prozess strahlen Teilchen, die aus dem Plasma in die Blase übergehen, ein weiteres Teilchen ab. Dieser Prozess wird verstärkt, wenn der Impuls des abgestrahlten Teilchens gering ist. Der daraus resultierende Reibungsdruck ist proportional zum Lorentzfaktor γ der sich ausdehnenden Wand der Blasen. Diese Abhängigkeit vom Lorenztfaktor führt dazu, dass die Expansionsgeschwindigkeit der Blasen nicht unendlich beschleunigt werden kann, sondern ab einer bestimmten Geschwindigkeit stagniert. Der Fokus dieser Arbeit liegt darauf den äquivalenten Reibungsdruck in Phansübergängen mit Symmetrie-Wiederherstellung zu berechnen. Es wird gezeigt, dass der Druck in solchen Übergängen für niedrige Werte des Lorentzfaktors negativ sein kann, was zu einer zusätzlichen Beschleunigung der Expansion führt. Jedoch wird für hohe Werte des Lorentzfaktors die gleiche positive Proportionalität zum Lorentzfaktor erreicht, wie in Übergängen mit Symmetrie-Brechung. Der finale Lorentzfaktor kann daher deutlich höher sein in Übergängen mit Symmetrie-Wiederherstellung. Dies hat wichtige Konsequenzen für unterschiedliche phänomenologische Anwendungen, zum Beispiel für Gravitationswellen bis hin zu Physik, die über das SM hinaus geht.

List of publications

This thesis is based on the following scientific articles:

- [1] J. Dutta, J. Lahiri, C. Li, G. Moortgat-Pick, S. Farah Tabira, and J. A. Ziegler, “Dark matter phenomenology in 2hdms in light of the 95 gev excess”, *The European Physical Journal C*, vol. 84, no. 926, 2024, ISSN: 1434-6052. arXiv: 2308.05653 `[hep-ph]`
- [2] J. Dutta, J. Lahiri, C. Li, G. Moortgat-Pick, S. F. Tabira, and J. A. Ziegler, *Search for dark matter in 2hdms at lhc and future lepton colliders*, 2025. arXiv: 2504.14529 `[hep-ph]`,
  to appear in the European Physical Journal C
- [3] A. J. Long, B. Shakya, and J. A. Ziegler, *Bubble friction in symmetry-restoring transitions*, 2025. arXiv: 2511.10415 `[hep-ph]`,
  to appear in the Journal of High Energy Physics

Acknowledgements

This really is the hardest part of this thesis. I am not a person of big words and often find it hard to express my gratitude to others. But I will give it a try...

First, I would like to thank my supervisors Gudi Moortgat-Pick and Bibhushan Shakya. They have been very supportive and made collaborations a great experience which has led me to apply for postdoc positions. I would like to thank Gudi for supporting me since my Master's and for giving me the opportunity to pursue a Ph.D. in her group. From an early stage on she encouraged me to go to conferences, give talks and network with other scientists which has made the experience of my Ph.D. not only fun but also has helped me to build connections in this field. I would like to thank Bibhushan for his support throughout my Ph.D., always making time not only to discuss work but also to help me with applications for postdoc positions and many other things. Both, Gudi and Bibhushan, were not only professionally great supervisors but also on a personal level I truly appreciate them.

I would also like to thank my co-supervisor Kai Schmidt-Hoberg for helpful discussions in our Ph.D. meetings and Alexander Wesphal who used to be my co-supervisor in the beginning of my Ph.D. and continued being a mentor.

I would like to thank Jochen Liske for agreeing to be the chair for my defence and also for writing reference letters for my postdoc applications. I thank also the other members of the defence committee, Thomas Konstandin and Peter Schleper for their valuable involvement in this.

Especially, I would also like to thank my collaborators Juhi Dutta, Sven Ha, Jayita Lahiri, Cheng Li, Andrew Long and Sheikh Farah Tabira, and Andrew also for writing reference letters for my postdoc applications. I have learned a lot from these collaborators and am grateful for the experience. They are not only brilliant scientists but also great people on a personal level and I enjoyed working with them. Also, I am grateful to Merle Schreiber for introducing me to the work on DM phenomenology, where I continued her work during the master's. Also, I would especially like to point out my thanks to Sven, who, as a master's student, worked with me on another project which is not part of this thesis, but will be finished afterwards. He has done great work and it was a joy to work with him.

Throughout my Ph.D. I had the chance to present my work in a few invited talks for which I would like to thank Ziyang Zheng for inviting me to give a talk in the cosmology seminar at the University of Heidelberg. Also I would like to thank Mina Ghodsi Yengejeh for suggesting me for the CosmoVerse Journal Club and Mahdi Najafi and Enrico Specogna for organising it. Furthermore, I would like to thank Simon Williams for inviting me to give a talk in the seminar at the IPPP

in Durham. These seminars were not only helpful on a professional level but also a great experience personally.

Also, I would like to thank Gudi, Georg Weiglein and Johannes Braathen for organising the weekly 2HDM working group meeting and everyone who is part of this group and the meetings.

I would also like to thank Elizabeth Monteiro Duarte for always helping me with administrative questions as well as Nafiseh Sadat Sajjadi for help on my application for an extension.

There are so many more people who I have met during my Ph.D., either at Desy/University of Hamburg or at schools and conferences - many people who I have had great and insightful conversations with. It would be too much to name everyone who I keep in positive memory and who have increased my experience in academia. But I guess who remembers me, will know that I remember them.

Furthermore, I would like to thank the Desy/University of Hamburg community and everyone taking part in the seminars, journal club, Friday cookies and board games. Again, there are too many people to name all of them. I am especially grateful to my friends who I have met during my Ph.D. and who have been the greatest support along this path: Kateryna, Andrii, Panos, Jonas, Max, Julian, Jayita, Monika, Mohamed, Wrishik, Fran, Felix, Adriana, Romal, Marten, Guilherme, Sara, Alain, Jacopo, Mathias, Tabea, ... and I really have to stop this list now even if there are many more amazing people. I especially want to thank Wrishik and Fran for reviewing my thesis and Wrishik also for supporting me during the application process and for amazing tea from India. Also, I would like to especially thank Kateryna, Andrii and Panos for lots of great moments, advice and an amazing trip to Lillo. Thank you Kateryna and (Kateryna's) Fran for inviting us. You are amazing. I hope all of us can reunite soon.

Finally, I would like to thank my friends outside-of-physics and my family. My girl-gang: Brini, Lini, Kristin, Malin and Marlene. They are always there for me to lift me up in private matters as well as professional advice. My cousin Judith for being a friend, even if we can not see each other often, has helped me with much great advice and always cheered me on along my path of physics. My brother Maxi and his partner Saskia for their support along this path and in many other matters. And, of course, my mom for always being there for me. Her calm and kind soul has helped me to overcome lots of stressful periods and her believe in me gave me trust in myself.

Contents

1 Introduction

The Standard Model (SM) of particle physics is one of the most successful theories in science. It is of high predictive power and experimentally very well confirmed. In 2012 its particle content was completed with the discovery of a Higgs boson [4, 5], about 50 years after its prediction by Peter Higgs [6] in the 1960s. The SM describes three of the four fundamental forces of nature and how the elementary particles interact via these forces. Its predictions are tested in collider experiments which give insights on the interactions between elementary particles. By colliding particles, high energies are concentrated in a small point, revealing the physics at higher energies as in the early Universe. So far no significant deviation to the SM has been observed.

However, other observational probes of the early Universe, like observations of the cosmic microwave background (CMB) reveal a different picture. This radiation was emitted in the early Universe after free electrons and protons combined to form neutral hydrogen atoms. The Universe became transparent and light was able to stream freely between the neutral atoms. This radiation was first observed in the same decade as the prediction of the Higgs mechanism, in the 1960, by the radio-astronomers Wilson and Penzias [7]. Later, more elaborate measurements of the anisotropies in the CMB radiation revealed that the Universe largely consists of another unknown type of matter. Other observations made earlier, like observations of the rotation curves of galaxies already showed that there must be more matter in the Universe than the known visible matter. This unknown type of matter does not seem to interact electromagnetically and hence does not emit light, which led to it being called dark matter (DM). Observations show that it must make up about five times the amount of the known ordinary matter. Furthermore, it plays an important part in the formations of structures in the Universe via its gravitational interaction. Without this type of matter, galaxies could not have formed and our Universe would look very different today. Yet, this type of matter is not accounted for in the SM - one of the most successful theories of science.

Many beyond-the-Standard Model (BSM) theories have been proposed in order to explain DM and many experiments have been built in order to detect it. But this type of matter interacts only very weakly and so far no significant signals have been observed in any experiment, leading to tighter constraints on the parameters of various models but not yet to a confirmed detection.

In this work one of these models will be investigated, namely the Two-Higgs-doublet model extended by an additional complex scalar singlet (2HDMS). This model is a well-motivated extension of the SM, adding a doublet and a singlet to the scalar sector of the SM. Other than the SM which includes one physical Higgs boson, this model includes seven physical Higgs bosons, of which one has the correct properties to explain DM. The DM candidate will be called A_S in this work and is given rise by the imaginary component of the additional scalar singlet. It is massive, electrically neutral, colour neutral and stable.

But DM is not the only phenomenon that can be explained by this model. Recently a few excesses have been observed in collider experiments. These are not strong enough to claim the detection of a new particle, but there are weak hints towards new physics. For example there has been an excess around 95 GeV observed both at the former Large Electron-Positron Collider (LEP) [8] in the $b\bar{b}$ mode as well as in the $\gamma\gamma$ mode at the Large Hadron Collider (LHC) experiments CMS [9] and ATLAS [10]. This excess can be embedded in several BSM models with extended scalar sectors [11–41] and also in the 2HDMS [20, 42].

The *first main focus* of this work is the investigation of the parameter space of the 2HDMS model with respect to DM and collider phenomenology, where different benchmark points will be analysed, some of which can also accommodate the excess at 95 GeV mentioned above.

But the story of the SM is not finished here, despite its huge success there are more shortcomings than just the lack of an explanation of DM. Another question which remains unanswered in the SM is where all the matter comes from. Due to the symmetries of the SM matter and antimatter should always be created and annihilated in equal amounts. However, our Universe is dominated by matter. If there were regions in the Universe dominated by antimatter one should observe highly energetic gamma-rays from matter-antimatter annihilations at the boundary of matter dominated regions and antimatter dominated regions. However, observations of the Universe show that no such regions exist, hence the whole observable Universe - a radius of about 46.5 billion light-years [43] - must be dominated by matter. The process generating the asymmetry between matter and antimatter is called baryogenesis. One possible explanation is via electroweak (EW) baryogenesis. This process requires the electroweak phase transition (EWPT), which is realised via spontaneous symmetry breaking, to have taken place through a first-order phase transition (FOPT) - rather than a second-order phase transition or a smooth cross-over as is the case for the SM.

The 2HDMS also provides a solution for this. Through the modification of the scalar sector, many regions of the parameter space naturally lead to a FOPT. Also this model gives the option of including explicit sources for charge and parity (CP) violation, which is another necessary ingredient for successful baryogenesis. The investigation of this is beyond the scope of this work, however, currently a follow-up on the investigation of a FOPT in the 2HDMS is being done but will not be included in this work.

FOPTs proceed via the formation of bubbles, which will be the *second main focus* of this work. One important parameter is the velocity of the expanding bubble walls. This has important consequences for the out-of-equilibrium conditions for baryogenesis. Furthermore, the wall velocity has an impact on observable signals, such as the gravitational wave (GW) signal from a FOPT. Leading order (LO) calculations of the wall velocity lead to constant friction terms which, for standard symmetry-breaking transitions, decelerate the wall velocity but can lead to a runaway of the wall if the force driving the expansion is greater than the friction [44]. Next-to-leading order (NLO) calculations of the wall velocity include higher-order terms called transition splitting, where particles from the surrounding plasma pass into the bubble of the new phase and radiate off an additional particle during the passing through the bubble wall. The inclusion of these terms leads to velocity dependent friction terms, which grow with growing wall velocity. This avoids runaway scenarios and leads to a terminal wall velocity [45]. There have been extensive studies on standard symmetry-breaking scenarios [44–50] which can naturally occur during the standard cooling of the Universe. Less investigation has been done on the inverse process, symmetry-restoring transitions, where the Universe starts from a phase of broken symmetry and undergoes a FOPT to a symmetric state. Such transitions could have occurred, for example, during reheating, but even in specific thermal histories during the standard cooling of the Universe [51]. Symmetry-restoring transitions will be the main focus, along with a review of standard symmetry-breaking transitions.

This work is organised is four main sections which concern the topics of particles physics phenomenology and cosmology. The first two sections give a theoretical background of the current status of these two fields of physics. In ‘The evolution of our Universe’ a short introduction is given on how our Universe evolved from the very early states until today. This is to set the stage and give an understanding of the chronological order of events in our Universe. In the next section ‘The current state of particle physics’ the current state-of-the-art theory of particle physics, the SM, is introduced. This section describes the symmetries of the SM, as well as the Higgs mechanism. After that the shortcomings of the SM are explained followed by a short discussion of the detection techniques relevant for this work.

Section 4 and 5 are the main part of this work. Section 4 covers the *first main focus*, the DM and collider phenomenology in the 2HDMS model, based on the publications [1] and [2]. First, the model is introduced, then, current theoretical and experimental constraints are discussed, followed by a discussion of the DM phenomenology in section 4.3 and the collider phenomenology in 4.4. The focus is on future lepton colliders (electron-positron colliders like the proposed International Linear Collider (ILC), Compact Linear Collider (CLIC), Circular Electron Positron Collider (CEPC) and Future Circular Collider in electron-positron mode (FCC-ee) and the proposed muon collider) but also the High-Luminosity Large Hadron Collider (LHC) and the Future Circular Collider in proton-proton mode (FCC-hh) will be considered. Section 5 covers the *second main focus*, the bubble wall velocity in FOPTs, with a special emphasis on symmetry-restoring transitions, based on the publication [3]. Here, a more general approach is followed which applies to various models in which a FOPT with a mass change across the different phases is induced. First, a general introduction of FOPTs is given along with the calculation of the wall velocity following the approach in Ref. [45]. After that, estimates of the calculation are given for both symmetry-restoring and symmetry-breaking scenarios along with a discussion on phenomenological implications. The last section concludes this thesis.

Note that the publications [1], [2] and [3] are works in collaboration with other authors. At the beginning of section 4 and 5 the contributions of collaborators and my own contributions to these works are pointed out, respectively.

Notation and Conventions:

In this work natural units will be used if not stated otherwise, meaning $c = \hbar = 1$, where c is the speed of light and $\hbar$ is the reduced Planck constant. Derivatives with respect to spacetime coordinates x^μ, with Lorentz indices $\mu = 0, 1, 2, 3$ are often written in the form: $\partial_\mu = \frac{\partial}{\partial x^\mu}$.

Furthermore, the following acronyms will be used:

SM	Standard Model (the Standard Model of particle physics)
BSM	Beyond-the-Standard Model
EW	Electroweak
EWSB	Electroweak symmetry breaking
EWPT	Electroweak phase transition
vev	Vacuum expectation value
DM	Dark matter
GW	Gravitational wave
FOPT	First-order phase transition
CMB	Cosmic microwave background
BBN	Big Bang nucleosynthesis
FLRW	Friedmann–Lemaître–Robertson–Walker (metric)
BH	Black hole

PBH	Primordial black hole
QFT	Quantum field theory
QCD	Quantum chromodynamics
QED	Quantum electrodynamics
CP	Charge-parity
FCNC	Flavour-changing neutral currents
BRST	Becchi–Rouet–Stora–Tyutin (symmetry)
LO	Leading order
NLO	Next-to-leading order
NNLO	Next-to-next-to-leading order
NNLL	Next-to-next-to-leading logarithmic
2HDM	Two-Higgs-doublet model
N2HDM	Next-to-minimal Two-Higgs-doublet model
2HDMS	Two-Higgs-doublet model with additional complex scalar singlet
LHC	Large Hadron Collider
HL-LHC	High-Luminosity Large Hadron Collider
LEP	Large Electron-Positron Collider (former collider)
ILC	International Linear Collider (proposed collider)
CLIC	Compact Linear Collider (proposed collider)
CEPC	Circular Electron Positron Collider (proposed collider)
FCC-ee	Future Circular Collider in electron-positron mode (proposed collider)
FCC-hh	Future Circular Collider in proton-proton mode (proposed collider)
SPPC	Super Proton–Proton Collider (proposed collider)
MET	Missing transverse energy
GGF	Gluon-gluon fusion
VBF	Vector boson fusion
BBH	$b\bar{b}$-associated Higgs boson production
LZ	LUX-ZEPLIN (experiment)
HB	`HiggsBounds` (public code)
PTA	Pulsar timing array
LISA	Laser Interferometer Space Antenna (planned experiment)
WMAP	Wilkinson Microwave Anisotropy Probe

2 The evolution of our Universe

Contents

In order to get an understanding of the events in the Universe important for this work and at what stage in the evolution of the Universe they have occurred, this section starts by explaining the ΛCDM model. This is the current standard model of cosmology. After that, a timeline of the evolution of our Universe is outlined and important events are pointed out. This section follows the descriptions in Refs. [43, 52–55].

The content of the SM model of particle physics will be introduced afterwards in section 3.1. However, for this section it is assumed that the particle content of our Universe is known. Furthermore this is only an introduction to get an approximate understanding of which events in the Universe were important and when they occurred. For a detailed understanding the references mentioned above should be consulted.

2.1 The ΛCDM model

The ΛCDM model is the currently accepted standard model of cosmology. It includes three major components: A cosmological constant which is associated with dark energy and denoted Λ, cold DM denoted CDM and ordinary matter, also referred to as baryonic matter. These components make up the energy content of our universe, where today dark energy comprises about 68%, DM about 26% and ordinary matter about 5% [56]. Another fourth component, radiation, which mainly consists of neutrinos and photons, makes up less than about 1% of the energy content of the Universe. This is schematically shown in Figure 1.

Dark energy is a form of energy responsible for the expansion of space, which can be observed by the recession of far away galaxies. The resulting redshift in the spectra of galaxies was first investigated by Hubble [57] using observations from supernovae (see Ref. [58] for an update of the original data). The expansion of space is experimentally well confirmed, however, the exact nature of dark energy is currently not known.

The other unknown component in the ΛCDM model is DM. This type of matter has only been observed via its gravitational interaction. Interactions with ordinary matter or electromagnetic interactions have not been observed so far, hence this form of matter does not interact with photons and is not luminous, which is the

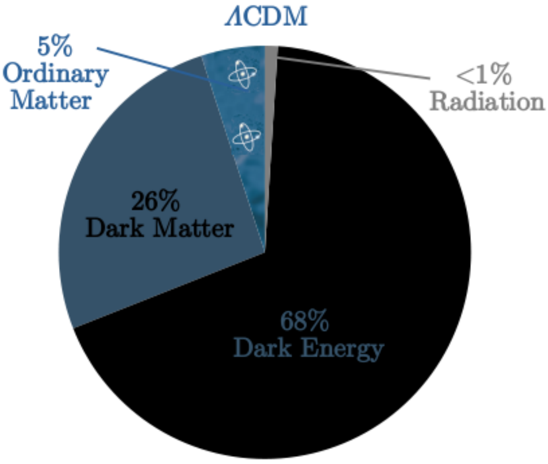

Figure 1: The energy content of our Universe today according to the ΛCDM model.

reason for its naming. The ΛCDM model assumes cold DM, meaning that it moves at non-relativistic velocities. Observational evidence comes from galaxy rotation curves, observations of hot gas in galactic clusters, bulk flows, structure formation, Big Bang nucleosynthesis (BBN) and CMB measurements (see for example section 2.12.1 of Ref. [55]). DM is a main focus of this work and will be discussed more in detail throughout this work.

Along with the components of the Universe mentioned above, the ΛCDM model assumes general relativity to be the correct theory of gravity and makes use of the cosmological principle:

Cosmological principle:

The cosmological principle states that the Universe is homogeneous and isotropic on large scales. Homogeneity means that the Universe is the same at every point in space and isotropy means that it looks the same in every direction. A visualisation of this can be seen in Figure 2. This can indeed be observed as the distribution of galactic clusters and superclusters becomes uniform on scales above 100 Mpc, which is about a few percent of the size of the observable Universe [55]. Furthermore, isotropy is supported by observations of the CMB by the Planck collaboration [59] and the Wilkinson Microwave Anisotropy Probe (WMAP) [60].

The assumption of our Universe being homogeneous and isotropic leads to invariance under spatial translations and rotations. Such a universe can be described by the Friedmann–Lemaître–Robertson–Walker (FLRW) metric. One form to write the line element is:

$$\mathrm{d}s^2 = g_{\mu\nu}\mathrm{d}x^\mu \mathrm{d}x^\nu = -\mathrm{d}t^2 + a^2(t)[\frac{\mathrm{d}r^2}{1-kr^2} + r^2(\mathrm{d}\theta^2 + \sin^2(\theta)\mathrm{d}\phi^2)]\,, \tag{2.1}$$

where r, θ and ϕ are polar coordinates. The metric tensor is described by $g_{\mu\nu}$ and

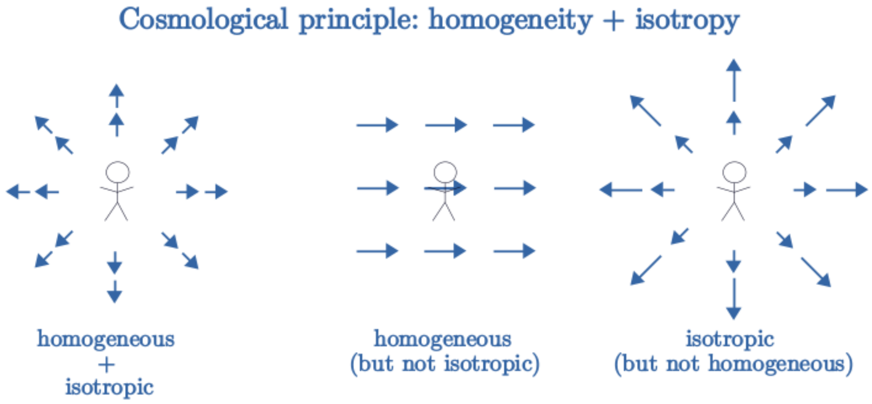

Figure 2: The cosmological principle. Our Universe is homogeneous and isotropic (left). A universe where an observer would see a preferred direction would not be isotropic (middle) and a universe where an observer sees inhomogeneity (right).

the indices μ and ν run over 0,1,2,3. The scale factor $a(t)$ describes the expansion of the Universe and k describes the curvature of the spatial coordinates, with $k = +1$ corresponding to a positively curved space (locally isometric to 3-spheres), $k = -1$ corresponding to a negatively curves space (locally hyperbolic) and $k = 0$ corresponding to a flat space. Our Universe corresponds to a remarkably flat geometry ($k \approx 0$) as indicated by measurements from the Planck collaboration [61] and WMAP [60].

From the scale factor $a(t)$ the Hubble factor can be defined as:

$$H(t) \equiv \frac{\dot{a}(t)}{a(t)}, \tag{2.2}$$

with an overdot denoting a derivative with respect to time t: $\dot{a}(t) = \frac{\mathrm{d}a(t)}{\mathrm{d}t}$. As mentioned above, the expansion of space can be observed for example through the cosmological redshift. Because of the expansion of space, distant galaxies recede and their light appears redshifted to a distant observer. The recession speed can be calculated via Hubble's law as: $v \simeq H_0 \cdot d$, where d is the distance between the observer and the galaxy and H_0 is the value of the Hubble factor evaluated today $H_0 = H(t)|_{t=t_0}$.

When applying the FLRW metric to the Einstein equation one obtains the first Friedmann equation:

$$H^2(t) = \left(\frac{\dot{a}(t)}{a(t)}\right)^2 = \frac{8\pi G}{3}\sum_i \rho_i - \frac{k}{2a^2(t)} \tag{2.3}$$

where G is Newton's gravitational constant and ρ_i are the densities of the different forms of energy in the Universe, i.e. dark energy, DM, ordinary matter and radiation. This equation describes the dynamics of the Universe determined by a balance between its geometry and its content.

Assuming that volumes grow with $V \propto a^3(t)$, since distances grow with $d = a(t) \cdot \chi$, where d is the proper distance and χ the comoving distance, the total energy density $\rho = \sum_i \rho_i$ can be related to the Hubble factor and one obtains the continuity equation:

$$\dot{\rho}(t) + 3H(t)[\rho(t) + p(t)] = 0\,, \tag{2.4}$$

where the pressure is given by $p(t) = -\frac{\rho(t)}{3H(t)}\frac{\dot{M}(t)}{M(t)}$, with M being the mass within a volume V. This equation is valid individually for all independent components i of the total energy density ρ, where independent components do not decay into each other. (One can also derive the continuity equation via application of the second Friedmann equation as done for example in Refs. [53, 54]. However the derivation can also be done without this. Here the description in Ref. [55] was followed.)

If one considers the energy content of the Universe as a barotropic fluid (a fluid whose density is a function of pressure only) one can write an equation of state for each energy component as:

$$p_i = w_i \rho_i\,, \tag{2.5}$$

where w_i are the equation of state parameters for each energy component. Inserting this definition into the continuity equation above and integrating gives the relation between the energy density and the scale factor:

$$\rho_i \propto a^{-3(1+w_i)}\,. \tag{2.6}$$

The different energy components of the Universe correspond to:

$$\begin{array}{rlcl} \text{matter:} & w_{\text{matter}} = 0 & \leftrightarrow & \rho_{\text{matter}} \propto a^{-3} \\ \text{radiation:} & w_{\text{radiation}} = 1/3 & \leftrightarrow & \rho_{\text{radiation}} \propto a^{-4} \\ \text{dark energy:} & w_{\Lambda} = -1 & \leftrightarrow & \rho_{\Lambda} \propto a^{0}\,. \end{array} \tag{2.7}$$

This means that matter dilutes as space expands with the scale factor to the power -3, since there are three spatial dimensions. Radiation dilutes with one more negative power since, additionally to the spacial dilution, wavelengths are redshifted. And finally, dark energy does not dilute with the expansion of space. This corresponds to a cosmological constant, it is also called a vacuum constant. A curvature term k would dilute with a^{-2}, however, it is not listed above since this is not a component of the energy content of the Universe.

One more point remains to be discussed, namely the curvature of our Universe. For the first Friedmann equation, written above, one can define a critical density corresponding to a flat ($k = 0$) universe:

$$\rho_c \equiv \frac{3H^2}{8\pi G}\,. \tag{2.8}$$

This is often used to define the density parameter:

$$\Omega = \frac{\sum_i \rho_i}{\rho_c}\,. \tag{2.9}$$

Now $\Omega > 1$ corresponds to a positively curved space ($k = +1$), $\Omega < 1$ to a negatively curved space ($k = -1$) and, by definition, $\Omega = 1$ corresponds to a flat space ($k = 0$). Hence, the density of the universe determines its geometry in an expanding space.

As mentioned, cosmological observations, in particular CMB precision measurements [60, 61], have shown that our Universe today is extremely spatially flat. Hence $k = 0$ and $\Omega = 1$ for our Universe.

In the next subsection the evolution from the early Universe until today will be discussed.

2.2 Chronology of our Universe

Our Universe is about 13.8 billion years old according to measurements from the Planck collaboration [61]. Its evolution can be divided according to the dominating energy components mentioned in the previous subsection. A schematic image of the chronology of our Universe is shown in Figure 3. On the top axis the division into three eras is marked. The first era from the end of inflation until about 10^4 years is radiation dominated. This can be understood by looking back at Equation 2.7. The radiation density decays with the scale factor a^{-4}, while matter density decays with a^{-3}. This means that radiation dilutes faster than matter, hence there must have been a time in the evolution of the Universe when there was more radiation than matter. The value of the scale factor today is defined as $a_0 = 1$. Since the Universe is always expanding, it is smaller at earlier times. The scale factor when both components were of equal amounts can be calculated by comparing their densities today. With a radiation density of about $9 \cdot 10^{-3}\%$ and a total matter density of about 31% (DM and ordinary matter) this amounts to about $a_{\text{eq}} = \frac{\rho_{\text{radiation}}}{\rho_{\text{matter}}} \approx 2.9 \cdot 10^{-4}$. The relation between time and the scale factor can be obtained from the Friedmann equation (see for example Ref. [53] for a derivation) and gives the time of matter-radiation equality: $t_{\text{eq}} \approx 5 \cdot 10^4$ years (In Figure 3, for simplicity, this was

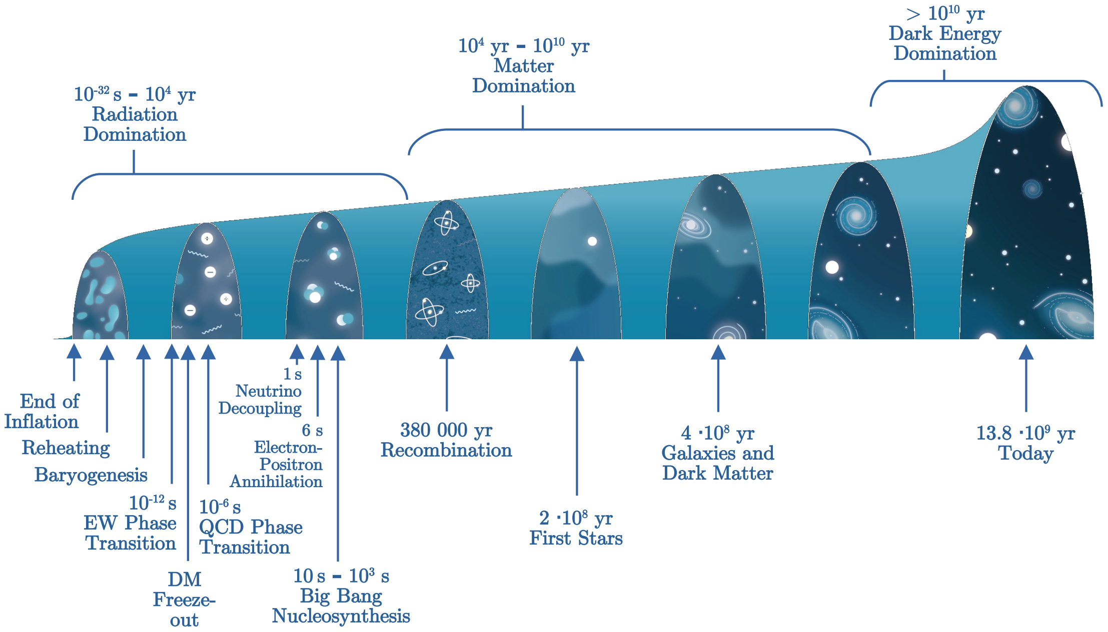

Figure 3: Chronology of the Universe, figure adapted from NASA Cosmic History Note: events without a time stamp are not well established. They are still marked here since they are believed to have happened and are of importance for the later content of this work.

rounded down to only give the rough order of magnitude 10^4 years).

The same procedure can be followed to determine the scale factor and the time at which matter and dark energy were of equal amounts: $a_{\mathrm{m}\Lambda} = \left(\frac{\rho_{\mathrm{matter}}}{\rho_{\Lambda}}\right)^{1/3} \approx 0.77$ (the power $1/3$ comes from the matter density decaying with a^{-3} while the density of dark energy does not decay with with the scale factor.), which results in the matter domination era lasting until about 10^{10} years and dark energy domination since then until today.

On the bottom axis of the image important events in the evolution of our Universe are marked and explained in the following. The Universe starts from a hot and dense state. As it expands the energy density is diluted and the temperature drops, hence time t and temperature $T \propto a(t)^{-3}$ can be linked to the size of the Universe. But before going through each event one important concept needs to be explained:

Thermal equilibrium and freeze-out:

To understand the thermal plasma of the early Universe and the densities of the different particle species different evolutionary stages need to be considered, namely when particles are relativistic, become non-relativistic and when they eventually drop out of thermal equilibrium as the Universe expands.

In thermal equilibrium particle densities are calculated via integrating over the Bose-Einstein (for bosons) or Fermi-Dirac (for fermions) distribution. Weighted by the degrees of freedom g of the particle species one obtains:

$$n(T) = \frac{g}{(2\pi)^3} \int \mathrm{d}^3p \frac{1}{e^{(E(p)-\mu)/T} \pm 1}\,, \tag{2.10}$$

with the '+' sign for fermions and the '−' sign for bosons. $E(p)$ denotes the total energy of a particle with momentum p, μ denotes the chemical potential and T the temperature. At energies much higher than the particle mass $T \gg m$, particles behave relativistic and their rest mass can be neglected compared to the temperature. At lower energies $T \ll m$ their rest mass becomes important. The particle densities in the relativistic and in the non-relativistic limit are then:

$$n(T) = \begin{cases} g\frac{\zeta(3)}{\pi}T^3 \begin{cases} 1, & \text{bosons,} \\ \frac{3}{4}, & \text{fermions,} \end{cases} & \text{relativistic limit } (\frac{m}{T} \to 0)\,, \\ \\ g\left(\frac{mT}{2\pi}\right)^{3/2} e^{-(m-\mu)/T}, & \text{non-relativistic limit } (\frac{m}{T} \gg 1)\,, \end{cases} \tag{2.11}$$

with the Riemann zeta function $\zeta(3) \approx 1.202$. The chemical potential μ can in general be neglected since $\mu \ll T$ in the early Universe and for photons (which dominate the early Universe) it is always zero.

As one can see, in the relativistic limit the particle density depends only on the temperature, whereas in the non-relativistic limit it becomes Boltzmann suppressed for $T < m$ via the exponential term. This can be interpreted as the annihilation of particles and antiparticles. At higher energies annihilation and production of particles and antiparticles are balanced. At low temperatures, however, the thermal energy of the particles is not sufficient for pair production. Annihilation becomes larger than production and the density of the particle species decreases.

This would mean that, as the temperature decreases, all particles would annihilate at some point and there would be no particles left today. But there are still a lot of particles present in the Universe today. Because, luckily, our Universe expands. When the interaction rate of particles becomes smaller than the expansion rate of the Universe, the particles drop out of equilibrium and decouple from the thermal bath. A relic distribution of the particles remains in the Universe. This process is called freeze-out and is described by the Boltzmann equation. The integrated form of the Boltzmann equation, for each particle species, can be written as:

$$\frac{1}{a^3}\frac{\mathrm{d}(n_i a^3)}{\mathrm{d}t} = C_i[\{n_j\}]\,, \tag{2.12}$$

where the function $C_i[\{n_j\}]$ on the right-hand side is a collision term describing the interactions of particle species i with particle species j and the left-hand side describes the dilution of particle numbers with the expansion via the scale factor a. When considering the process of some particle species 1 interacting with another species 2 to produce species 3 and 4 and the inverse process: $12 \leftrightarrow 34$ one arrives at the form (see section 3.2.1 of Ref. [43]):

$$\frac{1}{a^3}\frac{\mathrm{d}(n_1a^3)}{\mathrm{d}t} = -\langle\sigma v\rangle\left[n_1n_2 - \left(\frac{n_1n_2}{n_3n_4}\right)_{\mathrm{eq}} n_3n_4\right], \tag{2.13}$$

with the subscript 'eq' denoting the equilibrium densities and $\langle\sigma v\rangle$ the thermally averaged cross section for the interaction between particle species 1 and 2. This is schematically shown in Figure 4. At high temperatures the particle density follows the equilibrium distribution which becomes Boltzmann suppressed for lower temperatures (dashed line). When the interaction rate is much larger than the expansion $n_2\langle\sigma v\rangle \gg H$, where H is the Hubble factor, this equilibrium distribution is followed. However, at some point the interaction rate drops below the Hubble factor $n_2\langle\sigma v\rangle < H$ and the comoving density $N_1 \propto n_i a^3$ approaches a constant relic density (tail of the solid line). This is how a relic density forms in the early Universe. (A relic density can also develop via freeze-in, which describes the inverse process. Particles that were not in thermal equilibrium are produced via a relative increase in their interaction rate.)

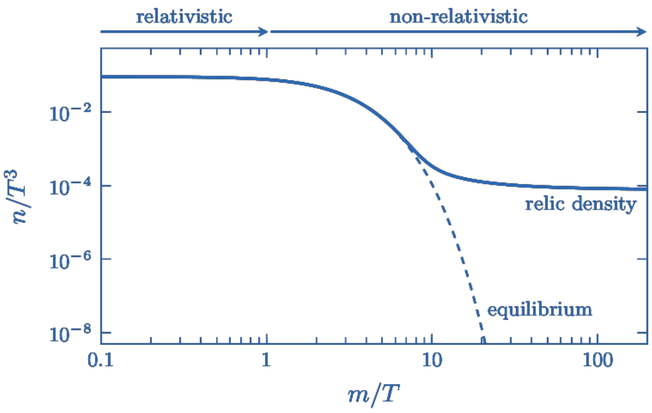

Figure 4: Schematic evolution of the particle density n against the ratio of mass m over temperature T, figure taken from Ref. [43].

This process of freeze-in will be important in understanding some of the events in the chronology of our Universe explained below:

Chronology of our Universe (see Figure 3):

Inflation:

The first event in the evolution of our Universe marked in Figure 3 is inflation. It is a period of exponential expansion. To be precise inflation is not experimentally confirmed, however, generally is accepted since there are strong indications for it to have occurred. It solves the horizon and flatness problem (see for example Refs. [62–64]). The horizon problem is the question why the Universe is so smooth on large scales (larger than galaxies and clusters) even if spatially separated regions have never been in causal contact. The flatness problem is the question why the observed spatial curvature of the Universe is so small. Inflation solves these questions by introducing a period of rapid expansion, where the Universe increased its size by a factor of about 10^{26}, smoothing out any curvature. This rapid expansion also means that the Universe used to be much smaller, hence regions which are very distant today could have been in causal contact earlier, explaining the homogeneity of the Universe. The temperature and time at which inflation happened is not known. Usually it is placed at around the order of $10^{-36}\,\mathrm{s}$ to $10^{-32}\,\mathrm{s}$. The simplest model of inflation assumes a scalar field, the inflaton field, to be responsible for the exponentially accelerated expansion by slowly rolling down a nearly flat potential hill. Inflation ends when the potential steepens and the field picks up kinetic energy. After inflation the energy is diluted so much that the Universe is basically empty.

Reheating:

After inflation most of the energy is stored in the inflaton field. Reheating converts this energy into a thermal bath of SM particles [65–67]. The Universe is then filled with particles. As for inflation, the time and temperature of the reheating phase are not known. The dynamics during reheating can be very rich and are important for understanding how the hot Big Bang began. Some observable relics from this phase can be isocurvature perturbations, stochastic GWs, non-Gaussianities, DM, dark radiation, primordial black holes (PBHs), matter-antimatter asymmetry, and primordial magnetic fields.

Isocurvature, or entropy, perturbations are the complement of adiabatic perturbations. Adiabatic perturbations can be generated by starting with a homogeneous universe and performing a common, local shift in time of all background quantities. Isocurvature perturbations, on the other hand, are defined by relative perturbations between different species. An overdensity in one species can compensate for an underdensity in another species, such that no net curvature perturbation results. Non-Gaussianities describe the deviation of the initial perturbations from a Gaussian probability distribution. The simplest inflationary models predict Gaussianity to be a good approximation. Dark radiation is a postulated form of a relativistic energy component that is not part of the known SM particles like photons and neutrinos. It is characterised by having very weak interactions with ordinary matter.

Baryogenesis:

Another event that is believed to have happened in the early stages of the Universe is baryogenesis (see for example Refs. [68, 69] or chapter 6 of Ref. [52]). This is the process leading to the observed matter-antimatter asymmetry. The required asymmetry to generate the amount of matter present in the Universe today is very small. For about 10^{10} antimatter particles there must have been one extra matter particle. Matter and antimatter would then annihilate into photons leaving 1 matter particle per 10^{10} annihilated matter-antimatter pairs behind and thus producing the observed matter-to-photon ratio. Since the details of this event are not known also time and temperature are not defined here.

Electroweak phase transition ($T \sim 100\,\mathrm{GeV}$, $t \sim 10^{-12}\,\mathrm{s}$)**:**

The first event that can be linked to a temperature and time is the EW phase transition. This event describes the breaking of the EW symmetry in the SM through which the gauge bosons and fermions obtain their mass (more on this will be explained in the section 3.1.2). It is currently under debate whether this transition was a first-order or second-order transition (also this will be discussed in more detail later).

Dark matter freeze-out:

It is currently not known when DM froze-out, or if it froze-out at all as it could also have been generated via freeze-in or be explained by PBH. If DM via freeze-out is considered, the time of the freeze-out depends on the chosen model. A rough estimate for the freeze-out temperature can be obtained via $T \sim \frac{m_{\mathrm{DM}}}{10}$, where m_{DM} is the mass of the DM candidate (see Section 3.2.2 of Ref. [43] for a derivation).

Quantum chromodynamics phase transition ($T \sim 150\,\mathrm{MeV}$, $t \sim 10^{-6}\,\mathrm{s}$)**:**

The next event is the quantum chromodynamics (QCD) phase transition. This describes the process where the quark-gluon plasma coalesces into hadrons. But this did not happen to all the quarks. As the temperature of the Universe drops, massive particles become non-relativistic and start to annihilate. Heavier particles become non-relativistic earlier and annihilate first. Top quarks are the heaviest SM particles and annihilate first (at roughly $T \sim \frac{1}{6} m_t \sim 30\,\mathrm{GeV}$). Next the SM Higgs boson and the gauge bosons $W^{\pm}$ and Z^0 annihilate, followed by bottom quarks, charm quarks and tau leptons. Then, before strange quarks annihilated, the QCD phase transition occurred, confining quarks and causing them to bind to hadrons together with gluons. Heavier hadrons are non-relativistic below the temperature of the QCD phase transition and are hence Boltzmann suppressed. The only particles left in large numbers after the QCD phase transition are pions, electrons, muons, neutrinos and photons. Soon after the QCD phase transition also pions and muons annihilate.

Neutrino decoupling ($T \sim 0.8\,\mathrm{MeV}$, $t \sim 1\,\mathrm{s}$)**:**

Neutrinos are the most weakly interacting particles of the SM since they only interact via the weak force, hence they decouple first from the thermal plasma and freeze out while they are still relativistic due to their small mass. They travel freely through the Universe and form the cosmic neutrino background.

Electron-position annihilation ($T \sim 500\,\mathrm{KeV}$, $t \sim 6\,\mathrm{s}$)**:**

As the Universe cools down further also electrons and positrons become non-relativistic. Hence, photons do not have sufficient energy to produce pairs of them. Annihilation of electron-position pairs into photons then dominates. Whenever a particle species becomes non-relativistic and annihilates, its entropy is transferred to the other relativistic species still present in the thermal plasma. Since neutrinos already decoupled from the thermal plasma this entropy can only be transferred to the photon bath, increasing its temperature relative to that of the neutrinos.

Big Bang nucleosynthesis ($T \sim 100\,\mathrm{KeV}$, $t \sim 3\,\mathrm{min}$)**:**

BBN is the process where protons and neutrons are bound into the first atomic nuclei. These are hydrogen and helium-4. Small amounts of deuterium, helium-3, and lithium-7 also form. The good agreement between observed amounts of these light elements and the predictions of the ΛCDM model are one of its great successes.

Recombination ($T \sim 0.3\,\mathrm{eV}$, $t \sim 3.8 \cdot 10^5\,\mathrm{years}$)**:**

At this point the Universe has cooled down enough so that it becomes energetically favourable for electrons and protons to stay bound and form neutral hydrogen atoms. The number of photons which are energetic enough to ionise hydrogen is very low now and this process become suppressed. Since the Universe is now primarily filled with neutral particles, rather than charged free electrons and protons, Thomson scattering becomes suppressed. Hence, at the end of recombination photons have decoupled from the thermal bath and can stream freely between the neutral atoms. At this point the Universe first becomes transparent. The photons emitted right after recombination form the CMB which carries important information about the anisotropies in the early Universe.

No information about the Universe before this epoch can be gained by observations based on photons, since Thomson scattering did not allow for photons to travel freely. However, GWs are unaffected by this and could give information about the early Universe even before recombination.

First stars and reionisation ($T \sim 5\,\mathrm{meV}$, $t \sim 2 \cdot 10^8\,\mathrm{years}$)**:**

After recombination and the emission of the CMB radiation a dark period follows. When the first stars form, photons are emitted by these and light the Universe again. The surrounding gas is ionised by these photons.

Later the first modern galaxies form within halos of DM.

Today ($T \sim 240\,\mu\text{eV}$, $t \sim 13.8 \cdot 10^9\,\text{years}$)**:**

As written above the current age of our Universe is about 13.8 billion years. Remnants of the CMB can still be detected today. In order to extract information about events earlier than recombination, measurements of GWs or primordial magnetic fields can be used. But also, particle colliders today give insights on the physics of the early universe.

Not all of the events above are part of the well established chronology. Inflation, reheating, baryogenesis and the DM freeze-out are current areas of active research. They are still mentioned here for completeness. In Figure 3 these events do not have a time stamp to distinguish them from experimentally confirmed events. This introduction should set the stage to understand the history of our Universe and the standard model of cosmology, the ΛCDM model.

In the next section the SM of particle physics will be explained.

3 The current state of particle physics

Contents

In this section a short introduction to the SM of particle physics is given. This will help understand the following section of the main part of this work where a particular extension of the SM, the 2HDMS, will be investigated. This model takes all ingredients from the SM and extends only its scalar sector. Therefore, in this introduction there will be a special emphasis on the scalar sector of the SM. After the introduction, the shortcomings and unresolved problems of the SM as well as possible solutions are discussed. This section follows the descriptions in Refs. [70, 71].

3.1 The Standard Model of particle physics

The SM of particle physics successfully describes how the elementary particles (which make up ordinary matter, corresponding to about 5% of the energy content of our Universe, as discussed earlier) interact via the fundamental interactions. However, the description only includes 3 of the 4 fundamental interactions, namely the electromagnetic, the weak and the strong interaction. The SM, however, does not include a quantum description of the gravitational interaction. In order to describe these interactions, the SM makes use of the framework of Quantum field theory (QFT), which combines the principles of quantum mechanics and special relativity. The fundamental components of nature are described via fields which are defined at every point in spacetime. Particles are then interpreted as quantum excitations of these fields.

The elementary particle content of the SM is depicted in Figure 5. In the outermost grey ring, the 12 fermions are depicted. Fermions have half-integer spin and are the main building blocks of matter. For each fermion there is an antifermion with the same mass and spin but opposite charge (electric charge and also colour charge in the case of quarks) and additive quantum numbers. The fermions are

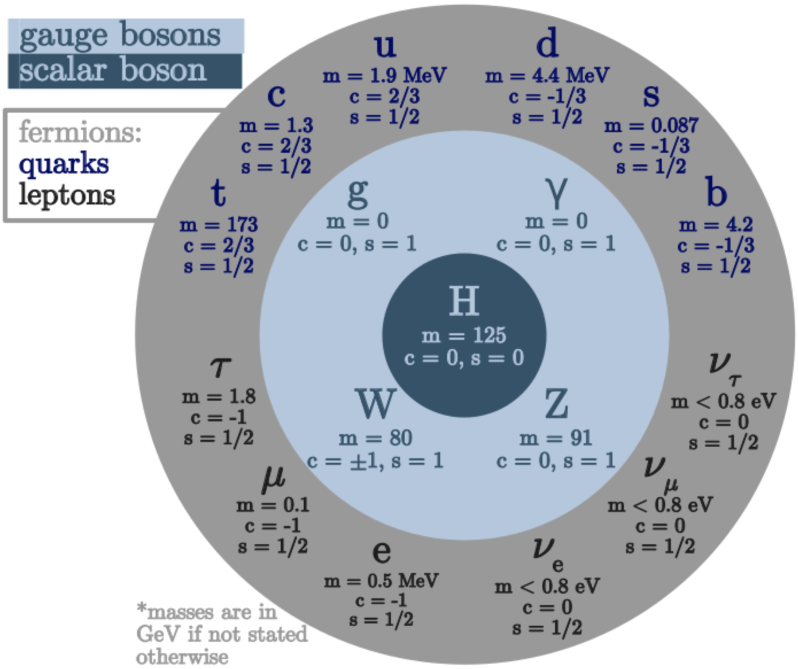

Figure 5: The elementary particle content of the Standard Model of particle physics, along with their mass m, electric charge c and spin s.

divided into quarks, which carry a colour charge and take part in strong interactions, and leptons. Both, quarks and leptons, take part in weak interactions. All electrically charged particles take part in electromagnetic interactions. The leptons are split into charged leptons, carrying -1 elementary charge, and neutral leptons, the neutrinos. The quarks are split into up-type quarks, carrying a charge of +2/3, and down-type quarks, carrying a charge of -1/3. All four fermion sub-types, i.e. up-type quarks, down-type quarks, charged leptons and neutrinos, further come in three generations, which have similar properties but different masses. The lightest generation consists of up-quarks, down-quarks and electrons which form the main components of atoms.

In the inner rings of the image, the bosons are depicted. Bosons have integer spin and act as force carriers. They are divided into gauge bosons which are vector bosons, meaning they have spin 1, and the Higgs boson which is a scalar boson, meaning it has spin 0. Bosons without a charge are their own antiparticles (The $W^{\pm}$-boson comes with a charge of either +1 or -1. They are each others antiparticles). The $W^{\pm}$ and Z- bosons are the force carriers of the weak force, photons γ are the force carriers of the electromagnetic interaction and gluons g are the force carriers of the strong force. The Higgs mechanism plays a special role in giving masses to the other particles. This mechanism will be explained in more detail later. As mentioned already, gravity is not part of the SM and currently there is no force carrier for it. In quantum theories of gravity, a hypothetical particle with spin 2 called graviton is proposed as a force carrier for the gravitational interaction, but it has not been experimentally observed.

The distinction between fermions and bosons can be understood by taking the wave function Φ of a composition of particles and exchanging two particles of the same species n with momenta $\mathbf{p}$ and $\mathbf{p}'$ and spins σ and σ' respectively:

$$\Phi_{\dots\mathbf{p}\sigma n\dots\mathbf{p}'\sigma' n\dots} \quad \rightarrow \quad \Phi_{\dots\mathbf{p}'\sigma' n\dots\mathbf{p}\sigma n\dots} = \pm\Phi_{\dots\mathbf{p}\sigma n\dots\mathbf{p}'\sigma' n\dots}\,, \tag{3.1}$$

where the '+' sign corresponds to bosons which are symmetric under the exchange of particles and the '−' sign corresponds to fermions which are antisymmetric under the exchange of particles and the dots represent other particles that might be present. As can be seen, since fermions are antisymmetric under the exchange of particles, the wave function of two particles having the same momentum $\mathbf{p}$ and spin σ, hence occupying the same quantum state, must vanish. This corresponds to the Pauli exclusion principle, which states that two or more identical particles with half-integer spin cannot simultaneously occupy the same quantum state. This does not apply to bosons. Multiple bosons can occupy the same quantum state. Accordingly, they follow Bose-Einstein statistics, whereas fermions follow Fermi-Dirac statistics. (These were already mentioned in the previous section in Equation 2.10, but no explanation was given at that point. In QFT, this symmetry property is implemented at the level of field operators and leads to the same statistical behaviour.)

The Standard Model Lagrangian:

The elementary particles and their interactions in the framework of QFT can be described mathematically by the SM Lagrangian. Here, the Lagrangian is first stated without deeper explanation. One important thing to note is that the fundamental interactions, namely the strong (with gluons as force carriers), weak (with $W^{\pm}$ and Z-bosons as force carriers) and electromagnetic (with photons as force carriers) can be described via symmetry groups: The strong interaction is described by the $SU(3)_C$ group with colour charge C and the EW interaction is described by the $SU(2)_L \times U(1)_Y$ group with weak isospin T charge and hypercharge Y. The electric charge Q is a combination of the third component T_3 of the weak isospin and of hypercharge Y: $Q = T_3 + \frac{1}{2}Y$. Also, the photon of the electromagnetic interaction and the Z-boson of the weak interaction are in fact linear combinations of the neutral gauge fields of the $U(1)_Y \times SU(2)_L$ group. After the spontaneous breaking of the EW symmetry, the electromagnetic interaction emerges as an unbroken $U(1)_{\text{em}}$ group. The process of spontaneous symmetry breaking will be explained in section 3.1.2. The role of these symmetry groups and how a Lagrangian can be constructed from them will be explained in the following section 3.1.1. First the final form is presented here and later the details behind it will be discussed.

The full form of the SM Lagrangian can be separated into four parts:

$$\mathcal{L}_{\mathrm{SM}} = \mathcal{L}_{\mathrm{YM}} + \mathcal{L}_{\mathrm{WD}} + \mathcal{L}_{\mathrm{Yu}} + \mathcal{L}_{\mathrm{H}} \,. \tag{3.2}$$

The Yang-Mills part $\mathcal{L}_{\mathrm{YM}}$ describes the fundamental gauge fields of the SM, namely the fields emerging from the full SM gauge group $SU(3)_C \times SU(2)_L \times U(1)_Y$. The Weyl-Dirac part $\mathcal{L}_{\mathrm{WD}}$ describes the fermion fields and their gauge interactions. The Yukawa part $\mathcal{L}_{\mathrm{Yu}}$ describes the interactions of the fermions with the Higgs field, which give rise to their mass terms after spontaneous symmetry breaking. The Higgs part $\mathcal{L}_{\mathrm{H}}$ describes the Higgs field and its scalar potential. There is no mass term for neutrinos included in the minimal SM and this is a subject of current research.

The Yang-Mills part can be written as:

$$\mathcal{L}_{\mathrm{YM}} = -\frac{1}{4} G^A_{\mu\nu} G^{\mu\nu A} - \frac{1}{4} W^a_{\mu\nu} W^{\mu\nu a} - \frac{1}{4} B_{\mu\nu} B^{\mu\nu} \,, \tag{3.3}$$

with the field strength tensors:

$$\begin{aligned}
G^A_{\mu\nu} &= \partial_\mu G^A_\nu - \partial_\nu G^A_\mu + g_3 f^{ABC} G^B_\mu G^C_\nu && (SU(3)_C, \text{ colour charge}), \\
W^a_{\mu\nu} &= \partial_\mu W^a_\nu - \partial_\nu W^a_\mu - g_2 \epsilon^{abc} W^b_\mu W^c_\nu && (SU(2)_L, \text{ weak isospin}), \\
B_{\mu\nu} &= \partial_\mu B_\nu - \partial_\nu B_\mu && (U(1)_Y, \text{ hypercharge}) \,,
\end{aligned} \tag{3.4}$$

where g_2 and g_3 denote the dimensionless coupling constants corresponding to the weak and strong interaction, respectively. The indices μ and ν are Lorentz indices which run over 0,1,2,3, the indices A, B and C run over the adjoint representation of $SU(3)$, hence over $1, \ldots, 8$ and the indices a, b and c run over the adjoint representation of $SU(2)$, hence over 1,2,3. G^A_μ represents the eight gluon fields, f^{ABC} are the structure functions of the Lie algebra of the $SU(3)_C$ group, W^a_μ and B_μ represent the intermediate vector bosons and ϵ^{abc} are the structure functions of the Lie algebra of the $SU(2)_L$ group.

The Weyl-Dirac part can be written in short as:

$$\mathcal{L}_{\mathrm{WD}} = \sum_f \bar{f} i \not{D} f \,, \tag{3.5}$$

describing the kinetic terms of the fermions and their interactions with the gauge bosons. With the covariant derivative:

$$D_\mu = \partial_\mu - ig_1 \frac{Y}{2} B_\mu - ig_2 W_\mu^a \frac{\sigma^a}{2} - ig_3 G_\mu^A \frac{\lambda^A}{2} \,, \tag{3.6}$$

where g_1 denotes the dimensionless coupling constant corresponding to the hypercharge gauge group and the sum above is taken over all fermion fields f. $\bar{f}$ denotes the antifermion fields, the slash indicates contraction of vector fields with gamma matrices $\not{D} = \gamma_\mu D^\mu$. Y is the generator of the $U(1)_Y$ group, the Pauli matrices σ^a are the generators of the $SU(2)_L$ group and the Gell-Mann matrices λ^A are the generators of the $SU(3)_C$ group.

The Yukawa part can be written as:

$$\mathcal{L}_{\text{Yu}} = -y_u \bar{Q}_L i\sigma^2 \Phi^* u_R - y_d \bar{Q}_L \Phi d_R - y_l \bar{L}_L \Phi l_R + \text{ h.c.} \,, \tag{3.7}$$

with the Higgs field, left-handed quark doublets and left-handed lepton doublets, respectively:

$$\Phi = \begin{pmatrix} \phi^+ \\ \phi \end{pmatrix}, \qquad Q_L = \begin{pmatrix} u_L \\ d_L \end{pmatrix}, \qquad L_L = \begin{pmatrix} \nu_L \\ e_L \end{pmatrix}. \tag{3.8}$$

The Higgs doublet Φ is an $SU(2)_L$ doublet, meaning that it transforms as an $SU(2)$ vector or, more technically expressed, that it transforms under the fundamental representation of $SU(2)$. It has two complex components. The upper component ϕ^+ is electrically charged and the lower component ϕ is neutral. For the left-handed quark and lepton doublets u_L denote the three up-type quark generations, d_L the three down-type quark generations, ν_L the three neutrino generations and e_L the three charged lepton generations. u_R, d_R and l_R denote the right-handed lepton singlets, again with three generations, and y_u, y_d and y_l are the Yukawa couplings for up-type quarks, down-type quarks and charged leptons, respectively and h.c. denotes the hermitian conjugate. Since neutrinos do not have mass terms in the minimal SM, there are no right-handed neutrino singlets included in the SM Lagrangian.

The Higgs part can be written as:

$$\mathcal{L}_{\text{H}} = (D_\mu \Phi)^\dagger (D^\mu \Phi) + V(\Phi) \,, \tag{3.9}$$

with the scalar potential:

$$V(\Phi) = -\mu^2 \Phi^\dagger \Phi + \lambda (\Phi^\dagger \Phi)^2 \,, \tag{3.10}$$

where $\mu^2 > 0$ and λ are coupling parameters with mass dimension 2 and 0, respectively, and Φ is the scalar doublet which gives rise to the Higgs boson.

These are the components of the SM Lagrangian. Of course, at this point one cannot understand where it comes from, how it is constructed, how the gauge bosons are related to the symmetry groups and what role spontaneous symmetry breaking plays. The following subsections will give a rough description of the ideas behind the formula above and help to understand these questions.

3.1.1 Symmetries of the Standard Model

Symmetries are an important tool in physics. The SM Lagrangian, which was given above in Equation 3.2 and explained in the subsequent equations, obeys a few symmetries. A symmetry can be defined as a transformation under which physical observables remain invariant, hence it does not change the results of possible experiments. One important concept in understanding symmetries of a physical system and their relation to conserved quantities is the Noether theorem.

Noether's theorem(s):

Noether's first theorem states that every continuous symmetry of the action of a physical system leads to a corresponding conservation law [72]. A symmetry of the action is a transformation τ of the fields φ which leaves the action $\mathcal{S}$ invariant. The action is defined as the integral over space and time of the Lagrangian density function: $\mathcal{S}[\varphi] = \int \mathrm{d}^4x \mathcal{L}(\varphi, \partial_\mu \varphi)$. The corresponding conservation law can then be written in form of a continuity equation with a conserved current. This statement can be written as follows:

$$\begin{aligned} &\mathcal{S}[\varphi] = \mathcal{S}[\tau(\varphi)] \quad (\tau \text{ is a symmetry of } \mathcal{S}) \\ &\Rightarrow \exists j^\mu(x) \quad \text{such that} \quad \partial_\mu j^\mu(x) = 0 \quad \text{and} \quad Q = \int \mathrm{d}^3x j^0, \quad \mathrm{d}Q/\mathrm{d}t = 0\,, \end{aligned} \tag{3.11}$$

where φ are differentiable fields on which the Lagrangian depends, x^μ are the space-time coordinates and $\mu = 0, 1, 2, 3$ as usual. j^μ is the conserved current which results from the symmetry of the action and Q is a constant of motion (or conserved charge) which can be constructed from it.

In order to better understand this statement, consider a schematic continuous infinitesimal transformation τ under which the action is invariant:

$$\tau : \varphi(x) \to \varphi(x) + \epsilon\psi(x)\,, \qquad \begin{cases} \epsilon = \text{const. (global)}, \\ \epsilon = \epsilon(x) \text{ (local)}, \end{cases} \tag{3.12}$$

where ϵ is a small parameter and ψ is a general function. If ϵ =const. does not depend on the coordinates x the symmetry is a global symmetry and Nother's first theorem applies. If $\epsilon = \epsilon(x)$ does depend on the coordinates x the symmetry is a local symmetry and Noether's second theorem applies, which will be discussed afterwards. The action is then invariant under τ if the Lagrangian density $\mathcal{L}$ itself is invariant under the transformation, but also if it changes only by a divergence term, hence if one can write the Lagrangian density of the transformed fields in the form:

$$\begin{aligned} &\tau : \mathcal{L} \to \mathcal{L} + \epsilon \partial_\mu \mathcal{J}^\mu && \text{for } \epsilon = \text{const. (global)}, \\ &\tau : \mathcal{L} \to \mathcal{L} + \epsilon \partial_\mu \mathcal{J}^\mu + (\partial_\mu \epsilon)\psi \frac{\partial \mathcal{L}}{\partial(\partial_\mu \phi)} && \text{for } \epsilon = \epsilon(x) \text{ (local)}. \end{aligned} \tag{3.13}$$

Then the action is invariant under the transformation τ since the integral of a divergence term becomes a boundary term according to Gauss's theorem. From this the conserved current can be constructed:

$$\begin{aligned} &j^\mu = \frac{\partial \mathcal{L}}{\partial(\partial_\mu \varphi)}\psi - \mathcal{J}^\mu \\ &\text{with } \partial_\mu j^\mu = 0 \quad \text{and } Q = \int \mathrm{d}^3 x j^0, \quad \mathrm{d}Q/\mathrm{d}t = 0\,. \end{aligned} \tag{3.14}$$

In general, there can be multiple symmetries leading to multiple conserved currents. For example, symmetry under time translation leads to the conservation of energy, symmetry under spatial translations leads to conservation of momentum, symmetry under spatial rotation leads to conservation of angular momentum and symmetry under a phase shift leads to conservation of electric charge. These are global symmetries for which Noether's first theorem is usually applied.

There is also Noether's second theorem which is often used in gauge theory which plays an important role in the SM. The second theorem applies when there is a collection of infinitesimal local symmetries the action and it states that then there exist corresponding differential relations between the Euler-Lagrange equations. The Euler–Lagrange equations describe the equations of motion of a system. They consist of a system of partial differential equations. Their solutions are stationary points of the action which can be obtained by the principle of least action: $\frac{\partial}{\partial x^\mu}\frac{\partial \mathcal{L}}{\partial(\partial_\mu \varphi)} = \frac{\partial \mathcal{L}}{\partial \varphi}$. The mathematical formulation of the theorem is somewhat involved but a good review can be found in Ref. [73]. The main message from this theorem is that the equations of motion are not all independent, and therefore some degrees of freedom remain. Since physical observables should be uniquely determined, these degrees of freedom are gauged, meaning that a term can be added to the fields of the theory which does not influence the experimental outcome. The connection between symmetries and group theory will be explained in the next paragraph.

Gauge theory and Lie groups:

Gauge theory relates to Noether's second theorem as explained above. Precisely a gauge theory is a type of field theory where the action is invariant under local continuous transformations. As explained above, local symmetries lead to redundancy in the field description due to differential dependencies among the equations of motion. This so called gauge freedom, allows for transformations of the fields without affecting physical observables. The fundamental interactions, i.e. the electromagnetic, the weak and the strong interaction, are all gauge theories. Their force carriers arise from gauge fields associated with the generators of the local symmetry group, hence they are called gauge bosons.

The examples of symmetries which follow from Noether's first theorem, i.e. symmetry under time translation, spatial translation, spatial rotation and phase shift, which were mentioned above, are global symmetries. They lead to conserved charges. Gauge (local) symmetries, on the other hand, reflect redundancies in the description and describe the effect of dynamical fields (the gauge bosons) which interact locally. These symmetries can be described by Lie groups.

A Lie group $(\mathcal{G}, \cdot)$ is defined as a group on a smooth (differentiable) manifold $\mathcal{G}$ such that group multiplication $\mu : \mathcal{G} \times \mathcal{G} \to \mathcal{G}, \quad \mu(x,y) = x \cdot y$ and taking inverses are both smooth (differentiable). The smoothness of the group operation provides a natural model for the concept of continuous symmetries.

For every Lie group there is also an associated Lie algebra which is the tangent space at the identity. A Lie algebra g is defined as a vector space g over a field F together with a binary operation $[\cdot, \cdot] : g \times g \to g$ called the Lie bracket, which is an alternating bilinear map that satisfies the Jacobi identity. (Side note: The commutators in quantum mechanics satisfy the same properties as the Lie bracket. Hence the generators of a Lie algebra satisfy commutation relations.) The Lie algebra is often a simpler object to study than the Lie group and the direct correspondence between them allows to study a Lie group by studying its associated algebra. One can map from the algebra to the group via the exponential operation: $\exp : g \to \mathcal{G}$, and the Lie group $(\mathcal{G}, \cdot)$ can be generated by mapping the elements of the algebra g onto the group $(\mathcal{G}, \cdot)$. This is where the term generator comes from. A set of generators of a Lie algebra g is a subset of g such that any Lie subalgebra that contains the set of generators must be all of g. Equivalently, the vector space g is spanned by all iterated Lie brackets of the elements of the set of generators.

Relating this to gauge theory, the transformations between possible gauges, called gauge transformations, form a Lie group which is also referred to as the symmetry group or the gauge group of the theory. The corresponding Lie algebra can then be seen as the infinitesimal transformations of fields under the respective symmetry group. The generators of the algebra can be mapped to generators of the group. For each generator of the Lie algebra, there is a corresponding component of the gauge fields, such that the gauge field is a Lie-algebra-values vector field. After quantisation of the theory, the quantum excitations of the gauge fields, also called quanta of the gauge fields, are associated with gauge bosons which can be interpreted as physical particles.

If the symmetry group is non-commutative, then the gauge theory is called a non-abelian gauge theory and the associated gauge bosons can couple to each other. If the symmetry group is commutative, it is called abelian and the associated gauge bosons do not couple to each other. The gauge group of the SM is the product group $SU(3)_C \times SU(2)_L \times U(1)_Y$.

The $U(1)$ and $U(1)_Y$ group:

The $U(1)$ group is the group of 1×1 unitary matrices, with the group operation of matrix multiplication. A unitary matrix U is an invertible complex square matrix with $U^{-1} = U^\dagger$, hence $UU^\dagger = U^\dagger U = \mathbb{1}$, where $\mathbb{1}$ is the identity matrix and $U^\dagger$ is the conjugate transpose of U. Since a 1×1 matrix is just a number this group consists of complex numbers z with $zz* = 1$, the elements z can also be written as $z = e^{i\alpha}$ with some phase α, hence it is also called the circle group, since the elements form a circle on the complex plane. It is an abelian Lie group with one generator.

As a gauge group, the $U(1)$ group describes quantum electrodynamics (QED). The generator of the symmetry gives rise to the electromagnetic field which in turn gives rise to the photon. Since the group is abelian photons do not interact with each other. In general a local $U(1)$ transformation can be written as multiplication with a complex number of norm 1 (a phase shift) $\psi(x) \to e^{i\alpha(x)}\psi(x)$. The Lagrangian density for the electromagnetic field can be written as $\mathcal{L}_{\text{EM}} = -\frac{1}{4}F_{\mu\nu}F^{\mu\nu}$, with $F_{\mu\nu} = \partial_\mu A_\nu - \partial_\nu A_\mu$ and A_μ the electromagnetic field. This term is invariant under a $U(1)$ transformation. The global form of the symmetry (if $\alpha =$const.) reveals that electric charge is the conserved charge associated with a global $U(1)$ transformation. The local form of the symmetry (if $\alpha = \alpha(x)$) has another interesting consequence. In order to include fermions (for example the electron and the positron) in the theory, their kinetic terms which include derivatives also need to be included in the Lagrangian. However, when transforming a fermion field as $\psi(x) \to e^{i\alpha(x)}\psi(x)$, its derivatives with respect to x will include an extra term due to the dependence of α on x. In order to compensate this the covariant derivative is introduced: $D_\mu = \partial_\mu + ieA_\mu$, with $\delta eA_\mu = \partial_\mu\alpha(x)$ and the elementary electric charge e. Now the Lagrangian for electrons and positrons can be written as $\mathcal{L}_{e^-,e^+} = \bar{\psi}(i\gamma^\mu D_\mu - m)\psi$, with $\bar{\psi} = \psi^\dagger\gamma^0$ and γ^μ being the Dirac matrices and m the mass of electrons e^- and positrons e^+. This term is invariant under $U(1)$ transformations and introduces the electromagnetic field, which gives rise to the photon, as a force carrier between the fermions. (The Noether current in this case is $j^\mu = e\bar{\psi}\gamma^\mu\psi$, which corresponds to the electromagnetic current.)

The $U(1)_Y$ group describes the weak hypercharge interaction with the hypercharge Y as a conserved charge. Together with the $SU(2)_L$ group it mixes to form the EW interaction describing the electromagnetic interaction (via QED as described above) and the weak interaction. The photon and the Z-boson arise from mixtures of the intermediate vector boson fields of the $U(1)_Y \times SU(2)_L$ group. The $W^\pm$-boson arises purely from vector boson fields of the $SU(2)_L$ group:

$$\begin{aligned}
&\text{photon field:} && A_\mu = \cos(\theta_W)B_\mu + \sin(\theta_W)W_\mu^3\,, \\
&Z\text{-boson field:} && Z_\mu = -\sin(\theta_W)B_\mu + \cos(\theta_W)W_\mu^3\,, \\
&W^\pm\text{-boson field:} && W_\mu^\pm = \frac{1}{\sqrt{2}}(W_\mu^1 \mp iW_\mu^2)\,,
\end{aligned} \tag{3.15}$$

where θ_W is the weak mixing angle and B_μ and W_μ^a are the intermediate vector boson fields of the $U(1)_Y$ and the $SU(2)_L$ group, respectively, from which the fields strength tensors in Equation 3.4 were constructed. Then the covariant derivative in Equation 3.6 can be constructed analogously to the covariant derivative of QED, described above. This mixing of the gauge fields is due to the spontaneous breaking of the EW symmetry which will be explained in more detail in the next subsection.

The $SU(2)_L$ group:

The $SU(2)$ group is the group of 2×2 unitary matrices with determinant 1, with the group operation of matrix multiplication. It is a non-abelian Lie group with three generators.

As a gauge group, the $SU(2)_L$ group describes the weak isospin interaction with the third component T_3 of the weak isospin as a conserved charge. The generators are the Pauli matrices which give rise to the weak boson fields. As mentioned above, together with the $U(1)_Y$ group it mixes to form the EW interaction. Since the $SU(2)$ group is a non-abelian Lie group, $W^\pm$ and Z-bosons can interact with each other. The subscript L indicates that only left-handed fermions (and right handed antifermions) take part in the weak interaction. For left-handed particles spin and momentum are aligned in opposite directions. For right-handed particles spin and momentum are aligned in the same direction. This preference for left-handed fermions results in weak interactions being asymmetric under parity transformations. A parity transformation is the flip in the sign of spatial coordinates, which corresponds to the mirror image. (Since spin can be described in the form of an angular momentum it does not change sign under a parity transformation, however momentum does change sign.) This phenomenon, that the weak interaction only includes left-handed fermions and hence interactions are not identical to their mirror image, was first observed by Wu in weak interaction particle decay [74]. The Wu experiment showed that experimentally left and right-handed processes can be distinguished in weak interactions. This is not the case for the other fundamental forces.

This results in left-handed fermions carrying weak isospin charge. They are usually arranged in doublets:

$$L_L = \begin{pmatrix} \nu_L \\ e_L \end{pmatrix}, \quad Q_L = \begin{pmatrix} u_L \\ d_L\,, \end{pmatrix} \tag{3.16}$$

where ν_L denote the three neutrino generations, e_L the charged lepton generations, u_L the up-type quark generations and d_L the down-type quark generations and the index L again indicates left-handedness. Right-handed fermions, on the other hand, do not carry isospin charge and are written as singlets l_R, u_R, d_R equivalently.

As mentioned earlier, due to the mixing of the $U(1)_Y \times SU(2)_L$ group, isospin T_3 as the conserved charge of the $SU(2)_L$ group and hypercharge Y as the conserved charge of the $U(1)_Y$ group mix to generate the electric charge $Q = T_3 + \frac{1}{2}Y$.

The $SU(3)_C$ group:

The $SU(3)$ group is the group of 3×3 unitary matrices with determinant 1, with the group operation of matrix multiplication. It is a non-abelian Lie group with eight generators.

As a gauge group, the $SU(3)_C$ group describes the strong interaction (QCD) with colour charge C as a conserved charge. The generators are the Gell-Mann matrices which give rise to the gluon fields from which the field strength tensors in Equation 3.4 were constructed. Since the $SU(3)$ group is a non-abelian Lie group, gluons can interact with each other. Fermions which carry colour charge take part in strong interaction, i.e. the quarks.

An overview of the gauge charges of the fermion fields of the SM can be found in Table 1.

Other symmetries of the Standard Model:

Above, the role of symmetries in the SM was discussed along with a short preview on how to construct parts of the Lagrangian, for example the covariant derivative, from these symmetries. A full derivation is beyond the scope of this work and pedagogical reviews or textbooks should be consulted in this case.

For completeness it remains to state that the full SM Lagrangian is invariant under Lorentz transformations. Lorentz transformations are a family of linear coordinate transformations from one inertial frame to another which moves at a constant

Fermion field	Spinor representation	$(SU(3)_C, SU(2)_L, U(1)_Y)$-charges
Q_L	$\begin{pmatrix} u_L \\ d_L \end{pmatrix}$	$(\mathbf{3}, \mathbf{2}, 1/6)$
u_R	u_R	$(\mathbf{3}, \mathbf{1}, 2/3)$
d_R	d_R	$(\mathbf{3}, \mathbf{1}, -1/3)$
L_L	$\begin{pmatrix} \nu_L \\ e_L \end{pmatrix}$	$(\mathbf{1}, \mathbf{2}, -1/2)$
e_R	e_R	$(\mathbf{1}, \mathbf{1}, -1)$

Table 1: The fermion fields of the Standard Model and their corresponding gauge charges [75], where u denote the three up-type quark generations, d the three down-type quark generations, ν the three neutrino generations and e the three lepton generations. The subindex L denotes left-handedness and R right-handedness. Bold numbers **1**, **2** and **3** denote singlets, doublets and triplets, respectively.

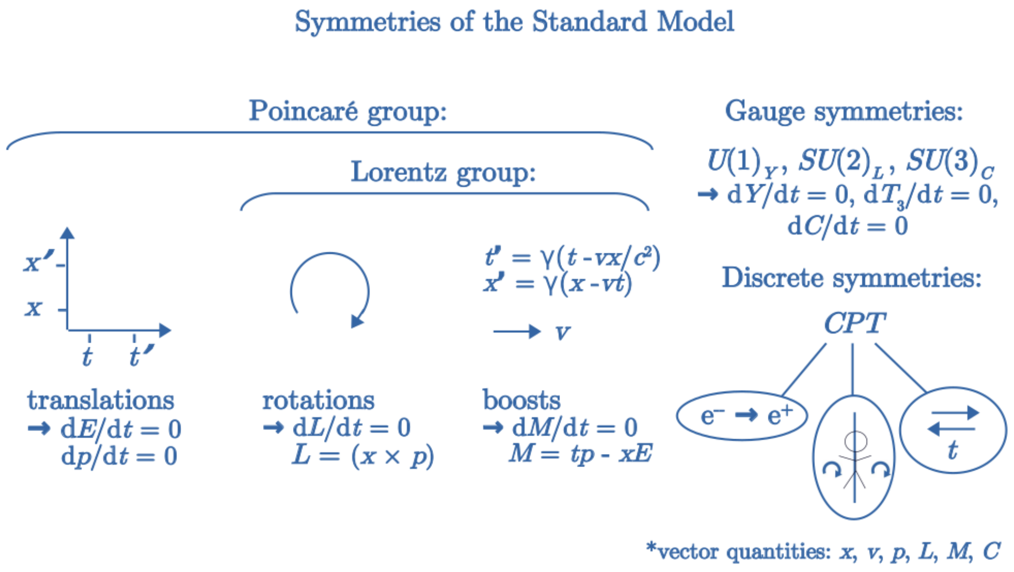

Figure 6: The symmetries of the Standard Model Lagrangian.

velocity relative to the first one. They are parameterised by six parameters which include boosts and rotations.

Lorentz transformations together with time and space translations generate the Poincaré group. The Poincaré group describes the full symmetry of special relativity.

Another symmetry in the SM is the symmetry under CPT transformations. This is a discrete, and not continuous, symmetry. (Noether's theorem does not apply here.) C denotes charge conjugation and turns particles into antiparticles. P is the parity transformation flipping the sign of spacial coordinates, as mentioned earlier, and T is time reversal. C and P-symmetry and the combined CP are violated by the weak interaction. (CP-violating terms are allowed in the SM if the quark mixing matrix, the Cabibbo–Kobayashi–Maskawa (CKM) matrix, contains a complex phase. A necessary condition for this is the existence of at least three fermion generations, which if fulfilled in the SM.) Only the combined CPT transformation is a global symmetry of the SM. It is a consequence of locality, causality and unitarity.

A schematic summary of the symmetries of the SM Lagrangian is depicted in Figure 6.

After having discussed the symmetries of the SM and how gauge symmetries give rise to the fundamental interactions, the next subsection will concentrate on the scalar potential and how the EW symmetry is spontaneously broken.

3.1.2 Scalar potential and spontaneous symmetry breaking

The scalar potential, also called the Higgs potential, can be written as above in Equation 3.10:

$$V(\Phi) = -\mu^2 \Phi^\dagger \Phi + \lambda (\Phi^\dagger \Phi)^2 \,,$$

with the scalar field which gives rise to the Higgs boson:

$$\Phi = \begin{pmatrix} \phi^+ \\ \phi \end{pmatrix} \,, \tag{3.17}$$

where $\mu^2 > 0$ and λ are parameters and the scalar field Φ is a scalar $SU(2)_L$ doublet, meaning that it has spin 0, transforms under the fundamental representation of $SU(2)$ and has two complex components. The upper component ϕ^+ is charged and the lower component ϕ is neutral. The shape of the potential is schematically shown in Figure 7. (This is the form the potential takes at zero temperature after electroweak symmetry breaking (EWSB). At higher temperatures thermal correc-

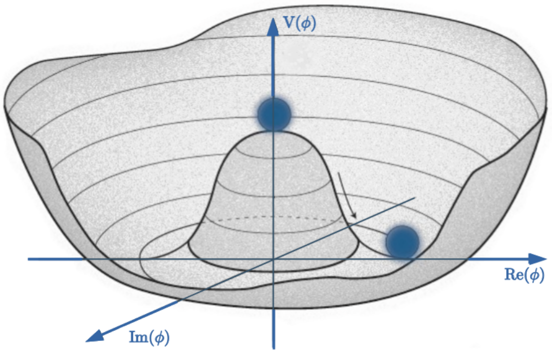

Figure 7: Schematic shape of the scalar potential V in dependence of the neutral component ϕ of the scalar field after spontaneous breaking of the electroweak symmetry. The spontaneous breaking of the symmetry through choosing one particular vacuum configuration is indicated by the large blue dots in the image, figure adapted from Oxford Department of Physics.

tions change its shape.) The potential has degenerate minima at $\Phi^\dagger\Phi = \frac{\mu^2}{2\lambda} = \frac{v^2}{2}$, where v is called the vacuum expectation value (vev) of the scalar field. This leads to the process of spontaneous symmetry breaking. (The spontaneous breaking of the EW symmetry is also referred to as electroweak symmetry breaking (EWSB) or electroweak phase transition (EWPT).)

Spontaneous symmetry breaking:

Spontaneous symmetry breaking refers to the process where a field acquires a nonzero expectation value that has a directional character and thus breaks the symmetry of the Lagrangian. This is analogous to the magnetisation of a ferromagnet. The ferromagnet undergoes a phase transition starting from a symmetric non-magnetic state to a magnetic state with a preferred direction.

The spontaneous breaking of the symmetry can be understood by taking the scalar potential above (for simplicity the upper component of the scalar field will be set to zero here and the scalar field will be treated as a singlet with only one component ϕ) and writing the scalar field as: $\phi = v + \rho$, where $v = \sqrt{\frac{\mu^2}{2\lambda}}$ is the chosen vev of the field (chosen vev meaning that without loss of generality one vacuum configuration can be chosen from the set of degenerate minima). Inserting this expression back into the potential gives:

$$\begin{aligned} V(\phi) &= -\mu^2\phi^\dagger\phi + \lambda(\phi^\dagger\phi)^2 \\ &\overset{\phi=v+\rho,\, v=\sqrt{\frac{\mu^2}{2\lambda}}}{=} -\frac{\mu^4}{4\lambda} + 2\mu^2\rho^2 + \mu\sqrt{8\lambda}\rho^3 + \lambda\rho^4\,, \end{aligned} \tag{3.18}$$

where, before inserting the form $\phi = v + \rho$, the potential was symmetric under a $U(1)$ transformation: $\phi \to e^{i\alpha}\phi$. After inserting the form $\phi = v + \rho$, however, this symmetry is not obvious anymore. Hence the symmetry is spontaneously broken.

When a global symmetry is broken spontaneously, the symmetry currents remain conserved and interactions still manifest in the same way as for the unbroken symmetry. However, the vacuum state does not respect the symmetry. According to Goldstone's theorem such a theory contains massless particles, called Goldstone bosons. For each generator of the symmetry which is spontaneously broken one such massless Goldstone boson appears. So, if taking the example of a global $U(1)$ symmetry, which has one generator, and breaking the symmetry spontaneously, then there must be one massless Goldstone boson. For the $SU(2)$, which has three generators, consequently three massless Goldstone bosons are generated by the spontaneous breaking of the symmetry.

The Higgs mechanism:

The discussion above is true for a global symmetry that is broken spontaneously.

For local symmetries, like the gauge symmetries, that are broken spontaneously it gets a little more complicated. Furthermore, in the SM the Higgs field is a scalar field coupled to both the $U(1)_Y$ and $SU(2)_L$ fields via the covariant derivative in Equation 3.6. It does not couple to the $SU(3)_C$ fields, hence the last term of the covariant derivative can be dropped and one obtains:

$$D_\mu \Phi = \left(\partial_\mu - i g_1 \frac{Y}{2} B_\mu - i g_2 W_\mu^a \frac{\sigma^a}{2} \right) \Phi \,, \tag{3.19}$$

with the $U(1)_Y$ and $SU(2)_L$ coupling constants g_1 and g_2 and the Pauli matrices σ^a, with $a = 1,2,3$ as the generators of the $SU(2)_L$ group. The generator Y of the $U(1)_Y$ group acts on a field Φ by multiplication with the hypercharge which is 1 for the Higgs field, hence it can be set to 1. Before going through the Higgs mechanism for the combination of the $U(1)_Y$ and $SU(2)_L$ gauge groups there are a few points to note:

- *Massive bosons:* Spontaneously broken gauge theories lead to nonzero mass terms for the gauge bosons. The interactions of these massive gauge bosons are constrained by the underlying gauge symmetry with observable consequences.

- *Goldstone bosons:* As mentioned above, in theories with spontaneously broken global symmetries massless Goldstone bosons arise. In spontaneously broken gauge theories the involvement of Goldstone bosons is necessary in order for the gauge bosons to acquire their mass. However, the Goldstone bosons can be formally eliminated from the theory but do not disappear completely. They form the longitudinal polarisation state, that the corresponding gauge bosons obtained when acquiring a mass term. It is often said that the gauge bosons acquired this extra degree of freedom by ‘eating’ the Goldstone boson. The influence of the Goldstone boson then still manifests via the Goldstone boson equivalence theorem, which sates that at high energies the amplitude for emission or absorption of a longitudinally polarised gauge boson becomes equal to the amplitude for emission or absorption of the Goldstone boson that was eaten.

- *Direction of the vacuum expectation value:* For a non-abelian example of the Higgs mechanism, consider the scalar field coupled only to the $SU(2)$ gauge fields. If the scalar field, which also is a vector of $SU(2)$, acquires a vev, one can choose (by rotations according to the generators, the Pauli matrices) the coordinates so that this vector points in a particular direction in internal space. Hence, the vev destroys the symmetry of rotation about two of the axes, but it preserves the symmetry of rotation about the third axis. Then only two of the three generators acquire mass terms. The third one remains unbroken and massless.

- *Interesting fact on superconductivity:* A purely abelian example of the Higgs mechanism is the Meissner effect. It describes the exclusion of macroscopic magnetic fields from a superconductor. When breaking the abelian $U(1)$ symmetry spontaneously, the gauge field acquires a nonzero mass term m_A. This is what happens in a superconductor. External electromagnetic fields then penetrate the superconductor only to the depth m_A^{-1}.

Now consider a simultaneous $U(1)_Y$ and $SU(2)_L$ gauge transformation of the scalar field and the following vev configuration for the scalar field:

$$\begin{aligned} \Phi &\to e^{i\alpha^a\sigma^a/2}e^{iY/2}\Phi\,, \\ \langle\Phi\rangle &= \frac{1}{\sqrt{2}}\begin{pmatrix}0\\ v\end{pmatrix}\,, \end{aligned} \tag{3.20}$$

where again $Y=1$ for the Higgs field. The gauge transformation can be chosen such that $\alpha^1=\alpha^2=0$ and $\alpha^3=Y$. This configuration leaves the vacuum configuration $\langle\Phi\rangle$ invariant. (This choice can be made since there is some freedom of rotations as in the example for the non-abelian case of the Higgs mechanism above.) This configuration of the gauge transformation will result in one massless gauge boson and three massive gauge bosons which acquire their masses through the Higgs mechanism.

The mass terms of the gauge bosons can be calculated via the kinetic term of the scalar field in Equation 3.9, which includes the covariant derivative, and evaluating the scalar field at the vev:

$$\begin{aligned} \mathcal{L}_{\text{H, kin}}|_{\Phi=\langle\Phi\rangle} &= (D_\mu\Phi)^\dagger(D^\mu\Phi)|_{\Phi=\langle\Phi\rangle} \\ \Delta\mathcal{L} &= \frac{1}{2}\begin{pmatrix}0 & v\end{pmatrix}\left(g_1\frac{1}{2}B_\mu+g_2W^a_\mu\frac{\sigma^a}{2}\right)\left(g_1\frac{1}{2}B^\mu+g_2W^{\mu a}\frac{\sigma^a}{2}\right)\begin{pmatrix}0\\ v\end{pmatrix} \\ &= \frac{1}{2}\frac{v^2}{4}[g_2^2(W^1_\mu)^2g_2^2(W^2_\mu)^2+(-g_2W^3_\mu+g_1B_\mu)^2]\,, \end{aligned} \tag{3.21}$$

where $\Delta\mathcal{L}$ includes only the terms relevant for the calculation of the mass terms and Y was set to 1. From the fields B_μ and W^a_μ, with $a=1,2,3$, now the photon, the Z and the $W^\pm$-boson can be constructed as in Equation 3.15 with $\cos(\theta_W)=\frac{g_2}{\sqrt{g_1^2+g_2^2}}$ and $\sin(\theta_W)=\frac{g_1}{\sqrt{g_1^2+g_2^2}}$. The masses of the gauge bosons are:

$$m_\gamma=0\,,\quad m_Z=\sqrt{g_1^2+g_2^2}\frac{v}{2}\,,\quad m_{W^\pm}=g_2\frac{v}{2}\,, \tag{3.22}$$

for the photon γ, the Z-boson and the $W^{\pm}$-boson, respectively. The derivation along with more details can be found for example in chapter 20 of Ref. [71]. As one can see, because of the breaking of the symmetry in three directions the Z and $W^{\pm}$-boson obtained mass terms. However, the photon does not obtain a mass term. The $SU(2)_L \times U(1)_Y$-symmetry was broken to a $U(1)_{\text{em}}$. This residual symmetry is the reason why the combination $Q = T_3 + \frac{Y}{2}$ is unbroken and the photon remains massless.

The masses m_f of the fermions arise from the Yukawa interactions in Equation 3.7 and also depend on the vev of the scalar field: $m_f = \frac{y_f v}{\sqrt{2}}$, where y_f is the Yukawa coupling constant of the corresponding fermion.

There is one more symmetry to be mentioned, the custodial symmetry. In general a custodial symmetry is a symmetry which remains unbroken after spontaneous symmetry breaking and can prevent higher-order radiative corrections from spoiling certain properties of the theory. In the case of the SM the custodial symmetry is a residual global $SU(2)$ symmetry. The scalar potential has a global symmetry under $SU(2)_L SU(2)_R$ transformations. (This is a symmetry of the scalar potential, not of the entire SM Lagrangian. For example gauge interactions and Yukawa couplings do not respect this symmetry, which makes it an approximate symmetry of the SM.) This symmetry is also spontaneously broken by the vev of the Higgs field to the diagonal subgroup $SU(2)_V$, which protects the following tree-level mass relation from higher-order radiative corrections: $\rho = \frac{m^2_{W^\pm}}{m^2_Z \cos^2(\theta_W)} = 1$. Experimentally ρ is very close to 1, which indicates that the custodial symmetry is nearly preserved. New physics is constrained by the requirement of preserving of the custodial symmetry which affects EW precision tests.

The Higgs boson, corresponding to the physical excitation of the neutral real component of the scalar $SU(2)$ doublet was discovered in 2012, about 50 years after its prediction by Higgs [6]. Its mass was measured to be about 125 GeV [4, 5]. The vev is related to the Fermi constant G_F via $v = \frac{1}{\sqrt{2} G_F}$, which in turn is related to the mass of the $W^{\pm}$-boson: $\frac{G_F}{\sqrt{2}} = \frac{g_2^2}{8 m^2_{W^\pm}}$. The Fermi constant gives the strength of the weak interactions at low energies (much lower than $m_{W^\pm}$). It can be measured experimentally from muon decay. The value of v calculated from this results to about 246 GeV.

3.1.3 Methods in quantum field theory

In order to calculate physical observables the Lagrangian in Equation 3.2 must be quantised. Here the path integral formalism will be followed. This method is manifestly Lorentz-invariant. The path integral formalism captures all possible paths connecting two points by taking the sum over all possible classical field configurations weighted by the exponential of the classical action $\mathcal{S} = \int \mathrm{d}^4x\mathcal{L}$. This is described by the generating functional:

$$\mathcal{Z}[J] = \int \mathcal{D}\phi e^{i(\mathcal{S}_{\mathrm{SM}} + \int \mathrm{d}^4x J(x)\phi(x))}, \tag{3.23}$$

where $\mathcal{S}_{\mathrm{SM}} = \int \mathrm{d}^4x\mathcal{L}_{\mathrm{SM}}$ is the SM action and $J(x)$ is an auxiliary field that captures external sources. ϕ is used here as a short notation to collect all dynamical fields, i.e. scalar, vector and fermion fields. The generating functional $\mathcal{Z}[J]$ is a functional integral, where $\mathcal{D}\phi$ and encodes all possible configurations of the fields ϕ.

Correlation functions, also called Green functions, then, can be computed by taking functional derivatives of $\mathcal{Z}[J]$. Before doing this, the gauge needs to be fixed. However, this will be described below, while here, first the general relations between correlation functions and scattering amplitudes will be described. So, assuming that the gauge was fixed already, one can go on to calculating the Green function. The Green function for the correlation between n points can be written as:

$$\begin{aligned} G_n(x_1,\ldots,x_n) &= \langle 0|T\phi(x_1)\ldots\phi(x_n)|0\rangle \\ &= \frac{1}{\mathcal{Z}[J=0]} \cdot \frac{\delta^n \mathcal{Z}[J]}{i^n \delta J(x_1)\ldots\delta J(x_n)}\Big|_{J=0}, \end{aligned} \tag{3.24}$$

where T is the time ordering operator. The functional derivative $\frac{\delta}{\delta J(x)}$ obeys the axiom: $\frac{\delta}{\delta J(x)} J(y) = \delta^{(4)}(x-y)$ or $\frac{\delta}{\delta J(x)} \int \mathrm{d}^4y J(y)\phi(y) = \phi(x)$. The n-point function $\langle 0|T\phi(x_1)\ldots\phi(x_n)|0\rangle$ corresponds to the sum of all full contractions. This can be obtained using Wick's theorem. For example the contraction of two fields is defined as: $\langle 0|T\phi(x_1)\phi(x_2)|0\rangle = D_F(x_1-x_2) = \frac{\int \mathcal{D}\phi e^{i\mathcal{S}}\phi(x_1)\phi(x_2)}{\int \mathcal{D}\phi e^{i\mathcal{S}}} = \int \frac{\mathrm{d}^4k}{(2\pi^4)} \frac{ie^{-ik\cdot(x_1-x_2)}}{k^2-m^2+i\epsilon}$, which is the form of a Feynman propagator. In the last step a Fourier expansion with momentum k has been done and $i\epsilon$ is a convergence factor (see chapter 9 of Ref. [71] for a full derivation). From the correlation function, the Feynman rules can be derived, which provide a more intuitive understanding of scattering amplitudes.

The scattering amplitude can then be related to the Green function via the Lehmann-Symanzik-Zimmermann (LSZ) reduction formula:

$$\begin{aligned} \langle f|S|i\rangle &= \delta_{fi} + i(2\pi)^4\delta^{(4)}(p_f-p_i)\mathcal{M}_{fi} \\ &= (2\pi)^4\delta^{(4)}(p_f-p_i)G_n^{\mathrm{trunc}}(p_1,\ldots,p_n)|_{p_j^2=m_j^2}, \end{aligned} \tag{3.25}$$

where i denotes the initial and f the final state with momenta p_i and p_f, respectively, $S = \mathbb{1} + iT$ is the scattering matrix describing the probability to go from an initial state to a final state, with $\mathbb{1}$ the identity matrix and T the transition matrix accounting for interactions between the states. $\mathcal{M}_{fi}$ is the scattering amplitude and G_n^{trunc} is the truncated Green function in momentum space (truncated meaning that external legs are removed). The relation of the scattering amplitude $\mathcal{M}$ and the cross section σ of a scattering process can be written as: $\sigma = \int \mathrm{d}\Pi \frac{1}{F} |\mathcal{M}_{fi}|^2$, where F is a flux factor describing incoming particles and $\mathrm{d}\Pi$ is the Lorentz invariant phase space for outgoing particles.

Gauge-fixing:

As mentioned above, the gauge still needs to be fixed. This is necessary since, because of gauge invariance, the functional integral $\int \mathcal{D}\phi$ in the expression for $\mathcal{Z}[J]$, above, redundantly integrates over a continuous infinity of physically equivalent field configurations. In order to isolate the interesting part of the functional integral, which counts each physical configuration only once, the gauge needs to be fixed. This can be done with the Faddeev-Popov method [76], where a representation of 1 is inserted into the integral in Equation 3.23:

$$1 = \int \mathcal{D}\alpha(x) \delta(G(\phi^\alpha)) \det\left(\frac{\delta G(\phi^\alpha)}{\delta\alpha}\right), \tag{3.26}$$

where ϕ^α denotes the gauge-transformed field and α is the parameter of the gauge transformation. For example, in the case of QED: $\phi = A$, where A denotes the electromagnetic field and the gauge transformed field can be written in the form: $A_\mu^\alpha(x) = A_\mu(x) + \frac{1}{e}\partial_\mu \alpha(x)$ (this comes from the definition $\delta e A_\mu = \partial_\mu \alpha(x)$ which was used in constructing the covariant derivative for the $U(1)$ gauge group, discussed above).

Now the condition $G(\phi) = 0$ is the gauge fixing condition. This condition is adhered to by the delta function $\delta(G(\phi))$ above. This delta function constrains the functional integral to cover only the configurations with $G(\phi) = 0$. For the example of QED, the Lorentz gauge would correspond to the choice $G(A) = \partial_\mu A^\mu$. This condition is Lorentz invariant. For the example of a spontaneously broken gauge theory, the gauge fixing function can be chosen such that mixing with the massless Goldstone boson is eliminated. For example, in the R_ξ-gauge for the Z-boson: $G[Z] = \partial_\mu Z^\mu + \xi_Z m_Z G^0$, where ξ_Z is the gauge fixing parameter, m_Z the mass of the Z-boson and G^0 is the neutral Goldstone boson. This gauge is commonly used in perturbative calculations. One can also choose the unitary gauge. In this gauge the Goldstone degrees of freedom are set to zero to disappear from the theory and are ‘eaten’ by the massive gauge bosons, as was mentioned earlier in the description of the Higgs mechanism.

This can be now inserted into the functional integral, giving:

$$\begin{aligned}\mathcal{Z}[J] &= \int \mathcal{D}\phi e^{i(\mathcal{S}_{\mathrm{SM}}+\int \mathrm{d}^4 x J(x)\phi(x))} \\ &= \det(\frac{\delta G(\phi^\alpha)}{\delta\alpha}) \int \mathcal{D}\alpha \int \mathcal{D}\phi e^{i(\mathcal{S}_{\mathrm{SM}}+\int \mathrm{d}^4 x J(x)\phi(x))} \delta(G(A))\,.\end{aligned} \tag{3.27}$$

The integral is now restricted by the delta function to cover only physically inequivalent field configurations. For perturbative computations, however, a Gaussian representation is more suitable than the delta function form: $\delta(G(\phi)) \to e^{-\frac{i}{2\xi}\int \mathrm{d}^4 x [G(x)]^2}$, where ξ is a gauge fixing parameter. The choice of the gauge fixing function $G(\phi)$ can now be inserted.

Another note on gauge fixing needs to be made. Gauge fixing introduces the Faddeev-Popov determinant. Using the identity this can be written as:

$$\det(\frac{\delta G(\phi^\alpha)}{\delta\alpha}) = \int \mathcal{D}\bar{c}\mathcal{D}c e^{i\int \mathrm{d}^4 x \bar{c}\frac{\delta G[\phi]}{\delta\alpha}c}\,, \tag{3.28}$$

where c and $\bar{c}$ are Grassmann-valued (anticommuting) scalars. They are auxiliary fields whose quantum excitations have the wrong relation between spin and statistics to be considered physical particles. They are Lorentz scalars but obey Fermi–Dirac statistics and only contribute through loop diagrams. Hence they are called Faddeev-Popov ghosts. Their excitations can be treated as additional particles in the computation of Feynman diagrams. One can write a Lagrangian $\mathcal{L}_{\mathrm{ghost}}$ for the ghosts and a Lagrangian $\mathcal{L}_{\mathrm{GF}}$ for the gauge fixing part and add them to the SM Lagrangian. The ghost part would look like $\mathcal{L}_{\mathrm{ghost}} = \bar{c}^a(-\partial^\mu D^{ab}_\mu)c^b$. And the gauge fixing part for the abelian example of QED would look like $\mathcal{L}_{\mathrm{GF,\ abelian}} = -\frac{1}{2\xi}(\partial^\mu A_\mu)^2$ and equivalently for the a non-abelian multiplet $\mathcal{L}_{\mathrm{GF,\ non\text{-}abelian}} = -\frac{1}{2\xi}(\partial^\mu A^a_\mu)^2$. The full effective Lagrangian then is:

$$\mathcal{L}^{\mathrm{eff.}}_{\mathrm{SM}} = \mathcal{L}_{\mathrm{SM}} + \mathcal{L}_{\mathrm{GF}} + \mathcal{L}_{\mathrm{ghost}}\,. \tag{3.29}$$

The action of this Lagrangian is invariant under a global fermionic transformation called Becchi–Rouet–Stora–Tyutin (BRST) symmetry [77], which is a transformation of the fields adding an anticommuting parameter. According to Noether's theorem this implies the existence of a conserved charge, which is described by the BRST operator Q. The BRST operator is nilpotent ($Q^2 = 0$) and divides the eigenstates of the Hamiltonian into three subspaces which correspond to: 1. forward-polarised gauge bosons and antighosts, 2. ghosts and backward-polarised gauge bosons and 3. transverse-polarised gauge bosons. This way the BRST operator separates ghosts and unphysical polarisation modes, which belong to the first two subspaces, from physical transversely-polarised gauge bosons (see chapter 16 of Ref. [71] for a more in-depth explanation).

Renormalisation:

In perturbative QFT, loop diagrams typically lead to divergent integrals. These divergences can be fixed in two steps. First, the theory is regularised making divergent expressions well-defined. Then, the theory is renormalised by redefining bare parameters in terms of finite renormalised quantities.

There are different ways to *regularise* a theory. One of the usual choices is the so-called cutoff regularisation where a cutoff scale Λ is introduced in the upper bound of momentum integrals. Another usual choice is dimensional regularisation where the dimension d of the integrals is first left as a free parameter $d = 4 - 2\epsilon$. Divergences then appear as poles in $1/\epsilon$. A renormalisation scale μ then needs to be introduced in order to assure the correct mass dimension of the integral.

After regularisation, which is a purely mathematical procedure to control divergences, *renormalisation* redefines the parameters of the Lagrangian through the introduction of counterterms. This removes infinities form the theory and maintains its physical meaning. For a coupling g and a field ϕ the bare quantities, with subindex 0, can be related to the renormalised quantities, with subindex R, as:

$$\begin{aligned} g_0 &= Z_g(\mu) g_R \simeq (1 + \delta Z_g(\mu)) g_R \\ \phi_0 &= Z_\phi^{1/2}(\mu) \phi_R \simeq (1 + \frac{1}{2}\delta Z_\phi(\mu)) \phi_R\,, \end{aligned} \tag{3.30}$$

where the second equalities are only valid to first perturbation order and Z_g and Z_ϕ are renormalisation constants. The terms δZ_g and δZ_ϕ are called counterterms with μ as the renormalisation scale. The Lagrangian can then be rewritten in terms of the renormalised quantities and the counterterms:

$$\mathcal{L}(\phi_0, g_0) = \mathcal{L}(\phi_R, g_R) + \mathcal{L}_{\mathrm{CT}}(\phi_R, g_R, \delta Z_\phi, \delta Z_g)\,. \tag{3.31}$$

The bare terms and the counterterms are infinite, however, the cancellations of these infinities gives the finite renormalised parameters calles subtraction. Again, there are different options of subtraction. One usual choice is the minimal subtraction (MS) scheme where the counter terms are defined such that they cancel divergent poles of the theory but preserve the finite parts. This scheme is mass-independent but a matching must be applied when comparing physical quantities at different energy scales. A similar subtraction scheme is the modified minimal subtraction ($\overline{\mathrm{MS}}$) scheme. In this scheme the divergent poles plus finite constant parts, like the Euler-Mascheroni constant γ_E and terms of $\ln(4\pi)$ which usually arise along with the divergent poles, are absorbed. Another usual choice is the On-shell scheme where the renormalised masses are equal to the physical masses of the particles. In this scheme the propagator has a pole at this mass.

3.2 Shortcomings of the Standard Model

The SM of particle physics is experimentally very well explored. Despite its success, however, there are several shortcomings and phenomena which it does not address:

- *Gravity:* As already mentioned, a quantum description of gravity, one of the four fundamental forces, is not included in the SM. The SM is considered to be incompatible with general relativity, as its inclusion in the QFT framework is non-renormalisable.

  Theories which could combine QFT and general relativity are theories of quantum gravity, such as for example string theories.

- *Neutrino masses:* Currently the SM does not include mass terms for neutrinos, however observations of neutrino oscillations indicate that at least two of the three neutrino generations do have mass. In theory, neutrino mass terms can be added to the SM, however, it is currently not clear how these mass terms arise in nature or whether they arise in the same way as for other fundamental particles of the SM.

  One possible inclusion of neutrino masses in BSM theories is as Majorana particles. Unlike Dirac fermions, like the other SM fermions, a Majorana fermion is its own antiparticle. This is a possibility for neutrinos since they do not carry electric charge or colour charge. With the seesaw mechanism and the inclusion of very massive right-handed neutrinos it is possible to explain why the masses of left-handed neutrinos are so small compared to other SM fermions.

- *Baryon asymmetry:* The asymmetry between baryons and antibaryons in the Universe is about: $\eta_s = \frac{n_B - n_{\bar{B}}}{s} \sim 6 \cdot 10^{-10}$, where n_B is the number of baryons, $n_{\bar{B}}$ the number of antibaryons and s is the entropy density. In the SM however, due to CPT-symmetry, baryons and antibaryons are always produced and annihilated in equal amounts. Thus a mechanism is needed to explain the observed asymmetry between baryons and antibaryons. This mechanism is called baryogenesis, as mentioned in the first section of this work. There are three necessary conditions, called the Sakharov conditions, for sufficient baryogenesis: baryon number violation, C- and CP-symmetry violation and departure from thermal equilibrium [78].

These conditions are present in the SM, however, not of sufficient amount to generate the observed asymmetry. One popular realisation of baryogenesis is via the EW phase transition, called EW bayogenesis (see for example Refs. [79–81]). This requires a strong first-order EW phase transition. In the SM the EW phase transition via the process of spontaneous symmetry breaking is a smooth cross-over rather than a first-order transition. Extensions of the scalar sector can modify the scalar potential in such a way that the transition becomes first-order. Such a transition proceeds via the formation of bubbles of the new broken phase, where the speed of the expanding bubble walls impacts the out-of-equilibrium conditions. Baryons are then created in the vicinity of the expanding bubble walls in three steps [82]: First, particles from the surrounding plasma (in the old symmetric phase) scatter with the bubble walls. If the theory contains CP violation, this scattering can generate CP (and C) asymmetries in particle number densities outside the bubble. Then, these asymmetries diffuse into the old symmetric phase outside the bubble, where EW sphaleron transitions lead to the production of more baryons than antibaryons. Finally, a part of the net baryon charge created outside the bubble becomes enclosed by the expanding bubble wall and is transferred into the new broken phase. The rate of sphaleron transitions is strongly suppressed in the new phase, hence the created baryons are not washed out.

(Sphalerons are unstable field configurations of the EW field equations that exist at high energies. They can be seen as a saddle point between two minima of the EW potential. Since they appear at high energies they play a role in non-perturbative effects and can lead to baryon number violation. Baryon number conservation is an accidental symmetry in the SM which can be violated in non-perturbative effects.)

- *Dark matter:* There is no explanation for the observed amount of DM in the SM. According to the ΛCDM model, DM must be cold (non-relativistic), non-baryonic and interacting very weakly with baryonic matter. Also self-interactions of DM are assumed to be weak. The main interaction is gravitationaly.

  Measurements of the luminosity of stars indicate that the amount of known ordinary matter is about 5% of the total energy content of the Universe, as mentioned in the first section. However observations from galaxy rotation curves, bulk flows, hot gas in galactic clusters, structure formation, and CMB observations indicate that there must be more matter present in the universe than this 5%. The aforementioned observations indicate that DM must comprise about 26% of the energy density of our Universe. BBN poses stringent bounds on the amount of baryonic matter. This suggests that most DM must be non-baryonic. (See Ref. [55] for more details.)

Some proposed candidates for DM are: weakly interacting massive particles (WIMPs) which are predicted in many supersymmetric theories and theories with extended scalar sectors, axions which were originally introduced to solve the strong CP problem, PBHs and sterile neutrinos. A good overview can be found for example in Ref. [83].

- *strong CP problem:* The strong CP problem is a fine-tuning problem concerning the question why QCD preserves CP-symmetry. QCD, in theory, allows for CP violation (which is also present in weak interactions as discussed earlier). However, measurements of the neutron electric dipole moment have shown that the CP-violating angle θ of QCD is very small ($\theta < 10^{-10}$) [84]. This smallness of the CP-violating angle is a fine tuning problem.

  There are several proposed solutions. A popular solution is the Peccei–Quinn mechanism which predicts the existence of a pseudo-Goldstone boson called axion which dynamically sets the CP-violating angle to 0 [85]. Axions are also a popular candidate for DM.

- *Hierarchy problem:* The hierarchy problem is another fine-tuning problem concerning the question why the weak force with the Fermi constant is much stronger than gravity with the Newtonian constant of gravitation. This can be translated to the question why the mass of the Higgs boson is much lighter than the Planck mass. When treating the SM as an effective field theory of a more complete description (for example including gravity), the mass of the Higgs boson would receive quantum corrections from loop diagrams involving all particles that couple to it. Since there is no symmetry protecting the mass of the Higgs boson from such large corrections, these quantum corrections would make the mass very large, unless there is a fine-tuned cancellation between these corrections and the bare mass.

  There are several proposed solutions to this fine-tuning problem, for example supersymmetry, composite Higgs models or the inclusion of extra dimensions which lower the energy cut-off scale.

- *Cosmological constant problem:* The cosmological constant problem is another fine-tuning problem concerning the large discrepancy between the observed small value of the cosmological constant and the much larger zero-point energy theoretical prediction by QFT.

There are several proposed solutions, for example modifications of gravity or arguments based on the anthropic principle.

The three fine-tuning problems mentioned above, the strong CP problem, the hierarchy problem and the cosmological constant problem, relate to the concept of naturalness. This is the requirement that the parameters of a theory should be of a similar order of magnitude.

3.2.1 Extended scalar sectors and first-order phase transitions

Some of the problems mentioned above, for example the explanation of DM or the baryon asymmetry, can be addressed with extended scalar sectors. In these theories additional scalar fields are added to the scalar potential in Equation 3.17. One example is the Two-Higgs-doublet model (2HDM) where an additional scalar $SU(2)$ doublet is added to the SM, or its further extensions with not only a scalar doublet but also an additional scalar singlet. In case of a real singlet the model is called Next-to-minimal Two-Higgs-doublet model (N2HDM) and in case of a complex singlet the model is called 2HDMS. The 2HDMS will be investigated further in section 4. The particle content of the scalar sector in this model is schematically shown in Figure 8. On the left, the SM doublet which gives rise to the SM-like Higgs boson is depicted. On the right, the 2HDMS which contains two doublets and one singlet and gives rise to seven scalar particles is depicted. (Each component is complex and in both cases three degrees of freedom become part of the massive $W^{\pm}$ and Z-boson via spontaneous symmetry breaking, as explained earlier.) This model provides a natural candidate for DM, when imposing certain symmetries, and also modifies the scalar potential such that the EW phase transition can be of first-order for parts of the parameter space. Furthermore, in the recent past there have been several

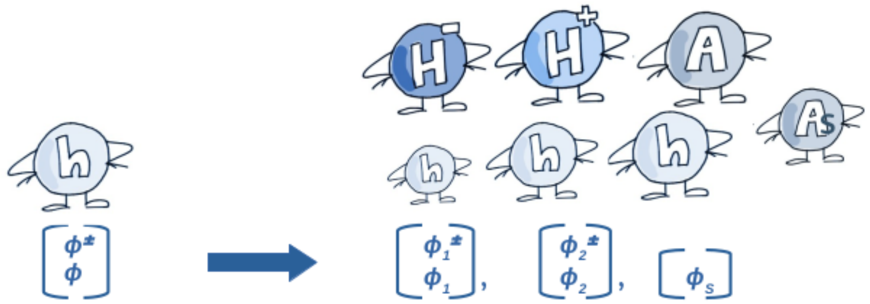

Figure 8: The particle content of the scalar sector in the SM (left) and in the 2HDMS extension (right). The SM contains one complex scalar doublet. The 2HDMS contains two complex scalar doublets and one complex scalar singlet, figure adapted from Ref. [86].

anomalies (also commonly called excesses) observed in collider experiments which can be explained in this model. An introduction to the model and the investigation of its phenomenological consequences will be provided in section 4.

As mentioned above, FOPTs proceed via the formation of bubbles. The speed of the expanding bubble walls is of importance for the out-of-equilibrium conditions in baryogenesis. The speed of bubble walls from FOPTs is the second main topic of this work treated in section 5, where there will be a special emphasis on transitions with symmetry restoration instead of symmetry breaking. In Figure 9 the difference between a second-order (or smooth cross-over) and a first-order EWPT is shown schematically. A FOPT is characterised by a discontinuous change in the relevant quantity (or order parameter). For the EWPT via spontaneous symmetry breaking, the relevant quantity is the vev which changes as the Universe cools down. Such a discontinuous change can happen when the scalar potential is modified in such a way that there is a potential barrier between the old symmetric vacuum and the new broken vacuum phase. This is depicted in the middle image, where on the left side of the vertical axis the smooth transition, as in the SM, is shown and on the right side of the vertical axis a small potential barrier can be seen. Thermal corrections modify the potential at higher temperatures such that at high temperatures the minimum of the potential is at $\phi = 0$. At the critical temperature T_c the potential is modified in such a way that there are two degenerate minima separated by a potential barrier. Below the critical temperature the new minimum at $\phi = v$ becomes favoured. As a result the field needs to tunnel through this potential barrier and changes its value discontinuously as shown in the right-most image. The left-most image shows the case for a second-order transition where the vev of the field changes smoothly. In many BSM scenarios the case of a FOPT is realised. In the 2HDMS

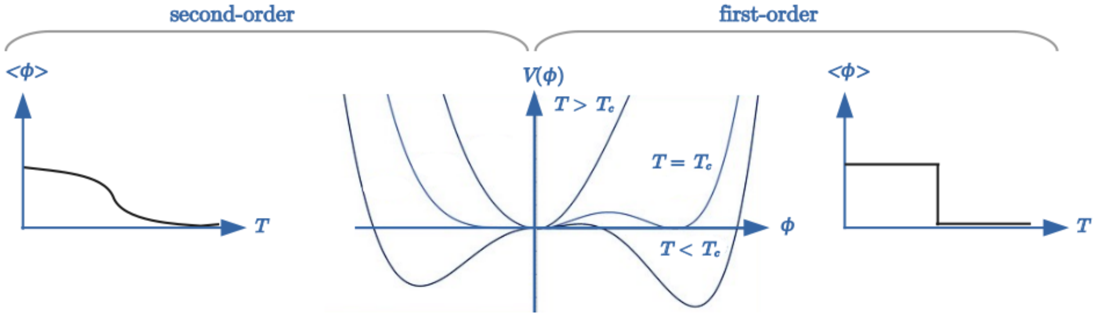

Figure 9: Schematic difference between a second-order and first-order electroweak phase transition. Left-hand side: Second-order transition. Shown is the continuous change of the vacuum expectation value $\langle\phi\rangle$ against temperature T and the scalar potential V against the scalar field value ϕ for different temperatures T. Right-hand side: First order transition. Shown are the same quantities as for the second-order case.

both, the first-order and the second-order scenario, can be realised, depending on the chosen parameters of the model. More information on FOPTs will be introduced in section 5.

3.3 Detection strategies

Since this work primarily studies phenomenology, a few detection strategies relevant for this work will be explained briefly in this section. A good overview of DM searches can be found in Ref. [87].

Dark matter relic density:

The DM relic density is a measure for the amount of DM particles found in the Universe today. To avoid the uncertainty of the Hubble rate it is usually given as Ωh^2, where h is the normalised Hubble expansion rate today ($H_0 = h \cdot \frac{100\,\mathrm{km}}{\mathrm{s\,Mpc}}$) [88]:

$$\Omega h^2 = \frac{m_{\mathrm{DM}}/\mathrm{GeV}}{10.57} \cdot Y_0 \cdot 2.889 \cdot 10^9 \,, \tag{3.32}$$

where m_{DM} is the DM mass, 10.57 is the critical density in [GeV/m^3] for $H = 100\frac{\mathrm{km}}{\mathrm{s\,Mpc}}$ and $2.889 \cdot 10^9$ is the entropy density today in [m^{-3}]. ($H = \frac{1}{M_{\mathrm{planck}}}\sqrt{\frac{8\pi}{3}\rho}$ is the Hubble expansion rate, which depends on the current matter density ρ.)

The DM abundance today Y_0 (number of particles divided by entropy density s) can be calculated by solving the equation:

$$\frac{\mathrm{d}Y}{\mathrm{d}s} = \frac{1}{3H}\langle\sigma v\rangle(Y^2 - Y_{eq}(T)^2) \,, \tag{3.33}$$

where the subscript eq denotes taking the abundance Y in thermal equilibrium, T is the temperature and $\langle\sigma v\rangle$ is the thermally averaged cross section of DM annihilating into SM particles.

Equation 3.33 can be solved numerically using the Runge-Kutta methods. With the assumptions as in Ref. [88] the freeze-out approximation for Y_0 can be written as:

$$\frac{1}{Y_0} = \frac{1}{2.5 \cdot Y_{eq}(s_f)} + \int_{s_0}^{s_f} \mathrm{d}s \frac{M_{\mathrm{planck}}\langle\sigma v\rangle}{\sqrt{24\pi\rho}} \,, \tag{3.34}$$

where the subscript f denotes the freeze-out value and the subscript 0 the present day value. This solution has an accuracy of $\approx 2\,\%$.

The term depending on the parameters of the considered model is the thermally averaged cross section $\langle\sigma v\rangle$. As can be seen from Equation 3.32 and Equation 3.33 the relic density depends on $\frac{1}{\langle\sigma v\rangle}$. $\langle\sigma v\rangle$ in turn depends on σ which is the total cross section for annihilation of a pair of DM particles. (See Equation (2.2) of Ref. [89]

for the full expression.)

Experimentally, the DM relic density can be measured from observations of CMB anisotropies. It was first measured by the WMAP collaboration [60] and later by the Planck collaboration [61]. The DM relic density measured by the more advanced Planck experiment is:

$$\Omega h^2 = 0.120 \pm 0.001\,.$$

Any model that predicts a higher amount of DM is excluded within the standard cosmological history according to this measurement. A model that predicts a lower amount of DM would be allowed. In that case the lack of predicted DM must be explained by another source of DM.

Dark matter direct detection:

When a DM particle comes close to a nucleon, it can scatter off elastically via effective couplings to quarks and gluons. In the 2HDMS, which is the model focused on in this work, this scattering is mediated by a scalar Higgs particle.

As in ref. [90, Equation (75)] the total cross section for scattering on protons and neutrons can be written as:

$$\sigma_N = \frac{4\mu_N^2}{\pi}(|A_N^{SI}|^2 + 3|A_N^{SD}|^2)\,, \tag{3.35}$$

where SI and SD stand for spin-independent and spin dependent amplitudes A and $\mu_N = \frac{m_{\mathrm{DM}} m_N}{m_{\mathrm{DM}} + m_N}$ is the reduced mass for protons ($N = p$) and neutrons ($N = n$) and m_{DM} is the DM mass. In this work, the considered DM candidate has spin 0, hence the spin dependent amplitude is zero and only the spin-independent amplitude A^{SI} needs to be considered:

$$|A_N^{SI}|^2 = 64(\lambda_N m_{\mathrm{DM}} m_N)^2\,, \tag{3.36}$$

where the coefficient λ_N depends on the trilinear couplings of two DM particles to one scalar Higgs particle and on the trilinear coupling of that scalar Higgs particle to two quarks.

One can also consider the rescaled indirect detection cross section. In this case the cross section is multiplied with the ratio of the predicted DM relic density over the measured DM relic density. This way, underabundance of DM can be accounted for. For this work the rescaled cross section will be considered.

Experimentally, the spin-independent DM direct detection cross section can be measured for example with liquid xenon time projection chambers, like the LUX-ZEPLIN (LZ), XENON and PANDAX experiments. These are chambers filled with large amounts of liquid xenon where the recoil of xenon nuclei from collisions with DM particles can be measured. Currently the strongest constraints come from the LZ experiment [91], hence these results will be used in this work.

Dark matter indirect detection:

The indirect detection of DM relies on detecting remnant photons from the annihilation of two DM particles. Hence, it depends on the thermally averaged cross section $\langle\sigma v\rangle$. If interactions are stronger and more DM annihilates, stronger direct detection signals can be observed. This means that the relic density goes down as, after annihilation, less DM is left in the Universe. As for the direct detection cross section, one can consider the rescaled cross section. In the case of indirect detection, the cross section is multiplied with the square of the ratio of the predicted DM relic density the over measured DM relic density. For this work the rescaled cross section will be considered.

The particles produced from the DM annihilation then decay further into SM particles and photons which can be detected by experiments.

Experimentally, the DM indirect detection cross section can be measured for example by satellite-based instruments like Fermi-LAT which detects low-energy gamma-rays ($\sim 20\,\text{Mev} - 300\,\text{GeV}$). For TeV-range gamma-ray detection, atmospheric Cherenkov telescopes can be used, like the MAGIC, HESS and VERITAS telescope. They can specifically look in the direction of objects where a large amount of DM is expected. In the keV-range, X-ray satellites can be used, like XMM- Newton and Chandra. For DM annihilations into neutrinos, large neutrino detectors like Ice Cube, ANTARES or Super- Kamiokande can be used. However, these experiments are not of relevance for the DM candidate considered in this work. The relevant range for this work is covered by the Fermi-LAT experiment [92, 93].

Dark matter production and detection at colliders:

As DM interacts very weakly with baryonic matter and since detector materials are made from baryonic matter, DM will only show up as missing transverse energy (MET). Only the by-products of the relevant process can be detected. Which channels are of interest depends on the chosen model.

In this work mainly lepton colliders (electron-positron colliders like the proposed ILC, CLIC, CEPC and FCC-ee and the proposed muon collider), will be considered. The production of DM via the collision of a lepton and antilepton depends again on the chosen model.

The relevant production channels, as well as interesting detection channels, for the 2HDMS will be discussed in the next section after introducing the model.

The detection strategies for DM are wrapped up in Figure 10. Since, so far,

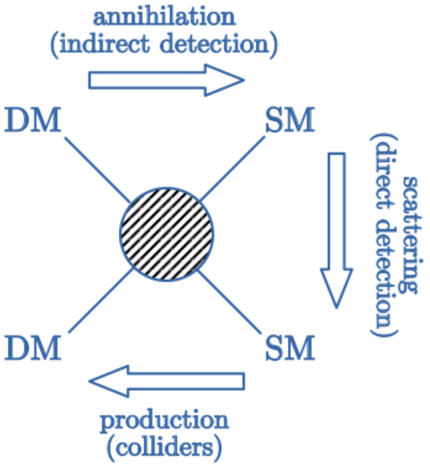

Figure 10: The detection strategies for dark matter. Annihilation of dark matter (DM) into Standard Model particles (SM) can be detected via indirect detection experiments, scattering of dark matter on Standard Model particles can be detected via direct detection experiments and the production of dark matter from Standard Model particles can be achieved in colliders.

no significant signal for the detection of DM has been observed, the experiments mentioned above only provide bounds on the model parameter space.

Gravitational waves:

As mentioned earlier, the second main topic of this work is the velocity of expanding bubble walls from FOPTs. Observable imprints of FOPTs are for example GWs. These can be produced via the collision of bubbles and via hydrodynamic turbulence. Good reviews can be found in Refs. [94–97].

The dynamics of bubble walls generate tensor perturbations which can be measured as GWs. However, most of the released energy is transferred to the surrounding plasma affecting its hydrodynamics. Hence hydrodynamical processes are the dominant sources of GWs from FOPTs. The frequencies of the GWs are set by the size of the bubble and the transition temperature.

Experimentally, GWs from FOPTs can be detected with interferometers such as the planned Laser Interferometer Space Antenna (LISA) [98], which could measure GWs directly by using laser interferometry. LISA would be the first space-based interferometer of this kind. But also already existing experiments such as pulsar timing array (PTA) experiments, like NANOGrav [99], the Parkes Pulsar Timing Array [100], the International Pulsar Timing Array [101] or the European Pulsar Timing Array [102], give insights on a stochastic GW background. The so far detected signals can be explained by cosmological FOPTs [95, 103, 104]. PTA experiments work by analysing signals from pulsars and searching for correlated signatures between them. This way they can detect a low-frequency GW background. A pulsar is a magnetised rotating neutron star. Because of its magnetisation electromagnetic radiation is emitted on its magnetic poles. Due to the rotation of the pulsar, this radiation can be observed periodically, where the intervals between the observed pulses are extremely precise. Information on GWs can be drawn from deviations from the exactly periodic signals.

Since the SM does not feature a FOPT, the detection would be a clear indicator for new physics. However, signals of GWs which have been detected so far can also be explained by SM processes or other BSM processes. Hence a cosmological FOPT is not confirmed yet but remains a popular phenomenon to study in the context of BSM physics.

4 Phenomenology of the 2HDMS

Contents

This section is based on the following publications:

- [1] J. Dutta, J. Lahiri, C. Li, G. Moortgat-Pick, S. Farah Tabira, and J. A. Ziegler, "Dark matter phenomenology in 2hdms in light of the 95 gev excess", *The European Physical Journal C*, vol. 84, no. 926, 2024, ISSN: 1434-6052. arXiv: 2308.05653 `[hep-ph]`
- [2] J. Dutta, J. Lahiri, C. Li, G. Moortgat-Pick, S. F. Tabira, and J. A. Ziegler, *Search for dark matter in 2hdms at lhc and future lepton colliders*, 2025. arXiv: 2504.14529 `[hep-ph]`,
  to appear in the European Physical Journal C

In this section a specific extension of the SM is investigated, namely the 2HDMS. First the model and current constraints are explained in the following subsections 4.1 and 4.2. In subsection 4.3 'Dark matter phenomenology' parameter scans are presented to investigate the influence of different model parameters on DM observables, namely DM relic density, direct and indirect detection cross section. In subsection 4.4 'Collider phenomenology' benchmarks which are interesting from the point of view of future colliders searches are presented along with their production cross section values for different detection channels. Moreover, some of the benchmark points presented can explain an excess around 95 GeV observed both at the former LEP [8] in the $b\bar{b}$ mode as well as in the $\gamma\gamma$ mode at the LHC experiments CMS [9] and ATLAS [10]. Such an excess can be explained in several BSM models with extended scalar sectors [11–41]. In the context of 2HDM extensions, it was shown in [20] and [42] that such an excess can be accommodated within the 2HDMS scenario.

Declaration on the content:

The content of this section is based on the publications [1] and [2]. The content is taken from those publications and adapted in parts. The theoretical background and the part on DM phenomenology was written by myself to a large extent for both publications. However, the collaborators named above also took part in the writing of this content. The basis change equations and bounded-from-below constraints were derived by myself and written into a Python code. The implementation of the 2HDMS model in the public code `SARAH` was done in parallel by myself and Juhi Dutta, in order to compare with each other. However, the implementation by Juhi Dutta was used in the end. The scan code which automatically scans over selected parameter regions, performs the basis change, runs `SPheno` and `micrOMEGAs` and checks for all constraints mentioned in the the constraints section was written by myself. I used this code to generate the data in Figure 17 - 23, which were also created by myself along with other figures in this section, like Feynman diagrams or Figure 21. The scans to find viable benchmark points were performed by both myself and Cheng Li. Figure 24 - 30 were generated by Juhi Dutta, Jahita Lahiri and Sheikh Farah Tabira. The collider phenomenology was also written to a large extent by them.

Furthermore, Figure 18 - 20 are reruns of the original scans presented in Ref. [1]. The reason for this is that in Ref. [2] a slightly different input basis was used than in Ref. [1]. For this thesis I decided to use only the basis as in Ref. [2] and rerun the old scans from Ref. [1] in this new basis, in order to avoid confusion.

4.1 The model

The 2HDMS extends the 2HDM by an additional scalar singlet. Compared to the SM, which contains one scalar $SU(2)$ doublet, this model contains two scalar doublets and a scalar singlet.[1] This type of model was investigated for example in [20, 106, 107]. The scalar potential can be written as the sum of the 2HDM potential V_{2HDM} and the singlet potential V_S. Considering a $U(1)$, Z_2 and Z_2' symmetry, the most general expression can be written as:

$$V_{\text{2HDMS}} = V_{\text{2HDM}} + V_S\,, \tag{4.1a}$$

$$\begin{aligned} V_{\text{2HDM}} = {}& m_{11}^2 \Phi_1^\dagger\Phi_1 + m_{22}^2\Phi_2^\dagger\Phi_2 - [m_{12}^2\Phi_1^\dagger\Phi_2 + h.c.] + \frac{\lambda_1}{2}(\Phi_1^\dagger\Phi_1)^2 \\ & + \frac{\lambda_2}{2}(\Phi_2^\dagger\Phi_2)^2 + \lambda_3(\Phi_1^\dagger\Phi_1)(\Phi_2^\dagger\Phi_2) + \lambda_4(\Phi_1^\dagger\Phi_2)(\Phi_2^\dagger\Phi_1) \\ & + \left[\frac{\lambda_5}{2}(\Phi_1^\dagger\Phi_2)^2 + h.c.\right], \end{aligned} \tag{4.1b}$$

$$\begin{aligned} V_S = {}& m_S^2 S^\dagger S + \left[\frac{m_S'^2}{2} S^2 + h.c.\right] \\ & + \left[\frac{\lambda_1''}{24}S^4 + h.c.\right] + \left[\frac{\lambda_2''}{6}(S^2 S^\dagger S) + h.c.\right] + \frac{\lambda_3''}{4}(S^\dagger S)^2 \\ & + S^\dagger S[\lambda_1'\Phi_1^\dagger\Phi_1 + \lambda_2'\Phi_2^\dagger\Phi_2] + [S^2(\lambda_4'\Phi_1^\dagger\Phi_1 + \lambda_5'\Phi_2^\dagger\Phi_2) + h.c.], \end{aligned} \tag{4.1c}$$

where Φ_1 and Φ_2 are the two $SU(2)$ doublets and S is the $SU(2)$ singlet field. The parameters m_{11}^2, m_{22}^2, m_{12}^2, m_S^2 and $m_{S'}^2$ have dimension mass squared and the parameters λ_1, λ_2, λ_3, λ_4, λ_5, λ_1', λ_2', λ_4', λ_5', λ_1'', λ_2'' and λ_3'' are dimensionless. All parameters are taken as real.

For this work a type II 2HDMS is considered. A type II structure of the model

---

[1] The $SU(2)$ group is the group of special unitary matrices of degree 2 which can be represented by complex rotations of the two dimensional complex space $\mathbf{C}^2$. An $SU(2)$ doublet (singlet) field is an object with two components (one component) such that its dynamics does not change under $SU(2)$ transformations. The form of the potential V_{2HDMS} in Equation 4.1a guarantees this symmetry [105, Equation 268].

means that right-handed down-type quarks and charged leptons couple only to Φ_1 and right-handed up-type quarks couple only to Φ_2.

The imaginary part of the scalar singlet will provide the DM candidate in this work.

4.1.1 Symmetries and their physical effects

The potential in Equation 4.1a is CP-conserving, does not allow flavour-changing neutral currents (FCNCs) and provides a stable DM candidate. In the following each symmetry that leads to these properties is explained.

$\boldsymbol{CP}$ conservation and symmetry under $\boldsymbol{U}(1)$:

As mentioned above the potential V_{2HDMS} conserves charge C and parity P. This means that the potential is invariant (symmetric) under transformations with the C and P operator:

$$V_{\text{2HDMS}}(\Phi_j) = V_{\text{2HDMS}}(CP[\Phi_j]), \tag{4.2}$$

with $j = 1,2,3$ and $\Phi_3 = S$. The parity operator P flips the sign of the spatial coordinates and the charge conjugation operator C changes particles into antiparticles and flips all charges:

$$\begin{aligned}
\Phi_j(t,x) &\xrightarrow{P} \eta_P \Phi_j(t,-x)\,, \\
\Phi_j(t,x) &\xrightarrow{C} \eta_C \Phi_j^\dagger(t,x)\,, \\
\Phi_j(t,x) &\xrightarrow{CP} \eta_C \eta_P \Phi_j^\dagger(t,-x)\,.
\end{aligned} \tag{4.3}$$

For CP-conserving fields $\eta_P \eta_C = 1$ and $\Phi_j^\dagger = \Phi_j$. As can been seen, requiring the potential to be symmetric under this transformation results in fields always appearing in combination with hermitian conjugates and parameters being real. To see this more clearly, below the transformation is performed for one example: The term in the potential containing the parameter λ_5, transforms under CP as:

$$\frac{\lambda_5}{2}(\Phi_1^\dagger\Phi_2)^2 + \frac{\lambda_5^*}{2}(\Phi_2^\dagger\Phi_1)^2 \xrightarrow{CP} \frac{\lambda_5}{2}(\Phi_2^\dagger\Phi_1)^2 + \frac{\lambda_5^*}{2}(\Phi_1^\dagger\Phi_2)^2. \tag{4.4}$$

As can be seen, because $\lambda_5 = \lambda_5^*$ and because fields appear as pairs with a hermitian conjugate, this term is invariant under CP transformations.

The explanation could be finished here, however it is customary to say the potential is $U(1)$ symmetric instead of referring to the CP operator. To see that $U(1)$ symmetry in combination with real-valued parameters results in CP conservation, it is useful to understand the $U(1)$ symmetry group: The $U(1)$ group is the group of unitary matrices of degree 1. Since a matrix of degree 1 (a 1×1 matrix) is simply a number and unitarity of an object A means that $A^{\dagger}A = 1$, this group consists of complex numbers with norm 1 and multiplication as group operation. The group can be written as: $(\{e^{i\theta}\}, \cdot)$, $\theta \in [0, 2\pi)$. Hence $U(1)$ transformations add a phase to the fields as:

$$\begin{aligned} \Phi_j &\overset{U(1)}{\to} e^{i\theta}\Phi_j \\ \Phi_j^{\dagger} &\overset{U(1)}{\to} e^{-i\theta}\Phi_j^{\dagger}. \end{aligned} \tag{4.5}$$

As can be seen, symmetry under $(U1)$ is achieved by requiring that fields always appear in combination with a hermitian conjugate which cancels the contribution of a complex phase: $\Phi_j^{\dagger}\Phi_k \overset{U(1)}{\to} e^{-i\theta}\Phi_j^{\dagger}e^{i\theta}\Phi_k = \underbrace{e^{-i\theta}e^{i\theta}}_{=1}\Phi_j^{\dagger}\Phi_k$, $j, k = 1, 2$. In practice it is enough to demand the 2HDM-part of the potential to be symmetric under $U(1)$ transformations and the singlet to appear in even orders along with all parameters being real in order to achieve CP conservation (and hence scalar and pseudo scalar sectors do not mix).

Phenomenologically CP violation is known to be very small [105, Chapter 1] which is the reason why it is not included here. However it can be interesting to include CP violation in order to achieve baryogenesis, but this is not considered in this work.

Avoiding Flavour-changing neutral currents and symmetry under Z_2:

FCNCs should be avoided, since they have not been observed so far. This can be achieved if all fermions with the same quantum numbers couple to the same Higgs multiplet [105, Chapter 2]. In the Type II model this is ensured by assuming symmetry under Z_2 transformations. The Z_2 group is the cyclic group of degree 2. (It is isomorphic to the symmetry group S_2 and contains 2 elements.) One realisation of the group is with the elements 1 and -1 and multiplication as group operation. The group can be written as: $(\{1, -1\}, \cdot)$. Using this realisation, Z_2 transformations can either change the sign of an object (object is odd under Z_2) or preserve the sign of an object (object is even under Z_2). In this case the Z_2 symmetry is chosen to transform the fields as:

$$\begin{aligned} \Phi_1 &\overset{Z_2}{\to} -\Phi_1\,, \\ \Phi_2 &\overset{Z_2}{\to} \Phi_2\,, \\ S &\overset{Z_2}{\to} S. \end{aligned} \tag{4.6}$$

And right-handed fermion singlets are transformed as:

$$\begin{aligned} e_{jR} &\overset{Z_2}{\to} -e_{jR}\,, \\ d_{jR} &\overset{Z_2}{\to} -d_{jR}\,, \\ u_{jR} &\overset{Z_2}{\to} u_{jR}, \end{aligned} \tag{4.7}$$

where $j = 1,2,3$ denotes the three lepton and quark generations and the R denotes right-handedness. By demanding symmetry under these transformations down-type quarks and leptons, couple only to Φ_1 (all are odd under Z_2) and up-type quarks couple only to Φ_2 (both are even under Z_2). The Yukawa potential describing the interaction of the fermions with the Higgs fields, then looks as [108, Equation (2.7)]:

$$\begin{aligned} V_{\text{Yukawa}} &= -(y^1_{ij}\bar{Q}_{iL}\Phi_1 d_{jR} + y^2_{ij}\bar{Q}_{iL}\bar{\Phi}_2 u_{jR} + y^5_{ij}\bar{L}_{iL}\Phi_1 e_{jR}) \\ &\overset{Z_2}{\to} -(y^1_{ij}\bar{Q}_{iL}\underbrace{(-\Phi_1)(-d_{jR})}_{=\Phi_1 d_{jR}} + y^2_{ij}\bar{Q}_{iL}\bar{\Phi}_2 u_{jR} + y^5_{ij}\bar{L}_{iL}\underbrace{(-\Phi_1)(-e_{jR})}_{=\Phi_1 e_{jR}}). \end{aligned} \tag{4.8}$$

As can be seen this potential is symmetric under the above Z_2 transformation of the scalar doublet fields and the fermion fields.

However, the Z_2 symmetry of the 2HDMS potential is softly broken by the parameter m^2_{12}. This is introduced because the symmetry is broken spontaneously by the vevs v_1 and v_2 (which will be introduced later) and the spontaneous breaking of an exact symmetry can result in the creation of domain walls. Domain walls are transitions between regions of space that live in different vacua, created through spontaneous symmetry breaking. Stable domain walls are cosmologically unfavourable. One solution is to introduce a term, here the m^2_{12}-term, which breaks the symmetry explicitly, where it is sufficient to break the symmetry softly [109] [110]. This parameter is called soft breaking parameter, since its term includes only quadratic powers of the fields and therefore does not spoil the behaviour of the potential at high energies (at high values of the fields the terms containing four powers of fields dominate the behaviour of the potential).

Stabilisation of DM and symmetry under Z'_2:

The Z'_2 symmetry transforms the fields as:

$$\begin{aligned} \Phi_1 &\overset{Z'_2}{\to} \Phi_1\,, \\ \Phi_2 &\overset{Z'_2}{\to} \Phi_2\,, \\ S &\overset{Z'_2}{\to} -S. \end{aligned} \tag{4.9}$$

This symmetry ensures that the field S only appears in even orders in the potential. This is needed as the pseudo-scalar (imaginary) component of the complex singlet S plays the role of the DM candidate in this work. The Z_2' symmetry then stabilises the DM by avoiding odd powers of S which would lead to decaying of S [111].

This symmetry is not broken explicitly, contrary to the Z_2 symmetry. Since there is more work needed on the domain wall sector of the singlet extension of the 2HDM a soft breaking parameter is not included here. The formation of domain walls, however, can still be avoided by assuming that they were created before inflation. Domain walls could then be inflated away such that they are absent in our observable Universe today [112].

The symmetries of the potential and their physical effects are summarised in Table 2.

Symmetry	Transformation of fields	Broken spontaneously	Broken softly	Physical effect
V_{2HDM} symmetric under $U(1)$, (+ all parameters real)	$\Phi_j \overset{U(1)}{\to} e^{i\theta}\Phi_j$, $\Phi_j^\dagger \overset{U(1)}{\to} e^{-i\theta}\Phi_j^\dagger$	No	No	Conservation of CP
V_{2HDM} symmetric under Z_2 (+ type II model)	$\Phi_1 \overset{Z_2}{\to} -\Phi_1$, $\Phi_2 \overset{Z_2}{\to} \Phi_2$	Yes via v_1, v_2	Yes via m_{12}^2	Avoiding of FCNC
V symmetric under Z_2'	$S \overset{Z_2'}{\to} -S$, $\Phi_j \overset{Z_2'}{\to} \Phi_j$	Yes via v_S	No	Stabilisation of DM

Table 2: Symmetries of the scalar potential and their physical effects.

4.1.2 Spontaneous symmetry breaking and eigenfields

Both symmetries, Z_2 and Z_2', are broken spontaneously, where a neutral minimum is considered. This means the fields acquire vevs, which are real-valued and only appear in the neutral component of the fields. This breaks the EW symmetry. One could have also include a charge breaking minimum by assigning a a non-zero vev to the charged components (upper components) of the fields, or a CP-breaking minimum by assigning a complex vev to the lower components of the fields [105]. However, as CP-breaking is small in nature and charge breaking has not been observed until now a neutral minimum is considered here.

Without loss of generality the vevs can be chosen to be positive and the fields, after EWSB, can be developed around the vevs as:

$$\begin{aligned} \Phi_i &= \begin{pmatrix} \phi_i^+ \\ \frac{1}{\sqrt{2}}(v_i+\rho_i+i\eta_i) \end{pmatrix}, & \langle\Phi_i\rangle &= \begin{pmatrix} 0 \\ \frac{v_i}{\sqrt{2}} \end{pmatrix}, \quad i=1,2, \\ S &= \frac{1}{\sqrt{2}}(v_S+\rho_S+iA_S), & \langle S\rangle &= \frac{v_S}{\sqrt{2}}, \end{aligned} \tag{4.10}$$

where ϕ_i^+ (and ϕ_i^- in case of the transposed fields) are the complex charged components, ρ_i are the real parts of the neutral components and η_i are the imaginary parts of the neutral components of the doublets Φ_i, $i = 1,2$. The singlet S has only a neutral component which is parameterised by the real part ρ_S and the imaginary part A_S. (By charged and neutral, electrically charged and neutral is meant in this case.) As mentioned earlier, the imaginary component A_S of the singlet S serves as DM candidate in this work.

The charged components of the doublets give rise to charged scalar particles $H^\pm$, the real parts of the neutral components of the doublets and the singlets give rise to neutral scalar particles h_1, h_2 and h_3 and the imaginary parts of the neutral components of the doublets and the singlets give rise to neutral pseudo-scalar particles A and A_S. (There are also a charged Goldstone bosons $G^\pm$ and a neutral pseudo-scalar Goldstone G^0, which are absorbed by the $W^\pm$ and Z-boson after EWSB.) Furthermore, one of the neutral scalar particles has to be the SM-like Higgs boson with a mass of about 125 GeV. For this work h_2 will always play this role. These are the eigenfields in the mass basis, which correspond to physical particles. They can be obtained via rotations of the fields in the interaction basis and their eigenvalues are the squares of their masses. They are summarised in Table 3.

	Mass basis		Interaction basis	Rotation
	Eigenfields	Eigenvalues	Eigenfields	
Charged	$H^\pm$, $G^\pm$	$m^2_{H^\pm}$, $m^2_{G^\pm} = 0$	$\phi_1^\pm$, $\phi_2^\pm$	$\begin{pmatrix} H^\pm \\ G^\pm \end{pmatrix} = R^\pm \begin{pmatrix} \phi_1^\pm \\ \phi_2^\pm \end{pmatrix}$
Scalar	h_1, h_2, h_3	$m^2_{h_1}$, $m^2_{h_2}$, $m^2_{h_3}$	ρ_1, ρ_2, ρ_S	$\begin{pmatrix} h_1 \\ h_2 \\ h_3 \end{pmatrix} = R \begin{pmatrix} \rho_1 \\ \rho_2 \\ \rho_S \end{pmatrix}$
Pseudo-scalar	A, G^0	m^2_A, $m^2_{G^0} = 0$	η_1, η_2	$\begin{pmatrix} A \\ G^0 \end{pmatrix} = R^A \begin{pmatrix} \eta_1 \\ \eta_2 \end{pmatrix}$
DM	A_S	$m^2_{A_S}$	A_S	$\begin{pmatrix} A_S \end{pmatrix} = \begin{pmatrix} A_S \end{pmatrix}$

Table 3: The eigenfields in the mass basis and interaction basis and the rotations to convert between them for each block (charged, scalar and pseudo-scalar). Since the vevs are real, the scalar mass basis eigenfields h_1, h_2 and h_3 are mixtures of the interaction basis fields ρ_1, ρ_2, ρ_S. However, there is no imaginary vev, hence the DM component does not mix with the other pseudo-scalar components.

Free parameters:

The 19 free parameters from Equation 4.1a are:

$$\lambda_1, \lambda_2, \lambda_3, \lambda_4, \lambda_5, m_{12}^2, m_{11}^2, m_{22}^2, \tan\beta, v_S, m_S^2, m_S'^2, \lambda_1', \lambda_2', \lambda_4', \lambda_5', \lambda_1'', \lambda_2'', \lambda_3'', \tag{4.11}$$

where $\tan\beta = \frac{v_2}{v_1}$, $v = \sqrt{v_1^2 + v_2^2} \approx 246\,\text{GeV}$ is fixed by measurements of the SM.

Minimisation conditions:

The 2HDMS potential in Equation 4.1a has three minima at the three vevs v_1, v_2 and v_S.

At a minimum the derivative of the potential is equal to zero. This results in three equations, the minimisation conditions, which can be used to eliminate three of the free parameters from the model:

$$0 = \frac{\partial V}{\partial \Phi_1}\Big|_{\substack{\Phi_1=\langle\Phi_1\rangle \\ \Phi_2=\langle\Phi_2\rangle \\ S=\langle S\rangle}} = \frac{1}{\sqrt{2}}[m_{11}^2 v_1 - m_{12}^2 v_2 + \frac{\lambda_1}{2} v_1^3 + \frac{\lambda_{345}}{2} v_1 v_2^2 + (\frac{\lambda_1'}{2} v_1 + \lambda_4' v_1) v_S^2], \tag{4.12a}$$

$$0 = \frac{\partial V}{\partial \Phi_2}\Big|_{\substack{\Phi_1=\langle\Phi_1\rangle \\ \Phi_2=\langle\Phi_2\rangle \\ S=\langle S\rangle}} = \frac{1}{\sqrt{2}}[m_{22}^2 v_2 - m_{12}^2 v_1 + \frac{\lambda_2}{2} v_2^3 + \frac{\lambda_{345}}{2} v_1^2 v_2 + (\frac{\lambda_2'}{2} v_2 + \lambda_5' v_2) v_S^2], \tag{4.12b}$$

$$\begin{aligned} 0 = \frac{\partial V}{\partial S}\Big|_{\substack{\Phi_1=\langle\Phi_1\rangle \\ \Phi_2=\langle\Phi_2\rangle \\ S=\langle S\rangle}} = \frac{1}{\sqrt{2}}[&m_S^2 v_S + m_S'^2 v_S + \frac{\lambda_1''}{12} v_S^3 + \frac{\lambda_2''}{3} v_S^3 + \frac{\lambda_3''}{4} v_S^3 \\ &+ \frac{v_S}{2}(\lambda_1' v_1^2 + \lambda_2' v_2^2) + v_S(\lambda_4' v_1^2 + \lambda_5' v_2^2)]. \end{aligned} \tag{4.12c}$$

The parameters m_{11}^2, m_{22}^2 and m_S^2 are chosen to be replaced. Furthermore, the choice $\lambda_2'' = \lambda_1''$ is made. In the tree-level calculation presented here, this simplification leaves the couplings of the DM candidate to other particles unchanged as can be seen in the next section in Equation 4.19, since the parameter λ_2'' does not appear in the couplings of the DM candidate to the scalars, but only in the DM self-couplings, see Equation 4.1a.

This results in 15 free parameters:

$$\lambda_1, \lambda_2, \lambda_3, \lambda_4, \lambda_5, m_{12}^2, \tan\beta, v_S, m_S'^2, \lambda_1', \lambda_2', \lambda_4', \lambda_5', \lambda_1'' = \lambda_2'', \lambda_3''. \tag{4.13}$$

These are the parameters of the *interaction basis*. One can change to the mass basis[2], as in Table 3. The 15 free parameters in the *mass basis* are:

$$\begin{gathered} m_{h_1}, m_{h_2}, m_{h_3}, m_A, m_{H^\pm}, m_{A_S}, \tan\beta, v_S, \tilde{\mu}^2, \alpha_1, \alpha_2, \alpha_3 \\ \lambda_{14}' = \lambda_1' - 2\lambda_4', \lambda_{25}' = \lambda_2' - 2\lambda_5', \lambda_{13}'' = \lambda_1'' - \lambda_3'', \end{gathered} \tag{4.14}$$

where m_{h_1}, m_{h_2}, m_{h_3}, m_A, m_{A_S} and $m_{H^\pm}$ are the masses of the three scalars, the

---

[2] To be precise the basis used here is a mixed mass basis, since some of the parameters from the interaction basis appear. The combinations $\lambda_{14}' = \lambda_1' - 2\lambda_4'$, $\lambda_{25}' = \lambda_2' - 2\lambda_5'$ and $\lambda_{13}'' = \lambda_1'' - \lambda_3''$ were chosen because they appear in the couplings of the DM candidate to the scalar particles h_1, h_2 and h_3, Equation 4.19. This gives some freedom to control these couplings in the analysis.

pseudo-scalar, the pseudo-scalar DM and the charged Higgs particle, respectively, as in Table 3, $\tilde{\mu}^2 = \frac{m_{12}^2}{\sin(\beta)\cos(\beta)}$ and α_1, α_2 and α_3 are the mixing angles of the scalar rotation matrix in Equation 4.16. Note that one of the scalars h_1, h_2, h_3 has to comply with the SM-like Higgs boson with a mass of about 125 GeV. In this work h_2 is chosen to be this particle.

The equations for how to change between the interaction basis and the mass basis can be found below.

Basis change equations:

One can choose to either work in the *interaction basis*, using the parameters as in Equation 4.13, or in the *mass basis*, using the parameters as in Equation 4.14 as input parameters. Since the mass basis is more physical this basis will be used for the input parameters. The corresponding parameters in the interaction basis can be obtained via the following basis change equations:

$$\begin{aligned}
m_{12}^2 &= \tilde{\mu}^2 \cdot \sin\beta\cos\beta, \\
\lambda_1 &= \frac{1}{v^2\cos^2\beta}(\Sigma_{i=1}^3 m_i^2 R_{i1}^2 - \tilde{\mu}^2\sin^2\beta), \\
\lambda_2 &= \frac{1}{v^2\sin^2\beta}(\Sigma_{i=1}^3 m_i^2 R_{i2}^2 - \tilde{\mu}^2\cos^2\beta), \\
\lambda_3 &= \frac{1}{v^2}(\frac{1}{\sin\beta\cos\beta}\Sigma_{i=1}^3 m_i^2 R_{i1}R_{i2} - \tilde{\mu}^2 + 2m_{H^\pm}^2), \\
\lambda_4 &= \frac{1}{v^2}(m_A^2 + \tilde{\mu}^2 - 2m_{H^\pm}^2), \\
\lambda_5 &= \frac{1}{v^2}(-m_A^2 + \tilde{\mu}^2), \\
\lambda_1' &= \frac{1}{2}(\frac{1}{v v_S \cos\beta}\Sigma_{i=1}^3 m_i^2 R_{i1}R_{i3} + \lambda_{14}'), \\
\lambda_2' &= \frac{1}{2}(\frac{1}{v v_S \sin\beta}\Sigma_{i=1}^3 m_i^2 R_{i2}R_{i3} + \lambda_{25}'), \\
\lambda_4' &= \frac{1}{4}(\frac{1}{v v_S \cos\beta}\Sigma_{i=1}^3 m_i^2 R_{i1}R_{i3} - \lambda_{14}'), \\
\lambda_5' &= \frac{1}{4}(\frac{1}{v v_S \sin\beta}\Sigma_{i=1}^3 m_i^2 R_{i2}R_{i3} - \lambda_{25}'), \\
\lambda_1'' &= \frac{3}{4v_S^2}(\Sigma_{i=1}^3 m_i^2 R_{i3}^2 + \frac{v_S^2}{2}\lambda_{13}''), \\
\lambda_3'' &= \frac{3}{4v_S^2}(\Sigma_{i=1}^3 m_i^2 R_{i3}^2 + \frac{5v_S^2}{6}\lambda_{13}''), \\
m_S'^2 &= -(\frac{1}{2}m_{A_S}^2 + \frac{1}{4}\Sigma_{i=1}^3 m_i^2(R_{i3}^2 + R_{i1}R_{i3}\frac{v\cos\beta}{v_S} + R_{i2}R_{i3}\frac{v\sin\beta}{v_S}) \\
&\quad - \frac{v^2}{4}(\lambda_{14}'\cos^2\beta + \lambda_{25}'\sin^2\beta) + \frac{v_S^2}{8}\lambda_{13}''),
\end{aligned} \tag{4.15}$$

where $\lambda_2'' = \lambda_1''$ was fixed, m_i, with $i = 1,2,3$, are the masses of the three scalars and R_{ij}, with $i,j = 1,2,3$ are the entries of the scalar rotation matrix in Table 3.

The scalar rotation matrix can be expressed via the mixing angles α_1, α_2 and α_3:

$$R = \begin{pmatrix} c_{\alpha_1}c_{\alpha_2} & s_{\alpha_1}c_{\alpha_2} & s_{\alpha_2} \\ -s_{\alpha_1}c_{\alpha_3} - c_{\alpha_1}s_{\alpha_2}s_{\alpha_3} & c_{\alpha_1}c_{\alpha_3} - s_{\alpha_1}s_{\alpha_2}s_{\alpha_3} & c_{\alpha_2}s_{\alpha_3} \\ s_{\alpha_1}s_{\alpha_3} - c_{\alpha_1}s_{\alpha_2}c_{\alpha_3} & -c_{\alpha_1}s_{\alpha_3} - s_{\alpha_1}s_{\alpha_2}c_{\alpha_3} & c_{\alpha_2}c_{\alpha_3} \end{pmatrix}, \tag{4.16}$$

where the short-hand notation $s_\alpha = \sin(\alpha)$, $c_\alpha = \cos(\alpha)$ is used.

Alignment limit:

The alignment limit corresponds to a specific setting of the scalar mixing angles α_1, α_2 and α_3 and the angle β such that the lowest-order couplings of the neutral scalar h_2 to fermions and gauge bosons are exactly the same as the couplings of the Higgs boson in the SM. This is the case for the setting [113]:

$$\cos(\beta - \alpha_1) = 0 = \alpha_2 = \alpha_3 \,. \tag{4.17}$$

4.1.3 Scalar-to-dark matter couplings and dark matter phenomenology

As written above, the DM candidate in this work will be the pseudo-scalar A_S, which arises from the imaginary component of the complex singlet S and it does not mix with the imaginary components from the doublets. Its mass can be obtained from Equation 4.1a and expressed as:

$$\begin{aligned} m_{A_S}^2 &= \frac{\partial^2 V}{\partial A_S^\dagger \partial A_S} \Big|_{\substack{\Phi_1 = \langle \Phi_1 \rangle \\ \Phi_2 = \langle \Phi_2 \rangle \\ S = \langle S \rangle}} \\ &= -(2m_S'^2 + v_S^2(\frac{\lambda_1''}{3} + \frac{\lambda_2''}{3}) + 2(\lambda_4' v_1^2 + \lambda_5' v_2^2)) \,. \end{aligned} \tag{4.18}$$

Furthermore, the couplings of the DM candidate to the scalar Higgs particles are of importance, since the DM does not couple to SM particles directly, but only via exchanges of scalar Higgs particles, the so called scalar portal. The trilinear and quatrilinear couplings are:

$$\frac{\lambda_{h_j A_S A_S}}{v} = -i[\lambda_{14}' c_\beta R_{j1} + \lambda_{25}' s_\beta R_{j2} - \frac{v_S}{2v}\lambda_{13}'' R_{j3}] \,, \tag{4.19a}$$

$$\lambda_{h_j h_k A_S A_S} = -i[\lambda_{14}' R_{j1} R_{k1} + \lambda_{25}' R_{j2} R_{k2} - \frac{1}{2}\lambda_{13}'' R_{j3} R_{k3}] \,, \tag{4.19b}$$

where h_j, h_k with $j,k = 1,2,3$ denote the three scalars and R_{jk} with $j,k = 1,2,3$ are the entries of the scalar rotation matrix in Table 3. $\lambda_{h_j A_S A_S}$ is normalised to

$v = \sqrt{v_1^2 + v_2^2}$ in order to obtain a dimensionless quantity and the short-hand notation $s_\beta = \sin\beta$, $c_\beta = \cos\beta$ is used.

These couplings play an important role for the phenomenology of DM observables such as DM relic density and direct and indirect detection of DM.

Relic density:

The calculation of the DM relic density was explained in section 3.3, where it was shown that the relic density depends on the total cross section for annihilation of a pair of DM particles. This cross section depends on couplings and propagators. As the DM could, for example, annihilate into two scalar Higgs particles or into other SM particles mediated by one scalar Higgs particle, both trilinear and quadrilinear vertices containing two DM particles and scalar Higgs particles need to be taken into account. The corresponding tree-level Feynman diagrams, relevant in this model, can be seen in Figure 11.

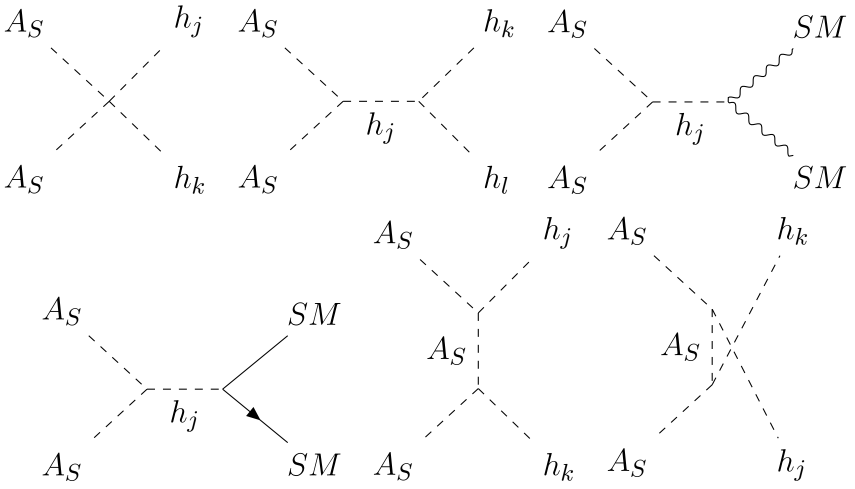

Figure 11: Tree-level Feynman diagrams relevant for calculation of relic density, created using `TikZ-Feynman` [114]

Direct detection cross section:

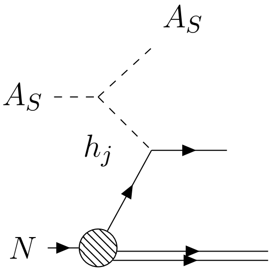

Figure 12: Tree-level Feynman diagram relevant for calculation of the direct detection cross section, created using `TikZ-Feynman` [114]

The calculation of the DM direct detection cross section was also explained in section 3.3, where it was shown that the cross section depends on the trilinear couplings of two DM particles to one scalar Higgs particle and on the trilinear coupling of that scalar Higgs particle to two quarks. The corresponding tree-level Feynman diagram, relevant in this model, can be seen in Figure 12.

Indirect detection cross section:

The calculation of the DM indirect detection cross section was also explained in section 3.3, where is was explained that similar diagrams as for the calculation of the DM relic density in Figure 11 play a role here.

Please note that the above discussion is focused on tree-level processes. Higher-order terms will also play a role, however at sub-leading order. The same applies to the discussion in the next section.

4.1.4 Scalar-to-fermion couplings and collider phenomenology

As mentioned earlier a type II 2HDMS is considered. In this model right-handed electrons and down-type quarks couple only to the doublet Φ_1 and right-handed up-type quarks only couple to the doublet Φ_2. This choice in combination with the Z_2 symmetry leads to the absence of FCNCs, as explained above. Other types of the 2HDMS which lead to natural flavour conservation can been seen in Table 4 below. It can be useful to define reduced couplings as the ratio between the coupling of the scalars h_i, $i=1,2,3$ in the 2HDMS and the corresponding coupling of the SM Higgs boson H_{SM} to fermions f [20]:

Type	e_{jR}	d_{jR}	u_{jR}
I	Φ_2	Φ_2	Φ_2
II	Φ_1	Φ_1	Φ_2
X (‘lepton specific’)	Φ_1	Φ_2	Φ_2
Y (‘flipped’)	Φ_2	Φ_1	Φ_2

Table 4: Couplings of the doublets Φ_1 and Φ_2 to right-handed fermions for models which lead to natural flavour conservation in the 2HDM and its extensions [105]. The subscript $j=1,2,3$ denotes the three lepton and quark generations and the R denotes right-handedness.

$$c_{h_iff} = \frac{g_{h_iff}}{g_{H_{\text{SM}}ff}}. \tag{4.20}$$

In the type II 2HDMS these are:

$$c_{h_i\tau\tau} = c_{h_ie_je_j} = \frac{R_{i1}}{\cos\beta}, \tag{4.21a}$$

$$c_{h_ibb} = c_{h_id_jd_j} = \frac{R_{i1}}{\cos\beta}, \tag{4.21b}$$

$$c_{h_itt} = c_{h_iu_ju_j} = \frac{R_{i2}}{\sin\beta}, \tag{4.21c}$$

where R is the scalar rotation matrix in Equation 4.16 and again $j = 1,2,3$ denotes the three lepton and quark generations with τ, b and t being the heaviest.

The couplings to gauge bosons are equivalently:

$$c_{h_iVV} = c_{h_iZZ} = c_{h_iWW} = \cos\beta R_{i1} + \sin\beta R_{i2}. \tag{4.22}$$

Along with the couplings of the DM candidate to scalar Higgs particles these play an important role for the collider phenomenology.

Dark matter production and detection at colliders:

Concerning the analysis of collider phenomenology, the main focus will be on future lepton colliders (electron-positron colliders and muon colliders), where one of the scalar Higgs particles can be produced directly via the collision of leptons. The produced scalar Higgs particle then acts as a mediator to DM particles. Since DM can not be detected directly, the following detection channels are considered, namely where two DM particles A_S are produced along with a photon γ (mono-photon channel), a Z-boson (mono-Z channel) or two b-quarks ($b\bar{b}$-channel or $t\bar{t}$-channel for sufficiently high energies). The two DM particles will show up as MET and only the γ, Z or b particles will be detected. The leading Feynman diagrams are shown below in Figure 13, 14 and 15.

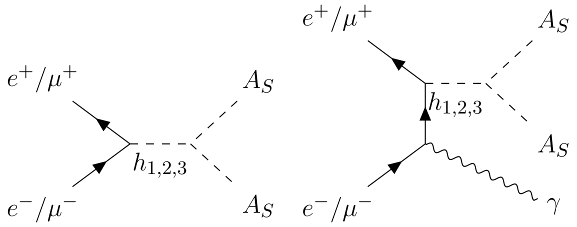

Figure 13: Feynman diagrams for A_SA_S and $A_SA_S\gamma$ production at lepton colliders, created using `TikZ-Feynman` [114].

At hadron colliders on the other hand, such as the LHC, a scalar Higgs particle can not be produced directly. The main production channels are via gluon-gluon fusion (GGF), vector boson fusion (VBF) and the production of two b-quarks along

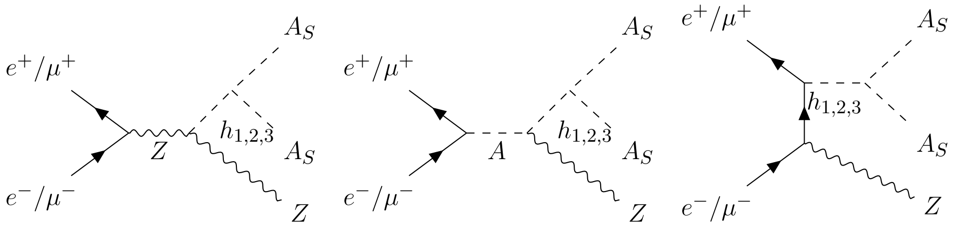

Figure 14: Feynman diagrams for ZA_SA_S production at lepton colliders, created using `TikZ-Feynman` [114].

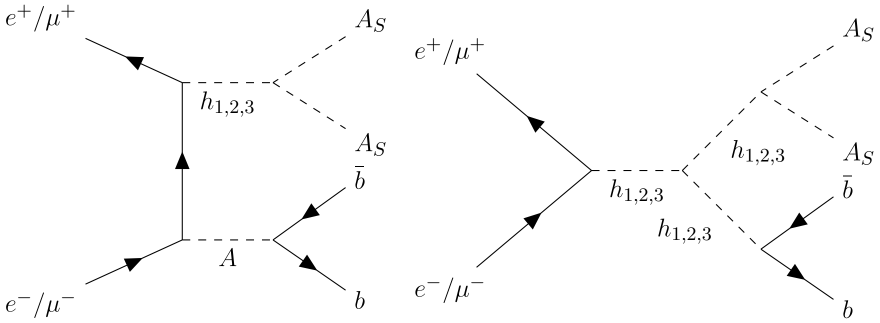

Figure 15: Feynman diagrams for $b\bar{b}A_SA_S$ production at lepton colliders, created using `TikZ-Feynman` [114]. Similar diagrams will take part in producing the final state $t\bar{t}A_SA_S$.

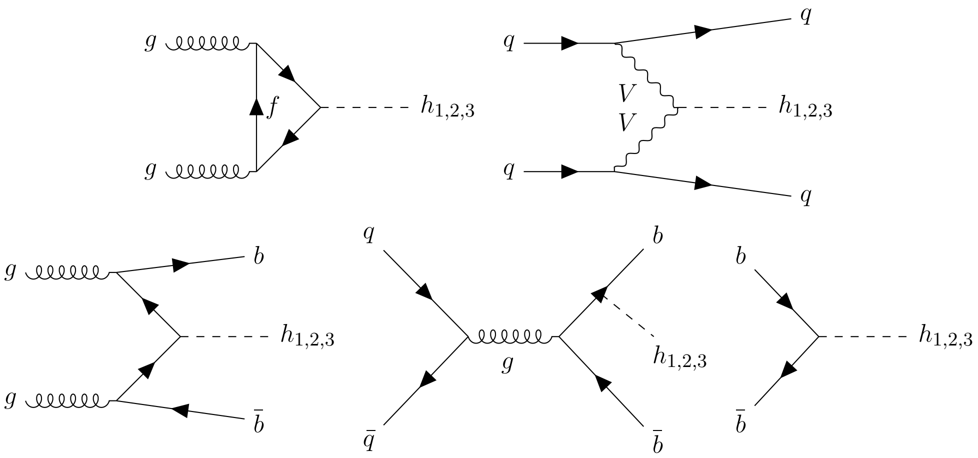

Figure 16: Feynman diagrams for the production of a scalar Higgs boson h_i, with $i = 1,2,3$ via GGF (top left), VBF (top right) and BBH (bottom row) at the LHC. The bottom left and middle diagrams correspond to four-flavour (4f) scheme and the bottom right diagram corresponds to the five-flavour (5f) scheme, created using `TikZ-Feynman` [114].

with a scalar Higgs particle (BBH). The corresponding Feynman diagrams can be seen in Figure 16.

4.2 Constraints

The aim of this work is to scan the parameter space of the 2HDMS and identify viable regions. Various theoretical and experimental constraints need to be taken into account.

4.2.1 Theoretical constraints

Important theoretical constraints for a viable extension of the SM are: the potential being bounded from below (bfb), tree-level perturbative unitarity and the stability of the vacuum. The constraints are explained below in detail.

- **Boundedness-from-Below (bfb) conditions:** The potential is required to be bounded from below, which means that at large field values it must remain positive. At large field values quadratic terms can are sub-dominant and the behaviour of the potential is dominated by the quartic terms. This puts constraints on the quartic couplings of the scalar potential. The part of the potential containing only quartic terms is denoted V_4. The bfb condition can then be expressed as:

  $$\lim_{\Phi_i, S \to \infty} V_4 > 0, \tag{4.23}$$

  where $i = 1, 2$. The required conditions for the 2HDM and its extension with a real singlet scalar have been calculated in [115–117]. Here the conditions for the complex singlet extension of the 2HDM are derived following the approach in Ref. [118] using copositivity criteria and the Cottle-Habetler-Lemke theorem [119]. The conditions are obtained as follows: First the minimum of the potential V_4 has to be found and written in matrix form in the basis $x = \left(\Phi_1^\dagger \Phi_1, \quad \Phi_2^\dagger \Phi_2, \quad \rho_S^2, \quad \eta_S^2\right)^T$, with $S = \rho_S + i\eta_S$:

  $$min[V_4] = \frac{1}{2} x^T A x, \tag{4.24}$$

  with

  $$A = \begin{pmatrix} \lambda_1 & \lambda_3 + \rho^2(\lambda_4 - |\lambda_5|) & \lambda_1' + 2\lambda_4' & \lambda_1' - 2\lambda_4' \\ \lambda_3 + \rho^2(\lambda_4 - |\lambda_5|) & \lambda_2 & \lambda_2' + 2\lambda_5' & \lambda_2' - 2\lambda_5' \\ \lambda_1' + 2\lambda_4' & \lambda_2' + 2\lambda_5' & \frac{5\lambda_1'' + 3\lambda_3''}{6} & \frac{-\lambda_1'' + \lambda_3''}{2} \\ \lambda_1' - 2\lambda_4' & \lambda_2' - 2\lambda_5' & \frac{-\lambda_1'' + \lambda_3''}{2} & \frac{-\lambda_1'' + \lambda_3''}{2} \end{pmatrix}, \tag{4.25}$$

where two cases are distinguished:

$$\begin{aligned} &\text{case 1: } (\lambda_4 - |\lambda_5|) \geq 0 \quad \Rightarrow \quad \min[V_4] = V_4|_{\rho=0}\,, \\ &\text{case 2: } (\lambda_4 - |\lambda_5|) < 0 \quad \Rightarrow \quad \min[V_4] = V_4|_{\rho=1}. \end{aligned} \tag{4.26}$$

Requiring the potential to be bounded from below then is equivalent to requiring the matrix A to be copositive. A matrix A is strictly copositive, if the form $x^T Ax > 0, \quad \forall x > 0$. A is a symmetric 4×4 matrix. In order to derive the copositivity conditions the Cottle-Habetler-Lemke theorem [119] can be followed, as described in Ref. [118]. This can be done in two steps:

- The order 3 principal submatrices of A are required to be copositive. (The order 3 principal submatrices are obtained by deleting the i-th row and column from A, $i = 1,2,3,4$. This results in 4 symmetric 3×3 matrices.) The explicit copositivity conditions for a symmetric order 3 matrix B with entries b_{ij}, $i,j = 1,2,3$ can be found in [118, eq. (5) and (6)] and are:

$$\begin{aligned} &b_{11} \geq 0, \quad b_{22} \geq 0, \quad b_{33} \geq 0, \\ &\bar{b}_{12} = b_{12} + \sqrt{b_{11}b_{22}} \geq 0, \\ &\bar{b}_{13} = b_{13} + \sqrt{b_{11}b_{33}} \geq 0, \\ &\bar{b}_{23} = b_{23} + \sqrt{b_{22}b_{33}} \geq 0, \\ &\sqrt{b_{11}b_{22}b_{33}} + b_{12}\sqrt{b_{33}} + b_{13}\sqrt{b_{22}} + b_{23}\sqrt{b_{11}} + \sqrt{2\bar{b}_{12}\bar{b}_{13}\bar{b}_{23}} \geq 0. \end{aligned} \tag{4.27}$$

- The matrix A has to satisfy: $\det(A) \geq 0 \quad \vee \quad (\mathrm{adj}A)_{ij} < 0$, for some i,j. The adjugate of A is defined as the transpose of the cofactor matrix: $(\mathrm{adj}A)_{ij} = (-1)^{i+j}D_{ji}$, with D_{ij} being the determinant of the submatrix that is obtained by deleting the i-th row and j-th column from A.

In practice each parameter point is checked for these conditions with a `Python` code using `numpy` [120].

- **Tree-level unitarity conditions:** The requirement of the model to be unitary at tree-level constrains the eigenvalues of the scattering matrices between the scalars and the longitudinal components of the gauge bosons to be lower than $\frac{1}{2}$ [121]. This condition is checked for each point of the scans using `SPheno-v4.0.5` [122, 123].

- **Vacuum stability conditions:** The requirement of vacuum stability at the EW scale places additional constraints on the parameter space. The strongest constraint comes from demanding the EW vacuum to be the global minimum of the full scalar potential. In this case the EW vacuum will be absolutely stable. The absolute stability implies that there exist no charge or CP-breaking minima, or non-EW vacuum lower than the EW vacuum. However this constraint can be relaxed if one demands the transition time from the EW vacuum to unphysical lower minima to be larger than the age of the Universe, thus indicating metastability. In that case the EW vacuum is not absolutely stable but sufficiently long-lived. In the considered model, although the bfb conditions put strong constraints on the quartic couplings, there can be further constraints on the quartic couplings, from the requirement of (meta)stability of the EW vacuum. For this work all chosen benchmark points are checked to have an absolutely stable EW vacuum. In the earlier stages of this project, `EVADE` [124, 125] was used for this purpose, which uses `HOM4SP2` [126] to find the tree-level minima and in case of an unphysical deeper minimum, calculates the bounce action using a straight path approximation [124]. However, as the project proceeded a switch to `BSMPT-v3.0.6` [127–129] was made. This change was due to convenience as for a follow-up project this code was used, too.

4.2.2 Experimental constraints

The relevant experimental constraints for this work are:

- One of the scalar particles needs to comply with the SM-like Higgs boson with a mass of $125.25 \pm 0.17\,\text{GeV}$ [130]. The second lightest scalar h_2 is chosen to be this particle.

- The invisible decay width of the SM-like Higgs boson to the DM candidate A_S, is constrained by ATLAS and CMS as below:

$$\begin{aligned} BR(h_2 \to A_S A_S) &\leq 0.07^{+0.030}_{-0.022}\ \text{(ATLAS) [131]}\,, \\ &\leq 0.15\ \text{(CMS) [132]}. \end{aligned}$$

  Note, that this constraint is automatically fulfilled if the mass of the DM candidate is too heavy for the SM-like Higgs boson to decay into two DM particles, hence if $m_{A_S} > 62.5\,\text{GeV}$.

- Constraints from flavour physics set the following bounds:

$$\begin{aligned} BR(b \to s\gamma) &= (3.55 \pm 0.24 \pm 0.09) \times 10^{-4}\ \text{[133]}, \\ BR(B_s \to \mu^+\mu^-) &= (3.2^{+1.4+0.5}_{-1.2-0.3}) \times 10^{-9}\ \text{[134, 135]}. \end{aligned}$$

Furthermore, the benchmark points are within the upper limit of $\Delta(g-2)_\mu = 261(63)(48)\times 10^{-11}$ [136].

- The EW precision observables are parameters sensitive to deviations from the SM. These are, for example, the masses of the gauge bosons m_Z, $m_{W^\pm}$, the Fermi constant G_F and the decay width Γ_Z of the Z-boson. For extensions of the scalar sector of the SM, as is the 2HDMS, some of these constraints can be expressed in terms of the oblique parameters S, T and U. The parameter S is sensitive to new physics affecting the Z-boson propagator and the photon propagator and is related to anomalies in neutral currents. The parameter T is sensitive to new physics affecting the ratio of the masses of the $W^\pm$ and the Z-boson and the parameter U is sensitive to new physics affecting the $W^\pm$-boson propagator.

  The EW precision tests constrain the STU parameters to [136]:

$$\begin{aligned} S &= 0.02 \pm 0.1\,, \\ T &= 0.07 \pm 0.12\,, \\ U &= 0.00 \pm 0.09\,. \end{aligned}$$

  The model predictions for the STU parameters are obtained from [137, 138].

- The DM relic density is constrained by the upper limit from the Planck experiment [61]:

$$\Omega h^2 = 0.120 \pm 0.001.$$

  The predictions of the model for the DM relic density are calculated using the code `micrOmegas-v5.3.35` [139–142].

- The spin-independent cross sections for scattering of DM on protons and neutrons is constrained by direct detection experiments from LZ [91]. The predictions of the model for the direct detection cross sections are calculated using `micrOmegas-v5.3.35` [139–142], where the direct detection cross section is rescaled by the fraction of the predicted relic density to the observed relic density [21, 143, 144].

- The spin-independent cross sections for DM annihilation are constrained by indirect detection experiments from Fermi-LAT (Fermi) [92, 93]. The predictions of the model for the indirect detection cross sections are calculated using `micrOmegas-v5.3.35` [139–142], where the indirect detection cross section is rescaled by the squared fraction of the predicted relic density to the observed relic density [21, 143, 144].

- The constraints from LEP [145], ATLAS [146] and CMS [147] on the heavy Higgs searches and the 125 GeV Higgs signal strength measurements [148] are taken into account.

4.2.3 Software used

In order to calculate the DM spectrum, which includes the masses of the Higgs sector particles, mixing angles of the Higgs sector, as well as couplings to fermions and vector bosons and branching ratios of decays, `SPheno-v4.0.5` [122, 123][3] is used.
The Spheno output is then used as input for `micrOmegas-v5.3.35` [139–142][4] which calculates the DM relic density and the direct and indirect detection cross sections of DM. The implementation of the 2HDMS model into `SPheno` and `micrOMEGAs` is done with the `Mathematica` package `SARAH-v4.14.3` [149]. Constraints on the Higgs sector are checked using `HiggsTools` [150–154] (which is a unification of the former `HiggsBounds-5` (HB) and `HiggsSignals-2`).

The constraints are applied as binary-cut, meaning only parameter points passing all constraints are considered allowed.

4.3 Dark matter phenomenology

In this section the impact of the free parameters on the DM phenomenology as well as the impact of the excess around 95 GeV is discussed. In order to do this an exemplary benchmark point $\mathbf{BP1_{w95}}$ satisfying all constraints explained in the section above is chosen. The parameters in the mass basis along with the reduced value of χ^2 to model the excess at 95 GeV can be found in Table 5. The low m_A region would be excluded by the LHC $A \to \tau^+\tau^-$ searches [155–157] for high $\tan\beta$ values. Therefore, m_A, m_{h_3} and $m_{H^\pm}$ are chosen appropriately heavy.

m_{h_1}	m_{h_2}	m_{h_3}	m_A	$m_{H^\pm}$	χ^2
95.4 GeV	125.09 GeV	900 GeV	900 GeV	900 GeV	1.01
m_{A_S}	$\lambda'_1 - 2\lambda'_4$	$\lambda'_2 - 2\lambda'_5$	$\lambda''_1 - \lambda''_3$	$\tan\beta$	
326 GeV	12.3	-0.31	-1.36	10	
v_S	$\tilde{\mu}$	α_1	α_2	α_3	
240 GeV	902 GeV	1.52	1.14	-1.60	

Table 5: The benchmark point $\mathbf{BP1_{w95}}$ in the mass basis.

---

[3] https://spheno.hepforge.org/

[4] https://lapth.cnrs.fr/micromegas/

In the following subsection more information on the excess at 95 GeV is given and the impact of it on the DM phenomenology is discussed. After that the impact of the other free parameters on the DM phenomenology is investigated by scanning around $\mathbf{BP1_{w95}}$, using fixed grids and varying two parameters at the same time. About 100 steps are used for each parameter. This leaves a total of $100 \times 100 = 10000$ points for each scan.

4.3.1 Impact of excess at 95 GeV

As mentioned earlier an experimental excess around 95 GeV was observed both at LEP [8] in the $b\bar{b}$ mode as well as at CMS [9] and ATLAS [10] in the $\gamma\gamma$ mode. This excess can be explained with a sclar particle with a mass of 95 GeV in the 2HDMS. Some of the benchmarks presented in the following sections include such a scalar in order to explain this excess in addition to providing a viable DM candidate.

For the benchmarks with a scalar Higgs particle at 95 GeV as a part of the mass spectrum, it must be ensured that its signal strengths satisfy the following: The lightest scalar h_1 has a mass of 95.4 GeV and plays the role of a scalar particle responsible for the observed signal strengths, which are for LEP in the $b\bar{b}$ mode ($\sim 2\sigma$) [8] and for LHC in the $\gamma\gamma$ mode ($\sim 3\sigma$) [9, 10]:

$$\mu^{b\bar{b}}_{\text{LEP}} = 0.117^{+0.057}_{-0.057}, \qquad \mu^{\gamma\gamma}_{\text{LHC}-\text{combined}} = 0.24^{+0.09}_{-0.08}, \tag{4.28}$$

where $\mu^{\gamma\gamma}_{\text{LHC}-\text{combined}}$ is a combination of the ATLAS and CMS results following Ref. [23]. The combined $\chi^2 = \chi^2_{b\bar{b}} + \chi^2_{\gamma\gamma}$ values are calculated according to Ref. [20] and [42] and given in Table 5 and 7 - 9.

According to Ref. [20], the coupling $c_{h_1 b\bar{b}}$ can not strongly affect the $h_1 \to b\bar{b}$ branching ratio, while the total width of h_1 is dominated by the $c_{h_1 b\bar{b}}$ coupling. In this case, the Higgs strahlung production plays the most important role of the LEP signal strength, and the $h_1 \to \gamma\gamma$ branching ratio is strongly dependent on the h_1 total width. Therefore, the signal strengths of the observed 95 GeV excess may be correlated with the reduced couplings and mixing angles as below:

$$\begin{aligned} \mu^{\text{pred}}_{\text{LEP}} &= \mu^{\text{2HDMS}}_{b\bar{b}} \propto |c_{h_1 VV}|^2, \\ \mu^{\text{pred}}_{\text{CMS/ATLAS}} &= \mu^{\text{2HDMS}}_{\gamma\gamma} \propto \frac{(|c_{h_1 t\bar{t}}|)^2}{(|c_{h_1 b\bar{b}}|)^2} \propto \left(\frac{\tan\alpha_1}{\tan\beta}\right)^2, \end{aligned} \tag{4.29}$$

where $\mu^{\text{2HDMS}}_{b\bar{b}}$ and $\mu^{\text{2HDMS}}_{\gamma\gamma}$ are the predicted signal strengths of the $b\bar{b}$ and $\gamma\gamma$-channels computed in the 2HDMS.

In order to remind the reader the relations between the reduced couplings of the lightest scalar particle h_1 and the scalar rotation matrix R from Equation 4.21 and

4.22 are repeated here:

$$\begin{aligned}
c_{h_1bb} &= \frac{R_{11}}{\cos\beta} = \frac{\cos(\alpha_1)\cos(\alpha_2)}{\cos(\beta)}\,,\\
c_{h_1tt} &= \frac{R_{12}}{\sin\beta} = \frac{\sin(\alpha_1)\cos(\alpha_2)}{\sin(\beta)}\\
c_{h_1VV} &= \cos\beta R_{11} + \sin\beta R_{12}\,,\\
&= \cos\beta\cos\alpha_1\cos\alpha_2 + \sin\beta\sin\alpha_1\cos\alpha_2\,.
\end{aligned}$$

This can be translated into expressions for the scalar mixing angles:

$$\begin{aligned}
\alpha_1 &= \arctan(\frac{\tan(\beta)c_{h_1tt}}{c_{h_1bb}})\\
\alpha_2 &= \arccos(\frac{\sin(\beta)/\cos(\alpha_1)}{\tan(\beta)+\tan(\alpha_1)}(c_{h_1bb}+c_{h_1tt}))\,.
\end{aligned} \tag{4.30}$$

Hence when performing a parameter scan the input parameters α_1 and α_2 can be replaced by c_{h_1bb} and c_{h_1tt} (or equivalently c_{h_1VV}), which in turn can be expressed via the predicted signal strengths $\mu^{\text{pred}}_{\text{LEP}}$ and $\mu^{\text{pred}}_{\text{CMS/ATLAS}}$. This was done for he following scan where the reduced couplings are varied in the ranges given below in Table 6 while all other parameters are kept fixed to the values in Table 5. These values for the reduced couplings are then translated to $\mu^{\text{pred}}_{\text{LEP}}$ and $\mu^{\text{pred}}_{\text{CMS/ATLAS}}$ and are shown on the x and y-axis of Figure 17. Theoretical constraints from bfb and tree-level unitarity and experimental constraints from the Higgs sector as well as constraints from DM observables, namely, spin-independent direct detection cross section for scattering on protons and on neutrons, indirect detection cross section for DM annihilation (for the dominant annihilation channels h_2h_2, WW and $b\bar{b}$) and relic density are shown as hatched areas on the $\mu^{\text{pred}}_{\text{CMS/ATLAS}}$-$\mu^{\text{pred}}_{\text{LEP}}$ plane.

Parameters	Range
c_{h_1bb}	$[0.0996, 0.320]$
c_{h_1tt}	$[0.309, 0.529]$

Table 6: Ranges of parameters varied. The rest of the parameters are kept fixed to $\mathbf{BP1_{w95}}$ in Table 5. (The ranges for c_{h_1bb} and c_{h_1tt} are chosen such that constraints from Ref. [20] are respected. This results in some areas in the $\mu^{\text{pred}}_{\text{LEP}}$-$\mu^{\text{pred}}_{\text{CMS/ATLAS}}$ plane in Figure 17 being white, as those values are not allowed by the constraints from the observed 95 GeV excess.)

As can be seen in Figure 17 from the top left plot the direct detection cross section has a minimum along an arched line. Close to this line lies $\mathbf{BP1_{w95}}$, marked with a red star. The regions where the cross section grows too large and exceeds the upper bounds from LZ are excluded and shown as a dotted area. This occurs due to

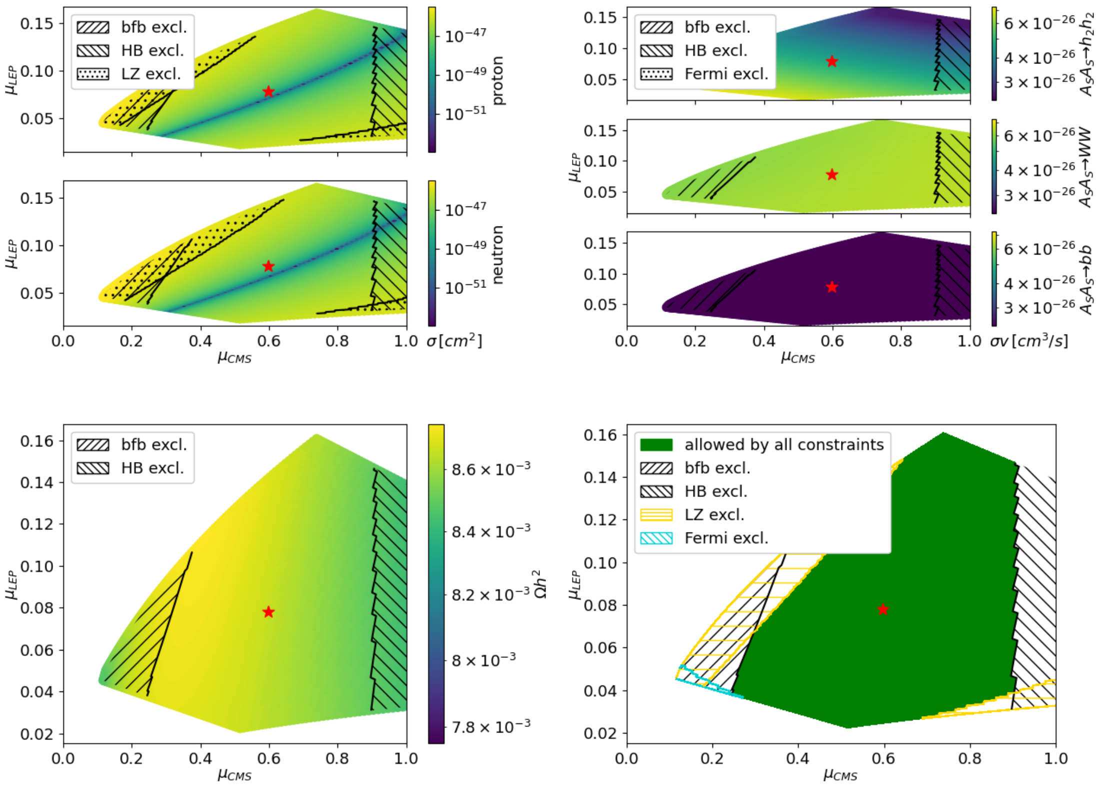

Figure 17: Variation of $\mu^{\text{pred}}_{\text{CMS/ATLAS}}$-$\mu^{\text{pred}}_{\text{LEP}}$ (the short-hand notation $\mu_{\text{CMS}} - \mu_{\text{LEP}}$ is used in the plots) to fit the 95 GeV excess signal strength for h_1. The relevant constraints which stringently restrict the allowed regions are shown in the plots. The coloured palette on the z-axis denote the spin-independent direct detection DM-proton/neutron cross section (top left), indirect detection DM annihilation cross section (top right), relic density (bottom left) and the allowed parameter regions under combining all constraints (bottom right). **BP1$_{\mathbf{w95}}$**, in Table 5, is marked with a red star. [1]

insufficient cancellations between the different contributions to the spin-independent direct detection cross section from h_1, h_2 and h_3.

From the top right plot one can see how the indirect detection cross sections for the channels h_2h_2, WW and $b\bar{b}$ behave. The cross section for the h_2h_2-channel decreases with $\mu^{\text{pred}}_{\text{LEP}}$, whereas the other two channels do not show large changes. Due to the h_2h_2-channel dominating for the chosen benchmark **BP1$_{\mathbf{w95}}$** the variations of the other channels are on a smaller scale. Only a thin line in the h_2h_2-channel with low $\mu^{\text{pred}}_{\text{CMS/ATLAS}}$ and low $\mu^{\text{pred}}_{\text{LEP}}$ is excluded by Fermi data.

In the bottom left plot the relic density is shown. It shows small changes and reaches the highest values around $\mu^{\text{pred}}_{\text{CMS/ATLAS}} \approx 0.3$. However, it is very low across the whole region and always remains underabundant.

In the bottom right plot all the constraints from bfb, unitarity, Higgs and DM searches are combined, revealing the allowed region, shown in green.

4.3.2 Impact of free parameters on dark matter observables

Before discussing the impact of the free parameters on DM observables, a few important comments should be made. The DM phenomenology in this model is crucially coupled with the chosen symmetries of the DM sector, which is a discrete Z_2' symmetry in this case. A relevant comparison can be made with several earlier works [21, 158, 159] with a complex singlet, where the DM sector is instead stabilised by a softly broken $U(1)$ symmetry along with a Z_2 symmetry. In those models, the spontaneous breaking of the continuous Z_2 symmetry by the singlet vev gives rise to a pseudo Nambu-Goldstone boson (pNGB) DM, which can evade direct detection constraints to a large extent and these models are difficult to probe even in future direct search experiments. This is not the case here. Spontaneous breaking of the Z_2' symmetry does not lead to pNGB DM, due to the presence of the $U(1)$ breaking terms in the singlet part of the potential allowed by the Z_2' symmetry. Therefore in this case the direct detection bounds constrain the parameter space significantly, as shown below. Furthermore, there are parts of parameter space in this models which will necessarily come under the reach of future direct search experiments.

Below the impact of the free parameters on the DM observables is studied, where again parameter scans are performed around $\mathbf{BP1_{w95}}$.

Influence of λ'_{14} and λ'_{25}

Earlier two variables were defined $\lambda'_{14} = \lambda'_1 - 2\lambda'_4$ and $\lambda'_{25} = \lambda'_2 - 2\lambda'_5$. These are varied around $\mathbf{BP1_{w95}}$ in the ranges as shown in Figure 18. The influence on the direct detection cross section for scattering on protons and on neutrons (top left plot), indirect detection cross section for DM annihilation (top right plot) and relic density (bottom left plot) are shown in the coloured palette. $\mathbf{BP1_{w95}}$ is marked with a red star and the excluded regions are shown as hatched areas. The bottom right plot shows a summary of all exclusions and the allowed region in green. As can be seen, the impact of λ'_{25} is stronger than the impact of λ'_{14} in this benchmark. This can be explained by the choice of $\tan\beta$. From Equation 4.19 it can be seen that by setting $\tan\beta = 10$ (see Table 5), $\cos\beta$ suppresses the influence of λ'_{14} and $\sin\beta$ enhances the influence of λ'_{25}. For the direct detection cross section a strong dip appears around $\lambda'_{25} \sim 0$. Such a dip can in principle occur due to a cancellation between the elastic scattering amplitudes involving h_1 and h_2 (owing to their closeness in mass), if their contribution comes with opposite signs. Such cancellations also arise in simple Higgs portal models such as the complex scalar extended SM [158]. For

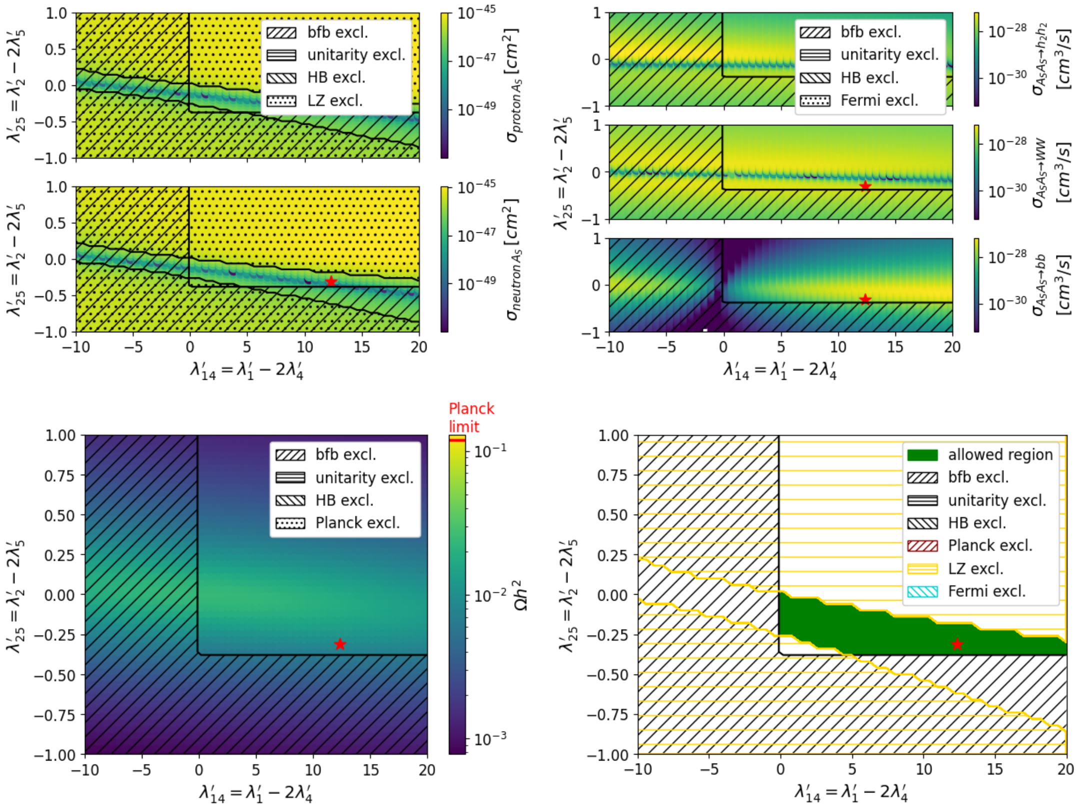

Figure 18: Influence of $\lambda'_{14} = \lambda'_1 - 2\lambda'_4$ and $\lambda'_{25} = \lambda'_2 - 2\lambda'_5$. The coloured palette on the z-axis denote the spin-independent direct detection DM-proton/neutron cross section (top left), indirect detection DM annihilation cross section (top right), relic density (bottom left) and the allowed parameter regions under combining all constraints (bottom right). $\mathbf{BP1_{w95}}$, in Table 5, is marked with a red star. (This figure is a rescan of the original in Ref. [1])

the chosen parameter space, it was checked that they indeed come with opposite signs. In addition the choice $\lambda'_{25} = 0$ minimises the scalar-to-DM coupling. The areas away from the dip are above the upper bounds from LZ and are therefore excluded, shown as dotted regions.

For the indirect detection cross section in the h_2h_2-channel and the WW-channel one can see similar dips around $\lambda'_{25} \sim 0$. For the parameter regions shown here the cross sections stay low enough to not be excluded by Fermi. The $b\bar{b}$-channel on the other hand shows a peak around $\lambda'_{25} \sim 0$ (except for the region around $\lambda'_{14} \sim 0$). Since fermions do not couple directly to the DM candidate in this model, this can be explained by an enhancement of the tilinear coupling between the mediating scalar, h_3 in this case, and b-quarks which gets enhanced by the $\frac{1}{\cos\beta}$-term.

The relic density also shows a slight peak around $\lambda'_{25} \sim 0$ as shown in the bottom left plot remaining below the upper bound from PLANCK. This can be explained as follows. As can be seen from Equation 4.19, increasing $|\lambda'_{25}|$ increases the trilinear and the quatrilinear scalar-to-DM couplings. This causes stronger interactions and hence more annihilation of DM particles. After annihilation there is less DM left in the Universe. Hence the relic density drops with higher values of $|\lambda'_{25}|$ and the inverse behaviour as for direct and indirect detection cross sections can be observed.

For all three observables, regions below $\lambda'_{25} \sim -0.3$ and $\lambda'_{14} \sim 0$ are excluded by bfb constraints, shown as hatched regions in the bottom right plot. There are no regions excluded by unitarity constraints or HB for the shown region. Combining all constraints from bfb, unitarity, Higgs and DM searches, this results in a narrow allowed band between $\lambda'_{25} \sim [-0.3, 0.1]$ and $\lambda'_{14} \sim [0, 20]$, shown in green.

Influence of v_S and $\tan\beta$

In this section, v_S and $\tan\beta$ are varied around **BP1$_{\mathbf{w95}}$** in the ranges as shown in Figure 19. The influence on the DM observables, as well as excluded and allowed regions are shown in the same manner as in the previous plots. As can be seen, both

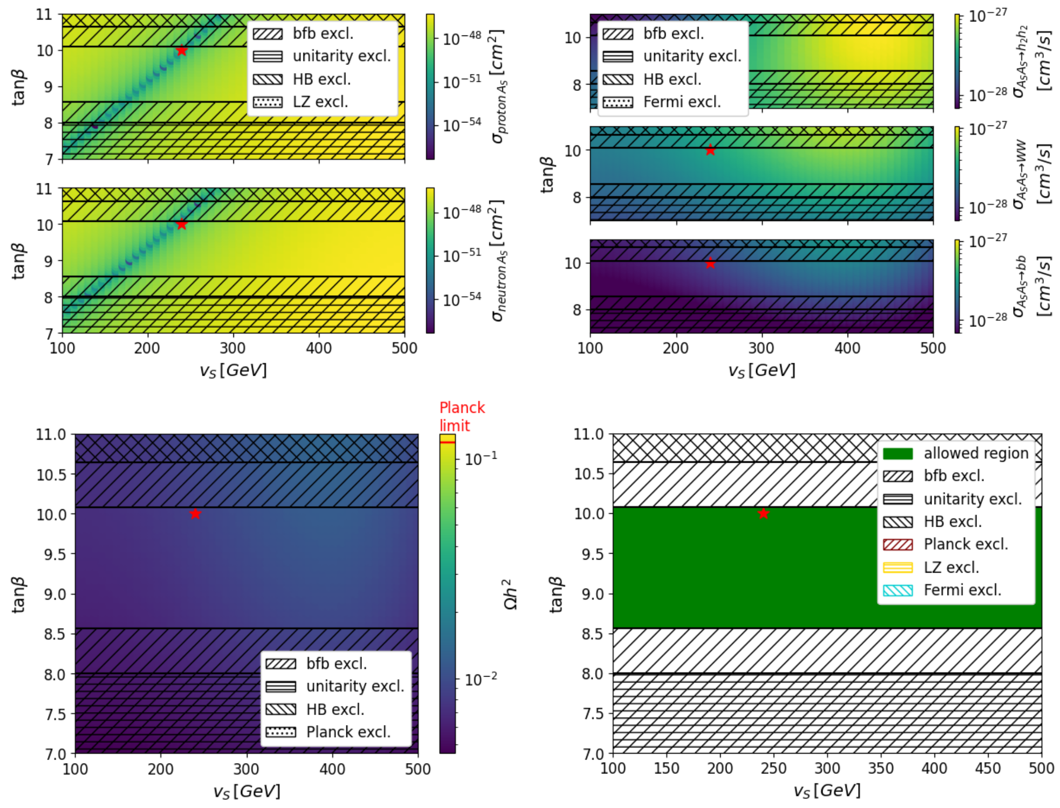

Figure 19: Influence of v_S and $\tan\beta$. The coloured palette on the z-axis denote the spin-independent direct detection DM-proton/neutron cross section (top left), indirect detection DM annihilation cross section (top right), relic density (bottom left) and the allowed parameter regions under combining all constraints (bottom right). **BP1$_{\mathbf{w95}}$**, in Table 5, is marked with a red star. (This figure is a rescan of the original in Ref. [1])

v_S and $\tan\beta$ have an impact on the direct detection cross section, which results in a dip visible as a straight diagonal line around $\mathbf{BP1_{w95}}$ which again can be explained by cancellations between diagrams involving h_1 and h_2. Areas away from this dip have a higher cross section but remain below the constraints from LZ.

Contrary to the results from the former subsection, here the dip from the direct detection cross section does not show up for the indirect detection cross section. This can be understood from looking at Equation 4.19, where v_S and $\tan\beta$ (via $\cos\beta$ and $\sin\beta$) show up directly in the trilinear scalar-to-DM couplings but not in the quatrilinear couplings. For indirect detection both couplings play an important role, whereas for direct detection the trilinear couplings are more important. The influence of v_S, increasing the last term in the trilinears coupling with a negative sign, can be seen best in the h_2h_2-channel. There are no areas excluded by Fermi here.

For the relic density the impact of v_S and $\tan\beta$ is difficult to observe as overall the values are quite low. However, v_S increases the relic density slightly. The influence of $\tan\beta$ is barely visible which can be explained by the fact that $\tan\beta$ was varied only over a small range and the $\sin\beta$ and $\cos\beta$-terms in Equation 4.19 do not vary over large ranges as v_S. Furthermore, with growing $\tan\beta$ the $\sin\beta$ increases, while $\cos\beta$ decreases, hence partly counterbalancing the effect of the first two terms in the trilinear couplings. There are no areas excluded by PLANCK here and the relic density remains underabundant throughout the ranges of the scan.

For all three observables, regions above $\tan\beta \sim 10.5$ and below ~ 8.5 are excluded by bfb constraints, shown as hatched regions in the bottom right plot. Regions above $\tan\beta \sim 10.7$ are further excluded by HB, shown as left directed hatches. Combining all constraints results in an allowed region between $\tan\beta \sim [8.5, 10]$ across the whole range of v_S.

Influence of m_{A_S} and λ''_{13}

Finally m_{A_S} and $\lambda''_{13} = \lambda''_1 - \lambda''_3$ are varied around $\mathbf{BP1_{w95}}$ in the ranges shown in Figure 20. Again the DM observables, as well as excluded and allowed regions are shown in the same manner as in the previous plots. As can be seen m_{A_S} and λ''_{13} change the direct detection cross section in such a way that two dips appear as a vertical line along $m_{A_S} \sim 450\,\mathrm{GeV} = \frac{m_{h_3}}{2}$ and as a horizontal line along $\lambda''_{13} \sim -1.5$ along which $\mathbf{BP1_{w95}}$ lies. The first can be explained by reminding that the shown cross sections are rescaled by the fraction of predicted relic density to observed relic density as mentioned in section 4.2.2. Hence when the relic density (bottom left plot) shows a strong enough dip, this will also show up in the direct and indirect detection cross sections. In the previous subsections the effects on the relic density were less strong and the direct effects of the parameters on direct and indirect detection

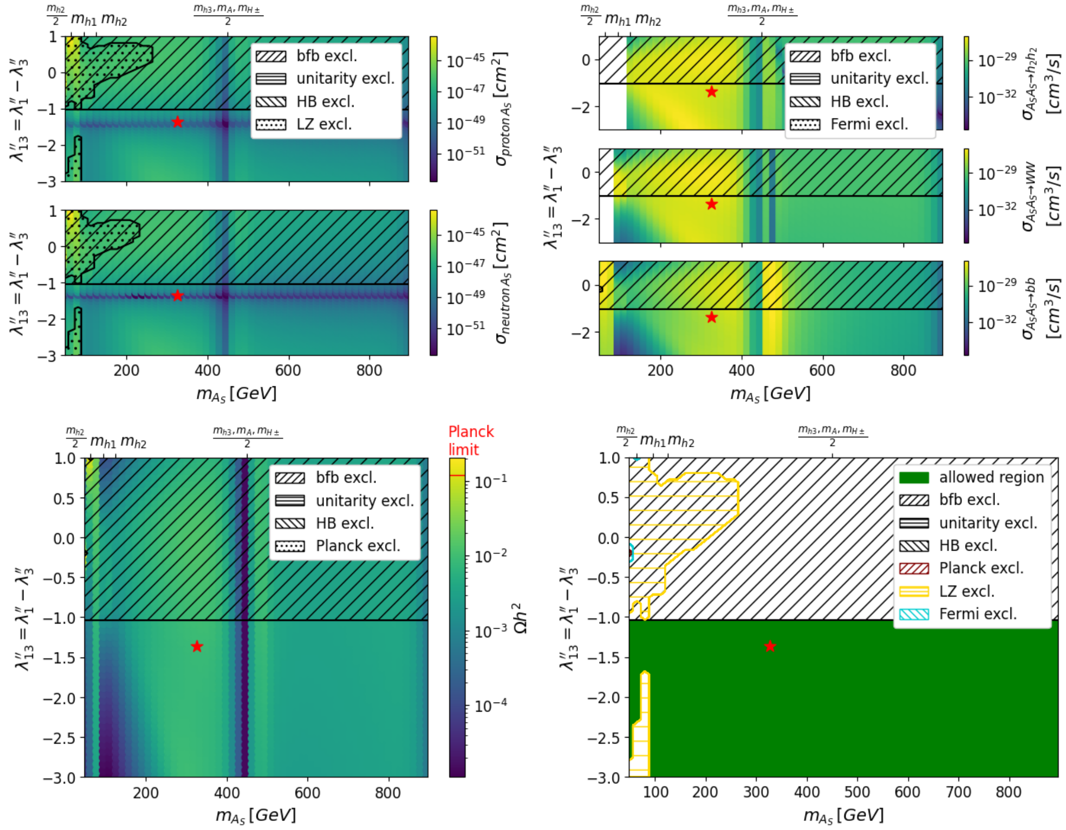

Figure 20: Influence of m_{A_S} and $\lambda''_{13} = \lambda''_1 - \lambda''_3$. The coloured palette on the z-axis denote the spin-independent direct detection DM-proton/neutron cross section (top left), indirect detection DM annihilation cross section (top right), relic density (bottom left) and the allowed parameter regions under combining all constraints (bottom right). **BP1$_{\mathbf{w95}}$**, in Table 5, is marked with a red star. (This figure is a rescan of the original in Ref. [1])

cross sections were stronger which is the reason why this argument did not play such an important role there. The peak at low m_{A_S} can be explained equivalently. The horizontal dip along $\lambda''_{13} \sim -1.5$, on the other hand, can be understood by looking at the trilinear scalar-to-DM couplings in Equation 4.19, where the λ''_{13}-term contributes with a negative sign and can cancel the first two terms. This corresponds to a cancellation between the contributions from h_1 and h_2 as was the case in the previous subsections. The areas excluded by LZ are shown as dotted areas.

The behaviour of the indirect detection cross section is quite interesting, as one can see some peaks and dips around $m_{A_S} \sim 450\,\text{GeV}$. This is half the mass of the heavy scalars $m_{h_3} = m_A = m_{H^\pm} = 900\,\text{GeV}$. The dips slightly below this value can be explained as above by using the rescaled cross sections. At the same time indirect detection cross sections and relic density behave roughly inversely. These counter acting effects can be responsible for the peak-dip structure. In the $b\bar{b}$-channel, for example, the peak can be due to the resonant annihilation of two DM particles into the heavy scalar h_3 which then, in turn, decays into $b\bar{b}$. In the WW-channel, on the other hand, another dip can be observed slightly above $m_{A_S} \sim 450\,\text{GeV}$ due to the preferred annihilation into $b\bar{b}$ and and other channels. In all three plots, some white areas can be seen. This is due to `micrOMEGAs` not returning values in these regions. This can happen when the cross section is too small. For example, in the h_2h_2-channel and the WW-channel, where $m_{A_S} < m_{h_2}$ and $m_{A_S} < m_W$, the respective annihilation processes are kinematically forbidden. Other channels dominate in this case. Regions excluded by Fermi are again shown as dotted areas.

The influence on the relic density is also interesting, as a peak can be seen around $m_{A_S} \sim 75\,\text{GeV}$. For lower masses $m_{A_S} \lesssim 62.5\,\text{GeV} \approx \frac{m_{h_2}}{2}$ resonant annihilation of two DM particles into one SM Higgs boson is possible and causes a drop in the relic density. For higher masses $m_{A_S} \gtrsim 95\,\text{GeV} \approx m_{h_1}$ the annihilation channel into one light scalar h_1 opens up and also causes the relic density to drop. This could explain why in between those areas the relic density appears higher and looks like a peak. Another interesting feature is the dip at $m_{A_S} \sim 450\,\text{GeV}$, which is half the mass of the heavy scalars $m_{h_3} = m_A = m_{H^\pm} = 900\,\text{GeV}$. Here resonant annihilation into those particles causes the relic density to drop. This drop is strong enough to show up in the direct and indirect detection cross sections as explained above. Regions excluded by PLANCK are shown as dotted areas.

For all three observables, the region above $\lambda''_{13} \sim -1$ is excluded by bfb constraints, shown as a hatched area in the bottom right plot. Small regions at low values of m_{A_S} are excluded by LZ. Combining all constraints shows an allowed area below $\lambda''_{13} \sim -1$.

4.4 Collider phenomenology

In this section the phenomenology od the 2HDMS and prospect of detection at future colliders and at HL-LHC is discussed. In order to do this, parameter regions which are interesting from the point of view of possible detection at future colliders are identified and benchmark points are selected in the following subsection. After that signal processes are generated for these benchmark points and the results are discussed.

4.4.1 Parameter regions of interest and benchmark selection

This work aims to perform a systematic analysis of DM phenomenology at current and future colliders. Therefore, different DM mass regions are considered: low, intermediate-range and heavy mass DM produced via the decay of the Higgs bosons.

The benchmark points presented here are consistent with all theoretical and experimental constraints mentioned earlier in the text. Further, the interplay of DM relic density and the invisible branching ratio of a mediating scalar Higgs particle to DM candidates is discussed as well as the dominant signal processes at different colliders and the signal topologies for each of the different DM mass regions. An exhaustive collider analysis is performed here and the efficacy of lepton colliders, particularly electron-positron colliders like ILC/CLIC/CEPC/FCC-ee for low and intermediate mass DM and muon colliders for heavy DM over HL-LHC is highlighted.

While this analysis is performed in the context of the 2HDMS, it is representative of generic DM models with a scalar portal. The proposed signatures for detecting low, intermediate-range and heavy mass DM signals produced from scalar mediators at colliders can serve as a general guide to probe DM at future colliders. Furthermore, the complimentarity of lepton colliders to HL-LHC is compared to further motivate the need for lepton colliders as a robust discovery probe for new physics.

The representative benchmark scenarios selected in the chosen model are now discussed in more detail. After imposing various constraints on the 2HDMS, a number of benchmark regions are selected (as shown schematically in Figure 21 and also explained in the paragraphs below), which satisfy all relevant constraints and at the same time are interesting from the point of view of discovery at future colliders.

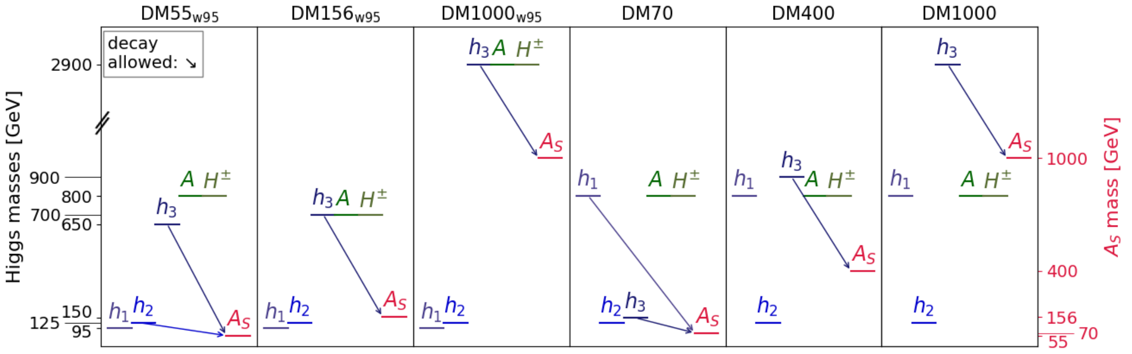

Figure 21: The masses of the scalar particles in the different benchmarks. The mass of the neutral scalars, charged and pseudo-scalar particles (in black) are on the left y-axis while the mass of the DM candidate (in magenta) are shown on right the y-axis. Please note that the point 2900 GeV is not to scale, but was lowered to make the plot more balanced. [2]

Since multiple future collider scenarios are explored with different energy reach, different mass-ranges are presented for the DM candidate as well as for the mediator (the scalar that acts as a major portal between DM and SM sector). Furthermore, in some benchmarks the recently observed excess at 95 GeV in the $b\bar{b}$ and $\gamma\gamma$ final state is also taken into account in this study, in order to see the impact of such a scalar on the DM phenomenology. In the rest of the benchmarks, such an excess is not considered. Furthermore, different possibilities in terms of the DM relic density are explored, namely when the DM candidate in the chosen model accounts for the total observed relic density and also when it accounts for only a part of it. As will be seen in the following, these two scenarios also have some correlation to the discovery potential at collider experiments. In the light of the discussion above, first the benchmarks with the 95 GeV excess are discussed followed by the benchmarks without it.

Notation: The benchmark points in the following subsections are labelled '**DM**' with the mass of the DM candidate and, for the benchmark points including the excess at 95 GeV a subscript '**w95**'.

Benchmarks with a 95 GeV scalar

For the benchmarks, with a scalar at 95 GeV as a part of the mass spectrum, it was ensured that its signal strengths satisfy the conditions mentioned in section 4.3.1, with lightest scalar h_1 having a mass of 95.4 GeV and playing the role of a scalar particle responsible for the observed excesses at LEP in the $b\bar{b}$ mode ($\sim 2\sigma$) [8] and at LHC in the $\gamma\gamma$ mode ($\sim 3\sigma$) [9, 10].

The combined $\chi^2 = \chi^2_{b\bar{b}} + \chi^2_{\gamma\gamma}$ values are calculated according to Ref. [20] and [42] and provided with each benchmark point (see Table 7 - 9).

- $\mathbf{DM55_{w95}}$: The low mass DM can be quite interesting, especially, when $m_{A_S} \lesssim$ 62.5 GeV. The benchmark point $\mathbf{DM55_{w95}}$ falls into this category and fully satisfies the observed relic density. In such a scenario, the 125 GeV SM-like Higgs boson acts as the major portal to the DM sector. By virtue of having an extended scalar sector, it is possible to achieve such couplings between the SM-like Higgs boson and the DM candidate, such that, it satisfies the stringent bounds from the direct detection experiments, while the observed relic density can also be accounted for. The dominant annihilation channel for a pair of DM candidates is into the $b\bar{b}$-state. Furthermore, the upper bound from the invisible decay of the 125 GeV Higgs boson is also respected, since the SM-like Higgs boson only has a small branching ratio to a pair of DM candidates in this case. Although the aforementioned invisible branching ratio is small, it is highly likely, that signals from such a scenario will be visible at future colliders. Therefore, it is quite important to explore this benchmark at the colliders and make predictions.

The parameters in the mass basis as well as the χ^2-value for the excess at 95 GeV are provided in Table 7.

- $\mathbf{DM156_{w95}}$: Furthermore, the region where a heavier scalar particle from the extended scalar sector acts as a portal to the DM sector is explored. In this case, the mass of the DM candidate is taken to be 156 GeV and the heavier scalar mediator

m_{h_1}	m_{h_2}	m_{h_3}	m_A	$m_{H^\pm}$	χ^2
95.4 GeV	125.09 GeV	650 GeV	800 GeV	800 GeV	0.973
m_{A_S}	$\lambda'_1 - 2\lambda'_4$	$\lambda'_2 - 2\lambda'_5$	$\lambda''_1 - \lambda''_3$	$\tan\beta$	
55.596 GeV	0.0020912	0.00074611	−0.025735	2	
v_S	$\tilde{\mu}$	α_1	α_2	α_3	
300 GeV	650 GeV	1.213	−1.270	−1.486	

Table 7: The benchmark point $\mathbf{DM55_{w95}}$ in the mass basis.

h_3 is taken to be of 700 GeV mass. This benchmark also accommodates the 95 GeV scalar with the required signal strengths. One should note that, since the 95 GeV scalar is mostly singlet-like (in order to satisfy all the experimental bounds so far), the heavier scalar h_3 is dominantly doublet-like. The DM portal couplings are scanned as well as the mixing angles between the two scalar doublets, and it was found that in this mass range, it is typically difficult to account for the entire relic density while ensuring a significant branching ratio $BR(h_3 \to A_S A_S)$ of the heavy mediator to the DM candidate. Since the focus in this work is the prospect of DM discovery at future colliders, the parameters for this benchmark are chosen leading to a considerable $BR(h_3 \to A_S A_S)$ and consequently larger production rate. The dominant annihilation channel for a pair of DM candidates in this scenario is into a pair of light scalars h_1.

The parameters in the mass basis as well as the χ^2-value for the excess at 95 GeV are provided in Table 8.

m_{h_1}	m_{h_2}	m_{h_3}	m_A	$m_{H^\pm}$	χ^2
95.4 GeV	125.09 GeV	700 GeV	700 GeV	700 GeV	0.983
m_{A_S}	$\lambda'_1 - 2\lambda'_4$	$\lambda'_2 - 2\lambda'_5$	$\lambda''_1 - \lambda''_3$	$\tan\beta$	
156 GeV	12.753	−0.31351	−2.6747	6.6	
v_S	$\tilde{\mu}$	α_1	α_2	α_3	
239.86 GeV	700 GeV	1.4661	1.1920	−1.5989	

Table 8: The benchmark point $\mathbf{DM156_{w95}}$ in the mass basis.

- $\mathbf{DM1000_{w95}}$: For the next case, a heavy DM scenario is considered which may be detectable at high energy future colliders. For this purpose, a DM mass of 1 TeV is chosen, and a mediator (h_3) mass of 2.9 TeV. The primary motivation for choosing this benchmark is to study a physics case for a future muon collider which will possibly operate at $\sqrt{s} = 3$ TeV and 10 TeV and therefore can produce the heavy scalar h_3 on-shell which can decay into a pair of heavy DM particles. Since here too, a singlet-like 95 GeV scalar is part of the mass spectrum, the 2.9 TeV scalar h_3 is doublet-like. However, in the heavy mass range for h_3 as well as the DM candidate A_S, satisfying the observed relic density could be achieved with a branching ratio of $BR(h_3 \to A_S A_S) \lesssim 4\%$. The dominant annihilation channel for a pair of DM particles in this scenario is into a pair of gauge bosons.

In this way three mass ranges for the DM candidate as well as scalar mediators is covered, namely light, intermediate-range and heavy scenarios in the presence of a 95 GeV excess.

The parameters in the mass basis as well as the χ^2-value for the excess at 95 GeV are provided in Table 9.

m_{h_1}	m_{h_2}	m_{h_3}	m_A	$m_{H^\pm}$	χ^2
95.4 GeV	125.09 GeV	2900 GeV	2900 GeV	2900 GeV	0.997
m_{A_S}	$\lambda_1' - 2\lambda_4'$	$\lambda_2' - 2\lambda_5'$	$\lambda_1'' - \lambda_3''$	$\tan\beta$	
1000 GeV	7.616	0	-0.463	5	
v_S	$\tilde{\mu}$	α_1	α_2	α_3	
1000 GeV	2900 GeV	1.358	-1.223	1.554	

Table 9: The benchmark point **DM1000$_{\mathbf{w95}}$** in the mass basis.

Benchmarks without a 95 GeV scalar

In the following, the interesting regions of parameter space without considering the 95 GeV excess are discussed.

- **DM70**: Again a low mass DM candidate is considered. However in this case, the focus is on a light scalar mediator h_3 which is singlet-dominated. In this case, the invisible branching ratios of the singlet-like mediator to a pair of DM particles are naturally large (close to 100%). Satisfying the observed DM relic density is easily achieved as well, especially close to the resonance region. The major annihilation channel is into a pair of gluons in this case. The gluons will further hadronize mostly into pions and and then finally lead to photons or charged leptons in the final state. The production of a singlet-dominated scalar state is challenging at future lepton colliders, because of the feeble coupling of the singlet to the gauge bosons. However, the lightness of the mass of the scalar h_3 (150 GeV) is kinematically advantageous in this benchmark, leading to its sufficient production cross section. Such scenarios may have good prospect at the LHC where GGF production dominates.

The parameters in the mass basis are provided in Table 10.

m_{h_1}	m_{h_2}	m_{h_3}	m_A	$m_{H^\pm}$
800 GeV	125.09 GeV	150 GeV	800 GeV	800 GeV
m_{A_S}	$\lambda_1' - 2\lambda_4'$	$\lambda_2' - 2\lambda_5'$	$\lambda_1'' - \lambda_3''$	$\tan\beta$
70 GeV	-0.10783	0.063127	-0.47818	1.3728
v_S	$\tilde{\mu}$	α_1	α_2	α_3
219.05 GeV	751.54 GeV	-0.60016	0.042445	-0.054807

Table 10: The benchmark point **DM70** in the mass basis.

- **DM400**: The next benchmark falls under the intermediate mass range category. The scalar mediator h_3 in this case is of 900 GeV and it is chosen to be singlet-dominated. Here too, a substantial invisible branching ratio is achievable along with the correct relic density. DM annihilation is dominated by the $t\bar{t}$ final state. On the other hand, the production at colliders is naturally challenging due to the singlet nature of the mediating scalar.

The parameters in the mass basis are provided in Table 11.

m_{h_1}	m_{h_2}	m_{h_3}	m_A	$m_{H^\pm}$
800 GeV	125.09 GeV	900 GeV	800 GeV	800 GeV
m_{A_S}	$\lambda_1' - 2\lambda_4'$	$\lambda_2' - 2\lambda_5'$	$\lambda_1'' - \lambda_3''$	$\tan\beta$
400 GeV	0.077784	0.036923	-0.42725	2.1309
v_S	$\tilde{\mu}$	α_1	α_2	α_3
587.17 GeV	755.39 GeV	-0.41245	-0.0086501	-0.0055431

Table 11: The benchmark point **DM400** in the mass basis.

- **DM1000**: Finally, a benchmark with heavy DM (1 TeV) is chosen as well as a heavy mediator h_3 (2.9 TeV). Interestingly, the other non-SM-like scalars, are at 800 GeV. Such a large mass-gap between the non-SM-like scalars is only possible because the heavy scalar is largely singlet-like in this case, the strong constraints from S, T, U parameters can be evaded. Achieving the observed DM relic density is possible in this scenario as well, but with a compromise on the invisible branching ratio. This benchmark has prospects to be discovered at high energy colliders. In this case, annihilation into a charged scalar and a pseudo-scalar opens up and dominates over other channels, owing to the mass hierarchy.

The parameters in the mass basis are provided in Table 12.

m_{h_1}	m_{h_2}	m_{h_3}	m_A	$m_{H^\pm}$
800 GeV	125.09 GeV	2900 GeV	800 GeV	800 GeV
m_{A_S}	$\lambda_1' - 2\lambda_4'$	$\lambda_2' - 2\lambda_5'$	$\lambda_1'' - \lambda_3''$	$\tan\beta$
1000 GeV	0.32873	0.21320	-0.41541	1.3414
v_S	$\tilde{\mu}$	α_1	α_2	α_3
2271.3 GeV	768.14 GeV	-0.54917	0.036530	-0.056095

Table 12: The benchmark point **DM1000** in the mass basis.

In order to summarise the various mass hierarchies pertaining to the chosen benchmarks, a schematic representation was provided above in Figure 21. Furthermore, an overview of the benchmarks including $\tan\beta$-values, corresponding DM observables as well as invisible branching ratios is presented in Table 13.

	$\tan\beta$	Ωh^2	$\sigma_{\mathrm{p}A_S}/\mathrm{pb}$	$\sigma_{\mathrm{n}A_S}/\mathrm{pb}$	$\sigma_{A_S A_S \to XX}/\frac{\mathrm{cm}^3}{\mathrm{s}}$	$BR(h_i \to A_S A_S)$		
						h_1	h_2	h_3
DM55$_{\mathbf{w95}}$	2	0.11	4.21×10^{-12}	4.08×10^{-12}	1.98×10^{-28}	-	0.0199	$3.81 \cdot 10^{-9}$
DM156$_{\mathbf{w95}}$	6.6	$1.61 \cdot 10^{-4}$	3.903×10^{-11}	4.160×10^{-11}	3.875×10^{-29}	-	-	0.692
DM1000$_{\mathbf{w95}}$	5	0.111	3.323×10^{-11}	3.369×10^{-11}	2.045×10^{-26}	-	-	0.0360
DM70	1.37	0.113	8.938×10^{-16}	2.651×10^{-13}	2.13×10^{-28}	$1.80 \cdot 10^{-4}$	-	0.999
DM400	2.13	0.106	4.960×10^{-11}	5.101×10^{-11}	3.67×10^{-26}	-	-	0.822
DM1000	1.34	0.117	8.263×10^{-11}	8.464×10^{-11}	2.018×10^{-26}	-	-	0.00514

Table 13: The benchmark points considered in this work. Shown are the values for $\tan\beta$, DM observables: relic density Ωh^2, direct detection cross section $\sigma_{\mathrm{p/n}A_S}$ for DM scattering on protons (p) and on neutrons (n), indirect detection cross section $\sigma_{A_S A_S \to XX}$ and the invisible branching ratios $BR(h_i \to A_S A_S)$, with $i = 1, 2, 3$, for the decays of the scalars h_1, h_2 and h_3 into two DM particles A_S. Decays which are kinematically not allowed are marked with a '-'. The direct and indirect detection cross sections are rescaled according to the relic density.

4.4.2 Search strategy for benchmark selection

This section describes how the benchmark points explained above were selected with respect to the DM phenomenology. In practice, first the regions of interest were identified, then detailed parameters scans were conducted within these regions and finally specific benchmark points, as given in Table 7 - 12, were chosen from these scans. As an example, the search strategy is explained for the benchmark point **DM400** below.

To find a benchmark point which has good prospects to be observed at a future collider a high invisible branching ratio (of one of the scalars, for example the heavy scalar h_3 to two DM particles A_S) is favourable. On the other hand, to explain the DM abundance in the Universe, the DM relic density should be close to the observed limit from the Planck collaboration. However, for the chosen model a high branching ratio and high relic density counteract each other in many of the chosen benchmark scenarios.

In the following this behaviour is shown and how benchmark points are selected using the example of a benchmark with intermediate DM mass, and not including the 95 GeV excess.

In order to find a suitable benchmark point, the first step was to randomly vary the parameters $\lambda'_{14} = \lambda'_1 - 2\lambda'_4$, $\lambda'_{25} = \lambda'_2 - 2\lambda'_5$, $\lambda''_{13} = \lambda''_1 - \lambda''_3$, v_S and $\tan\beta$ while fixing the masses of the scalar particles as for the point **DM400** in Table 11 and keeping the mixing angles α_1, α_2 and α_3 such that the scalar h_1 is singlet-dominated and h_2 and h_3 are doublet-dominated. (Note that the exact values as in Table 11 were not known before performing the scans. The point was selected from the results of these scans.) In Figure 22 one can see the invisible branching ratio (of the heavy scalar h_3 to two DM particles A_S) against the DM relic density.

As described above a higher branching ratio results in a lower relic density.

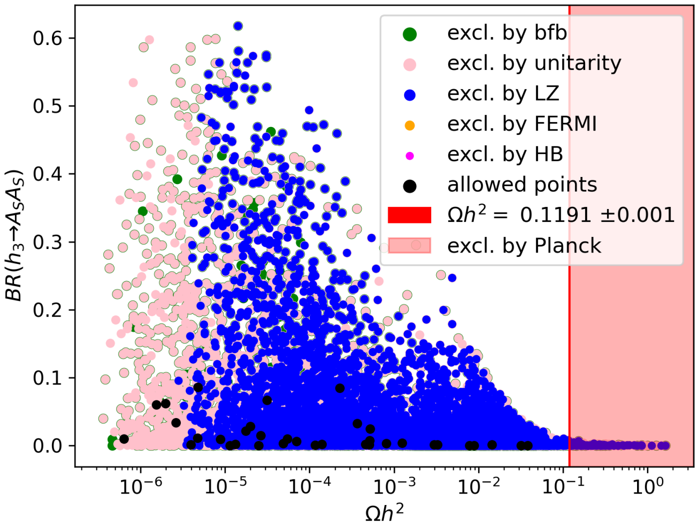

Figure 22: Invisible branching ratio $BR(h_3 \to A_S A_S)$ of the heavy scalar h_3 to two DM particles A_S against DM relic density Ωh^2 for randomly varying λ'_{14}, λ'_{25}, λ''_{13}, v_S and $\tan\beta$ around the region of **DM400**. The different constraints are shown by different colours. Please note that most points are excluded by more than one constraint, hence different point sizes were chosen to make overlapping constraints visible. The red line shows the relic density limit measured by Planck. Points in the red shaded area are above this limit and are excluded. The points passing all constraints are shown in black. [2]

Furthermore, there are strong constraints from LZ (blue), unitarity (light pink) and bfb (green). The points passing all constraints are shown in black and all lie in an area with low branching ratio.

In order to open up the area of high branching ratio and high relic density, also the scalar mixing angles α_1, α_2 and α_3 need to be varied. The results of this more elaborate scan can be see in Figure 23.

As can be seen now there are also strong constraints from HB (magenta). However, the new points split into two areas, one stretched along the x-axis with low branching ratio and one stretched along the y-axis with relic density around the limit from Planck. The splitting into these two areas results from the chosen scan regions for the mixing angles. With a different choice one could also fill the sparse white area with more points. The points passing all constraints are again shown in black. From these results the point **DM400** in Table 11 was selected.

To summarise the results one can say that, when only varying the coupling parameters λ'_{14}, λ'_{25} and λ''_{13}, branching ratio and relic density behave inversely. To find a point with high branching ratio and high relic density one needs to also vary the scalar mixing angles α_1, α_2 and α_3. Another conclusion is, that the allowed

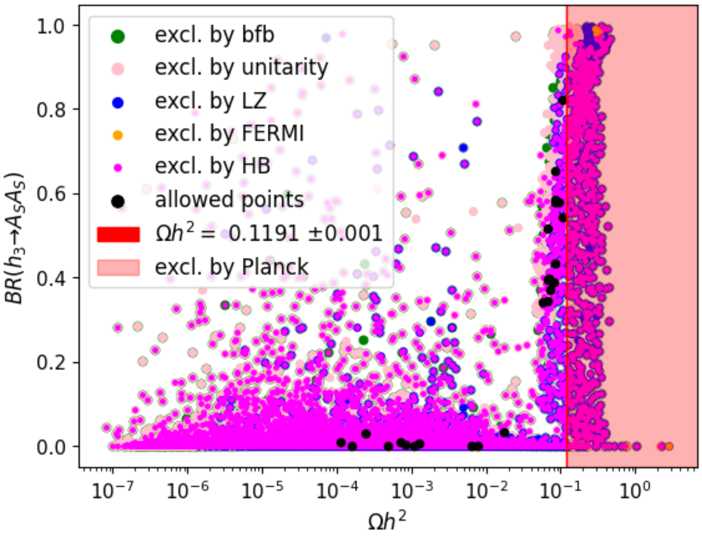

Figure 23: Invisible branching ratio $BR(h_3 \to A_S A_S)$ of the heavy scalar h_3 to two DM particles A_S against DM relic density Ωh^2 for randomly varying λ'_{14}, λ'_{25}, λ''_{13}, v_S, $\tan\beta$, $\tilde{\mu}^2$ and the scalar mixing angles α_1, α_2 and α_3 around the region of **DM400**. The different constraints are shown by different colours. Please note that most points are excluded by more than one constraint, hence different point sizes were chosen to make overlapping constraints visible. The red line shows the relic density limit measured by Planck. Points in the red shaded area are above this limit and are excluded. The points passing all constraints are shown in black. [2]

points (in black) which correspond to the observed relic density and also lead to a large invisible branching ratio of h_3, imply a combination of mixing angles, where h_3 is largely singlet-like. This is the scenario considered in **DM400** in Table 11.

4.4.3 Signals at future colliders and software used

Having identified interesting regions of parameter space in the 2HDMS, the next step is to probe such regions in future colliders. The focus lies on low, intermediate-range and high DM mass, as well as mediator mass (the scalar which acts as a portal between the DM candidate and SM particles), as discussed in the previous section. On the one hand, various possible final states are investigated, such as mono-photon (γ)+MET[5], mono-Z+MET, $b\bar{b}$+MET, $t\bar{t}$+MET. On the other hand, possibilities at various future colliders are considered, i.e. the hadron collider High-luminosity LHC (HL-LHC), e^+e^- colliders such as ILC, FCC-ee and CLIC, and finally a muon-collider.

---

[5] The term ‘MET’ is used in a generic sense in this work. At the LHC, MET is used to define missing transverse momenta. On the other hand, at lepton colliders, alongside missing transverse momenta, missing energy ($\not{E}$) and missing mass ($\not{M}$) also become important. Therefore, MET is used as a generic umbrella term to define all these quantities and the explicit definitions are presented specific to the particular collider and final state.

The LHC is currently in its Run 3 phase with centre-of-mass energy $\sqrt{s} = 13.6\,\text{TeV}$. Further upgrades to the high-luminosity run of the LHC [160], planned after Run 3, are set to further enhance the centre-of-mass energy up to $\sqrt{s} = 14\,\text{TeV}$ and the integrated luminosity up to $3000\,\text{fb}^{-1}$. Along with present Run 3 results and the future planned HL-LHC run, several New Physics models are expected to be constrained from experimental data. Further, upcoming lepton collider machines would also play a crucial role in looking for New Physics in potentially complimentary discovery channels. Lepton colliders would not only shed light on investigating indirect effects of New Physics via precision studies but also, via direct searches of new particles for high energy lepton colliders. Below some of the proposed upcoming high precision and high energy future lepton colliders are discussed.

The ILC [161–167], is a proposed linear e^+e^- collider with centre-of-mass energies in the range of $\sqrt{s} = 92$ and $250 - 550\,\text{GeV}$, which can be upgraded up to $\sqrt{s} = 1000$ GeV. The ILC provides a comprehensive and complementary physics potential [168] and an advantage over the HL-LHC due to its clean environment, high luminosity, tuneable energy as well as the possibility to apply precise and high polarisations of both the electron and positron beams. This not only leads to increased background suppression, higher rates and better control of systematics but also opens new windows in direct, as well as indirect searches for New Physics offering high precision measurements [161, 169]. Other proposed e^+e^- colliders are the CLIC [170, 171] with energy upgrades up to $\sqrt{s} = 1.5, 3\,\text{TeV}$, the Linear Collider Facility at CERN (LCF) [167, 172], the FCC-ee [173] with energy upgrades up to $\sqrt{s} = 350\,\text{GeV}$ and the CEPC [174] with energy upgrades up to $\sqrt{s} = 240\,\text{GeV}$.

A multi-TeV circular muon collider [175] is also proposed to be built with centre-of-mass energies $\sqrt{s} = 3$ and $10\,\text{TeV}$ with target integrated luminosity up to $\mathcal{L} = 10\,\text{ab}^{-1}$ [176]. While providing a cleaner environment compared to hadron machines, it also provides access to higher centre-of-mass energies, thereby extending the reach for New Physics searches. Besides, the enhanced muon Yukawa coupling compared to electron Yukawa coupling significantly enhances production cross sections of beyond-the-Standard-Model (BSM) particles compared to electron-positron colliders, especially in the context of models with extended scalar sectors. Beam polarisation may also be useful for a muon collider [177, 178], but since polarised muon beams are not yet foreseen in the current design, the focus lies on unpolarised muon beams for the present study.

In this work, the prospects of new physics searches for the 2HDMS in the high-luminosity LHC, electron-positron colliders and muon colliders are studied in the following subsections.

A detailed comparison between future colliders is presented in terms of probing various benchmark scenarios. Furthermore, complimentarity between various colliders as well as different final states is established. The parton-level events are generated at $\sqrt{s} = 14\,\text{TeV}$ using `MadGraph MG5_aMC_v3.4.1` [179, 180] followed by showering and hadronization using `Pythia_v8.3.06` [181], where the default parton distribution function `NNPDF2.3`[182] was used. The detector simulation for the hadron level events is performed using the fast detector simulator `Delphes-v3.5.0` [183]. The signal analyses at LHC have been performed using `MadAnalysis-v5` [184]. The signal processes are generated in `WHIZARD-v3.1.5` [185] for the e^+e^- and $\mu^+\mu^-$ collider studies.

4.4.4 Benchmarks at LHC

For the SM-like Higgs boson with a mass of 125 GeV at the LHC, the dominant production processes are GGF and VBF. For heavy scalar Higgs bosons, the associated production with $b\bar{b}$ (BBH) dominates both GGF and VBF for certain parameter regions due to the $\tan\beta$ enhancement of the bottom quark Yukawa coupling. Figure 16 shows the Feynman diagrams for GGF, VBF and BBH processes, respectively. For BBH, both four-flavour and the dominant five-flavour contributions are considered and the Santander matching [186] is performed with the matched cross section defined as a weighted average of the four- and five-flavour cross sections. The cross section then reads:

$$\sigma^{w_i} = \frac{\sigma^{4f} + w_i \sigma^{5f}}{1 + w_i}, \tag{4.31}$$

where $w_i = ln(\frac{m_{h_i}}{m_b}) - 2$, with $i = 1,2,3$. The production cross section of the Higgs bosons, with the Higgs decaying invisibly are presented in Table 14 and 15 for the light, intermediate-range and heavy benchmarks, respectively.

Process	Production cross section (fb) at $\sqrt{s} = 14\,\text{TeV}$		
	DM55$_{\mathbf{w95}}$	**DM156$_{\mathbf{w95}}$**	**DM70**
GGF($h_2 \to A_S A_S$)	533.9	-	19.29×10^3
GGF($h_3 \to A_S A_S$)	-	0.015	-
VBF($h_2 \to A_S A_S$)	54.33	-	2.72×10^3
VBF($h_3 \to A_S A_S$)	-	0.134	0.0022
BBH($h_2 \to A_S A_S$)	21.6	-	0.137
BBH($h_3 \to A_S A_S$)	-	47.24	-

Table 14: The production cross sections at leading order (LO) for the relevant processes at $\sqrt{s} = 14\,\text{TeV}$ at LHC. All cross sections below 10^{-6} fb are denoted by '-'. For BBH the Santander matched cross section is used as defined in the text.

For the light DM benchmark point, **DM55$_{\mathbf{w95}}$** the relevant scalar decaying into DM particles is the SM-like Higgs boson. Hence the dominant production processes

Process	Production cross section (fb) at $\sqrt{s} = 14\,\text{TeV}$		
	DM400	**DM1000**	**$\mathbf{DM1000_{w95}}$**
GGF($h_3 \to A_S A_S$)	0.013	6.35×10^{-7}	4.5×10^{-6}
VBF($h_3 \to A_S A_S$)	0.0008	-	-
BBH($h_3 \to A_S A_S$)	0.007	-	-

Table 15: The production cross sections at leading order (LO) for the relevant processes at $\sqrt{s} = 14\,\text{TeV}$ at LHC. All cross sections below $10^{-6}\,\text{fb}$ are denoted by '-'. For BBH the Santander matched cross section is used as defined in the text.

are GGF and VBF. While **$\mathbf{DM55_{w95}}$** has an invisible branching ratio of $\sim 2\%$, the cross section is appreciable. For **DM70** the singlet dominated scalar with a mass of $m_{h_3} = 150\,\text{GeV}$ almost always decays invisibly (99%) (meaning into a pair of DM particles). Despite the singlet admixture, the cross section for the production of h_3 using GGF in **DM70** is appreciable and benefits from the large invisible branching ratio which otherwise suppresses the cross section for **$\mathbf{DM55_{w95}}$**.

For the intermediate benchmark **$\mathbf{DM156_{w95}}$** the dominant processes for the production of the heavy scalar h_3 invisibly decaying into a pair of DM candidates are mainly from $b\bar{b}h_3$ which may benefit from the increase in the Yukawa coupling of the b-quark via its dependence on β for large values of $\tan\beta$ [105]. While this process is suppressed for the SM-like Higgs boson production, it may be comparable or even larger than traditional production channels, such as GGF or VBF and could be an alternative channel of discovery for heavy Higgs boson searches in Type II 2HDM.

The production cross sections for the intermediate and heavy benchmark points are shown in Table 15. For the intermediate DM benchmark **DM400**, the mass of the heavy scalar $m_{h_3} = 900\,\text{GeV}$, which dominantly decays invisibly, the dominant contribution to the production mainly arises from GGF owing to the heavy mass of the scalar while BBH and VBF are sub-dominant contributions. For the heavier DM benchmarks **$\mathbf{DM1000_{w95}}$** and **DM1000** with a heavy scalar such that $m_{h_3} = 2900\,\text{GeV}$, the production cross sections for GGF, VBF and BBH are shown in Table 15. The production cross section greatly suffers owing to the heavy mass of the scalar particle $m_{h_3} = 2900\,\text{GeV}$ and therefore does not produce an observable number of events at $\mathcal{L} = 3000\,\text{fb}^{-1}$. Such scenarios are beyond the reach of the HL-LHC. However, such benchmarks have a larger production cross section at a higher $\sqrt{s}$ such as at future hadron colliders like FCC-hh or the Super Proton–Proton Collider (SPPC) at $\sqrt{s} = 100\,\text{TeV}$ as will be discussed later in subsection 4.4.7.

The possible final states at LHC for this scenario are:

- Mono-jet + $\not{E}_T$,

- Two forward jets + $\not{E}_T$,
- Two b-jets + $\not{E}_T$.

Each of the final states from the production channels GGF, VBF and BBH is discussed in the following subsections. The prospective signals are studied at the LHC at $\sqrt{s} = 14\,\mathrm{TeV}$ with an integrated luminosity of $\mathcal{L} = 3000\,\mathrm{ab}^{-1}$.

Gluon-gluon fusion

In this paragraph the final state mono-jet+MET from the GGF production channel is considered. For the collider analyses the following cuts [187] are used:

- **C1**: The final state consists of up to four jets with $p_T > 30\,\mathrm{GeV}$ and $|\eta| < 2.8$,
- **C2**: Large MET is demanded, $\not{E}_T > 250\,\mathrm{GeV}$,
- **C3**: The hardest leading jet has $p_T > 250\,\mathrm{GeV}$ with $|\eta| < 2.4$,
- **C4**: $\Delta\Phi(j, \not{E}_T) > 0.4$ for all jets and $\Delta\Phi(j, \not{E}_T) > 0.6$ for the leading jet is demanded,
- **C5**: A lepton-veto is imposed for electrons with $p_T > 20\,\mathrm{GeV}$ and $|\eta| < 2.47$ and muons with $p_T > 10\,\mathrm{GeV}$ and $|\eta| < 2.5$.

The SM background of 7.07 pb is obtained from the mono-jet + $\not{E}_T$ search studied in Ref. [108].

The signal significance for GGF is shown in Table 16, using a K-factor of 1.91 (at Next-to-next-to-leading order (NNLO) plus Next-to-next-to-leading logarithmic (NNLL)). Only benchmarks which are sensitive at HL-LHC with significance at least greater than $0.05\,\sigma$ are listed. While both the light DM benchmarks have appreciable cross sections at LHC, their significance suffers due to the high-p_T cuts as in usual mono-jet searches at LHC.

Benchmark	Significance
DM55$_{\mathbf{w95}}$	$0.30\,\sigma$
DM70	$0.55\,\sigma$

Table 16: The signal significance from GGF for HL-LHC at an integrated luminosity of $3000\,\mathrm{fb}^{-1}$, for the benchmarks sensitive to this process.

Vector boson fusion

Now the final state with two forward-jets+MET from the VBF production channel is considered. For the collider analyses the following cuts [188] are used:

- **D1**: The final state consists of at least two jets with $p_T(j_1) > 80\,\text{GeV}$ and $p_T(j_2) > 40\,\text{GeV}$ and $\Delta\Phi(j_i, \not{E}_T) > 0.5$,
- **D2**: $\eta(j_1 j_2) < 0$ and $\Delta\Phi j_1 j_2 < 1.5$ is demanded,
- **D3**: $|\Delta\eta|_{jj} > 3.0$ is demanded,
- **D4**: The invariant mass of the two forward jets is required to be large, $M_{jj} > 600\,\text{GeV}$,
- **D5**: $\not{E}_T > 200\,\text{GeV}$ is demanded,
- **D6**: Furthermore, a lepton veto is imposed for electrons with $p_T > 20\,\text{GeV}$ or muons with $p_T > 10\,\text{GeV}$.

The signal significance for VBF is shown in Table 17, using a K-factor of 1.73 (NLO QCD + NLL). The VBF process, as can be seen, is only sensitive for **DM70** with nearly 2σ excess at HL-LHC.

Benchmark	Significance
DM70	$1.94\,\sigma$

Table 17: The signal significance from VBF for HL-LHC at an integrated luminosity of 3000 fb^{-1}, for the benchmarks sensitive to this process.

$b\bar{b}$-Higgs associated production

As next case, the associated production channel of a scalar Higgs boson along with $b\bar{b}$ is discussed, namely the BBH process, for $\mathbf{DM156_{w95}}$ with the heavy scalar decaying invisibly into a pair of DM candidates. The matched cross section for this process is estimated using Santander matching as discussed above. For $\mathbf{DM156_{w95}}$ the mass of the heavy scalar is 700 GeV and the mass of the DM candidate is 156 GeV. The heavy scalar decays into a pair of DM particles with a branching ratio of 69%. This high invisible branching ratio in combination with the large production cross section may yield a significant number of signal events at the HL-LHC. The prospects of the final state $b\bar{b}$+MET is studied at $\sqrt{s} = 14\,\text{TeV}$. Dominant SM backgrounds to this final state arise from $t\bar{t}$, Z+jets, $b\bar{b}Z$, $Z(\to \nu\bar{\nu})h$, semi-leptonic $Z(\to b\bar{b})Z(\to \nu\bar{\nu})$ and $b\bar{b}\nu\bar{\nu}$. The dominant SM backgrounds are generated with a MET cut of 100 GeV

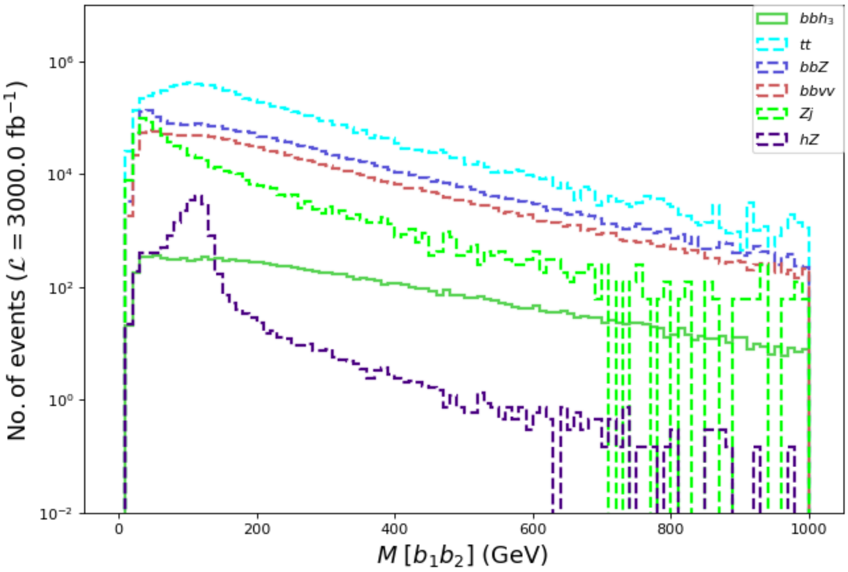

Figure 24: The distribution for the invariant mass of the $b\bar{b}$ pair for the two b-jets+MET $> 100\,\mathrm{GeV}$ (with photon and lepton veto) final state for the benchmark $\mathbf{DM156_{w95}}$ and dominant SM backgrounds, before applying further analyses cuts. [2]

in order to tame the production cross section. The distribution for the invariant mass $M(b_1 b_2)$ with two b-jets in the final state is presented in Figure 24. While the SM backgrounds from Higgs and Z-bosons typically have a peak at lower values of $M(b_1 b_2)$ the signal has a longer tail. Keeping this in mind, the following cuts are utilised to separate the signal from the background.

- **E1**: The final state consists of two b-jets and no photons or leptons. $\Delta R(b_1, b_2) > 0.4$, $p_T(b_1) > 150\,\mathrm{GeV}$ and $p_T(b_2) > 100\,\mathrm{GeV}$ are demanded,
- **E2**: A large MET $\not{E}_T > 200\,\mathrm{GeV}$ is demanded to reduce the SM background,
- **E3**: $M(b\bar{b}) > 200\,\mathrm{GeV}$ is demanded to reduce the SM background contributions.

In Table 18 the cross sections are presented after imposing the cuts for the BBH channel for $\mathbf{DM156_{w95}}$ and the dominant SM background.

The matched BBH channel for $\mathbf{DM156_{w95}}$ at the LHC was found to have a significance $\sim 2.65\sigma$ at LO at the HL-LHC. Using a higher-order K-factor of 1.94 for $t\bar{t}$ to match the predicted cross section at $\sqrt{s} = 14\,\mathrm{TeV}$ [189], 1.76 for $b\bar{b}Z$ [179] and $b\bar{b}\nu\bar{\nu}$ and an approximate K-factor of 1.2 for the processes Z+jet and hZ, where h is the SM-like Higgs boson, a total background cross section of $\sim 100\,\mathrm{fb}$ is obtained which reduces the signal significance to 1.95σ for the LO signal cross section. Thus,

Benchmark	Cross section after cuts (fb)
$\mathbf{DM156_{w95}}$	0.357
SM Background	
$b\bar{b}Z$	18.3
$b\bar{b}\nu\bar{\nu}$	13.46
$t\bar{t}$	66.46
$Z+j$	2.04
hZ	0.012
Total Background	100.27

Table 18: The cross sections for the signal and SM backgrounds after applying the cuts **E1-E4** as discussed in the text for signal-background distinction for BBH for HL-LHC at an integrated luminosity of $3000\,\text{fb}^{-1}$.

Benchmark	Significance
$\mathbf{DM156_{w95}}$	$1.95\,\sigma$

Table 19: The signal significance from BBH for HL-LHC at an integrated luminosity of $3000\,\text{fb}^{-1}$, for the benchmarks sensitive to this process.

it is observed that, while GGF and VBF are popular channels for heavy Higgs boson searches, BBH also is a competitive channel compared to VBF at HL-LHC as is the case here for $\mathbf{DM156_{w95}}$.

Future hadron colliders such as the proposed FCC-hh/SPPC to run at $\sqrt{s} = 100\,\text{TeV}$ may further enhance the discovery potential of this scenario especially for the heavy benchmarks **DM400**, $\mathbf{DM1000_{w95}}$ and **DM1000**. The discussion for these benchmarks at FCC-hh/SPPC is deferred to subsection 4.4.7. The signal cross sections for a $\sqrt{s} = 100\,\text{TeV}$ collider like FCC-hh/SPPC are presented in Table 20. One can clearly see the prospects of improvement of the GGF, VBF and BBH signals for the benchmarks $\mathbf{DM55_{w95}}$, $\mathbf{DM156_{w95}}$ and **DM70** at FCC-hh/SPPC at $\sqrt{s} = 100\,\text{TeV}$. From Table 20 an increase in the production cross sections is observed at FCC-hh/SPPC by a factor of 100-1000 over LHC and thus channels for heavy Higgs searches are favourable at FCC-hh/SPPC.

Besides LHC, the focus will be on future lepton colliders i.e. ILC and a muon collider as two possible future options, as will be discussed in the following subsections. However, these results can be used in the context of other lepton colliders as well, as demonstrated shortly.

Process	Production cross section (fb) at $\sqrt{s} = 100$ TeV		
	DM55$_{\mathbf{w95}}$	**DM156**$_{\mathbf{w95}}$	**DM70**
GGF$(h_2 \to A_S A_S)$	10.1×10^5	-	4.09×10^5
GGF$(h_3 \to A_S A_S)$	-	1.596	-
VBF$(h_2 \to A_S A_S)$	5.97×10^2	-	81.87
VBF$(h_3 \to A_S A_S)$	-	3.12	-
BBH$(h_2 \to A_S A_S)$	6.43×10^2	-	17.2×10^3
BBH$(h_3 \to A_S A_S)$	-	5.00	-

Table 20: The production cross sections at leading order (LO) for the relevant processes at $\sqrt{s} = 100$ TeV. All cross sections below 10^{-6} fb are denoted by '-'. For BBH the Santander matched cross section is used as defined in the text.

4.4.5 Benchmarks at electron-positron colliders

First the discovery prospects at e^+e^- colliders are discussed, i.e. at ILC, CEPC, CLIC and FCC-ee. Following ILC-TDR [161], three different centre-of-mass energies, $\sqrt{s} = 250$ GeV, 500 GeV and 1 TeV are considered for a comparative analysis. On the other hand, the design energy for CLIC is 3 TeV [170]. First the production cross sections for several benchmarks in different final states are show in Figure 25. It is clear from Figure 25, that for low DM mass benchmarks namely **DM55**$_{\mathbf{w95}}$ and **DM70**, the largest cross sections pertain to the mono-Z final state at e^+e^- colliders. Furthermore, the cross sections peak at the lowest value $\sqrt{s} = 250$ GeV for both aforementioned benchmarks.

Benchmark	Production cross section (fb)		
	at $\sqrt{s} = 250$ GeV	at $\sqrt{s} = 500$ GeV	at $\sqrt{s} = 1$ TeV
DM55$_{\mathbf{w95}}$	4.42	1.1	0.24
DM70	0.33	0.15	0.035
$\nu\bar{\nu}Z$ background	503	491	950

Table 21: The Production cross sections for signal (for **DM55**$_{\mathbf{w95}}$ and **DM70**) and background ($\nu\bar{\nu}Z$) for Z+MET final state at a $\sqrt{s} = 250$ GeV, 500 GeV and 1 TeV e^+e^- collider.

In case of **DM55**$_{\mathbf{w95}}$, the major production of DM at an e^+e^- machine is via the Higgsstrahlung process and further decay of the SM-like 125 GeV Higgs boson into a pair of DM particles. Therefore, Z+MET final states are considered to probe this scenario. The invisible branching ratio of the SM-like 125 GeV Higgs boson h_2 is 1.99% (see Table 13). Further, the benchmark **DM70** is examined, where the pair of DM particles results from a light singlet-like non-SM-like scalar (150 GeV), following Higgsstrahlung production of the mentioned scalar. The corresponding

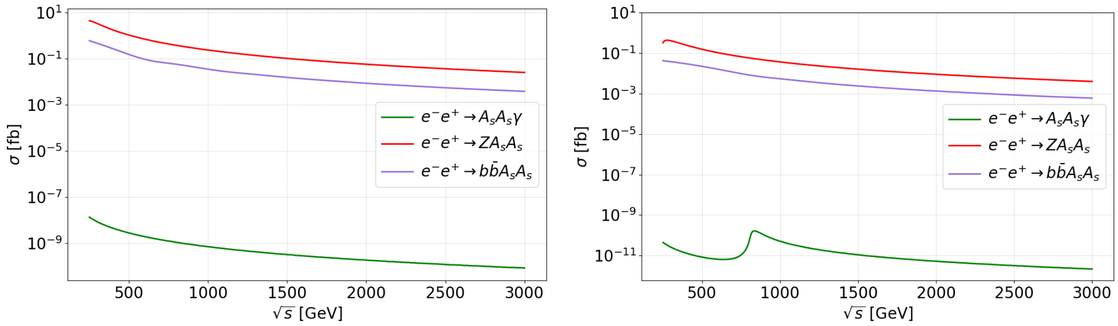

(a) $\mathbf{DM55_{w95}}$ (b) **DM70**

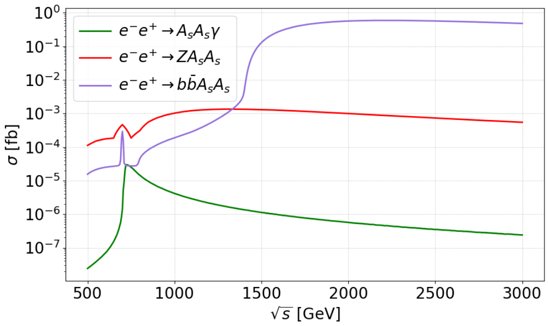

(c) $\mathbf{DM156_{w95}}$

Figure 25: Variation of the production cross section against $\sqrt{s}$ for the final states $A_sA_s\gamma$, ZA_sA_s, and $b\bar{b}A_sA_s$ at e^+e^- colliders, computed using `WHIZARD` [185] for different benchmark points. [2]

invisible branching ratio is almost 100%.

The production cross section of the Z+MET final state is presented in Table 21 at different $\sqrt{s}$ for both benchmarks. The major background corresponding to the Z+MET state comes from the $\nu\bar{\nu}Z$ final state.

For the signal-background analysis the most sensitive kinematic observable, the missing mass ($\not{M}$) is examined which is defined as follows:

$$\not{M}^2 = (p_{in} - p_{out})^2, \tag{4.32}$$

where p_{in} corresponds to incoming four-momenta and p_{out} corresponds to outgoing four-momenta of visible final states.

The analysis found that $\not{M}$ provides the best discrimination between signal and backgrounds. Therefore, the signal and background distribution is shown for this variable for the benchmarks $\mathbf{DM55_{w95}}$ and **DM70** and for backgrounds. For the benchmarks, $\not{M}$ peaks at the mass of the scalar, which decays into a pair of DM

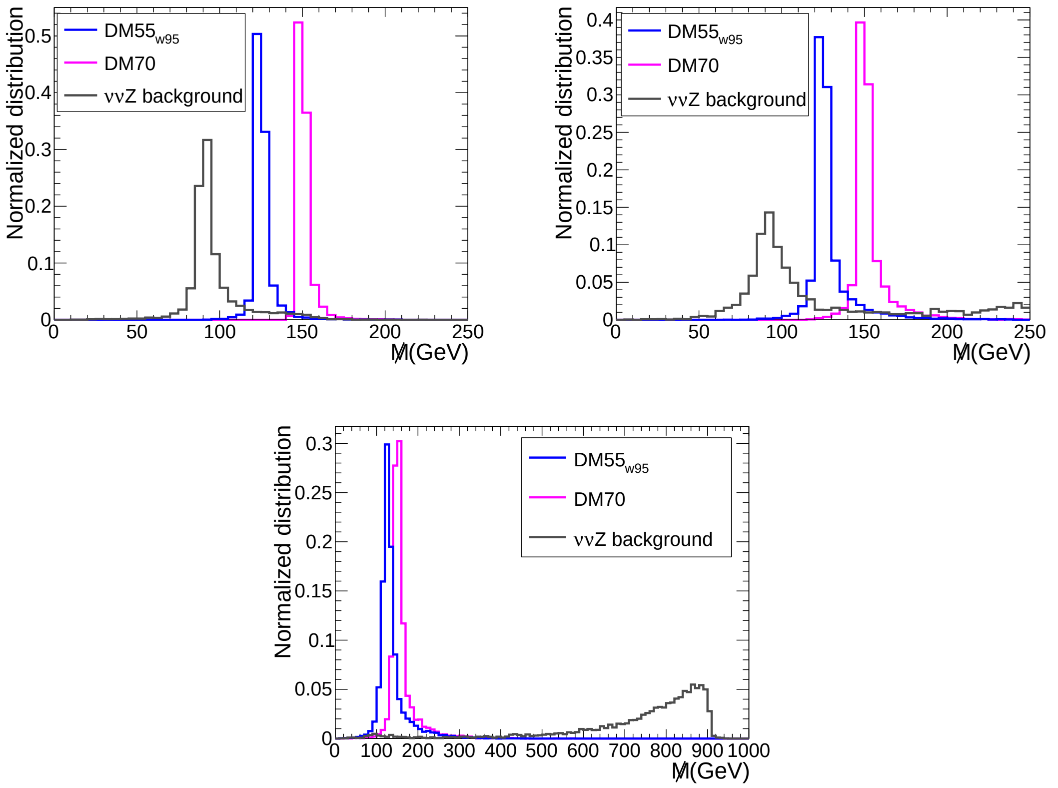

Figure 26: Distribution of missing mass $\not{M}$ for signal (for $\mathbf{DM55_{w95}}$ and **DM70**) and background ($\nu\bar{\nu}Z$) for Z+MET final state at a $\sqrt{s} = 250\,\text{GeV}$ (top left), $\sqrt{s} = 500\,\text{GeV}$ (top right) and $\sqrt{s} = 1\,\text{TeV}$ (bottom) e^+e^- collider. [2]

particles. On the other hand, at low $\sqrt{s}$, the major background contribution comes from the resonant $ZZ(\nu\bar{\nu})$ final state, and therefore $\not{M}$ peaks at the Z mass (see Figure 26 top left and top right). At higher $\sqrt{s}$, the dominant contribution to the background comes from the non-resonant $\nu\bar{\nu}Z$ final state, and as a result, $\not{M}$ peaks at a larger value (see Figure 26 bottom centre).

One can infer from Figure 26 and Table 21 that, at low $\sqrt{s}$, the event rate is larger, but the signal-background separation is best at higher $\sqrt{s}$. The signal significance for the two benchmarks $\mathbf{DM55_{w95}}$ and **DM70** is presented in Table 22. It is worth emphasising that the low mass DM is best probed with the mono-Z final state owing to a substantial event rate via Higgsstrahlung. Furthermore, low $\sqrt{s}$ is favoured in this context. Therefore, such low mass DM scenarios are best probed at e^+e^- colliders, namely at ILC, FCC-ee or CEPC at $\sqrt{s} = 250\,\text{GeV}$.

4.4.6 Benchmarks at a muon collider

In this section, the focus lies on the dominant channels for the study of the DM candidate at a muon collider for the chosen benchmarks, as shown in Figure 27. It is

Benchmark	$\sqrt{s}$	Cut	Significance
$\mathbf{DM55_{w95}}$	250 GeV	$\not{M} > 100\,\text{GeV}$	$11\,\sigma$ ($1\,\text{ab}^{-1}$)
DM70	250 GeV	$\not{M} > 130\,\text{GeV}$	$3\,\sigma$ ($3\,\text{ab}^{-1}$)
$\mathbf{DM55_{w95}}$	500 GeV	$\not{M} > 100\,\text{GeV}$ and $\not{M} < 150\,\text{GeV}$	$3.6\,\sigma$ ($1\,\text{ab}^{-1}$)
DM70	500 GeV	$\not{M} > 140\,\text{GeV}$ and $\not{M} < 190\,\text{GeV}$	$1.5\,\sigma$ ($3\,\text{ab}^{-1}$)
$\mathbf{DM55_{w95}}$	1 TeV	$\not{M} > 120\,\text{GeV}$ and $\not{M} < 250\,\text{GeV}$	$2.4\,\sigma$ ($3\,\text{ab}^{-1}$)
DM70	1 TeV	$\not{M} > 120\,\text{GeV}$ and $\not{M} < 250\,\text{GeV}$	$0.36\,\sigma$ ($3\,\text{ab}^{-1}$)

Table 22: The signal significance (for $\mathbf{DM55_{w95}}$ and **DM70**) for Z+MET final state at a $\sqrt{s} = 250\,\text{GeV}$, $500\,\text{GeV}$ and $1\,\text{TeV}$ e^+e^- collider.

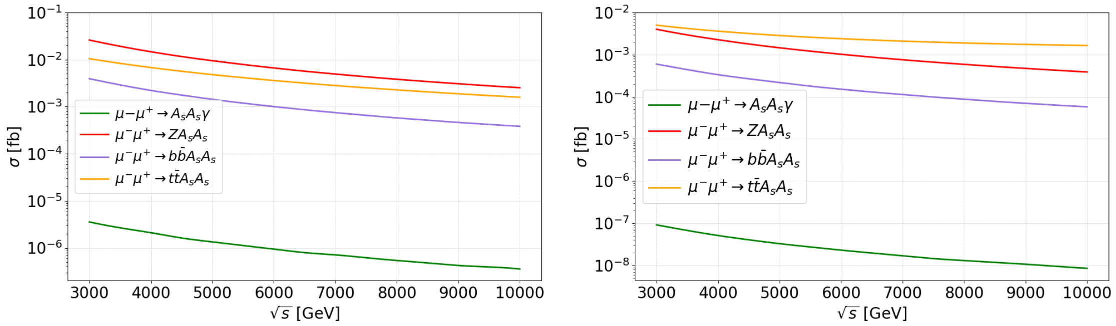

(a) $\mathbf{DM55_{w95}}$ (b) **DM70**

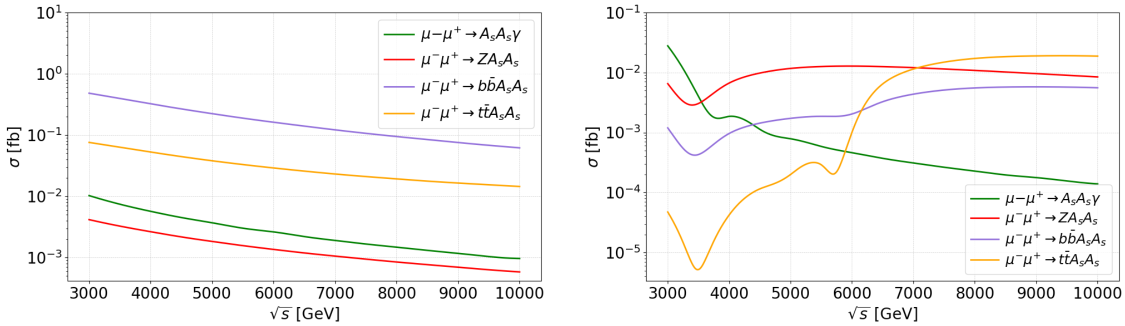

(c) $\mathbf{DM156_{w95}}$ (d) $\mathbf{DM1000_{w95}}$

Figure 27: Variation of the production cross section against $\sqrt{s}$ for the final states $A_sA_s\gamma$, ZA_sA_s, $b\bar{b}A_sA_s$, and $t\bar{t}A_sA_s$ at a muon collider, computed using `WHIZARD` [185] for different benchmark points. [2]

worth mentioning that the conventionally favoured VBF final state at a high energy muon collider is sub-leading for the chosen benchmarks. Furthermore, charged Higgs boson final states where the DM candidate comes from the cascade decay ($H^\pm \to h_iW^\pm, h_i \to A_SA_S$) are also suppressed in this case.

The possibility of probing $\mathbf{DM156_{w95}}$ at a muon collider is explored first. It is clear from Figure 27, that this scenario can be probed best, at a muon collider, in the final state where DM particles are pair-produced in association with $b\bar{b}$. The cross section for the signal is largest ($\approx 0.5\,\text{fb}$) at $\sqrt{s} = 3\,\text{TeV}$. The SM background contribution is considered in the $b\bar{b}\nu\bar{\nu}$ as well as $t\bar{t}$ final state. The total background cross section amounts to 800 fb. Two b-tagged jets are demanded in the final state for the analysis selection and the invariant mass distribution of the b-jet pair is investigated. This variable offers significant signal background separation (see Figure 28). After applying a suitable cut on this variable, a signal significance of $6.3\,\sigma$ can be achieved at an integrated luminosity of $3\,\text{ab}^{-1}$.

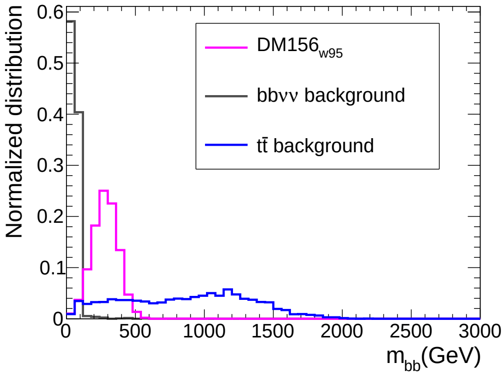

Figure 28: Distribution of invariant mass m_{bb} of a b-jet pair for signal (for $\mathbf{DM156_{w95}}$) and background ($b\bar{b}\nu\bar{\nu}$ and $t\bar{t}$) for $b\bar{b}$+MET final state at a $\sqrt{s} = 3\,\text{TeV}$ muon collider. [2]

Benchmark	Production cross section (fb)	
	at $\sqrt{s} = 3\,\text{TeV}$	at $\sqrt{s} = 10\,\text{TeV}$
$\mathbf{DM156_{w95}}$	0.48	0.063
$b\bar{b}\nu\nu$ background	758	1.3
$t\bar{t}$ background	20	1.7

Table 23: The Production cross section for signal (for $\mathbf{DM156_{w95}}$) and background ($b\bar{b}\nu\nu$ and $t\bar{t}$) for $b\bar{b}$+MET final state at a $\sqrt{s} = 3\,\text{TeV}$ and 10 TeV muon collider.

Benchmark	Cut	Significance
$\mathbf{DM156_{w95}}$	$100\,\text{GeV} < m_{bb} < 500\,\text{GeV}$	$6.3\,\sigma$ ($3\,\text{ab}^{-1}$)

Table 24: The Signal significance and corresponding cuts (for $\mathbf{DM156_{w95}}$) for $b\bar{b}$+MET final state at a $\sqrt{s} = 3\,\text{TeV}$ muon collider.

It is worth emphasising another interesting point. The analysis for $\mathbf{DM156_{w95}}$ at a muon collider is performed at $\sqrt{s} = 1\,\text{TeV}$. Although, the design energy for a muon collider starts at 3 TeV [175], the physics case at $\sqrt{s} = 1\,\mathrm{TeV}$ is investigated here. There is a possibility that a 1 TeV muon collider will have a stronger physics case compared to ILC or CLIC operating at 1 TeV. Here such an example is presented. The reason behind this are larger muon-Yukawa couplings compared to electron-Yukawa couplings. Owing to this significant enhancement, one can achieve substantial production cross sections (at least four orders of magnitude larger than at the e^+e^- collider [1]) in the mono-photon+MET final state, mediated via s-channel h_3 production at a muon collider.

Keeping this fact in mind the detection prospects of $\mathbf{DM156_{w95}}$ presented are at a muon-collider at 1 TeV in the mono-photon final state. The signal and background production cross sections are presented in Table 25. The missing-mass $\not{M}$ is found to offer best separation between signal and background. The distribution is presented in Figure 29. Choosing suitable cuts on this variable, an appreciable detection prospects for this benchmark is achieved, which can be seen in Table 26.

Benchmark	Production cross section (fb) at $\sqrt{s} = 1\,\mathrm{TeV}$
$\mathbf{DM156_{w95}}$	0.23
$\nu\nu\gamma$ background	2.45

Table 25: The Production cross section for signal (for $\mathbf{DM156_{w95}}$) and background ($\nu\nu\gamma$) for γ+MET final state at a $\sqrt{s} = 1\,\mathrm{TeV}$ muon collider.

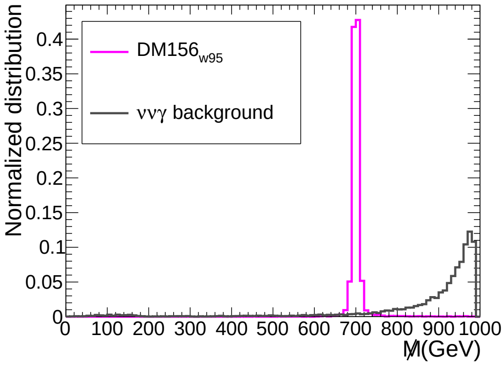

Figure 29: Distribution of missing mass $\not{M}$ for signal ($\mathbf{DM156_{w95}}$) and background ($\nu\nu\gamma$) for γ+MET final state at a $\sqrt{s} = 1\,\mathrm{TeV}$ muon collider. [2]

The motivation for this particular study may not be practical from the perspective of the current experimental designs of future colliders. However, as stated before, a muon collider at $\sqrt{s} = 1\,\mathrm{TeV}$ can be beneficial for specific regions of parameter space compared to e^+e^- colliders of the same $\sqrt{s}$. Furthermore, in the context of a muon collider, the mono-photon final state at $\sqrt{s} = 1\,\mathrm{TeV}$ can provide a good hint for the DM signal.

Benchmark	Cut	Significance
$\mathbf{DM156_{w95}}$	690 GeV $< \not{M} <$ 710 GeV	3σ ($3\,\mathrm{ab}^{-1}$), 5.3σ ($10\,\mathrm{ab}^{-1}$)

Table 26: The Signal significance and corresponding cuts (for $\mathbf{DM156_{w95}}$) for γ+MET final state at a $\sqrt{s} = 1$ TeV muon collider.

Benchmark	Production cross section (fb) at $\sqrt{s} = 10$ TeV
$\mathbf{DM1000_{w95}}$	0.027
SM $t\bar{t}$ background	1.66

Table 27: The Production cross section for signal ($\mathbf{DM1000_{w95}}$) and background ($t\bar{t}$) for $t\bar{t}$+MET final state at a $\sqrt{s} = 10$ TeV muon collider.

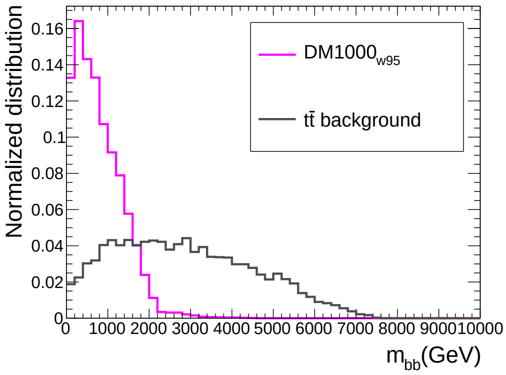

Figure 30: Distribution of invariant mass m_{bb} of a b-jet pair for signal ($\mathbf{DM1000_{w95}}$) and background (SM $t\bar{t}$) for $t\bar{t}$+MET final state at a $\sqrt{s} = 10$ TeV muon collider. [2]

Finally, the benchmark in the heavy mass region $\mathbf{DM1000_{w95}}$ is considered. Here the DM candidate is of 1 TeV mass, and the non-SM-like scalars h_3, A and $H^{\pm}$ are at 2.9 TeV. The production cross section of such a benchmark across various $\sqrt{s}$ is presented in Figure 27. One can see that the best prospects for this benchmark are at the high energy muon collider i.e. at $\sqrt{s} = 10$ TeV. And the most suitable channel in this case turns out to be pair-produced DM in association with $t\bar{t}$. The major reason behind this is the considerable branching ratio of h_3 to $t\bar{t}$. However, the large branching ratio of $t\bar{t}$ naturally leads to a somewhat reduced invisible branching ratio of h_3. In the performed scan, the largest invisible branching ratio was found to be of $\lesssim 21\%$. However, the large branching ratio of h_3 to $t\bar{t}$ fairly compensates for this when looking at the $t\bar{t}$+MET final state. The major SM background in this case is the SM $t\bar{t}$ process. The signal and background cross sections are presented in Table 27. One may note the generic feature in Figure 25 and 27, that there is an s-channel resonant enhancement when $\sqrt{s}$ is in the vicinity of the mediator mass, resulting in a peak. At higher $\sqrt{s}$ the t-channel processes start to dominate and

Benchmark	Cut	Significance
$\mathbf{DM1000_{w95}}$	$m_{bb} < 2\,\mathrm{TeV}$	2.9σ $(10\,\mathrm{ab}^{-1})$

Table 28: The Signal significance and corresponding cuts (for $\mathbf{DM1000_{w95}}$) for $t\bar{t}$+MET final state at a $\sqrt{s} = 10\,\mathrm{TeV}$ muon collider.

the production cross section rises again (see, in particular, the $b\bar{b}$ and $t\bar{t}$ associated production).

Finally, the invariant mass of a $b\bar{b}$ pair is shown for signal and background in Figure 30. Since in case of the signal the $b\bar{b}$ pair comes from a $t\bar{t}$ pair from the decay of h_3, they are relatively close, whereas in case of the $t\bar{t}$ background, the two b-quarks come from a $t\bar{t}$ pair, which are back-to-back. This leads to a larger invariant mass of the $b\bar{b}$ pair in case of the background compared to the signal. After choosing a suitable cut on the invariant mass, a signal significance of $\sim 3\sigma$ is achieved (see Table 28).

4.4.7 Challenging scenarios

Having discussed benchmark regions which can possibly be probed at HL-LHC and future lepton colliders, in this section the attention is shifted to the scenarios which are extremely difficult to probe at future colliders.

Final state	Production cross section (fb) at a muon collider	
	at $\sqrt{s} = 3\,\mathrm{TeV}$	at $\sqrt{s} = 10\,\mathrm{TeV}$
γ+MET	5.3×10^{-7}	4.9×10^{-8}
Z+MET	1.1×10^{-5}	1.5×10^{-6}
$b\bar{b}$+MET	2.7×10^{-3}	4.5×10^{-3}
$t\bar{t}$+MET	3.7×10^{-3}	8.9×10^{-3}

Table 29: The Production cross sections (for **DM400**) for different final states at a $\sqrt{s} = 3\,\mathrm{TeV}$ and $10\,\mathrm{TeV}$ muon collider.

Final state	Production cross section (fb) at a muon collider	
	at $\sqrt{s} = 3\,\mathrm{TeV}$	at $\sqrt{s} = 10\,\mathrm{TeV}$
γ+MET	3.5×10^{-9}	1.3×10^{-10}
Z+MET	4.4×10^{-8}	2.2×10^{-6}
$b\bar{b}$+MET	3.7×10^{-8}	2.0×10^{-5}
$t\bar{t}$+MET	7.8×10^{-9}	3.7×10^{-5}

Table 30: The Production cross sections (for **DM1000**) for different final states at a $\sqrt{s} = 3\,\mathrm{TeV}$ and $10\,\mathrm{TeV}$ muon collider.

It was found that in case of **DM400** and **DM1000**, where the mediating scalar h_3 is singlet-dominated, the production cross section decreases significantly, due to its suppressed couplings to SM particles. Due to the same reason the branching ratio of h_3 to DM particles can become quite significant, which is the case for **DM400** (82%). However, since the the production cross section is small, the resulting event rate in all the final states considered decreases significantly. This can be seen in Table 29 and 30 when compared with Figure 27. As stated earlier, both these benchmarks can fully account for the observed DM relic density, and are allowed by all relevant constraints. However, such scenarios will be extremely difficult to probe at future lepton colliders. The possibility of probing these at future high energy hadron colliders, such as FCC-hh/SPPC was explored for these benchmarks. Although no detailed study is presented, the production cross sections for these benchmarks at FCC-hh/SPPC are mentioned here. The production cross sections at LHC with $\sqrt{s} = 14\,\text{TeV}$ and FCC-hh/SPPC with $\sqrt{s} = 100\,\text{TeV}$ are listed in Table 32 and 31, respectively. As can be observed, at least an increase in the production cross section at FCC-hh/SPPC over LHC by a factor of $\sim 30-40$ can be achieved for VBF and BBH for **DM400**. While for GGF the increase in the production cross section is by a factor of 100. For **DM1000**, the increase in the production cross section is by a factor of 1000. Such a large production cross section provides a favourable case for probing heavier Higgs masses at FCC-hh/SPPC.

Process	Production cross section (fb) at $\sqrt{s} = 14\,\text{TeV}$	
	DM400	**DM1000**
GGF	0.016	1.27×10^{-4}
VBF	0.001	4.7×10^{-6}
BBH	0.008	1.96×10^{-6}

Table 31: The production cross sections at leading order (LO) of relevant processes at $\sqrt{s} = 14\,\text{TeV}$ at LHC.

Process	Production cross section (fb) at $\sqrt{s} = 100\,\text{TeV}$	
	DM400	**DM1000**
GGF	1.456	0.117
VBF	0.039	1.182
BBH	0.264	0.029

Table 32: The production cross sections at leading order (LO) of relevant processes at $\sqrt{s} = 100\,\text{TeV}$ at FCC-hh/SPPC.

4.4.8 Complimentarity in dark matter searches at future colliders

In this work, different regions of parameter spaces were studied in detail for the 2HDMS scenario as well as the prospects of their detection at future colliders. Here, the salient points highlighting the complimentarity of the different present and future colliders in the context of DM searches are summarised.

The dominant production channels at HL-LHC are GGF, VBF and BBH production. In the low mass range (i.e. $\mathbf{DM55_{w95}}$), while GGF and VBF processes dominate over BBH due to the small invisible branching ratio, the HL-LHC would not be sensitive to these channels. In the intermediate/heavy mass range, the production cross section is already too small. Interestingly, for **DM70**, where the pair of DM particles comes from a singlet-like light scalar, the production cross section is enhanced due to kinematic reasons. In this case, LHC yields a good signal significance in the GGF final state, owing to the substantial production cross section and an invisible branching ratio of almost 100%. For the intermediate mass benchmark $\mathbf{DM156_{w95}}$ the BBH channel can provide a possible hint with an excess of $\sim 2\sigma$ at the HL-LHC. These channels may have better detection prospects at a future high energy hadron colliders such as the FCC-hh/SPPC with a centre-of-mass energy of $\sqrt{s} = 100\,\text{TeV}$ owing to the larger enhancements in the production cross sections which are left for future studies.

The low mass benchmarks ($\mathbf{DM55_{w95}}$ and **DM70**) have best prospects at ILC/CEPC/FCC-ee operating at $\sqrt{s} = 250\,\text{GeV}$ in the mono-Z final state, due to the large Higgstrahlung cross section. Among lepton colliders the best prospects for the intermediate benchmark $\mathbf{DM156_{w95}}$ turns out to be at a muon collider with $\sqrt{s} = 3\,\text{TeV}$ in the associated $b\bar{b}$ final state. Interestingly, it is also possible to probe such a scenario at lower $\sqrt{s}$ at a muon collider, i.e. $\sqrt{s} = 1\,\text{TeV}$, in the mono-photon final state. The heavy DM as well as heavy mediator scenario $\mathbf{DM1000_{w95}}$ can only be probed at a muon collider with $\sqrt{s} = 10\,\text{TeV}$ in the associated $t\bar{t}$ final states. There are a few challenging scenarios. Especially when the DM candidate comes from the decay of a singlet-dominated scalar, which is rather heavy in mass, the production cross section becomes too small for such scenarios to be probed at any of the future lepton colliders. Proposed future hadron colliders such as FCC-hh/SPPC, operating at $\sqrt{s} = 100\,\text{TeV}$, can be helpful in probing such challenging scenarios due to the significant enhancement in the signal cross section.

4.5 Summary

In this work, the Two Higgs doublet model extended by a complex scalar singlet (2HDMS) was investigated in terms of DM phenomenology as well as searches at future colliders. The DM candidate in this model is provided by the imaginary component of the scalar singlet, which is stabilised by the imposition of a Z_2' symmetry. It is further assumed, that the imaginary part of the complex scalar singlet does not acquire a vev, but the real part does, giving rise to a mixing between the singlet and the scalar sector of the 2HDM.

In the first part, section 4.3, an example benchmark point satisfying all theoretical and experimental constraints was chosen and parameter scans were performed around this point. Where different model parameters were varied and DM observables, such as the DM relic density as well as the direct and the indirect detection cross sections of DM, were investigated. In addition the impact of an experimental excess on the DM phenomenology was explored. This excess was observed around 95 GeV both at LEP [8] in the $b\bar{b}$ mode as well as at CMS [9] and ATLAS [10] in the $\gamma\gamma$ mode. Due to the mixing between the singlet and the scalar sector of the 2HDM, this excess can be modelled in the 2HDMS while respecting current constraints from DM searches and explaining the content of DM in our Universe, all at the same time. Strong theoretical constraints arise from bfb and tree-level unitarity, while the strongest experimental constraints come from DM direct detection searches and precision observables. Allowed regions under these constraints were identified, where the first subsection focused on the observed excesses at LEP and the LHC experiments CMS and ATLAS and the region consistent with the observed signal strength μ of the 95 GeV state was identified.

In the second part, section 4.4, the focus shifted towards probing the 2HDMS model at future colliders. Different benchmarks were chosen which are interesting from the point of view of probing them at future colliders, where most of the benchmarks can account for the observed amount of DM in our Universe. In this regard, in some of the chosen benchmarks the possibility that one of the scalars in the particle spectrum has a mass of 95 GeV and can explain the aforementioned excess at LEP and the LHC experiments CMS and ATLAS was considered. However, this criterion is not central to this work. The main aim was a detailed comparison between various future colliders including HL-HLC, future e^+e^- colliders such as FCC-ee, ILC, CLIC and the proposed muon collider, exploring various final states which can possibly probe such DM scenarios at a substantial signal significance. The results of the analysis can be summarised in the following points:

It was found that future e^+e^- colliders such as FCC-ee, ILC and CEPC, are most promising in probing the low mass region, where the mass of the DM candidate and of the mediating scalar which acts as a portal between the DM candidate and the SM sector, are below 250 GeV. Especially the mono-Z+MET final state gives good prospects in these scenarios, where this channel yields $11\,\sigma$ signal significance for the benchmark $\mathbf{DM55_{w95}}$ and 3σ signal significance for the benchmark **DM70** at $\sqrt{s} = 250$ GeV.

The scenario with DM and mediator in the intermediate mass region, can produce an excess of $\sim 2\sigma$ the HL-LHC, when a pair of DM particles is produced in association with a $b\bar{b}$-pair. On the other hand, such a scenario can be probed at a muon collider operating at a high centre-of-mass energy ($\sqrt{s} = 3\,\text{TeV}$), with much larger significance of $\sim 6\sigma$ at $3\,\text{ab}^{-1}$ in associated production with a $b\bar{b}$-pair.

The benchmark with a heavy DM candidate and mediator mass is beyond the reach of the considered e^+e^- colliders as well as HL-LHC and can be probed at a muon collider with $\sqrt{s} = 10\,\text{TeV}$, with a signal significance of $\sim 3\sigma$.

Furthermore, it was found that, the benchmarks which are under-abundant in terms of DM relic density, are easier to probe at future colliders. This is due to the fact that a smaller DM relic density implies a larger annihilation cross section of a pair of DM particles and consequently larger branching fractions of heavier scalars to a DM pair. An example of this is the benchmark $\mathbf{DM156_{w95}}$ discussed in this work.

The results in this work apply to the HL-LHC, ILC and a muon collider for unpolarised beams. However, they can be easily tuned for other future colliders, including different polarisation setups and integrated luminosity.

There are a few challenging scenarios, where a cosmologically viable DM scenario can be out of reach for HL-LHC as well as future lepton colliders, due to feeble interaction strength. For example, scenarios where a pair of DM particles comes from a singlet-dominated heavy scalar, it is possible to achieve the observed DM relic density and a large invisible branching ratio simultaneously. However, such cases are challenged by small production cross sections of the singlet-dominated heavy scalar. Such scenarios could be probed at a future hadron collider FCC-hh/SPPC. A comparison of event rates for HL-LHC and FCC-hh was provided while a detailed analysis is left for future investigation.

Overall, this work uses the 2HDMS as a reference model to perform a systematic analysis of DM phenomenology and searches at future colliders as a probe of BSM physics. However there are other observables, for example GWs from FOPT which could potentially be used to probe the 2HDMS or other BSM models. This will be the focus of the next section.

5 Phenomenology of first-order phase transitions

Contents

This section is based on the following publication:

- [3] A. J. Long, B. Shakya, and J. A. Ziegler, *Bubble friction in symmetry-restoring transitions*, 2025. arXiv: 2511.10415 `[hep-ph]`,
  to appear in the Journal of High Energy Physics

In the last section the DM and collider phenomenology was investigated for the example of a specific model. Other phenomenological aspects are for example GWs which can be produced from FOPTs. Contrary to the SM of particle physics where the EW phase transition proceeds via a smooth cross-over, in many BSM models FOPTs arise naturally, such as in extended Higgs models as the 2HDMS discussed in the last section. FOPTs proceed through the formation of bubbles and can be divided into three important stages: Nucleation, expansion and collision. All of these stages play an important role for the GW signal. However, in this section the focus will be on the expansion of bubbles from cosmological FOPTs, where a model independent approach will be followed. Furthermore, there is a special focus on FOPTs with symmetry restoration. First a short introduction to the theoretical background of cosmological FOPTs is given. Then in subsection 5.2 ‘Thermal pressure on bubbles’ numerical results for the pressure on bubbles from cosmological FOPTs and estimates of terminal bubble velocities are given.

Declaration on the content:

The content of this section is based on the publication [3]. The content is taken from this publications and adapted in parts. All figures in this section were created by myself. The calculations were performed by both myself and Andrew Long, in order to compare with each other. Large parts of the text were written by Bibhushan Shakya and Andrew Long.

5.1 First-order phase transitions

FOPTs have received significant research scrutiny in recent years, driven primarily by the prospect that they are well-motivated early Universe events in several beyond-the-Standard-Model (BSM) frameworks that can produce observable stochastic GW signals. Interest in FOPTs has further grown with the recently published results from PTA experiments such as NANOGrav [99], the Parkes Pulsar Timing Array [100], the International Pulsar Timing Array [101] or the European Pulsar Timing Array [102], indicating a stochastic GW background which could, among other explanations, be explained by cosmological FOPTs [95, 103, 104] (see also Refs. [96, 97] for reviews on FOPTs and GWs).

In the SM, however, there is no indication for a FOPT. The EW phase transition is rather a smooth cross-over, meaning that the breaking of the EW symmetry is a smooth process and the vacuum transitions continuously from the old phase to the new stable vacuum phase. A first order phase transition, on the other hand, is characterised by a discontinuous change between the two phases. This can arise naturally in many BSM models via additional parameters which modify the scalar potential. The difference between a smooth and a first-order transition is schematically shown in Figure 31 (this image was already shown in Figure 9 and is repeated here for convenience), where the example of the scalar potential developing a non-zero vev during the cooling of the Universe was chosen. A strong FOPT is a necessary condition providing out-of-equilibrium conditions to explain the baryon asymmetry of the Universe via EW baryogenesis [78]. And the detection of a cosmological FOPT would be a clear indicator of BSM physics and require extensions of the SM. Many

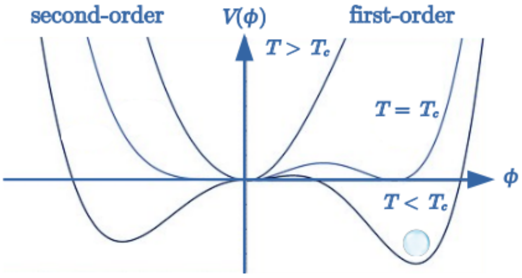

Figure 31: Schematic difference between a smooth (left) and a first-order (right) phase transition. Depicted is the example of the scalar potential developing a non-zero vev as the Universe cools down, with the field value ϕ of a scalar field on the x-axis and the value of the potential $V(\phi)$ on the y-axis. In the case of first-order, two degenerate minima develop at the critical temperature T_c separated by a potential barrier. As the field tunnels through this potential barrier its vev changes discontinuously and bubbles of the new phase form (indicated by the small bubble image at the minimum).

extensions involving additional scalar degrees of freedom (for example the 2HDM and its extensions), hidden sectors, or supersymmetric frameworks predict strong FOPTs capable of producing observable GW [95].

FOPTs proceed via the formation of bubbles, meaning that both, the old and the new phase can exist simultaneously. The bubbles of the new phase then expand and enclose the regions of the old unstable phase around them. In this work the focus lies on transitions between symmetric and broken vacuum phases, where particles obtain a mass in the broken phase and are massless in the symmetric phase. This is also what happens during the EW phase transition. Hence this work provides implications on the EW phase transition but can also be applied to more general phase transitions where a change of mass occurs when passing into the bubble of the new phase. Furthermore, as mentioned before, also transitions from a broken to a symmetric phase are considered in this work, where the following difference should be considered:

Symmetry-breaking transitions

In standard symmetry-breaking transitions the expansion of the bubbles is driven by the difference of the potential in the symmetric and broken phase. Such transitions are considered to have happened during the standard cooling of the Universe, such as during the EW phase transition. This scenario is well studied (for example in Refs. [44–50]) and the approach followed by Refs. [44, 45] will be reviewed in this work.

Symmetry-restoring transitions

In symmetry-restoring transitions, on the other hand, the expansion of the bubbles is against the difference of the potential and driven by thermal corrections (if one considers that the value of the potential in the symmetric phase is higher than in the broken phase, which is considered here). Such transitions could have occurred during reheating or preheating [190, 191]. This scenario is less well studied (see for example Refs. [191, 192]) and is the main objective of this work.

An important parameter in the phenomenology of FOPTs is the speed of the expanding bubble walls of the stable vacuum. This parameter is known to be of particular importance in models of EW baryogenesis (see e.g. [193] for a recent overview), where the interaction between the expanding bubble walls and the surrounding plasma is responsible for creating a nonvanishing baryon asymmetry, with the amount of asymmetry produced being sensitive to the speed of the bubble wall. Understanding whether the bubble walls achieve some terminal velocity or continue to accelerate (the so-called runaway regime) is also important for deducing the form of the GWs produced from such transitions. If the walls run away, most of the energy released in the phase transition is stored in the bubble walls, and GWs are sourced by the scalar field energy densities during bubble collision [44, 94, 194–204] or by the distribution of particles produced from bubble collisions [205]. On the other hand, in the presence of significant energy transfer from the walls to the particles surrounding the bubbles, most of the energy gets transferred to these particles, and GWs instead arise from sound waves [206–211] and turbulence [94, 209, 212–216] in the plasma, or through nontrivial spatial configurations of particles that do not thermalise [217]. Moreover, the speed (and consequently the energy density) of the bubble wall also determines the energy scale and efficiency of producing high energy or high mass particles from the bubble walls interacting with the plasma or with other bubbles, which has found many applications for various BSM phenomena such as DM production and baryogenesis [218–229].

In this work the approach studied in Refs. [44, 45] is followed to calculate the speed of the expanding bubble wall. Opposed to the original work, where symmetry-breaking transitions were studied, here the calculation will be extended to the case of symmetry-restoring transitions. It was shown that at LO, the plasma imparts some thermal pressure on the expanding bubble walls as the particles from the surrounding plasma move across the bubble wall and experience a change in mass. Whereas in the symmetry-breaking scenario particles obtain mass inside the bubble, hence their mass increases (and in the symmetry-restoring scenario particles become massless inside the bubble, hence their mass decreases). This change in the particle's mass introduces a change in their momentum which is transferred to the bubble wall and acts as friction (or thermal pressure). For the symmetry-breaking case (studied in Refs. [44, 45]), this pressure was calculated to be independent of the speed of the bubble walls. At NLO, a different process becomes crucial: transition radiation, the emission of a vector boson as particles cross into bubble walls, was shown to produce a pressure that scales linearly with the Lorentz factor of the bubble wall, which inevitably saturates the latent energy released from the vacuum and leads to a terminal velocity for the bubble wall [45]. The dominant effect comes from the emission of soft bosons, which has an enhanced probability and imparts the largest pressure on the bubble walls. While these calculations were performed with several approximations, other subsequent, more rigorous calculations in the literature have confirmed the general veracity of these results [46–50].

While the above results hold for symmetry-breaking transitions, which are the primary form of FOPTs studied in the literature, there has recently been growing interest in FOPTs with symmetry *restoration*. Such transitions could generally take place, in particular, during reheating or preheating [190, 191], including for the SM Higgs field [230, 231] (see Refs. [232–235] for other studies). In this work, the nature of plasma friction on the expanding bubble walls is studied for such symmetry-restoring transitions, as such configurations display several qualitatively different characteristics compared to the standard symmetry-breaking transitions. First, the LO pressure from particles crossing into the bubbles in this case is *negative*, since particles are massive outside the bubbles in the broken phase but lose mass when entering the symmetry restored phase inside the bubbles, thereby creating an *antifriction* effect. As will be demonstrated in the following, the NLO pressure arising from the emission of gauge bosons can also be negative, especially in the soft limit that dominates the distribution, producing the same antifrictional effect.

On the other hand, a recent calculation [192] demonstrated that the NLO pressure in symmetry-restoring phase transitions scales in the same manner as in the symmetry-breaking scenario (i.e, positive pressure that grows linearly with the wall Lorentz factor) in the limit of large Lorentz factor. Given the broad phenomenological importance of the bubble wall speed, it then becomes important to understand how the pressure transitions from a negative effect to a positive one, restoring the standard behaviour known from symmetry-breaking transitions, and how it impacts the terminal velocity achieved by the bubble walls. The following sections attempt to answer these questions by extending the original calculations of Bödeker and Moore [44, 45], which were performed for the symmetry-breaking scenario, to the symmetry-restoring scenario.[6] This will inherit the simplifying approximations used in these calculations, but should provide a correct order-of-magnitude estimate of the effect, and shed light on the underlying physics.

The calculation of the speed of the expanding bubble walls is explained in the following subsection.

5.1.1 Wall velocity of expanding bubbles

The bubble wall velocity is determined by the interactions between the bubble wall and the particles present in the surrounding plasma. These particles of the surrounding plasma exert friction (or thermal pressure) on the bubble wall when passing into the bubble. But also the expanding bubble wall can impact the plasma around it, where three different cases are distinguished: deflagration, detonation and hybrid-cases. These cases are schematically shown in Figure 32. For bubble walls moving slower than the speed of sound in the surrounding plasma ($c_s \approx 1/\sqrt{3}$ for a relativistic plasma) a shock front forms in front of the bubble. This case is called deflagration. The case where the bubble wall moves faster than the speed of sound

---

[6] Note that the calculation in Ref. [192] cannot answer these questions. This paper demonstrated that the standard (symmetry-breaking) result reemerges in the large Lorentz factor limit, but did not calculate at what value it is reached. In fact, Ref. [192] speculated that an intermediate regime of negative friction might be possible.

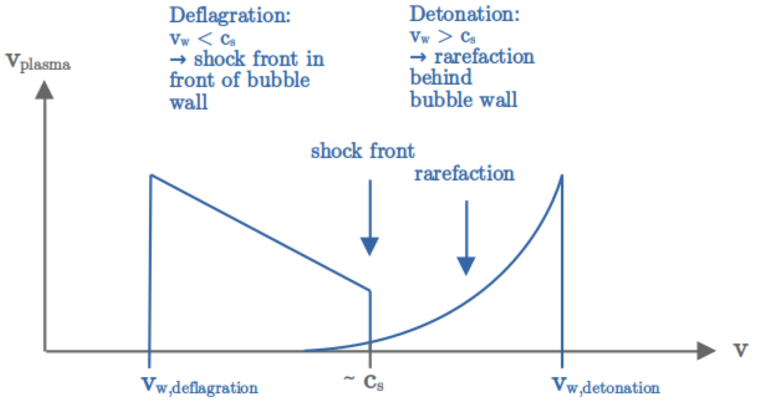

Figure 32: Schematic influence of the bubble wall velocity on the surrounding plasma, where v_w is the speed of the bubble wall and c_s is the speed of sound in the surrounding plasma. Depicted are the cases for slow (slower than c_s) moving bubble walls, called deflagration, and fast (faster than c_s) moving bubble walls, called detonation.

is called detonation, where rarefaction forms behind the bubble wall. Intermediate cases, where both, a shock front and rarefaction, form are called hybrid.

Throughout this work the attention is restricted to bubble walls that are moving at relativistic velocities relative to the plasma, hence the detonation case. If $\mathbf{v}_w$ denotes the wall's velocity in the rest frame of the plasma and $\gamma = 1/\sqrt{1-|\mathbf{v}_w|^2}$ is the associated Lorentz factor, then the regime of interest corresponds to $\gamma \gg 1$. The calculation of the thermal pressure is significantly simplified for relativistic walls [44]. Since the wall travels much faster than the speed of sound, nearly all particles from the surrounding plasma pass into the bubble with negligible reflections. Consequently, the plasma in front of the wall is unaffected by the wall's approach, and the flux of particles onto the wall is simply a thermal distribution. The assumption of relativistic bubble walls also allows to use the so called kick-approach which was studied in detail in the seminal papers by Bödeker and Moore [44, 45] for symmetry-breaking phase transitions. This approach is based on calculating the pressure from the imparting flux of of particles and, as mentioned above is only valid for relativistic bubble walls, while neglecting outgoing particles. Another approach to calculating the velocity of the expanding bubble wall is the kinetic approach, which is based on solving coupled equations of motion for the background scalar field and the surrounding plasma. This approach also includes non-equilibrium effects but no scattering processes. (See Ref. [50] for a comparison of the two approaches). Another assumption made in Refs. [44, 45] which will also be made in this work is the WKB approximation. This approximation applies for temperatures much lower than the critical temperature where the height of the potential barrier is small compared to the depth of the minimum and the bubble wall can be approximated as a thick wall [192]. This approximation can be used if the momentum of the particles which pass through the wall is much larger than the inverse width of the wall. As relativistic walls are considered here, this approximation can be applied.

In the following the kick-approach studied in Refs. [44, 45] is followed while discussing symmetry-breaking and symmetry-restoring transitions side-by-side.

As explained above, thermal pressure arises as the particles from the surrounding plasma move across the bubble wall into the new phase and undergo a change in mass. The two phases are denoted as the symmetric phase (subscript s) and the broken phase (subscript h for Higgsed, since particle become massive here). Particles in the symmetric phase are assumed to be massless, i.e. $m_{a,\mathrm{s}} = m_{b,\mathrm{s}} = m_{c,\mathrm{s}} = 0$, and particles in the broken phase have masses denoted by $m_{a,\mathrm{h}}$, $m_{b,\mathrm{h}}$, $m_{c,\mathrm{h}}$.[7] The mass change across the bubble wall results in a change of momentum which in turn is transferred to the bubble wall and acts as friction or antifriction, depending on the scenario. For the symmetry-breaking scenario, the broken phase is inside the bubble, and for the symmetry-restoring scenario, the broken phase is outside the bubble.

The aforementioned LO process is characterised by one particle passing into the bubble and continuing its travel inside the bubble, while not interacting with other particles during the transition. This process is also called 1-to-1 processes. The NLO process, on the other hand, is characterised by the original particle radiating off an additional particle while passing through the bubble wall. Inside the bubble there will then be two particles. This process is also called 1-to-2 process or transition radiation. These two cases will be discussed later separately. The 1-to-2 process for the symmetry-breaking and the symmetry-restoring scenario is illustrated in Figure 33.

The thermal pressure $\mathcal{P}_{\mathrm{th}}$ may be calculated using perturbation theory as a series in powers of squared couplings, $\mathcal{P}_{\mathrm{th}} = \mathcal{P}_{1\to1} + \mathcal{P}_{1\to2} + \cdots$. The leading term, called the 1-to-1 pressure and denoted by $\mathcal{P}_{1\to1}$, is zeroth order in the squared couplings [44]. Meaning that one particle passes into the bubble and interacts only with the bubble wall and no other particles. The next-to-leading term, called the 1-to-2 pressure and denoted by $\mathcal{P}_{1\to2}$, is first-order in the squared couplings, and it captures the effect of transition radiation [45], where one particle radiates off an additional particle as it passes into the bubble. See Refs. [46–50, 236, 237] for studies of thermal pressure on relativistic bubbles. In the following, the results from this literature for 1-to-1 and 1-to-2 contributions to the thermal pressure are summarised, emphasising differences between the symmetry-breaking and symmetry-restoring scenarios.

---

[7] It was checked that the results derived in this paper remain applicable if the particles have nonzero but small masses in the symmetric phase, on the order of $m_{\mathrm{s}} = 0.1 m_{\mathrm{h}}$.

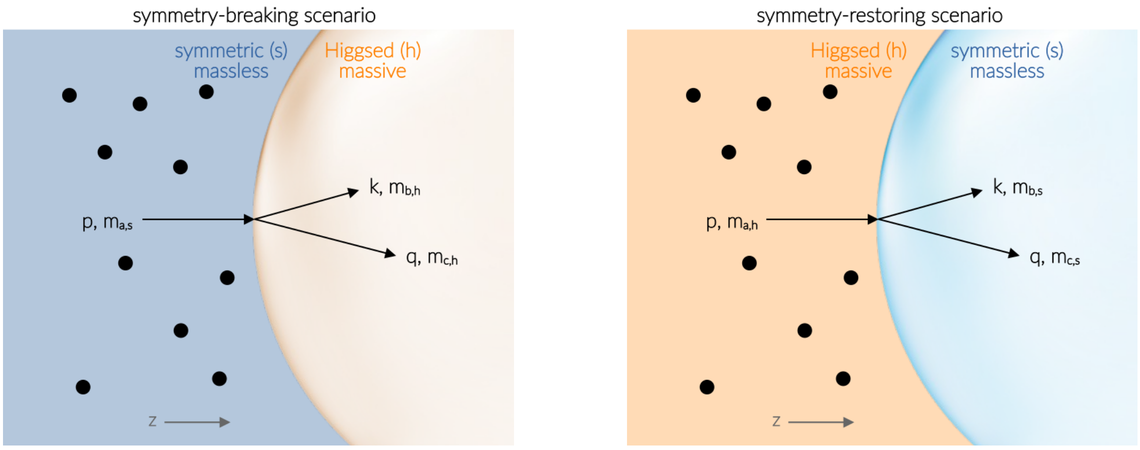

Figure 33: Illustration of the 1-to-2 transition, the main process studied in this work. *Left:* For the symmetry-breaking scenario, massless particles ($m_{a,\mathrm{s}} = 0$) are incident on the bubble wall from the symmetric phase, and they transition into pairs of massive particles ($m_{b,\mathrm{h}}, m_{c,\mathrm{h}} > 0$) in the broken phase. *Right:* For the symmetry-restoring scenario, the phases are switched, so that incident particles are massive and emergent particles are massless. In the rest frame of the plasma, the wall moves left with Lorentz factor γ; in the rest frame of the wall, the particles have a thermal distribution of momenta boosted to the right by the Lorentz factor γ. [3]

1-to-1 thermal pressure

Consider a particle, denoted a, that has mass $m_{a,\mathrm{s}} = 0$ in the symmetric phase and mass $m_{a,\mathrm{h}} > 0$ in the broken phase. For the symmetry-breaking scenario, the mass rises from $m_{a,\mathrm{out}} = m_{a,\mathrm{s}} = 0$ to $m_{a,\mathrm{in}} = m_{a,\mathrm{h}} > 0$ when the particle enters the bubble, where $m_{a,\mathrm{out}}$ denotes the particle's mass outside the bubble and $m_{a,\mathrm{in}}$ the mass inside. For the symmetry-restoring scenario, the mass decreases from $m_{a,\mathrm{out}} = m_{a,\mathrm{h}} > 0$ to $m_{a,\mathrm{in}} = m_{a,\mathrm{s}} = 0$. In the following the rest frame of the wall is considered, and the wall is treated as planar since its curvature radius is significantly larger than particle physics length scales. The background of the planar wall at rest maintains time-translation invariance and transverse spatial-translation invariance (along the wall), but it is not invariant under longitudinal spatial translations (normal to the wall, which is denoted as z-direction here). As a result, a particle may cross the wall while maintaining its energy E and transverse momentum $\mathbf{p}_\perp$, but while losing or gaining longitudinal momentum p_z to compensate for the increase or decrease of its mass. (Here, bold letters are used for vector quantities and non-bold letters are used for single components or scalar quantities in general.)

The change in the particle's longitudinal momentum p_z is calculated as [44]:

$$\begin{aligned} E_a^2 &= p_{a,z,\mathrm{in}}^2 + \mathbf{p}_{a,\perp}^2 + m_{a,\mathrm{in}}^2 = p_{a,z,\mathrm{out}}^2 + \mathbf{p}_{a,\perp}^2 + m_{a,\mathrm{out}}^2 \\ \Rightarrow\; p_{a,z,\mathrm{in}} - p_{a,z,\mathrm{out}} &= \frac{m_{a,\mathrm{out}}^2 - m_{a,\mathrm{in}}^2}{p_{a,z,\mathrm{in}} + p_{a,z,\mathrm{out}}} \approx \frac{m_{a,\mathrm{out}}^2 - m_{a,\mathrm{in}}^2}{2E_a}\,. \end{aligned} \tag{5.1}$$

The approximation follows because the particle is boosted in the longitudinal direction (in the rest frame of the wall). The wall's longitudinal momentum change, denoted by $\Delta p_{1\to 1}$, is opposite to the particle's longitudinal momentum change. Therefore, one can evaluate:

$$\Delta p_{1\to 1} \equiv p_{a,z,\mathrm{out}} - p_{a,z,\mathrm{in}} \approx \frac{m_{a,\mathrm{in}}^2 - m_{a,\mathrm{out}}^2}{2E_a} = \begin{cases} +\frac{1}{2E_a} m_{a,\mathrm{h}}^2, & \text{sym-breaking scenario}\,, \\ -\frac{1}{2E_a} m_{a,\mathrm{h}}^2, & \text{sym-restoring scenario}\,. \end{cases} \tag{5.2}$$

For the symmetry-breaking scenario, $m_{a,\mathrm{in}} = m_{a,\mathrm{h}}$ and $m_{a,\mathrm{out}} = m_{a,\mathrm{s}} = 0$; hence, the wall's longitudinal momentum change $\Delta p_{1\to 1} \approx m_{a,\mathrm{h}}^2/2E_a$ is positive. For the symmetry-restoring scenario, $m_{\mathrm{out}} = m_{a,\mathrm{h}}$ and $m_{\mathrm{in}} = m_{a,\mathrm{s}} = 0$; hence, the wall's longitudinal momentum change $\Delta p_{1\to 1} \approx -m_{a,\mathrm{h}}^2/2E_a$ is negative. In the rest frame of the plasma, the wall moves in negative z-direction, so the symmetry-breaking scenario's positive z-momentum change implies a deceleration, and the symmetry-restoring scenario's negative z-momentum change implies an acceleration.

This opposite behaviour carries over to the thermal pressure. The thermal pressure is calculated by integrating the wall's longitudinal momentum change over the thermal flux of incident particles [238]. Let $f_a(\mathbf{p})$ denote the thermal one-particle phase space distribution function of the incident a-type particles in the rest frame of the wall. Then the pressure is calculated by the following integral [44]:

$$\mathcal{P}_{1\to 1} = \int \frac{\mathrm{d}^3 p_{a,\mathrm{s}}}{(2\pi)^3} \frac{p_{a,z,\mathrm{s}}}{E_a} f_a(\mathbf{p}_{a,\mathrm{s}}) \, \Delta p_{1\to 1} \approx \begin{cases} +\frac{1}{24} m_{a,\mathrm{h}}^2 T^2, & \text{sym-breaking scenario}\,, \\ -\frac{1}{24} m_{a,\mathrm{h}}^2 T^2, & \text{sym-restoring scenario}\,. \end{cases} \tag{5.3}$$

For the symmetry-breaking scenario the wall experiences a positive thermal pressure, which is friction force that retards its motion [44]. For the symmetry-restoring scenario the wall experiences a negative thermal pressure, which is an *antifriction* force that accelerates its motion [190].

If the full thermal pressure were well-approximated by the 1-to-1 contribution, $\mathcal{P}_{\mathrm{th}} \approx \mathcal{P}_{1\to 1}$, then bubble walls in the symmetry-restoring scenario would achieve runaway behaviour [190]. That is to say, a wall's speed would approach $v_w = 1$ (in natural units) and its Lorentz factor would grow arbitrarily large $\gamma \to \infty$. The same can in principle happen in the symmetry-breaking scenario, if the driving force of the expansion is larger than the above calculated friction term, as was discussed in Ref. [44].

The next subsection will discuss how the 1-to-2 contribution $\mathcal{P}_{1\to 2}$ dominates over the 1-to-1 contribution at large wall speeds, and prohibits this runaway behaviour [192].

1-to-2 thermal pressure

Interactions allow for different behaviours when particles encounter the bubble wall [45]. Consider three species of particles having masses $m_{a,\mathrm{s}} = m_{b,\mathrm{s}} = m_{c,\mathrm{s}} = 0$ in the symmetric phase and $m_{a,\mathrm{h}}$, $m_{b,\mathrm{h}}$, $m_{c,\mathrm{h}} \geq 0$ in the broken phase. When a particle of species a is incident on the wall, there is a nonzero probability for it to convert into two particles, one each of species b and c, that pass into the bubble. This process is also called transition radiation. The wall's longitudinal momentum change is then calculated as:

$$\Delta p_{1\to 2} \equiv p_{z,\mathrm{out}} - k_{z,\mathrm{in}} - q_{z,\mathrm{in}} \approx \frac{1}{2E_a}\left(-m_{a,\mathrm{out}}^2 + \frac{m_{b,\mathrm{in}}^2}{x} + \frac{m_{c,\mathrm{in}}^2}{1-x} + \frac{k_\perp^2}{x(1-x)}\right), \tag{5.4}$$

where $\mathbf{p}_{\mathrm{out}}$ is the momentum of the incident a-particle, and where $\mathbf{k}_{\mathrm{in}}$ and $\mathbf{q}_{\mathrm{in}}$ are the momenta of the recoiling b and c-particles, respectively. The approximation uses $E_a = E_b + E_c$, $x \equiv E_b/E_a$, $\mathbf{p}_\perp = \mathbf{k}_\perp + \mathbf{q}_\perp = \mathbf{0}$ (since one can always transition to a frame where the transverse momentum of the incident particle is zero), $k_\perp \equiv |\mathbf{k}_\perp|$, $p_{z,\mathrm{out}} \gg m_{a,\mathrm{out}}, k_\perp$, $k_{z,\mathrm{in}} \gg m_{b,\mathrm{in}}, k_\perp$, and $q_{z,\mathrm{in}} \gg m_{c,\mathrm{in}}, k_\perp$. In what follows, additionally it will be assumed that the b-particle is soft, so that its energy $E_b = xE_a \ll E_a$ is much smaller than the incident a-particle's energy.

For the symmetry-breaking scenario out $= s$ and in $= h$, and for the symmetry-restoring scenario in $= s$ and out $= h$. The wall's longitudinal momentum change is then given by:

$$\Delta p_{1\to 2} \approx \frac{1}{2E_a}\begin{cases} \frac{m_{b,\mathrm{h}}^2}{x} + \frac{m_{c,\mathrm{h}}^2}{1-x} + \frac{k_\perp^2}{x(1-x)}, & \text{sym-breaking scenario}, \\ -m_{a,\mathrm{h}}^2 + \frac{k_\perp^2}{x(1-x)}, & \text{sym-restoring scenario}. \end{cases} \tag{5.5}$$

For the symmetry-breaking scenario, the wall's longitudinal momentum change $\Delta p_{1\to 2}$ is positive, which is the same sign as $\Delta p_{1\to 1}$. However, for the symmetry-restoring scenario, the wall's longitudinal momentum change $\Delta p_{1\to 2}$ may be either positive or negative depending on the kinematic variables $k_\perp$ and x. This is crucially different from the 1-to-1 calculation in Equation 5.2 where $\Delta p_{1\to 1}$ is always negative for the symmetry-restoring scenario. Note that $\Delta p_{1\to 2} < 0$ for $k_\perp < m_{a,\mathrm{h}}[x(1-x)]^{1/2}$. It follows that the thermal pressure $\mathcal{P}_{1\to 2}$ in the symmetry-restoring scenario is negative for small values of the Lorentz factor γ, and it is positive for large γ. Roughly speaking, this is because the phase space integral over $k_\perp$ is dominated by the region $k_\perp \sim m_{b,\mathrm{h}}$ and the x-integral is dominated by the IR cutoff $x_{\mathrm{min}} = m_{b,\mathrm{h}}/E_a$, and $E_a = \gamma T$ is the energy for a thermal distribution of a-particles, such that

$k_\perp^2/x \sim m_{b,\mathrm{h}}\gamma T$. Thus for large γ the phase space integrals are dominated by the positive terms, giving $\Delta p_{1\to 2} > 0$ for both the symmetry-breaking and restoring scenarios. This is consistent with the results of Ref. [192], whose authors found that the pressure in the symmetry-restoring scenario approaches its counterpart in the symmetry-breaking scenario in the limit of large Lorentz factor.

The thermal pressure is calculated by the integral [45] (see also Sec. 3B of Ref. [46]):

$$\mathcal{P}_{1\to 2} = \int \frac{\mathrm{d}^3 p_\mathrm{s}}{(2\pi)^3 2E_a} \int \frac{\mathrm{d}^3 k_\mathrm{s}}{(2\pi)^3 2E_b} \int \frac{\mathrm{d}^3 q_\mathrm{s}}{(2\pi)^3 2E_c} \frac{p_{z,\mathrm{s}}}{E_a} f_a(\mathbf{p}_\mathrm{s})\Big(1 \pm f_b(\mathbf{k}_\mathrm{s})\Big)\Big(1 \pm f_c(\mathbf{q}_\mathrm{s})\Big)$$
$$\times (2\pi)^3 \delta^2(\mathbf{p}_\perp - \mathbf{k}_\perp - \mathbf{q}_\perp)\,\delta(E_a - E_b - E_c)\,|\mathcal{M}|^2\,\Delta p_{1\to 2}\,.$$

For small occupation numbers one can approximate $(1 \pm f_{b,c}) \approx 1$. The matrix element $\mathcal{M}$ was calculated by the authors of Ref. [45] using the WKB approximation as

$$|\mathcal{M}|^2 = 4E_a^2 \left| \frac{V_\mathrm{h}}{A_\mathrm{h}} - \frac{V_\mathrm{s}}{A_\mathrm{s}} \right|^2 , \tag{5.6}$$

where V_s and V_h are the vertex functions in the symmetric and broken phases, respectively. The focus, in this work, is on the case where the emitted particle b is a transversely polarised vector boson[8] with energy E_b and transverse momentum $\mathbf{k}_\perp$ for which (see Tab. 1 in Ref. [45]):

$$|V_\mathrm{s}|^2 = |V_\mathrm{h}|^2 \approx 4g^2 C_2[R] \frac{1}{x^2} k_\perp^2 , \tag{5.7}$$

where g is the gauge coupling constant, $C_2[R]$ is the second Casimir, $x = E_b/E_a$ is assumed to be $0 \le x \ll 1$, and $k_\perp \equiv |\mathbf{k}_\perp|$. The kinematical factors are given by[9]

$$\begin{aligned} A_\mathrm{s} &= -2E_a\Big(p_{z,\mathrm{s}} - k_{z,\mathrm{s}} - q_{z,\mathrm{s}}\Big) \approx m_{a,\mathrm{s}}^2 - \frac{m_{b,\mathrm{s}}^2}{x} - \frac{m_{c,\mathrm{s}}^2}{1-x} - \frac{k_\perp^2}{x(1-x)} ,\\ A_\mathrm{h} &= -2E_a\Big(p_{z,\mathrm{h}} - k_{z,\mathrm{h}} - q_{z,\mathrm{h}}\Big) \approx m_{a,\mathrm{h}}^2 - \frac{m_{b,\mathrm{h}}^2}{x} - \frac{m_{c,\mathrm{h}}^2}{1-x} - \frac{k_\perp^2}{x(1-x)} . \end{aligned} \tag{5.8}$$

where the same approximations as in Equation 5.4 are made. Putting together these

---

[8] The transverse polarisation modes are conceptually and technically easier to study than the longitudinal polarisation mode. Whereas the vector boson's transverse polarisations are present in both the symmetric and broken phases, its longitudinal polarisation is only present in the broken phase. The authors of Ref. [239] found that both polarisations contribute comparably to the pressure for symmetry-breaking transitions with mild super-cooling. Therefore, it can be expected that no significant error arises by neglecting the longitudinal polarisation.

[9] It was verified, for this work, that the impact of these approximations on the thermal pressure is sub-$\mathcal{O}(10\%)$.

factors gives the squared matrix element [45] (see also App. B in Ref. [49]):

$$|\mathcal{M}|^2 = 16g^2 C_2[R] \frac{k_\perp^2 \left(m_{b,\mathrm{h}}^2 - m_{b,\mathrm{s}}^2\right)^2}{\left(k_\perp^2 + m_{b,\mathrm{h}}^2\right)^2 \left(k_\perp^2 + m_{b,\mathrm{s}}^2\right)^2} E_a^2 \,, \tag{5.9}$$

where only the terms that are leading as $x \to 0$ are kept. Note that this expression is identical for both the symmetry-breaking scenario (with $m_{b,\mathrm{out}} = m_{b,\mathrm{s}} = 0$ and $m_{b,\mathrm{in}} = m_{b,\mathrm{h}} = m_b$) and for the symmetry-restoring scenario (with $m_{b,\mathrm{out}} = m_{b,\mathrm{h}} = m_b$ and $m_{b,\mathrm{in}} = m_{b,\mathrm{s}} = 0$). This is to be expected, since the symmetry-breaking and restoring scenarios simply switch the “in" and “out" labels, and the squared matrix element in Equation 5.6 is invariant.

Combining the expressions above allows the thermal pressure in Equation 5.6 to be estimated as[10]:

$$\mathcal{P}_{1\to 2} \approx \frac{g^2 C_2[R] T^2}{4\pi^2} \int_{k_{\perp,\min}}^{k_{\perp,\max}} \frac{\mathrm{d}k_\perp}{k_\perp} \int_{x_{\min}}^{x_{\max}} \frac{\mathrm{d}x}{x} \frac{m_{b,\mathrm{h}}^4}{\left(k_\perp^2 + m_{b,\mathrm{h}}^2\right)^2} \times \begin{cases} \frac{m_{b,\mathrm{h}}^2}{x} + m_{c,\mathrm{h}}^2 + \frac{k_\perp^2}{x}, & \text{s-b,} \\ -m_{a,\mathrm{h}}^2 + \frac{k_\perp^2}{x}, & \text{s-r,} \end{cases} \tag{5.10}$$

where ‘symmetry-breaking’ was shortened ‘s-b’ and ‘symmetry-restoring’ was shortened ‘s-r’. For the limits of integration, infrared (IR) and ultraviolet (UV) cutoffs are introduced. This is because several approximations have been made when evaluating the integrand, and these approximations are only valid in a restricted domain of integration that gives the largest contribution to the integral. The UV cutoffs are taken $k_{\perp,\max} = [x^2 E_a^2 - m_{b,\mathrm{h}}^2]^{1/2}$ and $x_{\max} = 1 - m_{c,\mathrm{h}}/E_a$ in the symmetry-breaking scenario, and $k_{\perp,\max} = xE_a$ and $x_{\max} = 1$ in the symmetry-restoring scenario. The IR cutoffs are taken $k_{\perp,\min} = 0.1 m_{b,\mathrm{h}}$ and $x_{\min} = m_{b,\mathrm{h}}/E_a$. Various choices of IR cutoffs were discussed by the authors of Ref. [47], with the thermal mass of the b-particle or a phase-space saturation mass considered as viable options. Both of these evaluate to $\sim 0.1 m_{b,\mathrm{h}}$, hence this is used as an IR cutoff for $k_\perp$ in this work.

5.2 Thermal pressure on bubble walls

In this section the thermal pressure is calculated using numerical integration methods to evaluate the phase space integrals in Equation 5.10. It is examined how the pressure depends on the bubble wall’s velocity via the Lorentz factor γ, while contrasting the symmetry-breaking and symmetry-restoring scenarios. For the symmetry-restoring scenario, the value of the Lorentz factor where the pressure switches from

---

[10] The integration is performed only over $k_{z,\mathrm{s}} > 0$ corresponding to particles that pass into the bubble. Particles with $k_{z,\mathrm{s}} < 0$ would contribute a larger momentum transfer, but the probability is low enough to neglect them.

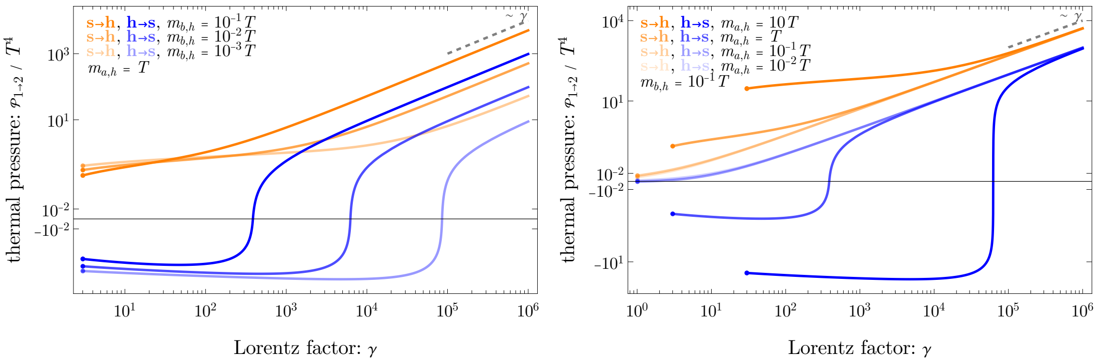

Figure 34: Dependence of the 1-to-2 thermal pressure $\mathcal{P}_{1\to2}$ as a function of the bubble wall's Lorentz factor γ, for various choices of particle masses for symmetry-restoring scenarios (h → s, blue curves) and symmetry-breaking scenarios (s → h, orange curves). In the first panel $m_{a,\mathrm{h}} = m_{c,\mathrm{h}} = T$ is fixed and $m_{b,\mathrm{h}}$ is varied, and in the second panel $m_{b,\mathrm{h}} = 0.1T$ is fixed and $m_{a,\mathrm{h}} = m_{c,\mathrm{h}}$ is varied. The gauge factor is taken to be $g^2 C_2[R] = 1$, and more generally the pressure scales linearly with this factor. [3]

negative to positive, and where the pressure approaches the same form as in the symmetry-breaking scenario is calculated. Finally, various phenomenological implications of this modified form of pressure are discussed.

In order to demonstrate a comparison of the symmetry-breaking and symmetry-restoring scenarios, the focus is on a model in which a and c are the same particle species. The pressure above is then determined by five independent parameters: the broken-phase masses $m_{a,\mathrm{h}} = m_{c,\mathrm{h}}$ and $m_{b,\mathrm{h}}$, the temperature T, the Lorentz factor of the bubble wall γ, and the gauge factor $g^2 C_2[R]$. Dimensionful parameters are evaluated in units of the temperature T of the surrounding plasma outside the bubble. The scaling with g is trivial, since it only appears as an overall normalisation via Equation 5.7. The three nontrivial independent parameters are thus $m_{a,\mathrm{h}}/T, m_{b,\mathrm{h}}/T, \gamma$. Note that the expectation value of the scalar SM-Higgs field in the broken phase v_h only affects the thermal pressure via the relation $m_{b,\mathrm{h}} = g v_\mathrm{h}$. It also impacts the bubble wall's terminal velocity via the latent vacuum energy, which is discussed in the next subsection.

5.2.1 Pressure comparison

Figure 34 illustrates how the 1-to-2 thermal pressure $\mathcal{P}_{1\to2}$ varies with the Lorentz factor γ for a few fiducial masses in both the symmetry-breaking (orange) and symmetry-restoring (blue) scenarios. Note that the gauge factor is fixed to $g^2 C_2[R] = 1$ while varying $m_{b,\mathrm{h}}$. If the b-particles are gauge bosons which receive their mass from the Higgs field that forms the bubble, then the coupling and mass are related by $m_{b,\mathrm{h}} = g v_\mathrm{h}$ where v_h is the expectation value of the Higgs field inside the bubble, so $v_{\mathrm{h}} = m_{b,\mathrm{h}}/g$ varies implicitly with $m_{b,\mathrm{h}}$. If the Lorentz factor γ becomes too small, then the approximations made in this work break down; thus the curves are truncated at $\gamma T < 3 \min[m_{a,\mathrm{h}}, m_{b,\mathrm{h}}]$, indicated by dots in the panels.

By inspecting the figure, several notable features can be observed. For large values of the Lorentz factor γ, the 1-to-2 thermal pressure scales as $\mathcal{P}_{1\to 2} \propto \gamma$ for both the symmetry-breaking and the symmetry-restoring scenarios and for all the masses shown. As noted in earlier studies [45, 47, 48, 50], this scaling arises because the average momentum transfer $\langle \Delta p_{1\to 2} \rangle \propto \gamma^0$ at large γ, and the pressure scales with the Lorentz-boosted flux $\propto \gamma^1$. Also for large values of γ, it can be observed that the pressure scales with the masses as $\mathcal{P}_{1\to 2} \propto m_{b,\mathrm{h}}^1 m_{a,\mathrm{h}}^0$. One can see from Equation 5.10 that the pressure behaves as $m_{b,\mathrm{h}}^2/x_{\mathrm{min}}$ and the IR cutoff is taken as $x_{\mathrm{min}} = m_{b,\mathrm{h}}/E_a$.

Regarding the sign of the 1-to-2 thermal pressure, a striking difference can be noted between the symmetry-breaking and symmetry-restoring scenarios. For the symmetry-breaking scenario, the pressure is positive for all values of γ, which implies that the thermal pressure always tends to retard the motion of the bubble wall. However, for the symmetry-restoring scenario, the pressure is negative for small values of γ, which tends to accelerate the bubble wall. The possibility of this negative pressure had been noted in earlier works [192], and here it is demonstrated with an explicit calculation. One can understand the negative pressure from the wall's longitudinal momentum change, which is also negative in a region of phase space. Note that $\Delta p_{1\to 2} \approx (-m_{a,\mathrm{h}}^2 + k_\perp^2/x)/2E_a$ in Equation 5.5, and since the integral over $k_\perp$ is dominated by the mass $k_\perp \approx m_{b,\mathrm{h}}$, and the integral over x is dominated by the IR cutoff $x \approx x_{\mathrm{min}} = m_{b,\mathrm{h}}/E_a$, then it follows that $\Delta p_{1\to 2} \sim (-m_{a,\mathrm{h}}^2 + m_{b,\mathrm{h}} \gamma T)/2E_a$. For small values of γ, the negative mass term dominates, which is why the 1-to-2 thermal pressure is negative for small γ. For large values of γ, the positive transverse momentum term dominates, and the pressure is positive. For intermediate values of γ, the pressure vanishes.

Figure 35 shows the ratio of the 1-to-2 thermal pressure in the symmetry-restoring scenario to that in the symmetry-breaking scenario, $\mathcal{P}_{1\to 2,\mathrm{h}\to\mathrm{s}}/\mathcal{P}_{1\to 2,\mathrm{s}\to\mathrm{h}}$. For large values of the Lorentz factor γ, the ratio asymptotes to ≈ 0.2 for all values of the masses that are shown. This universal scaling can be understood from the expression in Equation 5.5 for the wall's longitudinal momentum change $\Delta p_{1\to 2}$. For small x the leading terms are $\Delta p_{1\to 2} \approx (m_{b,\mathrm{h}}^2 + k_\perp^2)/2xE_a$ for the symmetry-breaking scenario and $\Delta p_{1\to 2} \approx k_\perp^2/2xE_a$ for the symmetry-restoring scenario. The absence of the $m_{b,\mathrm{h}}^2$ term causes the symmetry-restoring scenario to have a pressure that is smaller by an order one factor since the integral is dominated by $k_\perp \sim m_{b,\mathrm{h}}$.

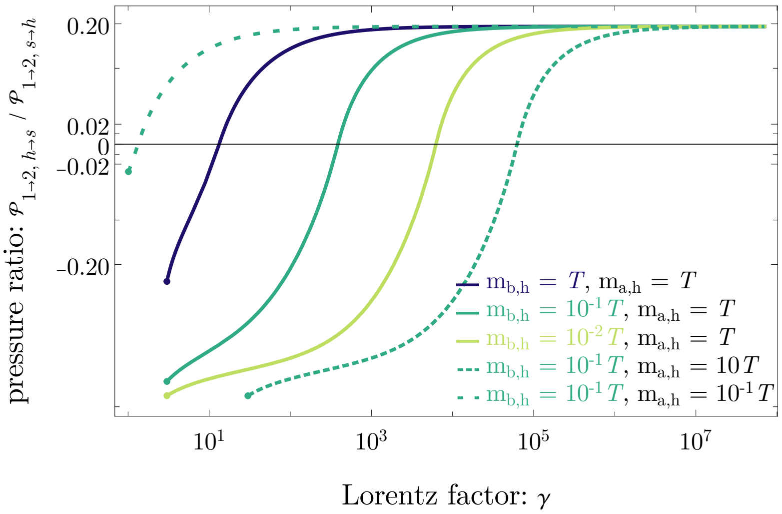

Figure 35: The ratio of the pressure in the symmetry-restoring scenario to that in the symmetry-breaking scenario as a function of the wall's Lorentz factor for several choices of masses. [3]

The curves in Figure 35 were found to admit a simple empirical fitting function:

$$\begin{aligned}\frac{\mathcal{P}_{1\to2,\mathrm{h}\to\mathrm{s}}}{\mathcal{P}_{1\to2,\mathrm{s}\to\mathrm{h}}} &\approx 0.5\tanh\left[\log(\gamma/\gamma_*)+\operatorname{arctanh}(0.6)\right]-0.3\,,\\ \gamma_* &\approx \frac{26\,(m_{a,\mathrm{h}}/T)^{2.2}}{(1+|\log m_{b,\mathrm{h}}/T|^{1.65})\,(m_{b,\mathrm{h}}/T)^{1.5}}-12\log(m_{a,\mathrm{h}}/T)-13\,,\end{aligned} \tag{5.11}$$

for $m_{b,\mathrm{h}} < T, m_{a,\mathrm{h}}$. This formula can be used to approximate the transition pressure in the symmetry-restoring scenario as a function of the masses $m_{a,\mathrm{h}}$ and $m_{b,\mathrm{h}}$ in a specific model without performing any numerical integrals.

5.2.2 Special Lorentz factors

Focusing now on the symmetry-restoring scenario, it is useful to identify two special values of the Lorentz factor γ. First γ_* is define to be the value of γ at which the pressure vanishes:

$$\mathcal{P}_{1\to2,\mathrm{h}\to\mathrm{s}}|_{\gamma_*} = 0\,. \tag{5.12}$$

Second γ_{90} is defined to be the value of γ at which the the pressure ratio, which appears in Figure 35, has reached 90% of its asymptotic value:

$$\left.\frac{\mathcal{P}_{1\to2,\mathrm{h}\to\mathrm{s}}}{\mathcal{P}_{1\to2,\mathrm{s}\to\mathrm{h}}}\right|_{\gamma_{90}} = 0.9\times\lim_{\gamma\to\infty}\frac{\mathcal{P}_{1\to2,\mathrm{h}\to\mathrm{s}}}{\mathcal{P}_{1\to2,\mathrm{s}\to\mathrm{h}}}\,. \tag{5.13}$$

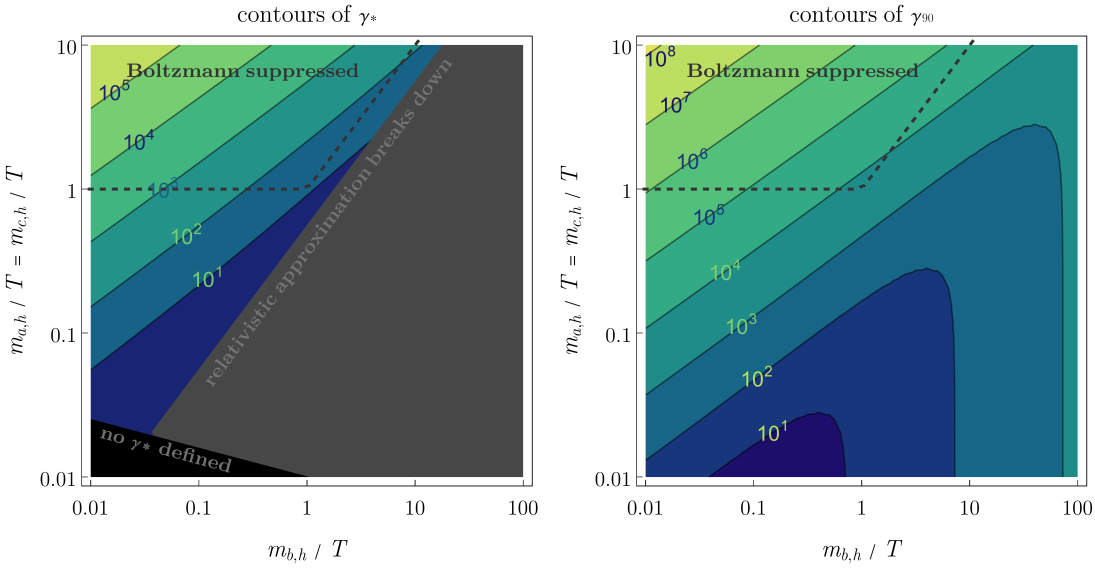

Figure 36: Special Lorentz factors across the parameter space of particle masses. In both panels the parameter space in which the broken-phase masses ($m_{a,\mathrm{h}} = m_{c,\mathrm{h}}$ and $m_{b,\mathrm{h}}$) are varied is shown. The first panel shows contours of γ_* (defined in Equation 5.12), and the second panel shows γ_{90} (defined in Equation 5.13). [3]

Note that $0 < \gamma_* < \gamma_{90}$. The choice of 90% is arbitrary. These two quantities, γ_* and γ_{90}, represent two important stages in the bubble expansion process where the pressure changes qualitatively. Below γ_*, the pressure is negative, hence thermal pressure does not slow the wall down. Above γ_*, the pressure switches to positive values, hence the pressure acts as a frictional force, as familiar in the standard (symmetry-breaking) phase transitions. However, the pressure is smaller in magnitude than in the symmetry-breaking scenario, hence the frictional force is not as efficient at slowing down the bubble wall. The behaviour familiar from the symmetry-breaking scenario, where pressure scales as $\sim \gamma m_{b,\mathrm{h}} T^3$, is achieved only at $\sim \gamma_{90}$. Beyond γ_{90}, the pressure can be expected to scale in the same way as the symmetry-breaking scenario for the same mass parameters.

In Figure 36 two contour plots are presented which show how γ_* and γ_{90} vary with the masses. For the plot of γ_*, in the bottom-left black region the thermal pressure does not vanish for any γ. For both plots, the top-left region bounded by the black-dashed lines, defined by the union of the two bounds $m_{a,\mathrm{h}} > T$ and $m_{a,\mathrm{h}} > m_{b,\mathrm{h}}$, represents the parameter space where the calculation is either inapplicable or requires additional model building. If $m_{a,\mathrm{h}} \gtrsim T$ *and* $m_{a,\mathrm{h}} > m_{b,\mathrm{h}}$, then Boltzmann suppression (depletion of the a-particle abundance via $aa \to bb$ annihilations) would prevent a-particles from achieving a thermal abundance $n_a \sim T^3$, which was assumed in the derivation of the pressure. This constraint can be circumvented with additional model-building: for example, if a-particles dropped out of thermal

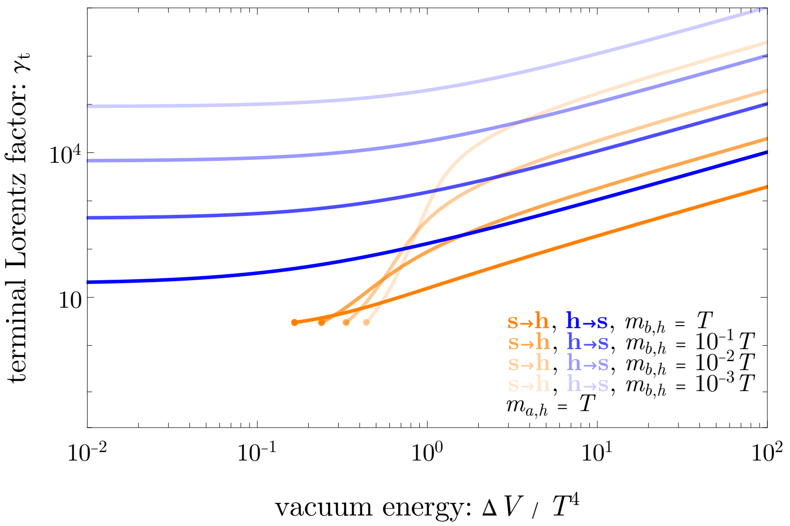

Figure 37: Terminal Lorentz factor γ_t as a function of the difference in vacuum energy $\Delta V/T^4$, for various choices of particle masses for symmetry-restoring scenarios (h $\to$ s, blue curves) and symmetry-breaking scenarios (s $\to$ h, orange curves). The gauge factor is taken to be $g^2 C_2[R] = 1$. [3]

equilibrium while they were still relativistic, then $aa \to bb$ annihilations are inactive at $T < m_{a,\mathrm{h}}$, and a thermal abundance can be maintained even for $m_{a,\mathrm{h}} > T$. Note that there is no analogous restriction on $m_{b,\mathrm{h}} > T$, since the pressure calculation only assumes a thermal population of a-particles, and the b-particles are not required to be present in the thermal bath. Recall that various approximations used in the Bödeker and Moore calculation break down if $\gamma_* T \lesssim m_{a,\mathrm{h}}, m_{b,\mathrm{h}}$; in the top panel, this region is represented by the bottom grey shaded region, where as a conservative boundary $\gamma_* T > 3m_{b,\mathrm{h}}$ was used.

5.2.3 Terminal velocity

Relativistic bubble walls can reach a terminal velocity at which the thermal pressure is balanced against the vacuum pressure [45]. For this discussion, the thermal pressure is denoted by $\mathcal{P}_{\mathrm{th}} \approx \mathcal{P}_{1\to1} + \mathcal{P}_{1\to2}$, and the vacuum pressure is denoted by $\mathcal{P}_{\mathrm{vac}} = -\Delta V$ where ΔV is the latent heat of the phase transition. If $P_{\mathrm{vac}} + P_{\mathrm{th}} < 0$ the bubble wall accelerates and the wall's Lorentz factor γ grows larger. As discussed above, $\mathcal{P}_{1\to1} \propto \gamma^0$ and $\mathcal{P}_{1\to2} \propto \gamma^1$ for large γ. Also, note that $\mathcal{P}_{\mathrm{vac}} \propto \gamma^0$. So as the wall accelerates, the bubble wall eventually reaches a terminal velocity at which $\gamma = \gamma_t$ and $P_{\mathrm{vac}} + P_{\mathrm{th}} = 0$.

In Figure 37 it is shown how the terminal Lorentz factor γ_t depends on the vacuum energy ΔV for several choices of the particle masses for symmetry-breaking (orange) and symmetry-restoring (blue) transitions. For large values of ΔV the terminal Lorentz factor grows as $\gamma_t \propto \Delta V$ for both the symmetry-breaking and symmetry-restoring scenarios. However, the bubble walls move more quickly in the symmetry-restoring scenario, and their γ_t is larger by a factor of ≈ 10.

As can be seen, this implies that the terminal behaviour is reached for $\gamma \sim \mathcal{O}(10 - 10^5)$ for the shown masses in the symmetry-breaking scenario. For smaller values of ΔV, it can be observed that γ_t decreases sharply for $\Delta V/T^4 \lesssim 1$ in the symmetry-breaking scenario. From comparing with Figure 34 one can see that in the symmetry-breaking scenario the pressure reaches a plateau for low γ, which comes from the positive contributions from $m_{b,\mathrm{h}}$ and $m_{c,\mathrm{h}}$ appearing in the momentum transfer in Equation 5.10. This plateau means that a small increase in ΔV leads to a large increase in γ_t. However, in the symmetry-restoring scenario the terminal Lorentz factor remains large even as $\Delta V/T^4 \ll 1$. This is because of the negative contributions for small γ in the symmetry-restoring scenario. Since the thermal pressure drops to zero at finite $\gamma = \gamma_*$, an arbitrarily small ΔV will not correspond to an arbitrarily small γ_t, but rather a finite $\gamma_t \sim \gamma_*$.

5.2.4 Implications for phenomenology

Various cosmological relics are expected to arise from cosmological FOPTs. These include GW radiation, primordial magnetic fields, particle asymmetries such as the cosmological baryon asymmetry, stable particles such as DM, topological defects, and PBHs. The detection of these relics in the Universe today is of paramount importance for understanding the physics of the early Universe. As demonstrated in this work, FOPTs in the symmetry-restoring scenario tend to produce faster bubbles than the symmetry-breaking scenario. A few consequences and observable signatures of these faster bubbles are briefly remarked here.

Gravitational waves:

A stochastic background of GW radiation is expected to arise from a cosmological FOPT. If the bubble walls achieve runaway behaviour, GWs are sourced by the scalar field energy densities during bubble collision [44, 94, 194–204] or by the distribution of particles produced from bubble collisions [205]. On the other hand, if the bubble walls achieve some terminal velocity long before the bubbles collide, GWs instead arise from sound waves [206–211] and turbulence [94, 209, 212–216] in the plasma, or through nontrivial spatial configurations of particles that do not thermalise [217]. The GWs produced by these various sources have different peak frequencies and spectral shapes (e.g. see Fig. 3 in Ref. [205]), as determined by the details of the underlying physics.

Since a symmetry-restoring phase transition tends to reach larger Lorentz factors, a greater fraction of the energy released in the phase transition is stored in the bubble walls at collision. This implies that the GW contribution from the first group of sources above (bubble collision, particles produced from collisions) is always greater in a symmetry-restoring transition. The amplitude of this GW component is expected to scale as the square of the energy density on the bubble walls, which scales linearly with γ_t; hence $\Omega_{GW} \propto \gamma_t^2$ for this component. The GW signal from symmetry-breaking and restoring transitions are therefore expected to be different even in the same theory (i.e. with the same particles and similar ΔV) (see also Ref. [190, 191, 232]).

Heavy relics:

During a cosmological FOPT, heavy particles can be produced even if their mass is far above the temperature of the phase transition [218–229]. This is possible because the energy scale of bubble collisions or bubble-plasma interactions is set by the boosted bubble wall energy $\sim \gamma T$, which can be several orders of magnitude higher than the temperature when $\gamma_t \gg 1$. Such interactions can produce massive states with mass $T < m < \gamma_t T$.

Since the symmetry-restoring transitions always reach larger γ_t values compared to the symmetry-breaking counterpart, they are more amenable to the production of such heavy states. For concreteness, consider the case where $m_{a,\mathrm{h}} = T, m_{b,\mathrm{h}} = 10^{-3}T$ and $\Delta V/T^4 = 1$ in Figure 37. Then $\gamma_t \sim 10^3(10^5)$ for the symmetry-breaking (restoring) scenario. In this case, states with mass $m \approx 10^4 T$ can be readily produced in the symmetry-restoring scenario, but not the symmetry-breaking scenario. Such particles could be DM [218, 221, 226, 227], source the baryon asymmetry of the Universe [219, 220, 222, 228, 229], or be of general interest for other reasons. In this sense, the phenomenology of symmetry-restoring transitions can be far richer than that of the symmetry-breaking ones due to the larger terminal Lorentz factors reached by the bubble walls.

5.3 Summary

In this section the dynamics of ultrarelativistic bubble walls during a cosmological FOPT were investigated. While there has been extensive research on symmetry-breaking scenarios in the past, this work focused on symmetry-restoring scenarios and the comparison of both. The thermal pressure that arises when particles in the plasma interact with the bubble wall was calculated. Earlier works by other authors have established that the 1-to-1 contribution to the thermal pressure is negative in the symmetry-restoring scenario, and that the 1-to-2 contribution is positive in the limit where the wall's Lorentz factor γ is large. In this work, there is a particular interest in understanding how the 1-to-2 thermal pressure behaves for small and intermediate values of γ. In the remainder of this summary, several qualitative results are highlighted which are important for various phenomenological applications.

The main result of this study is that the 1-to-2 thermal pressure can be *negative* if the bubble wall's Lorentz factor $\gamma < \gamma_*$ takes small-to-intermediate values (see Figure 34). This is in contrast with symmetry-breaking transitions, where the 1-to-2 pressure is always positive. The left panel of Figure 36 shows how γ_* depends on the masses of particles in the model (in which the 1-to-2 pressure is dominated by the emission of a transversely-polarised vector boson). This result is contrary to the intuition that the presence of significant interactions between the expanding bubble walls and the surrounding plasma produces a frictional force that slows the walls down.

For large values of $\gamma \gtrsim \gamma_{90}$, it was found that the 1-to-2 thermal pressure is positive and scales $\propto \gamma$, consistent with the results reported in Ref. [192]. The right panel of Figure 36 shows how γ_{90} depends on the particle masses.

A simple empirical fit function was provided in Equation 5.11 for the 1-to-2 thermal pressure as a function of the masses involved. This can be used to obtain an estimate of the pressure in a specific model of symmetry-restoring transitions in a straightforward manner without performing numerical phase-space integrations.

The Lorentz factor γ_t corresponding to the terminal velocity at which the thermal pressure balances the vacuum pressure was calculated. Since the thermal pressure in the symmetry-restoring scenario is smaller than the pressure in the symmetry-breaking scenario, it follows that the terminal velocity is larger. This enhancement factor is found to be $\gtrsim 10$ for the parameters illustrated in Figure 37.

The relatively larger terminal boost factor in a symmetry-restoring transition can have important phenomenological implications and applications. It can enhance the component of the GW signal produced from bubble collisions and from particles produced at bubble collisions, qualitatively modifying the peak, amplitude, and spectral features of the overall GW signal. Similarly, it can also enhance the production of particles with masses far higher than the temperature of the plasma, opening rich possibilities for various BSM applications such as the production of DM and the baryon asymmetry of the Universe.

In this work a model independent approach was followed. An interesting next step would be to apply the results to a specific model and compare for example the predicted GW signals to observed signals from PTA experiments such as NANOGrav [99], the Parkes Pulsar Timing Array [100] or the European Pulsar Timing Array [102]. Also the above mentioned implications for DM production and the baryon asymmetry are worth investigating further. Currently, a follow-up study is conducted where the parameter space of the 2HDMS, which was investigated earlier within the scope of this thesis, is checked for the possibility of a FOPT (see also the following references for studies on the 2HDM [42], the Minimal SM [240], Complex extension of the SM [241], N2HDM [242] and a study in the 2HDMS without the Z_2' symmetry [243]). Including the possibility of CP violation could give insights on whether this model can provide a strong enough phase transition to provide sufficient baryogenesis. However, the mentioned follow-up project will concentrate on the standard symmetry-breaking EW phase transition. Whether this model would in fact exhibit a symmetry-restoring FOPT during the evolution of our Universe remains to be investigated. In the aforementioned references on extensions of the SM, the possibility of restoring the EW symmetry at high energies was partly investigated which, however, is not a sufficient condition for a symmetry-restoring phase transition to indeed take place via the evolution of the Universe.

The results obtained here on the differences between symmetry-breaking and restoring transitions are only a first step which opens up new directions that need more investigation.

6 Conclusions

In this work two main topic were treated. The *first main topic* was on dark matter (DM) and collider phenomenology in a Two-Higgs-doublet model with an additional complex scalar singlet (2HDMS). The *second main topic* was on bubble wall velocity in FOPTs with symmetry restoration.

In the *first part* it was shown that the 2HDMS model can provide a viable DM candidate under consideration of all current theoretical and experimental constraints and explain the total relic amount of DM measured by the Planck experiment. At the same time this model can also accommodate the recently observed excess around 95 GeV observed both at the former Large Electron-Positron Collider (LEP) [8] in the $b\bar{b}$ mode as well as in the $\gamma\gamma$ mode at the Large Hadron Collider (LHC) experiments CMS [9] and ATLAS [10]. In section 4.3 scans over a large range of parameters were presented showing that a wide range of masses for the DM candidate can be accommodated within this model (see Figure 20). In section 4.4 six different benchmark points covering different regions of parameter space were chosen and investigated with respect to their prospects at future lepton colliders (electron-positron colliders like the proposed International Linear Collider (ILC), Compact Linear Collider (CLIC), Circular Electron Positron Collider (CEPC) and Future Circular Collider in electron-positron mode (FCC-ee) and the proposed muon collider) but also at the High-Luminosity Large Hadron Collider (LHC) and the Future Circular Collider in proton-proton mode (FCC-hh). It was shown that the selected benchmark scenarios have different prospects of discovery at the different proposed colliders. A general guide with different proposed final states to search for DM at these colliders was provided. At the HL-LHC the best prospects were found for **DM70** in the vector boson fusion (VBF) mode with a signal significance of $1.94\,\sigma$ and for $\mathbf{DM156_{w95}}$ in the $b\bar{b}$-associated Higgs boson production (BBH) mode with a signal significance of $1.95\,\sigma$. For electron-positron colliders the best prospects were found for $\mathbf{DM55_{w95}}$ in the Z+Missing transverse energy (MET) mode with a signal significance of $11\,\sigma$ and for **DM70** in the same mode with a significance of $3\,\sigma$, both at $\sqrt{s} = 250\,\text{GeV}$. For the proposed muon collider the best prospects were found for $\mathbf{DM156_{w95}}$ in the $b\bar{b}$+MET mode with a signal significance of 6.3σ at $\sqrt{s} = 3\,\text{TeV}$ and for the same benchmark is the γ+MET mode with a signal significance of $3\,\sigma$ at $\sqrt{s} = 1\,\text{TeV}$ and for $\mathbf{DM1000_{w95}}$ in the $t\bar{t}$+MET mode with a signal significance of $2.9\,\sigma$ at $\sqrt{s} = 10\,\text{TeV}$. The choice to also investigate the prospect of a muon collider at 1 TeV even though the starting energy was proposed to be 3 TeV mas made in order to show that even at low energies a muon collider can give good prospects for some of the benchmarks. In cases where the scalar Higgs boson, which mediates between the DM candidate and SM particles, is singlet dominated, detection at the proposed colliders can be extremely difficult. Hence, there exist viable DM scenarios which maybe can not be detected at any of these colliders. However, a rough analysis shows that the production cross section for these scenarios at future hadron colliders, like the FCC-hh or the Super Proton–Proton Collider (SPPC), can be improved by a factor of about $\sim 30-40$ compared to the current LHC.

In the *second part* the bubble wall velocity in first-order phase transitions (FOPTs) was investigated. Here, a more general approach was followed which can be applied to various models in which a FOPT occurs where in one phase particles are massless and in the other massive. This applies for example to the electroweak phase transition (EWPT) but also includes more general scenarios of phase transitions. The pressure on the bubble wall from transitions radiation, a process where a particle from the surrounding plasma passes into the bubble and radiates off an additional particle, was calculated for symmetry-restoring transitions and compared to the results for standard symmetry-breaking transitions following the approach in Ref. [45]. It was shown that in both scenarios runaway behaviour is inhibited by transition radiation processes and a terminal wall velocity is reached. However, in the symmetry-restoring scenario an intermediate regime, where the wall velocity gets further accelerated, was found. This leads to higher terminal velocities in the symmetry-restoring scenario than in the symmetry-breaking scenario. The terminal velocity of bubble walls can have an important impact on phenomenological consequences for example on the gravitational wave (GW) signal or on the production of heavy particles.

An interesting next step can be to apply the results for the bubble wall velocity to a specific model and check its viability. Currently a follow-up on the *first topic* is being done, investigating the parameter space of the 2HDMS model with respect to FOPTs. The investigation of the possibility of a symmetry-restoring transition in that model could be a next step and might open interesting phenomenological insights. In general the interplay of particles physics and cosmology is an interesting direction with still many topics to investigate.

References

[1] J. Dutta, J. Lahiri, C. Li, G. Moortgat-Pick, S. Farah Tabira, and J. A. Ziegler, “Dark matter phenomenology in 2hdms in light of the 95 gev excess”, *The European Physical Journal C*, vol. 84, no. 926, 2024, ISSN: 1434-6052. arXiv: 2308.05653 `[hep-ph]`.

[2] J. Dutta, J. Lahiri, C. Li, G. Moortgat-Pick, S. F. Tabira, and J. A. Ziegler, *Search for dark matter in 2hdms at lhc and future lepton colliders*, 2025. arXiv: 2504.14529 `[hep-ph]`.

[3] A. J. Long, B. Shakya, and J. A. Ziegler, *Bubble friction in symmetry-restoring transitions*, 2025. arXiv: 2511.10415 `[hep-ph]`.

[4] G. Aad et al., “Observation of a new particle in the search for the Standard Model Higgs boson with the ATLAS detector at the LHC”, *Phys. Lett. B*, vol. 716, pp. 1–29, 2012 . arXiv: 1207.7214 `[hep-ex]`.

[5] S. Chatrchyan et al., “Observation of a New Boson at a Mass of 125 GeV with the CMS Experiment at the LHC”, *Phys. Lett. B*, vol. 716, pp. 30–61, 2012 . arXiv: 1207.7235 `[hep-ex]`.

[6] P. W. Higgs, “Broken symmetries, massless particles and gauge fields”, *Phys. Lett.*, vol. 12, pp. 132–133, 1964 .

[7] A. A. Penzias and R. W. Wilson, “A Measurement of excess antenna temperature at 4080-Mc/s”, *Astrophys. J.*, vol. 142, pp. 419–421, 1965 .

[8] R. Barate et al., “Search for the standard model Higgs boson at LEP”, *Phys. Lett. B*, vol. 565, pp. 61–75, 2003 . arXiv: hep-ex/0306033.

[9] “Search for a standard model-like Higgs boson in the mass range between 70 and 110 GeV in the diphoton final state in proton-proton collisions at $\sqrt{s} = 13$ TeV”, 2023. arXiv: 2405.18149 `[hep-ex]`.

[10] G. Aad et al., “Search for diphoton resonances in the 66 to 110 GeV mass range using pp collisions at $\sqrt{s} = 13$ TeV with the ATLAS detector”, *Journal of High Energy Physics*, vol. 2025, no. 1, 2025, ISSN: 1029-8479. arXiv: 2407.07546 `[hep-ex]`.

[11] P. J. Fox and N. Weiner, “Light Signals from a Lighter Higgs”, *JHEP*, vol. 08, p. 025, 2018 . arXiv: 1710.07649 `[hep-ph]`.

[12] U. Haisch and A. Malinauskas, “Let there be light from a second light Higgs doublet”, *JHEP*, vol. 03, p. 135, 2018 . arXiv: 1712.06599 `[hep-ph]`.

[13] R. Benbrik, M. Boukidi, S. Moretti, and S. Semlali, “Explaining the 96 GeV Di-photon anomaly in a generic 2HDM Type-III”, *Phys. Lett. B*, vol. 832, p. 137 245, 2022 . arXiv: 2204.07470 `[hep-ph]`.

[14] R. Benbrik, M. Boukidi, and B. Manaut, “W-mass and 96 GeV excess in type-III 2HDM”, 2022. arXiv: 2204.11755 `[hep-ph]`.

[15] D. Azevedo, T. Biekötter, and P. M. Ferreira, “2HDM interpretations of the CMS diphoton excess at 95 GeV”, 2023. arXiv: 2305.19716 `[hep-ph]`.

[16] A. Belyaev, R. Benbrik, M. Boukidi, M. Chakraborti, S. Moretti, and S. Semlali, “Explanation of the Hints for a 95 GeV Higgs Boson within a 2-Higgs Doublet Model”, 2023. arXiv: 2306.09029 `[hep-ph]`.

[17] T. Biekötter, M. Chakraborti, and S. Heinemeyer, “A 96 GeV Higgs boson in the N2HDM”, *Eur. Phys. J. C*, vol. 80, no. 1, p. 2, 2020 . arXiv: 1903.11661 `[hep-ph]`.

[18] J. A. Aguilar-Saavedra, H. B. Câmara, F. R. Joaquim, and J. F. Seabra, “Confronting the 95 GeV excesses within the UN2HDM”, 2023. arXiv: 2307.03768 `[hep-ph]`.

[19] S. Banik, A. Crivellin, S. Iguro, and T. Kitahara, “Asymmetric Di-Higgs Signals of the N2HDM-$U(1)$”, 2023. arXiv: 2303.11351 `[hep-ph]`.

[20] S. Heinemeyer, C. Li, F. Lika, G. Moortgat-Pick, and S. Paasch, “Phenomenology of a 96 GeV Higgs boson in the 2HDM with an additional singlet”, *Phys. Rev. D*, vol. 106, no. 7, p. 075 003, 2022 . arXiv: 2112.11958 `[hep-ph]`.

[21] T. Biekötter and M. O. Olea-Romacho, “Reconciling Higgs physics and pseudo-Nambu-Goldstone dark matter in the S2HDM using a genetic algorithm”, *JHEP*, vol. 10, p. 215, 2021 . arXiv: 2108.10864 `[hep-ph]`.

[22] T. Biekötter, S. Heinemeyer, and G. Weiglein, “The CMS di-photon excess at 95 GeV in view of the LHC Run 2 results”, 2023. arXiv: 2303.12018 `[hep-ph]`.

[23] T. Biekötter, S. Heinemeyer, and G. Weiglein, “The 95.4 GeV di-photon excess at ATLAS and CMS”, 2023. arXiv: 2306.03889 `[hep-ph]`.

[24] J. Cao, X. Guo, Y. He, P. Wu, and Y. Zhang, “Diphoton signal of the light Higgs boson in natural NMSSM”, *Phys. Rev. D*, vol. 95, no. 11, p. 116 001, 2017 . arXiv: 1612.08522 `[hep-ph]`.

[25] J. Cao, X. Jia, Y. Yue, H. Zhou, and P. Zhu, “96 GeV diphoton excess in seesaw extensions of the natural NMSSM”, *Phys. Rev. D*, vol. 101, no. 5, p. 055 008, 2020 . arXiv: 1908.07206 `[hep-ph]`.

[26] K. Choi, S. H. Im, K. S. Jeong, and C. B. Park, “Light Higgs bosons in the general NMSSM”, *Eur. Phys. J. C*, vol. 79, no. 11, p. 956, 2019 . arXiv: 1906.03389 `[hep-ph]`.

[27] T. Biekötter, A. Grohsjean, S. Heinemeyer, C. Schwanenberger, and G. Weiglein, “Possible indications for new Higgs bosons in the reach of the LHC: N2HDM and NMSSM interpretations”, *Eur. Phys. J. C*, vol. 82, no. 2, p. 178, 2022 . arXiv: 2109.01128 `[hep-ph]`.

[28] W. Li, J. Zhu, K. Wang, S. Ma, P. Tian, and H. Qiao, “A light Higgs boson in the NMSSM confronted with the CMS di-photon and di-tau excesses”, 2022. arXiv: 2212.11739 `[hep-ph]`.

[29] J. M. Cline and T. Toma, “Pseudo-goldstone dark matter confronts cosmic ray and collider anomalies”, *Phys. Rev. D*, vol. 100, p. 035 023, 2019 .

[30] T. Biekötter, S. Heinemeyer, and C. Muñoz, “Precise prediction for the Higgs-boson masses in the $\mu\nu$ SSM”, *Eur. Phys. J. C*, vol. 78, no. 6, p. 504, 2018 . arXiv: 1712.07475 `[hep-ph]`.

[31] L. Liu, H. Qiao, K. Wang, and J. Zhu, “A Light Scalar in the Minimal Dilaton Model in Light of LHC Constraints”, *Chin. Phys. C*, vol. 43, no. 2, p. 023 104, 2019 . arXiv: 1812.00107 `[hep-ph]`.

[32] D. Liu, J. Liu, C. E. M. Wagner, and X.-P. Wang, “A Light Higgs at the LHC and the B-Anomalies”, *JHEP*, vol. 06, p. 150, 2018 . arXiv: 1805.01476 `[hep-ph]`.

[33] T. Biekötter, S. Heinemeyer, and C. Muñoz, “Precise prediction for the Higgs-Boson masses in the $\mu\nu$SSM with three right-handed neutrino superfields”, *Eur. Phys. J. C*, vol. 79, no. 8, p. 667, 2019 . arXiv: 1906.06173 `[hep-ph]`.

[34] F. Richard, “Search for a light radion at HL-LHC and ILC250”, 2017. arXiv: 1712.06410 `[hep-ex]`.

[35] J. A. Aguilar-Saavedra and F. R. Joaquim, “Multiphoton signals of a (96 GeV?) stealth boson”, *Eur. Phys. J. C*, vol. 80, no. 5, p. 403, 2020 . arXiv: 2002.07697 `[hep-ph]`.

[36] T. Biekötter, M. Chakraborti, and S. Heinemeyer, “The “96 GeV excess” at the LHC”, *Int. J. Mod. Phys. A*, vol. 36, no. 22, p. 2 142 018, 2021 . arXiv: 2003.05422 `[hep-ph]`.

[37] G. Coloretti, A. Crivellin, S. Bhattacharya, and B. Mellado, “Searching for Low-Mass Resonances Decaying into W Bosons”, 2023. arXiv: 2302.07276 `[hep-ph]`.

[38] S. Bhattacharya et al., "Growing Excesses of New Scalars at the Electroweak Scale", 2023. arXiv: 2306.17209 [hep-ph].

[39] S. Ashanujjaman, S. Banik, G. Coloretti, A. Crivellin, B. Mellado, and A.-T. Mulaudzi, "$SU(2)_L$ triplet scalar as the origin of the 95 GeV excess?", 2023. arXiv: 2306.15722 [hep-ph].

[40] P. Escribano, V. M. Lozano, and A. Vicente, "A Scotogenic explanation for the 95 GeV excesses", 2023. arXiv: 2306.03735 [hep-ph].

[41] D. Borah, S. Mahapatra, P. K. Paul, and N. Sahu, "Scotogenic U(1)Lμ-Lτ origin of (g-2)μ, W-mass anomaly and 95 GeV excess", *Phys. Rev. D*, vol. 109, no. 5, p. 055 021, 2024 . arXiv: 2310.11953 [hep-ph].

[42] T. Biekötter, S. Heinemeyer, and G. Weiglein, "95.4 GeV diphoton excess at ATLAS and CMS", *Physical Review D*, vol. 109, no. 3, 2024, ISSN: 2470-0029. arXiv: 2306.03889 [hep-ph].

[43] D. Baumann, *Cosmology*. Cambridge University Press, 2022.

[44] D. Bodeker and G. D. Moore, "Can electroweak bubble walls run away?", *JCAP*, vol. 05, p. 009, 2009 . arXiv: 0903.4099 [hep-ph].

[45] D. Bodeker and G. D. Moore, "Electroweak Bubble Wall Speed Limit", *JCAP*, vol. 05, p. 025, 2017 . arXiv: 1703.08215 [hep-ph].

[46] S. Höche, J. Kozaczuk, A. J. Long, J. Turner, and Y. Wang, "Towards an all-orders calculation of the electroweak bubble wall velocity", *JCAP*, vol. 03, p. 009, 2021 . arXiv: 2007.10343 [hep-ph].

[47] Y. Gouttenoire, R. Jinno, and F. Sala, "Friction pressure on relativistic bubble walls", 2021. arXiv: 2112.07686 [hep-ph].

[48] W.-Y. Ai, X. Nagels, and M. Vanvlasselaer, "Criterion for ultra-fast bubble walls: the impact of hydrodynamic obstruction", *JCAP*, vol. 03, p. 037, 2024 . arXiv: 2401.05911 [hep-ph].

[49] A. J. Long and J. Turner, "Thermal pressure on ultrarelativistic bubbles from a semiclassical formalism", *JCAP*, vol. 11, p. 024, 2024 . arXiv: 2407.18196 [hep-ph].

[50] W.-Y. Ai, M. Carosi, B. Garbrecht, C. Tamarit, and M. Vanvlasselaer, "Bubble wall dynamics from nonequilibrium quantum field theory", *JHEP*, vol. 08, p. 077, 2025 . arXiv: 2504.13725 [hep-ph].

[51] G. Barni, S. Blasi, and M. Vanvlasselaer, "The hydrodynamics of inverse phase transitions", *JCAP*, vol. 10, p. 042, 2024 . arXiv: 2406.01596 [hep-ph].

[52] E. W. Kolb and M. S. Turner, *The Early Universe*. Westview Press, 1990, vol. 69, ISBN: 978-0-201-62674-2.

[53] D. Baumann, *Tasi lectures on primordial cosmology*, 2018. arXiv: 1807.03098 `[hep-th]`.

[54] M. Trodden and S. M. Carroll, *Tasi lectures: Introduction to cosmology*, 2004. arXiv: astro-ph/0401547 `[astro-ph]`.

[55] K. Dimopoulos, *Introduction to Cosmic Inflation and Dark Energy*. CRC Press, Nov. 2020, ISBN: 978-1-351-17486-2, 978-0-367-61104-0.

[56] S. Navas et al., "Review of particle physics", *Phys. Rev. D*, vol. 110, no. 3, p. 030 001, 2024 .

[57] E. Hubble, "A relation between distance and radial velocity among extra-galactic nebulae", *Proceedings of the National Academy of Sciences*, vol. 15, no. 3, pp. 168–173, 1929 . eprint: https://www.pnas.org/doi/pdf/10.1073/pnas.15.3.168.

[58] A. G. Riess, W. H. Press, and R. P. Kirshner, "A Precise distance indicator: Type Ia supernova multicolor light curve shapes", *Astrophys. J.*, vol. 473, p. 88, 1996 . arXiv: astro-ph/9604143.

[59] P. A. R. Ade et al., "Planck 2013 results. I. Overview of products and scientific results", *Astron. Astrophys.*, vol. 571, A1, 2014 . arXiv: 1303.5062 `[astro-ph.CO]`.

[60] G. Hinshaw et al., "Nine-Year Wilkinson Microwave Anisotropy Probe (WMAP) Observations: Cosmological Parameter Results", *Astrophys. J. Suppl.*, vol. 208, p. 19, 2013 . arXiv: 1212.5226 `[astro-ph.CO]`.

[61] N. Aghanim et al., "Planck 2018 results. VI. Cosmological parameters", *Astron. Astrophys.*, vol. 641, [Erratum: Astron.Astrophys. 652, C4 (2021)], A6, 2020 . arXiv: 1807.06209 `[astro-ph.CO]`.

[62] A. H. Guth, "The Inflationary Universe: A Possible Solution to the Horizon and Flatness Problems", *Phys. Rev. D*, vol. 23, L.-Z. Fang and R. Ruffini, Eds., pp. 347–356, 1981 .

[63] A. Linde, "A new inflationary universe scenario: A possible solution of the horizon, flatness, homogeneity, isotropy and primordial monopole problems", *Physics Letters B*, vol. 108, no. 6, pp. 389–393, 1982, ISSN: 0370-2693.

[64] D. Baumann, "Inflation", in *Theoretical Advanced Study Institute in Elementary Particle Physics: Physics of the Large and the Small*, 2011, pp. 523–686. arXiv: 0907.5424 `[hep-th]`.

[65] L. Kofman, A. D. Linde, and A. A. Starobinsky, “Reheating after inflation”, *Phys. Rev. Lett.*, vol. 73, pp. 3195–3198, 1994 . arXiv: hep-th/9405187.

[66] L. Kofman, A. D. Linde, and A. A. Starobinsky, “Towards the theory of reheating after inflation”, *Phys. Rev. D*, vol. 56, pp. 3258–3295, 1997 . arXiv: hep-ph/9704452.

[67] K. D. Lozanov, *Lectures on reheating after inflation*, 2019. arXiv: 1907.04402 `[astro-ph.CO]`.

[68] I. Affleck and M. Dine, “A New Mechanism for Baryogenesis”, *Nucl. Phys. B*, vol. 249, pp. 361–380, 1985 .

[69] M. Fukugita and T. Yanagida, “Baryogenesis Without Grand Unification”, *Phys. Lett. B*, vol. 174, pp. 45–47, 1986 .

[70] S. Weinberg, *The Quantum theory of fields. Vol. 1: Foundations.* Cambridge University Press, Jun. 2005, ISBN: 978-0-521-67053-1, 978-0-511-25204-4.

[71] M. E. Peskin and D. V. Schroeder, *An Introduction to quantum field theory.* Reading, USA: Addison-Wesley, 1995, ISBN: 978-0-201-50397-5, 978-0-429-50355-9, 978-0-429-49417-8.

[72] E. Noether, “Invariante variationsprobleme”, ger, *Nachrichten von der Gesellschaft der Wissenschaften zu Göttingen, Mathematisch-Physikalische Klasse*, vol. 1918, pp. 235–257, 1918.

[73] S. G. Avery and B. U. W. Schwab, “Noether’s second theorem and Ward identities for gauge symmetries”, *Journal of High Energy Physics*, vol. 02, p. 031, 2016, ISSN: 1029-8479. arXiv: 1510.07038 `[hep-th]`.

[74] C. S. Wu, E. Ambler, R. W. Hayward, D. D. Hoppes, and R. P. Hudson, “Experimental Test of Parity Conservation in β Decay”, *Phys. Rev.*, vol. 105, pp. 1413–1414, 1957 .

[75] M. Gell-Mann, “The interpretation of the new particles as displaced charge multiplets”, *Nuovo Cim.*, vol. 4, no. S2, pp. 848–866, 1956 .

[76] L. Faddeev and V. Popov, “Feynman diagrams for the yang-mills field”, *Physics Letters B*, vol. 25, no. 1, pp. 29–30, 1967, ISSN: 0370-2693.

[77] C. Becchi, A. Rouet, and R. Stora, “Renormalization of gauge theories”, *Annals of Physics*, vol. 98, no. 2, pp. 287–321, 1976, ISSN: 0003-4916.

[78] A. D. Sakharov, “Violation of CP Invariance, C asymmetry, and baryon asymmetry of the universe”, *Pisma Zh. Eksp. Teor. Fiz.*, vol. 5, pp. 32–35, 1967 .

[79] M. Trodden, “Electroweak baryogenesis”, *Reviews of Modern Physics*, vol. 71, no. 5, pp. 1463–1500, 1999 .

[80] G. White, *Electroweak Baryogenesis (Second Edition)*. IOP, Apr. 2022, ISBN: 978-0-7503-3569-0, 978-0-7503-3570-6, 978-0-7503-3571-3.

[81] D. E. Morrissey and M. J. Ramsey-Musolf, “Electroweak baryogenesis”, *New J. Phys.*, vol. 14, p. 125 003, 2012 . arXiv: 1206.2942 `[hep-ph]`.

[82] A. G. Cohen, D. B. Kaplan, and A. E. Nelson, “Progress in electroweak baryogenesis”, *Ann. Rev. Nucl. Part. Sci.*, vol. 43, pp. 27–70, 1993 . arXiv: hep-ph/9302210.

[83] G. Bertone, D. Hooper, and J. Silk, “Particle dark matter: Evidence, candidates and constraints”, *Phys. Rept.*, vol. 405, pp. 279–390, 2005 . arXiv: hep-ph/0404175.

[84] J. M. Pendlebury et al., “Revised experimental upper limit on the electric dipole moment of the neutron”, *Phys. Rev. D*, vol. 92, no. 9, p. 092 003, 2015 . arXiv: 1509.04411 `[hep-ex]`.

[85] R. D. Peccei, “The Strong CP problem and axions”, *Lect. Notes Phys.*, vol. 741, M. Kuster, G. Raffelt, and B. Beltran, Eds., pp. 3–17, 2008 . arXiv: hep-ph/0607268.

[86] K. Radchenko Serdula, “Unlocking the Higgs Potential: from Colliders to the Cosmos”, Ph.D. dissertation, University of Hamburg, U. Hamburg (main), U. Hamburg (main), 2025.

[87] T. Marrodán Undagoitia and L. Rauch, “Dark matter direct-detection experiments”, *J. Phys. G*, vol. 43, no. 1, p. 013 001, 2016 . arXiv: 1509.08767 `[physics.ins-det]`.

[88] G. Belanger, F. Boudjema, and A. Pukhov, *Micromegas : A code for the calculation of dark matter properties in generic models of particle interaction*, 2014. arXiv: 1402.0787 `[hep-ph]`.

[89] G. Bélanger, F. Boudjema, A. Pukhov, and A. Semenov, “micrOMEGAs: Version 1.3”, *Computer Physics Communications*, vol. 174, no. 7, pp. 577–604, 2006 .

[90] G. Bélanger, F. Boudjema, A. Pukhov, and A. Semenov, “Dark matter direct detection rate in a generic model with micromegas_2.2”, *Computer Physics Communications*, vol. 180, no. 5, pp. 747–767, 2009, ISSN: 0010-4655.

[91] J. Aalbers et al., "First Dark Matter Search Results from the LUX-ZEPLIN (LZ) Experiment", *Physical Review Letters*, vol. 131, no. 4, 2023, ISSN: 1079-7114. arXiv: 2207.03764 `[hep-ex]`.

[92] M. Ackermann et al., "Constraining Dark Matter Models from a Combined Analysis of Milky Way Satellites with the Fermi Large Area Telescope", *Phys. Rev. Lett.*, vol. 107, p. 241 302, 2011 . arXiv: 1108.3546 `[astro-ph.HE]`.

[93] A. Albert et al., "Searching for Dark Matter Annihilation in Recently Discovered Milky Way Satellites with Fermi-LAT", *Astrophys. J.*, vol. 834, no. 2, p. 110, 2017 . arXiv: 1611.03184 `[astro-ph.HE]`.

[94] M. Kamionkowski, A. Kosowsky, and M. S. Turner, "Gravitational radiation from first order phase transitions", *Phys. Rev. D*, vol. 49, pp. 2837–2851, 1994 . arXiv: astro-ph/9310044.

[95] A. Maleknejad, *When geometry radiates review: Gravitational waves in theory, cosmology, and observation*, 2025. arXiv: 2512.21328 `[gr-qc]`.

[96] R. Allahverdi et al., "The first three seconds: A review of possible expansion histories of the early universe", *The Open Journal of Astrophysics*, vol. 4, no. 1, 2021, ISSN: 2565-6120. arXiv: 2006.16182 `[astro-ph]`.

[97] A. Mazumdar and G. White, "Review of cosmic phase transitions: their significance and experimental signatures", *Rept. Prog. Phys.*, vol. 82, no. 7, p. 076 901, 2019 . arXiv: 1811.01948 `[hep-ph]`.

[98] P. Auclair et al., "Cosmology with the Laser Interferometer Space Antenna", *Living Rev. Rel.*, vol. 26, no. 1, p. 5, 2023 . arXiv: 2204.05434 `[astro-ph.CO]`.

[99] G. Agazie et al., "The NANOGrav 15 yr Data Set: Evidence for a Gravitational-wave Background", *Astrophys. J. Lett.*, vol. 951, no. 1, p. L8, 2023 . arXiv: 2306.16213 `[astro-ph.HE]`.

[100] B. Goncharov et al., "On the evidence for a common-spectrum process in the search for the nanohertz gravitational-wave background with the parkes pulsar timing array", *The Astrophysical Journal Letters*, vol. 917, no. 2, p. L19, 2021, ISSN: 2041-8213. arXiv: 2107.12112 `[astro-ph]`.

[101] M. Falxa et al., "Searching for continuous Gravitational Waves in the second data release of the International Pulsar Timing Array", *Mon. Not. Roy. Astron. Soc.*, vol. 521, no. 4, pp. 5077–5086, 2023 . arXiv: 2303.10767 `[gr-qc]`.

[102] S. Chen et al., “Common-red-signal analysis with 24-yr high-precision timing of the european pulsar timing array: Inferences in the stochastic gravitational-wave background search”, *Monthly Notices of the Royal Astronomical Society*, vol. 508, no. 4, pp. 4970–4993, 2021, ISSN: 1365-2966. arXiv: 2110.13184 `[astro-ph]`.

[103] Y. Gouttenoire, “First-order phase transition interpretation of pulsar timing array signal is consistent with solar-mass black holes”, *Physical Review Letters*, vol. 131, no. 17, 2023, ISSN: 1079-7114. arXiv: 2307.04239 `[hep-ph]`.

[104] M. Wang, Z. Zhang, and H. Xu, *Discriminating between models of the nanohertz gravitational-wave background with pulsar timing arrays*, 2025. arXiv: 2510.22713 `[astro-ph.CO]`.

[105] G. Branco, P. Ferreira, L. Lavoura, M. Rebelo, M. Sher, and J. P. Silva, “Theory and phenomenology of two-higgs-doublet models”, *Physics Reports*, vol. 516, no. 1-2, pp. 1–102, 2012, ISSN: 0370-1573. arXiv: 1106.0034 `[hep-ph]`.

[106] S. Baum and N. R. Shah, “Two Higgs Doublets and a Complex Singlet: Disentangling the Decay Topologies and Associated Phenomenology”, *JHEP*, vol. 12, p. 044, 2018 . arXiv: 1808.02667 `[hep-ph]`.

[107] J. Dutta, G. Moortgat-Pick, and M. Schreiber, “Phenomenology of the dark matter sector in the 2HDM extended with complex scalar singlet”, *Eur. Phys. J. Plus*, vol. 140, no. 1, p. 87, 2025 . arXiv: 2203.05509 `[hep-ph]`.

[108] A. Dey, J. Lahiri, and B. Mukhopadhyaya, “LHC signals of a heavy doublet higgs as dark matter portal: Cut-based approach and improvement with gradient boosting and neural networks”, *Journal of High Energy Physics*, vol. 2019, no. 9, 2019 . arXiv: 1905.02242 `[hep-ph]`.

[109] R. A. Battye, A. Pilaftsis, and D. G. Viatic, “Domain wall constraints on two-higgs-doublet models with Z_2 symmetry”, *Physical Review D*, vol. 102, no. 12, 2020 .

[110] K. Saikawa, “A review of gravitational waves from cosmic domain walls”, *Universe*, vol. 3, no. 2, p. 40, 2017 .

[111] J. McDonald, “Gauge singlet scalars as cold dark matter”, *Physical Review D*, vol. 50, no. 6, pp. 3637–3649, 1994 .

[112] S. Chigusa and K. Nakayama, “Anomalous discrete flavor symmetry and domain wall problem”, *Physics Letters B*, vol. 788, pp. 249–255, 2019, ISSN: 0370-2693.

[113] C. Li, J. Li, S. Su, and W. Su, “The electroweak precision constraints of the 2HDM+S”, 2025. arXiv: 2507.14288 `[hep-ph]`.

[114] J. P. Ellis, “TikZ-Feynman: Feynman diagrams with TikZ”, *Computer Physics Communications*, vol. 210, pp. 103–123, 2017 . arXiv: 1601.05437 `[hep-ph]`.

[115] K. G. Klimenko, “On Necessary and Sufficient Conditions for Some Higgs Potentials to Be Bounded From Below”, *Theor. Math. Phys.*, vol. 62, pp. 58–65, 1985 .

[116] S. Nie and M. Sher, “Vacuum stability bounds in the two Higgs doublet model”, *Phys. Lett. B*, vol. 449, pp. 89–92, 1999 . arXiv: hep-ph/9811234.

[117] A. Drozd, B. Grzadkowski, J. F. Gunion, and Y. Jiang, “Extending two-Higgs-doublet models by a singlet scalar field - the Case for Dark Matter”, *JHEP*, vol. 11, p. 105, 2014 . arXiv: 1408.2106 `[hep-ph]`.

[118] K. Kannike, “Vacuum Stability Conditions From Copositivity Criteria”, *Eur. Phys. J. C*, vol. 72, p. 2093, 2012 . arXiv: 1205.3781 `[hep-ph]`.

[119] R. W. Cottle, G. J. Habetler, and C. E. Lemke, “On classes of copositive matrices”, *Linear Algebra and its Applications*, vol. 3, pp. 295–310, 1970 .

[120] C. R. Harris et al., “Array programming with NumPy”, *Nature*, vol. 585, no. 7825, pp. 357–362, 2020 . arXiv: 2006.10256 `[cs.MS]`.

[121] M. D. Goodsell and F. Staub, “Unitarity constraints on general scalar couplings with SARAH”, *Eur. Phys. J. C*, vol. 78, no. 8, p. 649, 2018 . arXiv: 1805.07306 `[hep-ph]`.

[122] W. Porod, “SPheno, a program for calculating supersymmetric spectra, SUSY particle decays and SUSY particle production at e+ e- colliders”, *Comput. Phys. Commun.*, vol. 153, pp. 275–315, 2003 . arXiv: hep-ph/0301101 `[hep-ph]`.

[123] W. Porod and F. Staub, “Spheno 3.1: Extensions including flavour, cp-phases and models beyond the mssm”, *Computer Physics Communications*, vol. 183, no. 11, pp. 2458–2469, 2012, ISSN: 0010-4655. arXiv: 1104.1573 `[hep-ph]`.

[124] W. G. Hollik, G. Weiglein, and J. Wittbrodt, “Impact of Vacuum Stability Constraints on the Phenomenology of Supersymmetric Models”, *JHEP*, vol. 03, p. 109, 2019 . arXiv: 1812.04644 `[hep-ph]`.

[125] P. M. Ferreira, M. Mühlleitner, R. Santos, G. Weiglein, and J. Wittbrodt, “Vacuum Instabilities in the N2HDM”, *JHEP*, vol. 09, p. 006, 2019 . arXiv: 1905.10234 `[hep-ph]`.

[126] T. L. Lee, T. Y. Li, and C. H. Tsai, “HOM4PS-2.0: a software package for solving polynomial systems by the polyhedral homotopy continuation method”, *Computing*, vol. 83, pp. 109–133, 2008 .

[127] P. Basler and M. Mühlleitner, “Bsmpt (beyond the standard model phase transitions): A tool for the electroweak phase transition in extended higgs sectors”, *Computer Physics Communications*, vol. 237, pp. 62–85, 2019, ISSN: 0010-4655. arXiv: 1803.02846 `[hep-ph]`.

[128] P. Basler, M. Mühlleitner, and J. Müller, “Bsmpt v2 a tool for the electroweak phase transition and the baryon asymmetry of the universe in extended higgs sectors”, *Computer Physics Communications*, vol. 269, p. 108 124, 2021, ISSN: 0010-4655. arXiv: 2007.01725 `[hep-ph]`.

[129] P. Basler, L. Biermann, M. Mühlleitner, J. Müller, R. Santos, and J. Viana, *Bsmpt v3 a tool for phase transitions and primordial gravitational waves in extended higgs sectors*, 2025. arXiv: 2404.19037 `[hep-ph]`.

[130] G. Aad et al., “Measurement of the Higgs boson mass in the $H \to ZZ^* \to 4\ell$ decay channel using 139 fb^{-1} of $\sqrt{s} = 13$ TeV pp collisions recorded by the ATLAS detector at the LHC”, *Physics Letters B*, vol. 843, p. 137 880, 2023, ISSN: 0370-2693. arXiv: 2207.00320 `[hep-ex]`.

[131] G. Aad et al., “Combination of searches for invisible decays of the Higgs boson using 139 fb−1 of proton-proton collision data at s=13 TeV collected with the ATLAS experiment”, *Phys. Lett. B*, vol. 842, p. 137 963, 2023 . arXiv: 2301.10731 `[hep-ex]`.

[132] A. Tumasyan et al., “A search for decays of the Higgs boson to invisible particles in events with a top-antitop quark pair or a vector boson in proton-proton collisions at $\sqrt{s} = 13$ TeV”, *The European Physical Journal C*, vol. 83, no. 10, 2023, ISSN: 1434-6052. arXiv: 2303.01214 `[hep-ex]`.

[133] J. Lees et al., “Precision Measurement of the $B \to X_s\gamma$ Photon Energy Spectrum, Branching Fraction, and Direct CP Asymmetry $A_{CP}(B \to X_{s+d}\gamma)$”, *Phys.Rev.Lett.*, vol. 109, p. 191 801, 2012 . arXiv: 1207.2690 `[hep-ex]`.

[134] R. Aaij et al., “Measurement of the $B_s^0 \to \mu^+\mu^-$ branching fraction and search for $B^0 \to \mu^+\mu^-$ decays at the LHCb experiment”, *Phys.Rev.Lett.*, vol. 111, p. 101 805, 2013 . arXiv: 1307.5024 `[hep-ex]`.

[135] S. Chatrchyan et al., “Measurement of the B(s) to mu+ mu- branching fraction and search for B0 to mu+ mu- with the CMS Experiment”, *Phys.Rev.Lett.*, vol. 111, p. 101 804, 2013 . arXiv: 1307.5025 `[hep-ex]`.

[136] “Review of Particle Physics”, *Progress of Theoretical and Experimental Physics*, vol. 2020, no. 8, https://academic.oup.com/ptep/article-pdf/2020/8/083C01/33653179/ptaa104.pdf, 2020, ISSN: 2050-3911.

[137] W. Grimus, L. Lavoura, O. M. Ogreid, and P. Osland, “A Precision constraint on multi-Higgs-doublet models”, *J. Phys. G*, vol. 35, p. 075 001, 2008 . arXiv: 0711.4022 `[hep-ph]`.

[138] W. Grimus, L. Lavoura, O. M. Ogreid, and P. Osland, “The Oblique parameters in multi-Higgs-doublet models”, *Nucl. Phys. B*, vol. 801, pp. 81–96, 2008 . arXiv: 0802.4353 `[hep-ph]`.

[139] G. Bélanger, F. Boudjema, A. Goudelis, A. Pukhov, and B. Zaldívar, “micrOMEGAs5.0 : Freeze-in”, *Computer Physics Communications*, vol. 231, pp. 173–186, 2018 . arXiv: 1801.03509 `[hep-ph]`.

[140] G. Alguero, G. Bélanger, S. Kraml, and A. Pukhov, “Co-scattering in micromegas: A case study for the singlet-triplet dark matter model”, *SciPost Physics*, vol. 13, no. 6, 2022, ISSN: 2542-4653. arXiv: 2207.10536 `[hep-ph]`.

[141] G. Bélanger et al., “Leptoquark manoeuvres in the dark: A simultaneous solution of the dark matter problem and the $R_{D^{(*)}}$ anomalies”, *Journal of High Energy Physics*, vol. 2022, no. 2, 2022, ISSN: 1029-8479. arXiv: 2111.08027 `[hep-ph]`.

[142] G. Bélanger, A. Mjallal, and A. Pukhov, “Recasting direct detection limits within micromegas and implication for non-standard dark matter scenarios”, *The European Physical Journal C*, vol. 81, no. 3, 2021, ISSN: 1434-6052. arXiv: 2003.08621 `[hep-ph]`.

[143] V. Barger, P. Langacker, M. McCaskey, M. Ramsey-Musolf, and G. Shaughnessy, “Complex Singlet Extension of the Standard Model”, *Phys. Rev. D*, vol. 79, p. 015 018, 2009 . arXiv: 0811.0393 `[hep-ph]`.

[144] G. Bélanger, A. Pukhov, C. E. Yaguna, and Ó. Zapata, “The Z_7 model of three-component scalar dark matter”, *JHEP*, vol. 03, p. 100, 2023 . arXiv: 2212.07488 `[hep-ph]`.

[145] G. Abbiendi et al., “Search for Charged Higgs bosons: Combined Results Using LEP Data”, *Eur. Phys. J. C*, vol. 73, p. 2463, 2013 . arXiv: 1301.6065 `[hep-ex]`.

[146] https://atlas.web.cern.ch/Atlas/GROUPS/PHYSICS/CombinedSummaryPlots/HDBS/.

[147] https://twiki.cern.ch/twiki/bin/view/CMSPublic/Summary2HDMSRun2.

[148] “A combination of measurements of Higgs boson production and decay using up to 139 fb^{-1} of proton–proton collision data at $\sqrt{s} = 13$ TeV collected with the ATLAS experiment”, CERN, Geneva, Tech. Rep. ATLAS-CONF-2020-027, Aug. 2020.

[149] F. Staub, “SARAH 4 : A tool for (not only SUSY) model builders”, *Comput. Phys. Commun.*, vol. 185, pp. 1773–1790, 2014 . arXiv: 1309.7223 `[hep-ph]`.

[150] H. Bahl et al., “HiggsTools: BSM scalar phenomenology with new versions of HiggsBounds and HiggsSignals”, *Comput. Phys. Commun.*, vol. 291, p. 108 803, 2023 . arXiv: 2210.09332 `[hep-ph]`.

[151] P. Bechtle, S. Heinemeyer, O. Stål, T. Stefaniak, and G. Weiglein, “$HiggsSignals$: Confronting arbitrary Higgs sectors with measurements at the Tevatron and the LHC”, *Eur. Phys. J. C*, vol. 74, no. 2, p. 2711, 2014 . arXiv: 1305.1933 `[hep-ph]`.

[152] P. Bechtle et al., “HiggsBounds $-$ 4: Improved Tests of Extended Higgs Sectors against Exclusion Bounds from LEP, the Tevatron and the LHC”, *Eur. Phys. J. C*, vol. 74, no. 3, p. 2693, 2014 . arXiv: 1311.0055 `[hep-ph]`.

[153] P. Bechtle et al., “HiggsBounds-5: Testing Higgs Sectors in the LHC 13 TeV Era”, *Eur. Phys. J. C*, vol. 80, no. 12, p. 1211, 2020 . arXiv: 2006.06007 `[hep-ph]`.

[154] P. Bechtle, S. Heinemeyer, T. Klingl, T. Stefaniak, G. Weiglein, and J. Wittbrodt, “HiggsSignals-2: Probing new physics with precision Higgs measurements in the LHC 13 TeV era”, *Eur. Phys. J. C*, vol. 81, no. 2, p. 145, 2021 . arXiv: 2012.09197 `[hep-ph]`.

[155] A. M. Sirunyan et al., “Search for additional neutral MSSM Higgs bosons in the $\tau\tau$ final state in proton-proton collisions at $\sqrt{s} = 13$ TeV”, *JHEP*, vol. 09, p. 007, 2018 . arXiv: 1803.06553 `[hep-ex]`.

[156] G. Aad et al., “Search for heavy Higgs bosons decaying into two tau leptons with the ATLAS detector using pp collisions at $\sqrt{s} = 13$ TeV”, *Phys. Rev. Lett.*, vol. 125, no. 5, p. 051 801, 2020 . arXiv: 2002.12223 `[hep-ex]`.

[157] “Searches for additional Higgs bosons and vector leptoquarks in $\tau\tau$ final states in proton-proton collisions at $\sqrt{s} = 13$ TeV”, 2022.

[158] C. Gross, O. Lebedev, and T. Toma, “Cancellation Mechanism for Dark-Matter–Nucleon Interaction”, *Phys. Rev. Lett.*, vol. 119, no. 19, p. 191 801, 2017 . arXiv: 1708.02253 `[hep-ph]`.

[159] T. Biekötter, P. Gabriel, M. O. Olea-Romacho, and R. Santos, “Direct detection of pseudo-Nambu-Goldstone dark matter in a two Higgs doublet plus singlet extension of the SM”, *JHEP*, vol. 10, p. 126, 2022 . arXiv: 2207.04973 `[hep-ph]`.

[160] O. e. Aberle, *High-Luminosity Large Hadron Collider (HL-LHC): Technical design report* (CERN Yellow Reports: Monographs). Geneva: CERN, 2020.

[161] H. Abramowicz et al., "The International Linear Collider Technical Design Report - Volume 4: Detectors", T. Behnke et al., Eds., 2013. arXiv: 1306.6329 `[physics.ins-det]`.

[162] "The International Linear Collider Technical Design Report - Volume 2: Physics", H. Baer et al., Eds., 2013. arXiv: 1306.6352 `[hep-ph]`.

[163] "The International Linear Collider Technical Design Report - Volume 3.I: Accelerator \& in the Technical Design Phase", C. Adolphsen et al., Eds., 2013. arXiv: 1306.6353 `[physics.acc-ph]`.

[164] "The International Linear Collider Technical Design Report - Volume 3.II: Accelerator Baseline Design", C. Adolphsen et al., Eds., 2013. arXiv: 1306.6328 `[physics.acc-ph]`.

[165] L. Evans and S. Michizono, "The International Linear Collider Machine Staging Report 2017", 2017. arXiv: 1711.00568 `[physics.acc-ph]`.

[166] P. Bambade et al., "The International Linear Collider: A Global Project", 2019. arXiv: 1903.01629 `[hep-ex]`.

[167] H. Abramowicz et al., "A Linear Collider Vision for the Future of Particle Physics", 2025. arXiv: 2503.19983 `[hep-ex]`.

[168] G. Moortgat-Pick et al., "Physics at the e+ e- Linear Collider", *Eur. Phys. J. C*, vol. 75, no. 8, G. Moortgat-Pick et al., Eds., p. 371, 2015 . arXiv: 1504.01726 `[hep-ph]`.

[169] G. Moortgat-Pick et al., "Polarized positrons and electrons at the linear collider", *Physics Reports*, vol. 460, no. 4, pp. 131–243, 2008, ISSN: 0370-1573. arXiv: hep-ph/0507011 `[hep-ph]`.

[170] T. K. Charles et al., "The Compact Linear Collider (CLIC) - 2018 Summary Report", vol. 2/2018, P. N. Burrows et al., Eds., 2018 . arXiv: 1812.06018 `[acc-ph]`.

[171] https://indico.cern.ch/event/1439855/contributions/6461475/.

[172] https://indico.cern.ch/event/1439855/contributions/6461433/.

[173] M. Benedikt et al., "FCC-ee: The Lepton Collider: Future Circular Collider Conceptual Design Report Volume 2. Future Circular Collider", CERN, Geneva, Tech. Rep. 2, 2019.

[174] "CEPC Conceptual Design Report: Volume 1 - Accelerator", 2018. arXiv: 1809.00285 `[physics.acc-ph]`.

[175] C. Accettura et al., "Interim report for the International Muon Collider Collaboration (IMCC)", vol. 2/2024, 2024 . arXiv: 2407.12450 `[physics.acc-ph]`.

[176] T. Han, Z. Liu, L.-T. Wang, and X. Wang, “WIMP Dark Matter at High Energy Muon Colliders –A White Paper for Snowmass 2021”, in *Snowmass 2021*, Mar. 2022. arXiv: 2203.07351 [hep-ph].

[177] O. Kittel and F. von der Pahlen, “Higgs boson interference in $\mu^+\mu^- \to \tilde{\chi}_i^+\tilde{\chi}_j^-$ with longitudinally polarized beams”, *Phys. Rev. D*, vol. 72, p. 095 004, 2005 . arXiv: hep-ph/0508267.

[178] C. Blöchinger et al., *Physics opportunities at mu+mu- higgs factories*, 2002. arXiv: hep-ph/0202199 [hep-ph].

[179] J. Alwall et al., “The automated computation of tree-level and next-to-leading order differential cross sections, and their matching to parton shower simulations”, *JHEP*, vol. 07, p. 079, 2014 . arXiv: 1405.0301 [hep-ph].

[180] J. Alwall, M. Herquet, F. Maltoni, O. Mattelaer, and T. Stelzer, “MadGraph 5 : Going Beyond”, *JHEP*, vol. 06, p. 128, 2011 . arXiv: 1106.0522 [hep-ph].

[181] C. Bierlich et al., “A comprehensive guide to the physics and usage of PYTHIA 8.3”, *SciPost Phys. Codeb.*, vol. 2022, p. 8, 2022 . arXiv: 2203.11601 [hep-ph].

[182] R. D. Ball et al., “Parton distributions with QED corrections”, *Nucl. Phys. B*, vol. 877, pp. 290–320, 2013 . arXiv: 1308.0598 [hep-ph].

[183] M. Selvaggi, “DELPHES 3: A modular framework for fast-simulation of generic collider experiments”, *J. Phys. Conf. Ser.*, vol. 523, J. Wang, Ed., p. 012 033, 2014 . arXiv: 1307.6346 [hep-ex].

[184] E. Conte, B. Fuks, and G. Serret, “MadAnalysis 5, A User-Friendly Framework for Collider Phenomenology”, *Comput. Phys. Commun.*, vol. 184, pp. 222–256, 2013 . arXiv: 1206.1599 [hep-ph].

[185] W. Kilian, T. Ohl, and J. Reuter, “WHIZARD: Simulating Multi-Particle Processes at LHC and ILC”, *Eur. Phys. J. C*, vol. 71, p. 1742, 2011 . arXiv: 0708.4233 [hep-ph].

[186] R. Harlander, M. Kramer, and M. Schumacher, “Bottom-quark associated Higgs-boson production: reconciling the four- and five-flavour scheme approach”, 2011. arXiv: 1112.3478 [hep-ph].

[187] M. Aaboud et al., “Search for dark matter and other new phenomena in events with an energetic jet and large missing transverse momentum using the ATLAS detector”, *JHEP*, vol. 01, p. 126, 2018 . arXiv: 1711.03301 [hep-ex].

[188] A. M. Sirunyan et al., “Search for invisible decays of a Higgs boson produced through vector boson fusion in proton-proton collisions at $\sqrt{s} = 13$ TeV”, *Phys. Lett. B*, vol. 793, pp. 520–551, 2019 . arXiv: 1809.05937 [hep-ex].

[189] M. Czakon and A. Mitov, “Top++: A Program for the Calculation of the Top-Pair Cross-Section at Hadron Colliders”, *Comput. Phys. Commun.*, vol. 185, p. 2930, 2014 . arXiv: 1112.5675 `[hep-ph]`.

[190] M. A. Buen-Abad, J. H. Chang, and A. Hook, “Gravitational wave signatures from reheating”, *Phys. Rev. D*, vol. 108, no. 3, p. 036 006, 2023 . arXiv: 2305.09712 `[hep-ph]`.

[191] G. Barni and A. Tesi, “Super-heated first order phase transitions”, 2025. arXiv: 2508.08362 `[hep-ph]`.

[192] A. Azatov, G. Barni, and R. Petrossian-Byrne, “NLO friction in symmetry restoring phase transitions”, *JHEP*, vol. 12, p. 056, 2024 . arXiv: 2405.19447 `[hep-ph]`.

[193] J. L. Barrow et al., “Theories and Experiments for Testable Baryogenesis Mechanisms: A Snowmass White Paper”, 2022. arXiv: 2203.07059 `[hep-ph]`.

[194] A. Kosowsky, M. S. Turner, and R. Watkins, “Gravitational radiation from colliding vacuum bubbles”, *Phys. Rev. D*, vol. 45, pp. 4514–4535, 1992 .

[195] A. Kosowsky, M. S. Turner, and R. Watkins, “Gravitational waves from first order cosmological phase transitions”, *Phys. Rev. Lett.*, vol. 69, pp. 2026–2029, 1992 .

[196] A. Kosowsky and M. S. Turner, “Gravitational radiation from colliding vacuum bubbles: envelope approximation to many bubble collisions”, *Phys. Rev. D*, vol. 47, pp. 4372–4391, 1993 . arXiv: astro-ph/9211004.

[197] C. Caprini, R. Durrer, and G. Servant, “Gravitational wave generation from bubble collisions in first-order phase transitions: An analytic approach”, *Phys. Rev. D*, vol. 77, p. 124 015, 2008 . arXiv: 0711.2593 `[astro-ph]`.

[198] S. J. Huber and T. Konstandin, “Gravitational Wave Production by Collisions: More Bubbles”, *JCAP*, vol. 09, p. 022, 2008 . arXiv: 0806.1828 `[hep-ph]`.

[199] R. Jinno and M. Takimoto, “Gravitational waves from bubble collisions: An analytic derivation”, *Phys. Rev. D*, vol. 95, no. 2, p. 024 009, 2017 . arXiv: 1605.01403 `[astro-ph.CO]`.

[200] R. Jinno and M. Takimoto, “Gravitational waves from bubble dynamics: Beyond the Envelope”, *JCAP*, vol. 01, p. 060, 2019 . arXiv: 1707.03111 `[hep-ph]`.

[201] T. Konstandin, “Gravitational radiation from a bulk flow model”, *JCAP*, vol. 03, p. 047, 2018 . arXiv: 1712.06869 `[astro-ph.CO]`.

[202] D. Cutting, M. Hindmarsh, and D. J. Weir, “Gravitational waves from vacuum first-order phase transitions: from the envelope to the lattice”, *Phys. Rev. D*, vol. 97, no. 12, p. 123 513, 2018 . arXiv: 1802.05712 `[astro-ph.CO]`.

[203] D. Cutting, E. G. Escartin, M. Hindmarsh, and D. J. Weir, “Gravitational waves from vacuum first order phase transitions II: from thin to thick walls”, 2020. arXiv: 2005.13537 `[astro-ph.CO]`.

[204] M. Lewicki and V. Vaskonen, “Gravitational waves from colliding vacuum bubbles in gauge theories”, *Eur. Phys. J. C*, vol. 81, no. 5, [Erratum: Eur.Phys.J.C 81, 1077 (2021)], p. 437, 2021 . arXiv: 2012.07826 `[astro-ph.CO]`.

[205] K. Inomata, M. Kamionkowski, K. Kasai, and B. Shakya, “Gravitational Waves from Particles Produced from Bubble Collisions in First-Order Phase Transitions”, 2024. arXiv: 2412.17912 `[astro-ph.CO]`.

[206] M. Hindmarsh, S. J. Huber, K. Rummukainen, and D. J. Weir, “Gravitational waves from the sound of a first order phase transition”, *Phys. Rev. Lett.*, vol. 112, p. 041 301, 2014 . arXiv: 1304.2433 `[hep-ph]`.

[207] M. Hindmarsh, S. J. Huber, K. Rummukainen, and D. J. Weir, “Numerical simulations of acoustically generated gravitational waves at a first order phase transition”, *Phys. Rev. D*, vol. 92, no. 12, p. 123 009, 2015 . arXiv: 1504.03291 `[astro-ph.CO]`.

[208] M. Hindmarsh, S. J. Huber, K. Rummukainen, and D. J. Weir, “Shape of the acoustic gravitational wave power spectrum from a first order phase transition”, *Phys. Rev. D*, vol. 96, no. 10, [Erratum: Phys.Rev.D 101, 089902 (2020)], p. 103 520, 2017 . arXiv: 1704.05871 `[astro-ph.CO]`.

[209] D. Cutting, M. Hindmarsh, and D. J. Weir, “Vorticity, kinetic energy, and suppressed gravitational wave production in strong first order phase transitions”, *Phys. Rev. Lett.*, vol. 125, no. 2, p. 021 302, 2020 . arXiv: 1906.00480 `[hep-ph]`.

[210] M. Hindmarsh, “Sound shell model for acoustic gravitational wave production at a first-order phase transition in the early Universe”, *Phys. Rev. Lett.*, vol. 120, no. 7, p. 071 301, 2018 . arXiv: 1608.04735 `[astro-ph.CO]`.

[211] M. Hindmarsh and M. Hijazi, “Gravitational waves from first order cosmological phase transitions in the Sound Shell Model”, *JCAP*, vol. 12, p. 062, 2019 . arXiv: 1909.10040 `[astro-ph.CO]`.

[212] C. Caprini, R. Durrer, and G. Servant, “The stochastic gravitational wave background from turbulence and magnetic fields generated by a first-order phase transition”, *JCAP*, vol. 12, p. 024, 2009 . arXiv: 0909.0622 `[astro-ph.CO]`.

[213] A. Brandenburg, T. Kahniashvili, S. Mandal, A. Roper Pol, A. G. Tevzadze, and T. Vachaspati, “Evolution of hydromagnetic turbulence from the electroweak phase transition”, *Phys. Rev. D*, vol. 96, no. 12, p. 123 528, 2017 . arXiv: 1711.03804 `[astro-ph.CO]`.

[214] A. Roper Pol, S. Mandal, A. Brandenburg, T. Kahniashvili, and A. Kosowsky, “Numerical simulations of gravitational waves from early-universe turbulence”, *Phys. Rev. D*, vol. 102, no. 8, p. 083 512, 2020 . arXiv: 1903.08585 `[astro-ph.CO]`.

[215] J. Dahl, M. Hindmarsh, K. Rummukainen, and D. Weir, “Decay of acoustic turbulence in two dimensions and implications for cosmological gravitational waves”, 2021. arXiv: 2112.12013 `[gr-qc]`.

[216] P. Auclair et al., “Generation of gravitational waves from freely decaying turbulence”, *JCAP*, vol. 09, p. 029, 2022 . arXiv: 2205.02588 `[astro-ph.CO]`.

[217] R. Jinno, B. Shakya, and J. van de Vis, “Gravitational Waves from Feebly Interacting Particles in a First Order Phase Transition”, 2022. arXiv: 2211.06405 `[gr-qc]`.

[218] A. Azatov, M. Vanvlasselaer, and W. Yin, “Dark Matter production from relativistic bubble walls”, *JHEP*, vol. 03, p. 288, 2021 . arXiv: 2101.05721 `[hep-ph]`.

[219] I. Baldes, S. Blasi, A. Mariotti, A. Sevrin, and K. Turbang, “Baryogenesis via relativistic bubble expansion”, *Phys. Rev. D*, vol. 104, no. 11, p. 115 029, 2021 . arXiv: 2106.15602 `[hep-ph]`.

[220] A. Azatov, M. Vanvlasselaer, and W. Yin, “Baryogenesis via relativistic bubble walls”, *JHEP*, vol. 10, p. 043, 2021 . arXiv: 2106.14913 `[hep-ph]`.

[221] I. Baldes, Y. Gouttenoire, and F. Sala, “Hot and heavy dark matter from a weak scale phase transition”, *SciPost Phys.*, vol. 14, no. 3, p. 033, 2023 . arXiv: 2207.05096 `[hep-ph]`.

[222] E. J. Chun, T. P. Dutka, T. H. Jung, X. Nagels, and M. Vanvlasselaer, “Bubble-assisted leptogenesis”, *JHEP*, vol. 09, p. 164, 2023 . arXiv: 2305.10759 `[hep-ph]`.

[223] I. Baldes, M. Dichtl, Y. Gouttenoire, and F. Sala, “Ultrahigh-Energy Particle Collisions and Heavy Dark Matter at Phase Transitions”, *Phys. Rev. Lett.*, vol. 134, no. 6, p. 061 001, 2025 . arXiv: 2306.15555 `[hep-ph]`.

[224] H. Mansour and B. Shakya, “Particle production from phase transition bubbles”, *Phys. Rev. D*, vol. 111, no. 2, p. 023 520, 2025 . arXiv: 2308.13070 `[hep-ph]`.

[225] B. Shakya, “Aspects of particle production from bubble dynamics at a first order phase transition”, *Phys. Rev. D*, vol. 111, no. 2, p. 023 521, 2025 . arXiv: 2308.16224 `[hep-ph]`.

[226] W.-Y. Ai, M. Fairbairn, K. Mimasu, and T. You, “Non-thermal production of heavy vector dark matter from relativistic bubble walls”, 2024. arXiv: 2406.20051 `[hep-ph]`.

[227] G. F. Giudice, H. M. Lee, A. Pomarol, and B. Shakya, “Nonthermal heavy dark matter from a first-order phase transition”, *JHEP*, vol. 12, p. 190, 2024 . arXiv: 2403.03252 `[hep-ph]`.

[228] M. Cataldi and B. Shakya, “Leptogenesis via bubble collisions”, *JCAP*, vol. 11, p. 047, 2024 . arXiv: 2407.16747 `[hep-ph]`.

[229] M. Cataldi, K. Müürsepp, and M. Vanvlasselaer, “CP-violation in production of heavy neutrinos from bubble collisions”, 2025. arXiv: 2506.12123 `[hep-ph]`.

[230] B. Shakya, “Did our Universe Tunnel out of the Wrong Higgs Vacuum?”, 2025. arXiv: 2511.08843 `[hep-ph]`.

[231] B. Shakya, “A Cosmic Higgs Collider”, 2025. arXiv: 2512.13815 `[hep-ph]`.

[232] G. Barni, S. Blasi, E. Madge, and M. Vanvlasselaer, “Gravitational waves from the sound shell model: direct and inverse phase transitions in the early Universe”, 2025. arXiv: 2510.21439 `[hep-ph]`.

[233] G. Barni, S. Blasi, and M. Vanvlasselaer, “Inverse bubbles from broken supersymmetry”, 2025. arXiv: 2503.01951 `[hep-ph]`.

[234] D. Suematsu, “Symmetry restoration due to preheating and lepton number asymmetry”, *Phys. Rev. D*, vol. 96, no. 5, p. 055 015, 2017 . arXiv: 1703.02740 `[hep-ph]`.

[235] W.-Y. Ai, P. Huang, and K.-P. Xie, “When inverse seesaw meets inverse electroweak phase transition: a novel path to leptogenesis”, 2025. arXiv: 2510.09000 `[hep-ph]`.

[236] J. R. Espinosa, T. Konstandin, J. M. No, and G. Servant, “Energy Budget of Cosmological First-order Phase Transitions”, *JCAP*, vol. 06, p. 028, 2010 . arXiv: 1004.4187 `[hep-ph]`.

[237] G. C. Dorsch, S. J. Huber, and T. Konstandin, “Bubble wall velocities in the Standard Model and beyond”, *JCAP*, vol. 1812, no. 12, p. 034, 2018 . arXiv: 1809.04907 `[hep-ph]`.

[238] P. B. Arnold, “One loop fluctuation - dissipation formula for bubble wall velocity”, *Phys. Rev. D*, vol. 48, pp. 1539–1545, 1993 . arXiv: hep-ph/9302258.

[239] A. Azatov, G. Barni, R. Petrossian-Byrne, and M. Vanvlasselaer, “Quantisation Across Bubble Walls and Friction”, 2023. arXiv: 2310.06972 `[hep-ph]`.

[240] P. B. Arnold and O. Espinosa, “The Effective potential and first order phase transitions: Beyond leading-order”, *Phys. Rev. D*, vol. 47, [Erratum: Phys.Rev.D 50, 6662 (1994)], p. 3546, 1993 . arXiv: hep-ph/9212235.

[241] V. Barger, P. Langacker, M. McCaskey, M. Ramsey-Musolf, and G. Shaughnessy, “Complex singlet extension of the standard model”, *Physical Review D*, vol. 79, no. 1, 2009, ISSN: 1550-2368. arXiv: 0811.0393 `[hep-ph]`.

[242] T. Biekötter, S. Heinemeyer, J. M. No, M. O. Olea, and G. Weiglein, “Fate of electroweak symmetry in the early universe: Non-restoration and trapped vacua in the n2hdm”, *Journal of Cosmology and Astroparticle Physics*, vol. 2021, no. 06, p. 018, 2021, ISSN: 1475-7516. arXiv: 2103.12707 `[hep-ph]`.

[243] G.-C. Cho and C. Idegawa, *Degenerate scalar scenario of two higgs doublet model with a complex singlet scalar*, 2025. arXiv: 2410.14328 `[hep-ph]`.

Eidesstattliche Versicherung

Hiermit versichere ich an Eides statt, die vorliegende Dissertationsschrift selbst verfasst und keine anderen als die angegebenen Hilfsmittel und Quellen benutzt zu haben.
Sofern im Zuge der Erstellung der vorliegenden Dissertationsschrift generative Künstliche Intelligenz (gKI) basierte elektronische Hilfsmittel verwendet wurden, versichere ich, dass meine eigene Leistung im Vordergrund stand und dass eine vollständige Dokumentation aller verwendeten Hilfsmittel gemäß der Guten wissenschaftlichen Praxis vorliegt. Ich trage die Verantwortung für eventuell durch die gKI generierte fehlerhafte oder verzerrte Inhalte, fehlerhafte Referenzen, Verstöße gegen das Datenschutz- und Urheberrecht oder Plagiate.

Ich versichere, dass dieses elektronische Exemplar der Dissertation und die in gebundener Form eingereichten Dissertationsexemplare identisch sind

Hamburg, 11. Mai 2026
Ort, Datum

Unterschrift